# Radar Cross Section Data Inversion for Snow-Covered Sea Ice Remote Sensing

by

Nariman Firoozy

A Thesis submitted to the Faculty of Graduate Studies of

the University of Manitoba

in partial fulfilment of the requirements of the degree of

DOCTOR OF PHILOSOPHY

Department of Electrical and Computer Engineering

University of Manitoba

Winnipeg

# Abstract

This thesis reports on my Ph.D. research in the area of microwave remote sensing of the Arctic. The main objective of this research is to reconstruct the dielectric profile of the snow-covered sea ice, and indirectly retrieve some of its geophysical and thermodynamic properties. To meet this objective, a nonlinear electromagnetic inverse scattering algorithm is developed that consists of forward and inverse solvers. The input to this algorithm is the normalized radar cross section (NRCS) data collected by radar systems from the snow-covered sea ice profile. The proposed inversion algorithm iteratively minimizes a discrepancy between the measured and simulated NRCS data (*i.e.*, the misfit cost function term) to achieve an accurate reconstruction. Herein, the boundary perturbation theory and the cloud model are utilized as the forward solver, and the differential evolution algorithm is used as the inverse solver.

Two main challenges associated with this inverse problem are its ill-posedness (which is often associated with the non-uniqueness of the solution and the instability of the associated mathematical problem) and its limited available scattering data. To tackle these challenges, the utilization of appropriate regularization and weighting schemes as well as the incorporation of prior information into the inversion algorithm are employed. These include the utilization of (*i*) appropriate weighting factors for the misfit cost function, (*ii*) more sensitive NRCS data with respect to the unknown parameters, (*iii*) further parametrization of the profile based on the expected permittivity distribution, (*iv*) time-series NRCS data to better initialize the inversion process, and (*v*) NRCS data collected by the satellite and on-site scatterometer to be inverted simultaneously for profile reconstruction.

The experimental data utilized in this thesis are collected by the author in collaboration with the Centre for Earth Observation Science. These measurements are performed on (*i*) the artificially-grown sea ice in the Sea-ice Environmental Research Facility, located at the University of Manitoba during Winter 2014, and (*ii*) the landfast sea ice located in the Arctic (Cambridge Bay, Nunavut) during May 2014. The measurement procedure includes NRCS data collection through an on-site C-band scatterometer and a spaceborne SAR satellite (*i.e.*, radarsat-2), and physical sampling of the snow and sea ice.

The proposed electromagnetic inverse scattering algorithm is utilized to invert these experimental data sets, as well as some synthetic data sets. It will be shown that the use of various techniques developed in this thesis in conjunction with the developed inversion algorithm results in reasonable snow-covered sea ice profile reconstruction.

# Acronyms and Symbols

| Acronym | Description |
|---|---|
| NRCS | Normalized radar cross section. |
| SERF | Sea-ice environmental research facility. |
| DE | Differential evolution. |
| BPT | Boundary perturbation theory. |
| SAR | Synthetic aperture radar. |
| VV | Vertical-sent vertical-receive polarization. |
| HH | Horizontal-sent horizontal-receive polarization. |
| VH | Vertical-sent horizontal-receive polarization. |
| HV | Horizontal-sent vertical-receive polarization. |
| FYI | First year ice. |
| MYI | Multi year ice. |
| YI | Young ice. |
| NI | New ice. |
| ppt | Part per thousand. |
| SPM | Small perturbation method. |
| NL | Noise level. |
| CF | Cost function. |
| TG | Temperature gradient. |
| GO | Geometric optics. |
| IEM | Integral equation method. |
| SFT | Strong fluctuation theory. |
| DMRT | dense medium radiative transfer theory. |
| FMCW | Frequency-modulated continuous-wave. |

| Symbol | Description |
|---|---|
| $\hat{x}$, $\hat{y}$, $\hat{z}$ | Unit vectors along $x$, $y$ and $z$ directions. |
| $j$ | Imaginary unit ($j^2 = -1$). |
| $k_b$ | Wavenumber of the background medium. |
| $\lambda_b$ | Wavelength of the background medium. |
| $\boldsymbol{E}^{\text{inc}}$ | Incident electric field. |
| $\boldsymbol{E}^{\text{scat}}$ | Scattered electric field. |
| $\boldsymbol{E}^{\text{scat}}_{\text{meas}}$ | Measured scattered electric field on the measurement domain $\mathcal{S}$. |
| $\boldsymbol{S}^{\text{p}}_{\text{s}}$ | Scattered power density with $p$ polarization. |
| $\boldsymbol{S}^{\text{q}}_{\text{i}}$ | Incident power density with $q$ polarization. |
| $\sigma^{pq}$ or $\sigma_{pq}$ | NRCS with $p$-sent $q$-receive polarization. |
| $(.)^*$ | Complex conjugate operator. |
| $(.)^{-1}$ | Inverse operator. |
| Re | Real part operator. |
| Imag | Imaginary part operator. |
| $\epsilon'$ | Real part of the relative complex permittivity. |
| $\epsilon''$ | Imaginary part of the relative complex permittivity. |
| $T$ | Temperature. |
| $S$ | Salinity. |
| $\rho$ | Density. |
| $\tau$ | Relaxation time. |
| $\kappa$ | Thermal diffusivity. |
| $C^P$ | Specific heat capacity. |
| $L^P$ | Latent heat. |
| $k^T$ | Thermal conductivity. |
| $\chi$ | Dielectric profile. |
| $\mathcal{L}(\chi)$ | Regularization cost function. |
| $\mathcal{C}(\chi)$ | Regularized cost function. |
| $\mathcal{F}(\chi)$ | Cost function. |
| $\kappa_{pq}$ | Regularized cost function weighting factor. |
| $\mathfrak{T}$ | Generalized transmission coefficient. |
| $\mathcal{R}$ | Generalized reflection coefficient. |
| $h$ | rms height. |
| $l$ | Correlation length. |
| $\Delta$ | Layer thickness. |

# Publications and Authorship Contribution

*Refereed Journal Papers (Accepted or Published)*

1. N. Firoozy, P. Mojabi, and D. Barber, "Nonlinear inversion of microwave scattering data for snow-covered sea-ice dielectric profile reconstruction," in *Geoscience and Remote Sensing Letters, IEEE*, vol. 12, no. 1, pp. 209-213, Jan 2015.
   - N. Firoozy: manuscript preparation, data processing, and interpretation
   - D. Barber, and P. Mojabi: advisory role
2. N. Firoozy, P. Mojabi, and D. G. Barber, "Balanced inversion of simulated bistatic radar cross-section data for remote sensing of snow-covered sea ice," in *Remote Sensing Letters, Taylor & Francis*, vol. 6, no. 5, pp. 399-408, 2015.
   - N. Firoozy: manuscript preparation, data processing, and interpretation
   - D. Barber, and P. Mojabi: advisory role
3. N. Firoozy, A. Komarov, J. Landy, D. Barber, P. Mojabi, and R. Scharien, "Inversion-based sensitivity analysis of snow-covered sea ice electromagnetic profiles," in *Selected Topics in Applied Earth Observations and Remote Sensing, IEEE Journal of*, vol. 8, no. 7, pp. 3643-3655, 2015.
   - N. Firoozy: manuscript preparation, data collection, processing, and interpretation
   - A. Komarov, J. Landy, and R. Scharien: data collection
   - D. Barber, and P. Mojabi: advisory role
4. N. Firoozy, A. Komarov, P. Mojabi, D. Barber, J. Landy, and R. Scharien, "Retrieval of young snow-covered sea-ice temperature and salinity evolution through radar cross-section inversion," in *Oceanic Engineering, IEEE Journal of*, vol. 41, no. 2, pp. 326-338, 2016.

- N. Firoozy: manuscript preparation, data collection, processing, and interpretation
- A. Komarov, J. Landy, and R. Scharien: data collection
- D. Barber, and P. Mojabi: advisory role

5. N. Firoozy, P. Mojabi, J. Landy, and D. Barber, "Landfast first-year snow-covered sea ice reconstruction via electromagnetic inversion," in *Selected Topics in Applied Earth Observations and Remote Sensing, IEEE Journal of*, vol. PP, no. 99, pp. 1-16, 2016, *Early Access*.

    - N. Firoozy: manuscript preparation, data collection[(1)], processing, and interpretation
    - J. Landy: data collection
    - D. Barber, and P. Mojabi: advisory role

*Refereed Conference Papers And Abstracts*

1. N. Firoozy, A. S. Komarov , P. Mojabi , J. C. Landy , D. G. Barber, "First-year snow covered sea ice polarimetric NRCS inversion in Cambridge Bay, Nunavut," in *Geoscience and Remote Sensing Symposium (IGARSS), 2015 IEEE International*, Italy, July 2015.

    - N. Firoozy: manuscript preparation, data collection, processing, and interpretation
    - A. Komarov, and J. Landy: data collection
    - D. Barber, and P. Mojabi: advisory role

2. N. Firoozy, and D. Barber, "Snow-covered sea ice parameter retrieval via electromagnetic global optimization inversion," in *Earth Observation for Ocean-Atmosphere Interactions Science*, Frascati, Italy Oct. 2014.

    - N. Firoozy: manuscript preparation, data processing, and interpretation
    - D. Barber: advisory role

3. N. Firoozy, P. Mojabi, and D. Barber, "Balanced inversion of radar cross section data for snow-covered sea ice dielectric profile reconstruction," in *Radio Science Meeting (Joint with AP-S Symposium)*, 2014 USNC-URSI, July 2014, pp. 176-176.

    - N. Firoozy: manuscript preparation, data processing, and interpretation
    - D. Barber, and P. Mojabi: advisory role

[(1)] The collaboration of Dr. Alexander Komarov in data collection is acknowledged.

4. N. Firoozy, P. Mojabi, and D. Barber, "Microwave remote sensing of multi-layered rough-surface snow-covered sea ice dielectric profile: sensitivity analysis and inversion," in *Geoscience and Remote Sensing Symposium (IGARSS), 2014 IEEE International*, July 2014, pp. 4872-4875.

    - N. Firoozy: manuscript preparation, data processing, and interpretation
    - D. Barber, and P. Mojabi: advisory role

5. N. Firoozy, P. Mojabi, D. Barber, "Sea ice electromagnetic profile reconstruction through inverse scattering solution by optimization," in *International Symposium on Sea Ice in a Changing Environment*, Hobart, Australia, March 2014.

    - N. Firoozy: manuscript preparation, data processing, and interpretation
    - D. Barber, and P. Mojabi: advisory role

# Acknowledgments

First and foremost, I would like to thank my academic advisors, Dr. Puyan Mojabi and Dr. David G. Barber, for their direction, support and encouragement during my Ph.D. studies. Furthermore, I would like to thank my colleagues Dr. Alexander Komarov, and Mr. Jack Landy.

I would also like to express my appreciation for my Ph.D. committee members, Dr. Joe LoVetri, Dr. Tim Papakyriakou, and Dr. Leif Pedersen for their efforts in the evaluation and improvement of my work.

Finally, I would like to extend my gratitude to the Natural Sciences and Engineering Research (NSERC) Council of Canada, the Canada Research Chair (CRC), and the Canada Excellence Research Chairs (CERC) programs for their financial support.

*To my parents*

# Contents

*Abstract* . . . . . i

*Acronyms and Symbols* . . . . . iii

*Publications and Authorship Contribution* . . . . . v

*Acknowledgments* . . . . . viii

*1. Introduction* . . . . . 1
1.1 Motivation and Rationale . . . . . 1
1.2 Research Objectives . . . . . 2
1.3 Thesis Structure and Outline . . . . . 4

*2. Background and Framework* . . . . . 7
2.1 Overview . . . . . 7
2.2 Snow-Covered Sea Ice Geophysics . . . . . 8
2.3 Snow-Covered Sea Ice Dielectric Properties . . . . . 12
2.4 Snow-Covered Sea Ice Thermodynamics . . . . . 21
2.5 Electromagnetic Inverse Scattering . . . . . 31

*3. Nonlinear Inverse Scattering Algorithm* . . . . . 47
3.1 Overview . . . . . 47
3.2 Introduction . . . . . 48
3.3 Problem Statement . . . . . 49
3.4 Parameterization of Snow-Covered Sea Ice Dielectric Profile . . . . . 50
3.5 Forward Solver . . . . . 51
3.6 Inverse Solver . . . . . 53
3.7 Inversion Results . . . . . 55
3.8 Conclusion . . . . . 62

*4. Balanced Inversion of Bistatic Data* . . . . . 63
4.1 Overview . . . . . 63
4.2 Introduction . . . . . 64

4.3 Inversion Methodology . . . . . 65
4.4 Balanced Inversion . . . . . 67
4.5 Synthetic Data Reconstruction Results . . . . . 71
4.6 Conclusion . . . . . 76

*5. SERF Experiment I: Inversion and Sensitivity Analysis* . . . . . 78
5.1 Overview . . . . . 78
5.2 Introduction . . . . . 80
5.3 Problem Statement . . . . . 82
5.4 Forward Scattering Solver . . . . . 83
5.5 Sensitivity Analysis . . . . . 86
5.6 Inversion Algorithm . . . . . 89
5.7 Synthetic Results . . . . . 90
5.8 Experimental Results . . . . . 91
5.9 Conclusion . . . . . 104

*6. SERF Experiment II: Temporal Evolution Retrieval* . . . . . 106
6.1 Overview . . . . . 106
6.2 Introduction . . . . . 108
6.3 Problem Statement . . . . . 109
6.4 General Strategy . . . . . 110
6.5 Measurements . . . . . 111
6.6 Inversion Algorithm . . . . . 122
6.7 Use of prior Information in Inversion . . . . . 126
6.8 Results . . . . . 130
6.9 Conclusion . . . . . 134

*7. Cambridge Bay Experiment: Enhanced Electromagnetic Modeling for Inversion* 136
7.1 Overview . . . . . 136
7.2 Introduction . . . . . 139
7.3 Measurements . . . . . 140
7.4 Forward Solver . . . . . 148
7.5 Inversion Algorithm . . . . . 157
7.6 Inversion Strategy . . . . . 158
7.7 Inversion Results . . . . . 163
7.8 Conclusion . . . . . 166

*8. Conclusion and Future Work* . . . . . 168
8.1 Conclusion . . . . . 168
8.2 Future Work . . . . . 173

*Appendix* 176

*A. Appendix A* . . . . . 177

*B. Appendix B* . . . . . 191

*C. Appendix C* . . . . . 196
C.1 Volume Scattering . . . . . 196
C.2 Surface Scattering . . . . . 203

# List of Tables


3.1 Dielectric profile specifications used for snow-covered YI in Section 3.7.1. The complex permittivity values are assumed to be constant within the frequency range of 3 to 4 GHz. . . . . 57

3.2 Reconstruction of surface roughness parameters; all roughness parameters are in centimetres. . . . . 61

4.1 Specifications of the snow-covered sea ice numerical model studied in Section 4.5 (Example 1). All length values are in (cm). Here, Half-Space refers to a medium with a boundary at infinity. . . . . 68

4.2 Specifications of the snow-covered sea ice numerical model studied in Section 4.5 (Example 2). All length values are in (cm). Here, Half-Space refers to a medium with a boundary at infinity. . . . . 72

4.3 Specifications of the snow-covered sea ice numerical model studied in Section 4.5 (Example 3). All length values are in (cm). Here, Half-Space refers to a medium with a boundary at infinity. . . . . 74

5.1 Dielectric profile specifications of the snow-covered ice profile considered in Section 5.4.2. $h$ and $l$ are the surface roughness parameters of rms height and correlation length, respectively. . . . . 85

5.2 Four possible states of top layer and their corresponding physical/chemical properties permittivity at the middle point. . . . . 98

5.3 Roughness parameters of rms height and correlation length ($i$) Approach A: along rectangular, with sampling interval scale of 2 $mm$, $1m \times 1m$ window ($ii$) Approach B: along arc, with sampling interval scale of 5 $mm$, $1m \times 1m$ window ($iii$) Chosen Values: based on lidar suggestions and electromagnetic modeling result comparison with measurement. *NA* refers to not available data. Values are in $cm$ . . . . . 100

6.1 The rms height, $h$, and correlation length, $l$, regarding the roughness parameters of the air-snow interface at 9 different incidence angles . . . 122

6.2 Salinity and temperature changes for the top four measurement reference points withing the time of interest interval . . . . . 130

7.1 The rms height, $h$, and correlation length, $l$, for the air-snow rough interface for different incidence angles $\theta$. The subscripts 1 and 2 denote two different sampling intervals having 0.2 cm and 0.5 cm grids respectively. NA refers to not available data. . . . . 148

7.2 The averaged parameters for each layer within the reference snow-covered sea ice profile. . . . . 160

A.1 Dielectric profile specifications of the multi-layered profile with rough boundaries. NA, $k_0$, and $\lambda$ denote not applicable, wave number in air, and wavelength in air. The looking angles are $\theta_{inc} = 45°$, $\phi_{inc} = 0°$, and $\phi_{scat} = 45°$. . . . . 187

A.2 Dielectric profile specifications of the multi-layered profile with rough boundaries. NA, $k_0$, and $\lambda$ denote not applicable, wave number in air, and wavelength in air. The looking angles are $\theta_{inc} = 45°$, $\phi_{inc} = 0°$, and $\phi_{scat} = 0°$. . . . . 188

A.3 Dielectric profile specifications of the multi-layered profile with rough boundaries. NA and $\lambda$ denote not applicable, wave number in air, and wavelength in air. The looking angles are $\theta_{inc} = 40°$, $\phi_{inc} = 0°$, and $\phi_{scat} = 0°$. . . . . 189

A.4 Dielectric profile specifications of the multi-layered profile with rough boundaries. NA denotes not applicable. The looking angles are $\theta_{inc} = \theta^{\circ}_{scat}$, $\phi_{inc} = 0°$, and $\phi_{scat} = 0°$. . . . . 190

# List of Figures


2.1 Ice growth evolution under various conditions . . . . . 9

2.2 Typical values for (a) real part of sea ice permittivity, (b) imaginary part of sea ice permittivity, (c) real part of brine-wetted dry snow permittivity, and (d) imaginary part of brine-wetted dry snow permittivity. ($T$ represents the temperature in $^{\circ}C$ and $S$ denotes the salinity in $ppt$.) PVS/de Loor method is utilized for mixture dielectric formula in this figure. . . . . 22

2.3 Schematic of one dimensional heat transfer, surface energy balance, and boundary conditions. The air-snow interface is at $z = 0$. . . . . 25

2.4 Seasonal evolution of the normalized radar cross section data with vertical-sent vertical-receive polarization, denoted by $\sigma_{VV}$, for the first-year sea ice measured at 5.3 GHz. . . . . 28

2.5 The nonlinear inversion algorithm scheme. . . . . 40

3.1 Parameterization of the snow-covered sea ice profile into rough layered media. . . . . 49

3.2 Reconstruction of the snow-covered YI for three different cases of Table 3.1 from bistatic data sets. . . . . 58

3.3 Reconstruction of the snow-covered YI for three different cases of Table 3.1 from monostatic data sets. . . . . 59

3.4 Reconstruction of Case I Profile in Table 3.1 from noisy data sets, with varying noise level $NL$, in both bistatic and monostatic (mono) configurations. . . . . 60

4.1 NRCS ratios when the profile of Table 4.1 is irradiated from $\psi_{\text{inc}} = (45^\circ, 0^\circ)$ direction, and the emanating scattered data is collected at different scattering angles. . . . . 69

4.2 The common logarithm ($\log_{10}$) of relative error in the reconstruction of the 12 unknowns using four different cost functions (CF) of the profiles of (a) Table 4.1, and (b) Table 4.2. The horizontal axis shows the parameter of interest, and the vertical axis is its corresponding error. Re and Imag denote the real-part and imaginary-part of the permittivity for the corresponding layer. $\Delta$ denotes the thickness parameter. In (a), 1st, 2nd, 3rd refer to as air-snow, snow-ice and ice-ocean interfaces. In (b), Layer I, Layer II, and Layer III refer to the layers within the ice as in Table 4.2. . . . . 73

4.3 Reconstructed permittivity and thickness values using (a) blind inversion of noiseless NRCS data for the profile shown in Table 4.2, (b) balanced inversion of noiseless NRCS data for the profile shown in Table 4.2, (c) blind inversion of noiseless NRCS data for the profile shown in Table 4.3, (d) balanced inversion of noiseless data for the profile shown in Table 4.3, (e) blind inversion of noisy NRCS data for the profile shown in Table 4.2, (f) balanced inversion of noisy NRCS data for the profile shown in Table 4.2, (g) blind inversion of noisy NRCS data for the profile shown in Table 4.3, and (h) balanced inversion of noisy data for the profile shown in Table 4.3. The horizontal lines in each figure represent the named interfaces (numbered from top to bottom). Real and Imag indicate the real and imaginary parts of the reconstructed relative permittivity (denoted by $\epsilon$). . . . . 77

5.1 Schematic of radar cross section measurements of a simplified snow-covered sea ice profile with rough interfaces through a scatterometer. As can be seen the incident direction $\Psi^{\text{inc}}$ is characterized by two angles; i.e., $\Psi^{\text{inc}} = (\theta^{\text{inc}}, \varphi^{\text{inc}})$. Also, the scattered direction $\Psi^{\text{scat}}$ is characterized by two angles; i.e., $\Psi^{\text{scat}} = (\theta^{\text{scat}}, \varphi^{\text{scat}})$. In the case of a monostatic setup, $\theta^{\text{scat}} = \theta^{\text{inc}}$, and $\varphi^{\text{scat}} = 180^\circ - \varphi^{\text{inc}}$. . . . . 84

5.2 NRCS (denoted by $\sigma$) for HH polarizations at 5 and 6 GHz for values of Table I in (a) Monostatic, and (b) Bistatic configurations. . . . . 86

5.3 Monostatic sensitivity analysis for the HH polarizations at 5.5 GHz for the profile of Table 5.1 (a) NRCS sensitivity with respect to permittivity, (b) NRCS sensitivity with respect to thickness. Here, $\Delta$ denotes the thickness values. . . . . 88

5.4 Bistatic sensitivity analysis for the HH polarizations at 5.5 GHz for the profile of Table 5.1 at 45° incidence angle (a) NRCS sensitivity with respect to permittivity, (b) NRCS sensitivity with respect to thickness. Here, $\Delta$ denotes the thickness values. . . . . 89

5.5 Reconstruction of the snow-covered sea ice dielectric profile of interest using two different synthetic data sets, Case I and Case II. The $y = 0$ line indicates the air-snow interface, (a) monostatic configuration, Case I, (b) monostatic configuration, Case II, (c) bistatic configuration, Case I, and (d) bistatic configuration, Case II . . . . . 91

5.6 SERF facility (a) The initial stage of sea-ice growth, (b) Calibration setup using a trihedral corner reflector at the last day of measurement. 93

5.7 Surface roughness measurement at SERF (a) Lidar placement under scatterometer in the shed, (b) Oblique view of the profile's surface. The scatterometer scanning area on the surface is outlined in black lines. . . 96

5.8 True profile (a) salinity and temperature measurements, (b) calculated permittivity. . . . . 98

5.9 Measured $\sigma_{VV}$ at sampling frequencies of 5.3, 5.4, 5.5, 5.6 and 5.7 GHz with error margin at each measurement. The inner box is a magnifier for more detailed view. (b) Comparison of $\sigma_{VV}$ between the simulated, denoted by Sim, and measured, denoted by Meas, at 5.5 GHz. . . . . 101

5.10 Comparison of $\sigma_{VV}$ between the simulated, denoted by Sim, and measured, denoted by Meas, at 5.5 GHz. . . . . 102

5.11 Reconstruction of the snow-covered sea ice dielectric profile of interest using two different data sets, Case I and Case II through monostatic configuration experimental data. (a) real permittivity profile, Case I, (b) imaginary permittivity profile, Case I, (c) real permittivity profile, Case II, (d) imaginary permittivity profile, Case II . . . . . 103

6.1 Simplified stair-cased snow-covered sea ice profile with rough interfaces. The top thin snow layer is assumed to have a homogeneous complex permittivity. The ice layer is assumed to have varying complex permittivity. . . . . 110

6.2 Measurements at the SERF (a) Scaffolding setup on which the scatterometer (on the roof of the scaffolding) and lidar (located on a tripod) are mounted. Both Scatterometer and lidar are looking toward the pool and scanning the snow-covered sea ice; (b) Scatterometer calibration through a trihedral corner reflector mounted on a tripod in the middle of the pool. . . . . 113

6.3 Air temperature measurements at the SERF through the MET station and the manual temperature meter. . . . . 116

6.4 Temperature string color map. First sensor is at the depth of 1.5 cm, and the rest of the sensors are placed with an interval of 2 cm. The colorbar represents the temperature in °C. The manually measured (total) ice thickness is projected on the plot as squares. . . . . 117

6.5 Manual ice temperature profiling. The solid line is only to connect the measurement points of the same profile height. . . . . 118

6.6 Manual salinity profiling (a) 0.75 cm up to 2.5 cm; (b) 9 cm up to 29 cm. 119

6.7 Time-series measured NRCS (denoted by $\sigma$) at 5.5 GHz for (a) HH polarization; (b) VV polarization; (c) VH polarization. The vertical lines denote the time intervals for (1) period of initial ice formation and rapid changes due snow-fall from January 25th 13pm to January 27th 7am, (2) period of stabilization from January 27th 7am to 30th 12am, (3) period of interest from January 30th 12am to February 3rd 2pm, (4) period of measurement halt, and (5) period of post measurement from February 7th 2pm to February 10th 8am. . . . . 121

6.8 Lidar scan of SERF's pool surface at 12pm on February 4th showing surface height for (a) the whole pool surface; (b) near detrended; and (c) far detrended. The colorbar scale is in [cm] in (a), and is in [m] in (b) and (c). . . . . 123

6.9 Time-series reconstruction results from January 30th 11am to February 3nd 2pm for the (a) Temperature profile; (b) Salinity Profile; and (c) Top layer (slush) density profile. Depth is given in cm. *Rec* and *Meas* stand for reconstructed and measured data. . . . . 131

6.10 The relationship of reconstructed points from 30th of January 11am to 3rd of February 2pm between (a) salinity and real part of the permittivity; (b) salinity and imaginary part of the permittivity; (c) temperature and real part of the permittivity; and (d) temperature and imaginary part of the permittivity. *Real* and *Imag* stand for real and imaginary part respectively. . . . . 134

6.11 (a) Trend comparison between the reconstructed temperature profile at 0.75 cm and the measured air temperature as well as the measured NRCS at 30°; (b) Trend comparison between the reconstructed salinity profile at 0.75 cm and the measured NRCS at 30°. *Rec* and *Meas* stand for reconstructed and measured data. The vertical axis is not to scale to accommodate comparison of data having different dimensions. . . . . 135

7.1 The measurement location (black square) at Cambridge Bay, Nunavut, Canada, both on a world-map and a magnified view. . . . . 141

7.2 Snowpack on May 22nd, 2014 at 4 pm. . . . . 142

7.3 Physical sampling data (temperature) from 9 am on May 20th, 2014 to 9 pm on May 28th, 2014. The solid horizontal line (*i.e.*, $y = 0$ line) is the snow-ice interface and the vertical dashed line mark the measurements performed at 6 pm on May 25th, 2014. . . . . 142

7.4 Physical sampling (salinity) data from 9 am on May 20th, 2014 to 9 pm on May 28th, 2014. The solid horizontal line (*i.e.*, $y = 0$ line) is the snow-ice interface and the vertical dashed line mark the measurements performed at 6 pm on May 25th, 2014. . . . . 143

7.5 Physical sampling (density) data from 9 am on May 20th, 2014 to 9 pm on May 28th, 2014. The horizontal line $y = 0$ is the snow-ice interface and the vertical dashed line mark the measurements performed at 6 pm on May 25th, 2014. . . . . 144

7.6 On-site measurements of snow-covered sea ice at Cambridge Bay, Nunavut. (a) Scatterometer NRCS measurement along side lidar on 23rd of May, 2014, (b) Scatterometer calibration using a metallic trihedral on 28th of May, 2014. . . . . 145

7.7 Measured time-series NRCS data (denoted by $\sigma$) at 5.5 GHz. The vertical lines represent (*i*) first period from 9am on May 20th to 4pm on May 24th, (*ii*) measurement halt from 4pm on May 24th to 5pm on May 25th, and (*iii*) second period of NRCS measurement from 5pm on May 25th to 12am on May 28th. . . . . 146

7.8 Radarsat-2 ScanSAR images cropped around Cambridge Bay area (approximately $115 \times 115$ $km^2$). The measurement area is marked by the yellow rectangles. (a) May 17th, HH Polarization. (b) May 17th, HV Polarization. (c) May 18th, HH Polarization. (d) May 18th, HV Polarization. Radarsat-2 Data and Products MacDonald, Dettwiler and Associates Ltd. 2014 - All Rights Reserved. Radarsat is an official mark of the Canadian Space Agency. . . . . 147

7.9 Lidar scan of the snow-covered sea ice profile measured through scatterometer on May 23rd. (a) The calculated rms height. (b) The calculated correlation length. The black arcs represent the scanning path of scatterometer. . . . . 148

7.10 Comparison of measured and simulated NRCS for 2pm on 24th of May. Subscripts *(sim)*, *(sim-cal)*, *(meas-scat)*, and *(meas-sat)* refer to simulated, calibrated simulated, measured by scatterometer, and measured through satellite respectively. Also subscripts $s$ and $v$ refer to surface and volume components. . . . . 156

7.11 The temporally-averaged physically measured values of snow-covered sea ice for (a) temperature, (b) salinity and (c) density, all of which up to 26th of May 2014. The uncertainty bars are their respective standard deviation values. (The top two points have large bars due to considering snowpack thickness (average) to be 18 cm for what is actually a variable thickness.) The horizontal dashed line at zero is the snow-ice interface. 162

7.12 The reconstructed (a) temperature, (b) salinity, and (c) density & snow grain size. The solid colored vertical lines are the retrieved parameter, the dashed colored vertical lines are the parameters derived based on the retrieved parameter, and the vertical colored dash-dot lines are the extra information (*i.e.*, not used in inversion). The colors blue (square), red (downside triangle), and green (upside triangle) represent the inversion in Scenario (I) (using satellite data), Scenario (II) (scatterometer data), and Scenario (III) (satellite plus scatterometer data) as inversion algorithm input. Circles in (c) are the reference (black) and reconstructed (colored) relative snow grain sizes for the basal snow layer, following the same color coding scheme. . . . . 163

A.1 Three-layer medium with flat surfaces. . . . . 178

A.2 The NRCS values associated with the profile of Table A.1 utilizing the implemented BPT. The superscript $ref$ denotes the NRCS values for the aforementioned profile. . . . . 188

A.3 The NRCS values associated with the profile of Table A.2 utilizing the implemented BPT. The superscript $ref$ denotes the NRCS values for the aforementioned profile, calculated through Sarabandi method. . . . 189

A.4 The NRCS values associated with the profile of (a) Table A.3 for comparison through MoM, and (b) Table A.4 for comparison through FVTD.190

C.1 Different wave configurations for (a) into the back-scattering tube from above, (b) into the back-scattering tube from below and bi-scattering tube, (c) exiting the back-scattering tube from above and bi-scattering tube, and (d) exiting the back-scattering tube from below. . . . . 198

# 1

# Introduction

This dissertation presents my doctoral research in the area of microwave remote sensing of the Arctic. The primarily objective was to retrieve some parameters of interest from the snow-covered sea ice profile utilizing the measured microwave scattering data. To achieve this objective, an electromagnetic inverse scattering algorithm[(1)] was developed, various profiles were studied, and new contributions were made to improve the accuracy of the reconstructed profiles.

## *1.1 Motivation and Rationale*

The Arctic has shown a trend of warming and an increase in the precipitation for the past few decades [1]. These have had a significant effect in the Arctic in the form of reduction of summer sea ice extent and lower sea ice thickness [2]. Moreover, a positive thermodynamic feedback mechanism in the Arctic has accelerated the sea ice

[(1)] Within the context of this thesis, inverse scattering algorithms may be referred to as nonlinear inversion algorithms (or, simply, inversion algorithms), reconstruction algorithms, or retrieval algorithms.

melt further. This melt pattern is projected to further unfold well into the 21$^{st}$ century with major environmental, social, sovereign, and economic impacts, on regional and global levels. Changes due to these impacts concern Canada significantly as it has almost 40% of its landmass within the Arctic boundary, and also neighbors vast arctic bodies of water on its northern coasts.

Despite negative impacts of the climate change, the altered Arctic has also laid the groundwork for some new opportunities. For instance, Canada is involved in the renewed development of energy and mineral resource extraction and the transportation in the Arctic tout de suite. Responsible and sustainable planning for such developments requires continuous monitoring and accurate modeling of the current and future physical state of the Arctic, amongst other measures. To achieve these monitoring and modeling goals, microwave remote sensing has been introduced as an effective tool to the Arctic sciences' toolbox. The usefulness of this tool is better understood considering the Arctic's remoteness, sheer size, and hazardous environment. Moreover, microwave remote sensing can provide day-and-night measurements regardless of weather conditions. As one of its objectives, microwave remote sensing investigates the utilization of the remotely collected electromagnetic data from the Arctic profile to retrieve some of its parameters of interest (*e.g.*, snow thickness). Despite prodigious progress in the past, the accurate parameter retrieval and profile classification through microwave remote sensing is still a challenging topic. Therefore, I set out to contribute to the solution of this problem as my Ph.D. research topic.

## *1.2 Research Objectives*

New remote sensing techniques and algorithms need to be developed so as to extract as much information as possible about the geophysical and thermodynamics state of the snow-covered sea ice in the Arctic. From microwave remote sensing perspective, an im-

portant piece of information about this profile is its dielectric properties. The dielectric properties of the snow-covered sea ice profile determines the way it interacts with an impinging electromagnetic wave. This quantitative information is dependent on other geophysical and thermodynamic properties of snow and sea ice (*e.g.*, temperature, salinity, and brine volume fraction); *e.g.*, see proxy formulas in [3–6]. These secondary parameters are of great interest as being the input data to various thermodynamic and climate models. Therefore, the focus of this thesis is on the reconstruction of the dielectric profile (*i.e.*, thickness values, complex permittivities, and roughness parameters) and the indirect retrieval of its thermodynamic and physical parameters (*e.g.*, temperature profile).

In this research, the snow-covered sea ice profile is reconstructed within the framework of electromagnetic inverse scattering. Performing three different steps is commonly required in this framework: (*i*) data collection, (*ii*) data calibration, and (*iii*) data processing [7]. In the data collection step, the domain of interest is irradiated by an antenna and the scattered data is then collected by a receiving antenna (same as transmitting antenna in the case of monostatic configuration). In the next step, the measured data set is calibrated against another data set collected from a scatterer with a known scattering matrix. Finally, in the data processing step, the calibrated measured data is utilized as the input to an appropriate electromagnetic inverse scattering algorithm to find[(2)] the quantitative dielectric profile of the snow-covered sea ice. This research will utilize all these three steps with an emphasis on data processing. Therefore, our principal goal can further be categorized into the following items.

1. Development of an inversion algorithm that is capable of retrieval of snow-covered sea ice parameters. This algorithm iteratively minimizes the discrepancy between the measured and simulated microwave scattering data. This process requires the

[(2)] Within the context of this thesis, finding the dielectric profile may be referred to as reconstructing the dielectric profile or retrieving the dielectric profile.

utilization of an electromagnetic inverse solver in conjunction with an electromagnetic forward scattering solver.

2. Collection of physical and polarimetric normalized radar cross section (NRCS) data from various snow-covered sea ice profiles. Physical sampling includes the *in-situ* measurement of density, salinity, and temperature of the snow and sea ice. Herein, the NRCS data collection is performed through a ground-based radar system (*i.e.*, C-band scatterometer), and a space-borne satellite (*i.e.*, radarsat-2). The inversion algorithm will then utilize the collected NRCS data to retrieve the parameters of interest. Within this thesis, this process is sometimes referred to as the inversion of the NRCS data.

3. Development of strategies to tackle the challenges (*e.g.*, ill-posedness[3], lack of *sufficient* data, nonlinearity) associated with this electromagnetic inverse scattering problem.

4. Validation and improvement of the inversion algorithm for various measurement configurations and snow-covered sea ice profiles.

It should finally be noted that the contributions made as a result of my Ph.D. research to meet the objectives mentioned above are outlined in Chapter 8.

## *1.3 Thesis Structure and Outline*

This thesis is structured based on the grouped manuscript style (*i.e.*, sandwich thesis). Therefore, Chapters 3 to 7 are the candidate's peer-reviewed journal papers. The

[3] Based on Jacques Hadamard, a problem is well-posed if it satisfies the following three criteria: (*i*) existence of the solution, (*ii*) uniqueness of the solution, (*iii*) the solution depends continuously on the data [8]. The violation of any of these criteria results in an ill-posed problem. The first criterion is often satisfied in the sense that a physical solution exists. However, it should be noted that the mathematical problem set up to represent the actual problem may not have a solution; *e.g.*, due to the use of a poor model. The second and third criteria are usually treated by collecting as much reliable information as possible, use of prior information, and various regularization techniques.

collection of these papers contributes towards the principal goal of the thesis, as defined in Section 1.2. Moreover, it should be mentioned that the papers enclosed in this thesis are slightly edited to avoid repetitions and to achieve a consistent format throughout. Nonetheless, some general concepts might be repeated for the benefit of the reader (*e.g.*, the cost function formulation).

The outlines of each chapter are presented below.

- In Chapter 2, the background required for a general comprehension of microwave remote sensing of the snow-covered sea ice is presented. This includes investigation of the geophysics, thermodynamics, and dielectric properties of the snow and sea ice. At the end, the basics of electromagnetic inverse scattering algorithm associated with the snow-covered sea ice profile are explained.
- Chapter 3 introduces the nonlinear inversion algorithm developed to reconstruct the dielectric profile of the snow-covered sea ice. In this chapter, the inversion is performed on noisy and noiseless synthetic NRCS data. It is demonstrated that the algorithm is capable of reconstructing the unknowns (*e.g.*, complex permittivity, roughness parameters, and thickness) accurately.
- The bistatic configuration is investigated in Chapter 4. For this configuration, a new weighting factor for the cost function is introduced. It is shown that the utilization of the introduced weighting factor results in higher reconstruction accuracy compared to the conventional weighting factors. The study presented in Chapter 4 is based on noisy and noiseless synthetic NRCS data.
- In Chapter 5, the sensitivity of the NRCS data with respect to the unknown profile parameters is studied. It is demonstrated that the use of more sensitive NRCS data results in enhanced reconstruction. In addition, in an attempt to reduce the number of unknowns, I propose a new parametrization so as to incorporate prior information about the complex permittivity profile of the snow-covered sea ice

of interest into the inversion algorithm. This chapter utilizes both synthetic and measured NRCS data. The measured data were collected via a monostatic C-band scatterometer that irradiated the snow-covered sea ice profile grown artificially at the Sea-ice Environmental Research Facility (SERF) in winter 2014. Within the context of this thesis, I refer to this experiment as SERF Experiment I.

– A new inversion strategy is introduced in Chapter 6 to take advantage of the time-series NRCS data so as to retrieve the temporal evolution of temperature, salinity, and density profiles of the snow-covered sea ice. The employment of the time-series NRCS data allows the minimization of the search space for problem unknowns, thus, achieving better reconstruction accuracy. The experimental data utilized in this chapter were collected at the SERF in winter 2014. Within the context of this thesis, I refer to this experiment as SERF Experiment II.

– Chapter 7 investigates the retrieval of snowpack parameters of the snow-covered sea ice profile. To this end, the inversion algorithm is equipped with an enhanced forward solver. The enhancement is focused on incorporating a volume scattering component into the forward solver. This is important due to the existence of large inclusions within the snowpack. The temporal NRCS and physical sampling data in this chapter were collected in Cambridge Bay, NU, located within the Arctic Circle, during May 2014. Both scatterometer and satellite data are inverted in this chapter. (A profile averaging technique is also applied to reduce the number of unknown parameters.) Within the context of this thesis, I refer to the experiment considered in this chapter as Cambridge Bay Experiment.

– A conclusion is presented in Chapter 8. This chapter includes a summary of the thesis and my contributions to the area of microwave remote sensing of the snow-covered sea. Furthermore, my recommendations for future work based on the findings of this research are outlined.

# 2

# Background and Framework

## *2.1 Overview*

In this chapter, the background on the snow-covered sea ice (*i*) geophysics, (*ii*) dielectric properties, and (*iii*) thermodynamics are presented. In addition, a background concept for inversion algorithms is explained. In Section 2.2, the geophysics of the snow and sea ice, as the constituents of the snow-covered sea ice profile, are described. In particular, the sea ice formation process and the presence of brine inclusions in the sea ice are studied. Furthermore, the snow structure and its variations are investigated. Next, in Section 2.3, the formulas to calculate the permittivity values of single and multi-phase dielectric materials are presented. These include the Debye, mixing, and semi-empirical formulas that are utilized to calculate the permittivity values of various dielectric materials, including snow and sea ice. Subsequently, it is shown that the dielectric properties of snow and sea ice are dependent on their geophysical state. In Section 2.4, the thermodynamics of the snow-covered sea ice profile in the arctic environment is presented. To this end, the formulas to calculate various thermody-

namic parameters of the snow and sea ice (*e.g.*, specific heat) are presented. Next, a one-dimensional heat transfer model is introduced that relates the transfer of energy through snow-covered sea ice profile, to the growth or melt of each layer. Afterwords, the thermodynamics of the snow-covered sea ice is put in perspective with respect to its geophysics and dielectric properties. Finally, the concept of the electromagnetic inverse scattering associated with the snow-covered sea ice is introduced in Section 2.5. This includes the description of the electromagnetic forward and inverse solvers. At the end, the topics of parameterization and use of prior information to tackle the ill-posedness associated with the snow-covered sea ice electromagnetic inverse scattering are briefly explained.

## *2.2 Snow-Covered Sea Ice Geophysics*

This section investigates the geophysics of snow and ice in the Arctic. First, in Section 2.2.1, the ice formation process and geophysics are explained. This topic is then followed by a description of the snow geophysics and metamorphism in Section 2.2.2. It should be noted that the focus of the research presented in this thesis is on snow-covered sea ice formed under calm conditions.

### *2.2.1 Sea Ice*

*Sea Ice Formation*

Sea ice is a product of cooling saline ocean water. The initial formation of sea ice is influenced by presence of snow fall and water turbulence due to wind or wave, as shown in Figure 2.1. The general sea ice formation process under calm conditions is explained as follows. (This explanation is based on [10].) When the open water surface temperature drops down to the freezing point ($-1.8\,^{\circ}\mathrm{C}$ for 32 ppt salinity), minute disks

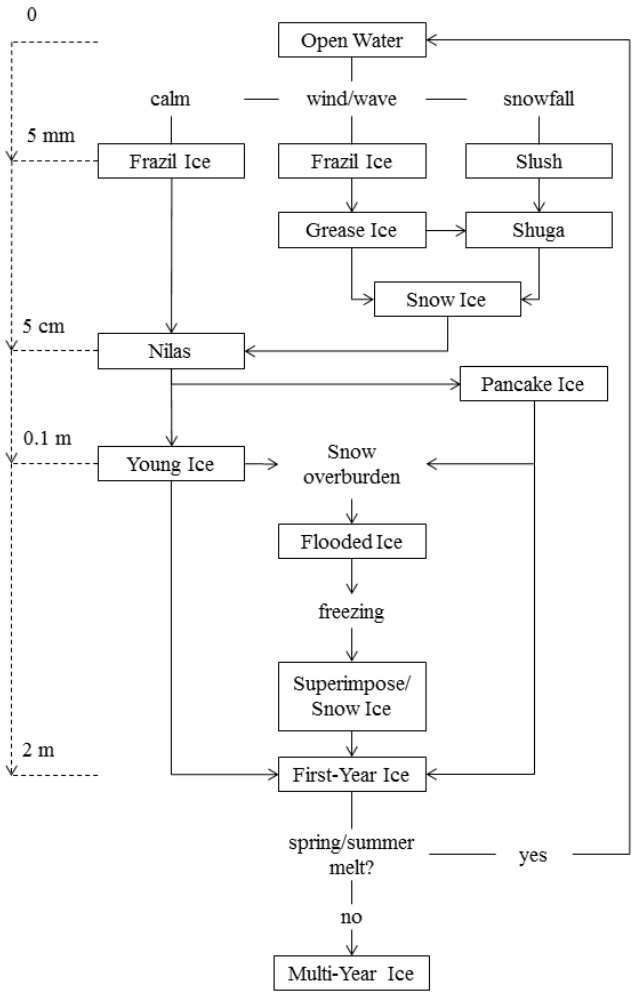


*Fig. 2.1:* Ice growth evolution under various conditions. This figure is based on [9].

of ice form on the surface of the water. As the heat is transferred upwards towards the surface, a layer of randomly oriented needles and platelets, referred to as frazil ice, begins to accumulate. If there is a snow fall event at this stage, a mixture of ice and snow will develop on surface, referred to as slush. Over time, the frazil ice develops into grease ice and then solidifies into a thin elastic layer, referred to as nilas ice. From this point on, the sea ice grows from the bottom of the ice (*i.e.*, congelation growth) into new ice. During the cold season, ice growth continues in the form of a columnar structure to reach to the so-called first year ice (FYI). If this ice can survive the melt of the next warm season, it will be referred to as multi year ice (MYI).

*Brine and Salinity*

As sea water solidifies into ice, its salt content is ejected into pockets within the formed ice. These inclusions, referred to as brine pockets, are in liquid or solid form depending on the ice temperature. As the ice grows, the brine moves upwards and downwards and forms channels within the ice, resulting in a C-shaped salinity structure for different ice types having various thickness values. The upward expulsion of brine is primarily due to pressure buildup in the brine pockets caused by ice growth. This forces the brine upwards through microscopic cracks within the ice. This upward move leads to ($i$) formations of millimeter crystal structures on the ice surface, referred to as frost-flowers in lack of a snow layer [11,12], or ($ii$) a saline layer at the bottom of snow in the case of snow-covered sea ice [13] [(1)]. The downward migration of brine is primarily due to gravity drainage. This process involves the movement of brine due to differences in density between the brine in the ice and that in the seawater. This occurs due to the development of a buoyancy driven convection system. This drainage of brine releases a considerable amount of salt into the ocean. Another mechanism which contributes towards the downward movement of brine is the solute diffusion. This occurs since brine tends to move towards the warmer end of the ice (*i.e.*, the ice-ocean interface). Finally, it should be mentioned that there might be other inclusions in the ice (*e.g.*, air bubbles). In the sea ice type of interest (*i.e.*, young and first year sea ice), the volume fractions of these other inclusions are negligible compared to that of brine [14].

### *2.2.2 Snow*

Snow is the ice crystals formed in the atmosphere. But the snow layer on the ice is a mixture of single or clusters of crystals with its pores initially filled with air. There could also be water vapor and liquid water in this layer if the snow is wet. Finally,

[(1)] It should be noted that we can have both brine skim and frost flowers.

the snow could even be brine-wetted at its interface with ice, as explained above. The snow density can vary significantly, as reported in [15]. Snow plays a major role in climate models for the Arctic. This is due to two major properties of the snow. First, the albedo (*i.e.*, the fraction of solar shortwave radiation reflected from the surface) of snow is higher than that of ice [16]. Second, the thermal conductivity of snow is smaller than ice [17]. Therefore, the snow layer is an effective thermal blanket for the ice beneath which slows both its growth and melt rate.

As the snow falls on the ice, it goes through a metamorphism process. Snow metamorphism is the change of the structure and texture of snow grains due to a varying temperature, migration of liquid water and/or water vapors, and gravitational pressure within the snow cover. There are two major metamorphism processes [18]. First is the equi-temperature metamorphism (*i.e.*, equilibrium state). This happens in isothermal and deep snowpacks. During this process, the snow crystals go through an erosion period and end up as well-rounded snow grains. Snow grains also develop bonds (known as necks) with each other. The result of this metamorphism is a packed layer with higher density. Second is the temperature gradient (TG) metamorphism. This occurs when there is a large temperature change within the snowpack. This process is also referred to as kinetic growth in which grains become faceted and the bonds are poor. As water vapor is deposited on the snow grains, they grow larger, and eventually form the large crystals referred to as depth hoars. Depth hoars normally form at the snow-ice interface, where the vapor pressure gradient is strong and persistent. Other metamorphism are the gravitational (*i.e.*, overburden) and freeze-melt (*i.e.*, freeze-thaw cycles) metamorphism, both resulting in a denser snowpack.

*Dry and Wet Snow*

To simplify the study of snow properties and its metamorphism, the snow is categorized into two types here. These are dry snow and wet snow; *i.e.*, snow with less and

more than 2% liquid water content respectively. The metamorphism in dry snow is mainly governed by temperature gradient [19]. After the snow fall and based on the daily temperature gradient, the snowpack fluctuates between either well-rounded (*i.e.*, equi-temperature metamorphism), or faceted (*i.e.*, temperature gradient metamorphism) grains. Snow grains evolve into hoars at the bottom of the snowpack, when the temperature gradient is large enough. As time goes by, the faceted crystal formation moves upward since the rounded ice crystals (*i.e.*, vapor sources) are depleted. This process means that in a typical snowpack, snow-grain size increases with depth while the density decreases.

Wet snow has a higher grain growth rate compared to dry snow with a similar metamorphism [19]. As the water content in the wet snow increases, the grain growth rate increases as well. For lower liquid contents (*i.e.*, pendular regime)[(2)], air-filled gaps among the clusters of ice crystals are reduced, forming larger connected units. For higher liquid contents (*i.e.*, funicular regime), water freely moves to the bottom of the snowpack where smaller grains melt and contribute to the formation of large snow grains. Therefore, the grains cluster together with liquid water bonding them.

## *2.3 Snow-Covered Sea Ice Dielectric Properties*

This section presents the formulas relating the dielectric properties of snow-covered sea ice to its geophysical properties as described in Section 2.2. To this end, a dielectric material, or simply a dielectric, is defined in Section 2.3.1, and general formulas to calculate dielectric properties are cast. Next, Section 2.3.2 presents the parameters in these formulas for various single-phased materials of interest. Finally, in Sections 2.3.3 and 2.3.4, the dielectric properties of ice and snow are investigated respectively. It should be noted that the methodology utilized in this thesis to calculate the permit-

[(2)] The snow pendular regime spans from dry snow up to a water saturation level of roughly 8% of the snow mixture [20].

tivity of the snow and sea ice is presented in Appendix B.

### *2.3.1 Permittivity General Formulation*

A dielectric is a material whose dominant charges are bound (not free to move); when an external field is applied to it, its charges shift slightly in place (*i.e.*, polarization) [21]. If the dielectric is considered to be lossy, its dielectric value (*i.e.*, permittivty) will be a complex number[(3)]. In what follows, I initially attempt to describe the relations that outlines the frequency-dependence of permittivity for a single-phase material. To this end, let's define the electric polarization vector, denoted by $\boldsymbol{P}$, as the dipole moment per unit volume. When an electric field is applied to a dielectric with no dipole to dipole interactions (*i.e.*, Debye model), the time-dependency of the polarization can be characterized as [22]

$$\frac{d\boldsymbol{P}(t)}{dt} = \frac{1}{\tau}[-\boldsymbol{P}(t)] \tag{2.1}$$

In (2.1), $\boldsymbol{P}_s$ is the static value of $\boldsymbol{P}$, and $\tau$ is the relaxation time (momentary delay to transfer to equilibrium). In the phasor domain[(4)], we can solve for $\boldsymbol{P}(\omega)$ as

$$\boldsymbol{P}(\omega) = \frac{\boldsymbol{P}_s}{1 - j\omega\tau} \tag{2.2}$$

Furthermore, for the electric flux density, denoted by $\boldsymbol{D}$, we have [22]

$$\boldsymbol{D}(\omega) = \boldsymbol{P}(\omega) + \boldsymbol{P}_{res}(\omega) + \boldsymbol{D}_{vac}(\omega) \tag{2.3}$$

In (2.3), $\boldsymbol{P}_{res}$ denotes the resonant part of the polarization and $\boldsymbol{D}_{vac}$ denotes the vacuum contribution to $\boldsymbol{D}$. Using $\boldsymbol{P}_{res}(\omega) + \boldsymbol{D}_{vac}(\omega) = \epsilon_0\epsilon_\infty\boldsymbol{E}(\omega)$, and $\boldsymbol{P}_s = \epsilon_0(\epsilon_s -$

(3) Any contributions due to a finite conductivity of the dielectric can be incorporated into an effective complex permittivity.

(4) We assume a time-dependency of $e^{-j\omega t}$.

$\epsilon_\infty)\boldsymbol{E}(\omega)$ [22] along with (2.2) and (2.3) we arrive at

$$\boldsymbol{D}(\omega) = \frac{\epsilon_0(\epsilon_s - \epsilon_\infty)}{1 - j\omega\tau}\boldsymbol{E}(\omega) + \epsilon_0\epsilon_\infty\boldsymbol{E}(\omega) \tag{2.4}$$

By substituting $\boldsymbol{D} = \epsilon_0\epsilon_r\boldsymbol{E}$ in (2.4), the Debye equation for frequency dependent permittivity is found to be

$$\epsilon_r(\omega) = \epsilon_\infty + \frac{\epsilon_s - \epsilon_\infty}{1 - j\omega\tau} \tag{2.5}$$

It should be noted that (2.5) is now consistent with the definition of $\epsilon_\infty$ and $\epsilon_s$ as

$$\lim_{\omega\to\infty} \epsilon_r(\omega) = \epsilon_\infty \tag{2.6}$$

$$\lim_{\omega\to 0} \epsilon_r(\omega) = \epsilon_s \tag{2.7}$$

Finally, the presence of a finite conductivity, $\sigma$, can be incorporated into the complex permittivity by using the concept of effective complex permittivity which combines the effect of $\sigma$ and $\epsilon_r$ into the effective complex permittivity, $\epsilon_{r,eff}$, as follows [23, 24][(5)]

$$\epsilon_{r,eff}(\omega) = \epsilon_\infty + \frac{\epsilon_s - \epsilon_\infty}{1 - j\omega\tau} + \frac{j\sigma}{\omega\epsilon_\circ} \tag{2.8}$$

If the dielectric material under investigation is a mixture of a number of dielectrics (*e.g.*, dry snow that is pure ice crystals in an air background) its macroscopic effective permittivity can be defined as[(6)] [25]

$$< \boldsymbol{D} >= \epsilon_{eff} < \boldsymbol{E} > \tag{2.9}$$

The effective permittivity can be calculated through various homogenization (mixing formula) methods. One such popular method in the remote sensing community is the

[(5)] $\nabla \times \boldsymbol{H}(\omega) = -j\omega\boldsymbol{D}(\omega) + \sigma\boldsymbol{E}(\omega) = -j\omega\epsilon_0 \overbrace{(\epsilon_r(\omega) + \frac{j\sigma}{\omega\epsilon_0})}^{\epsilon_{r,eff}(\omega)}\boldsymbol{E}(\omega)$.

[(6)] The averaging is performed through $< f(r) >= \frac{1}{V}\int_V f(r)dV$.

Polder-Van Santen[7]. To this end, Polder introduces the following procedure for a mixture dielectric consisting of a host medium and inclusions. Herein, we assume a two-phase mixture in which we have a host medium with one type of inclusions [26].

$$< \boldsymbol{D} >= \epsilon_{eff} < \boldsymbol{E} >= \epsilon_h < \boldsymbol{E} > + < \boldsymbol{P} >= \epsilon_h < \boldsymbol{E} > + v_i(\epsilon_i - \epsilon_h)\frac{1}{V_i}\int_{V_i} \boldsymbol{E} dV \tag{2.10}$$

In (2.10), the subscripts $h$ and $i$ refer to the host and inclusion respectively. Also, $v_i$ denotes the volume fraction of the inclusion, and $V_i$ is the actual volume of the inclusions. For example, if the inclusions are random identical ellipsoids, $v_i$ is related to the physical dimension of the inclusions by

$$v_i = \frac{4}{3}\pi a_o b_o c_o N \tag{2.11}$$

In (2.11), $N$ is the number of inclusions per meter cube. Also $a_o$, $b_o$, and $c_o$ are half of the ellipsoid dimensions along its major $a$, $b$, and $c$ axes. Next, Polder assumes that the mean field within a particle, denoted by $\boldsymbol{E}_m$, is linearly related to the homogenous field away from the particle (*i.e.*, $< \boldsymbol{E} >$)[8] via a tensor $\alpha$. The mean value of the field in the interior of a randomly oriented ellipsoidal particles will then be [26]

$$\frac{1}{V_i}\int_{V_i} \boldsymbol{E} dV = \frac{1}{3}(\alpha_{aa} + \alpha_{bb} + \alpha_{cc}) < \boldsymbol{E} > \tag{2.12}$$

In (2.12), $u = a, b, c$ are the axes of the ellipsoid, and $\alpha_{uu}$ relates to the polarisability of the ellipsoid in $u$ direction when an external field in $u$ direction is applied. Utilizing (2.12) and (2.10), we have [26]

$$\epsilon_{eff} = \epsilon_h + v_i(\epsilon_i - \epsilon_h)\frac{1}{3}(\alpha_{aa} + \alpha_{bb} + \alpha_{cc}) \tag{2.13}$$

[7] This method is sometimes referred to as the Bruggeman or de Loor method [25].
[8] This homogeneous field is associated with the effective permittivity of the mixture.

In an external field of $< \boldsymbol{E}^{(u)} >$[9], the mean internal field in an ellipsoid will be [26]

$$\boldsymbol{E}_{int}^{(u)} = \frac{1}{1 + (\frac{\epsilon_i}{\epsilon_{eff}} - 1)A_u} < \boldsymbol{E}^{(u)} >= \alpha_{uu} < \boldsymbol{E}^{(u)} > \tag{2.14}$$

In (2.14), $A_u$ is the depolarization factor of the ellipsoid along its $u$ axis defined as [26]

$$A_u = \frac{a_o b_o c_o}{2} \int_0^\infty \frac{dh}{(h + u^2)\sqrt{(h + a_o^2)(h + b_o^2)(h + c_o^2)}} \tag{2.15}$$

As an example, $A_u = 1/3$ in the case of spherical inclusions (*i.e.*, $a_o = b_o = c_o$). Finally, utilizing (2.13) and (2.14), the effective permittivity of the mixture is calculated as [26]

$$\epsilon_{eff} = \epsilon_h + \frac{v_i}{3}(\epsilon_i - \epsilon_h) \sum_{u=a,b,c} \left[ \frac{1}{1 + A_u(\frac{\epsilon_i}{\epsilon_{eff}} - 1)} \right]. \tag{2.16}$$

Finally, de Loor suggests that for the low values associated with the inclusion's volume fraction (*i.e.*, $v_i \leq 0.1$), the $\epsilon_{eff}$ on the right hand side of (2.16) can be replaced by the permittivity of the host medium[10] [27].

### *2.3.2 Single-Phase Materials*

Below, the components of (2.8) for various single-phase materials of interest are presented to calculate their permittivity values.

*Pure Water*

For pure water, the conductivity is taken to be zero. The rest of Debye parameters are

[9] $< \boldsymbol{E}^{(u)} >$ denotes $< \boldsymbol{E} >$ along the $u$ direction.

[10] Conceptually, in a series expansion of $\epsilon_{eff}$, the surrounding permittivity of the inclusions can be approximated by $\epsilon_h$ as the first term of the series for low values of $v_i$. But for large values of $v_i$, the interactions between inclusions may not be ignored. This interaction is partly accounted for by considering the inclusions being surrounded by $\epsilon_{eff}$ rather than $\epsilon_h$ [26, 27].

as follows [28]. For the static permittivity of pure water, denoted by $\epsilon_{w_s}$, we have[(11)]

$$\epsilon_{w_s}(T) = 88.045 - 0.4147T + 6.295 \times 10^{-4}T^2 + 1.075 \times 10^{-5}T^3 \tag{2.17}$$

In (2.17), $T$ is the temperature (and also throughout this thesis). The relaxation time is

$$\begin{aligned} 2\pi\tau_w(T) =& 1.1109 \times 10^{-10} - 3.824 \times 10^{-12}T + \\ & 6.938 \times 10^{-14}T^2 - 5.09610^{-6}T^3 \end{aligned} \tag{2.18}$$

The permittivity of pure water in high frequency is equal to 4.9. Finally, it should be noted that Debye parameters are temperature dependent.

*Pure Ice*

The relaxation frequency, defined as $f_r = 1/2\pi\tau$, of pure ice is much lower than liquid water. Therefore, some consider pure ice to be a non-dispersive material at microwave regime with a slight temperature dependance. In [23], an empirical equation is introduced which describes the temperature dependency of the pure ice permittivity, denoted by $\epsilon_{pi}$, as

$$\epsilon_{pi}(T) = 3.1884 + 0.00091T. \tag{2.19}$$

The above formula only presents the real part of the relative complex permittivity. The imaginary part of this model is presented in Appendix B; see (B.2). This complex permittivity model is utilized to calculate the pure ice permittivity in this thesis.

*Liquid Brine*

Although liquid brine is a mixture of pure water and various salts (*e.g.*, $Na_2S0_4$, $NaCl$, with $NaCl$ being the principle component), it is commonly considered to be

[(11)] Throughout this thesis, the temperature denoted by $T$, is in $^\circ C$, the density denoted by $\rho$, is in $g/cm^3$, and the salinity denoted by $S$, is in $ppt$, unless mentioned specifically to be otherwise.

a single-phase material at microwave frequencies [27–29]. Therefore, its permittivity is calculated through the Debye formula rather than the mixing formulas. The Debye parameters associated with liquid brine are introduced as follows [29]. The static permittivity is equal to

$$\epsilon_{b_s}(T) = \frac{939.66 - 19.068T}{10.737 - T} \tag{2.20}$$

Also, for high frequency (optical) permittivity we have

$$\epsilon_{b_\infty}(T) = \frac{82.79 + 8.19T^2}{15.68 + T^2}. \tag{2.21}$$

Furthermore, the relaxation time is equal to

$$\begin{aligned} 2\pi\tau_{b_\circ}(T) &= 0.10990 + 0.13603 \times 10^{-}2T \\ &\quad + 0.20894 \times 10^{-}3T^2 + 0.28167 \times 10^{-}5T^3 \end{aligned} \tag{2.22}$$

And finally, for conductivity

$$\sigma_b(T) = \begin{cases} -T\exp(0.5193 + 0.08755T), & T \geq -22.9\ ^\circ C \\ -T\exp(1.0334 + 0.11T), & T < -22.9\ ^\circ C \end{cases} \tag{2.23}$$

where exp denotes the natural exponential function. Finally, it should be noted that a similar method to calculate the brine permittivity is utilized in this thesis, as introduced in Appendix B.

### *2.3.3 Sea Ice*

The sea ice of our interest consists of a pure ice background with brine pockets as the most important inclusions, as previously discussed in Section 2.2. Therefore, sea ice can be considered a two-phase medium and its permittivity can be calculated using (2.16). To determine if the sea ice under study is a tenuous material or not, the brine volume

fraction needs to be calculated [27, 30] as

$$V_b = \frac{S_{si} \times \rho_{si}}{S_b \times \rho_b} \tag{2.24}$$

In (2.24), $S$ is the salinity $[ppt]$ and $\rho$ is the density $[g/cm^3]$ with the subscripts $si$ and $b$ denoting the sea ice and brine respectively. Moreover, an empirical equation for brine volume fraction in sea ice can be written as [31]

$$V_b = \begin{cases} 10^{-3} S_{si} \left( \frac{-52.56}{T} - 2.28 \right), & -2.06 < T \leq -0.5 \ ^\circ C \\ 10^{-3} S_{si} \left( \frac{-45.917}{T} + 0.930 \right), & -8.2 < T \leq -2.06 \ ^\circ C \\ 10^{-3} S_{si} \left( \frac{-43.795}{T} + 1.189 \right), & -22.9 < T \leq -8.2 \ ^\circ C \end{cases} \tag{2.25}$$

Herein, we consider (2.25) for $V_b$ calculation.

The sea ice permittivity, $\epsilon_{si}$, can now be calculated based on the Polder-Van Santen/de Loor formulation presented above. Therefore, $\epsilon_{si}$ will be [27]

$$\epsilon_{si} = \begin{cases} \epsilon_{pi} + \frac{3V_b \epsilon_{pi}(\epsilon_b - \epsilon_{pi})}{\epsilon_b + 2\epsilon_{pi}}, & V_b \leq 0.1 \\ \epsilon_{pi} + \frac{3V_b \epsilon_{si}(\epsilon_b - \epsilon_{pi})}{\epsilon_b + 2\epsilon_{si}}, & V_b > 0.1 \end{cases} \tag{2.26}$$

### *2.3.4 Snow*

Snowpack is considered to be a mixture of air and ice crystals. The addition of water changes the status of snow from dry to wet. Therefore, the permittivity of snowpack can be determined using mixture formulas. Although, it should be mentioned that due to the metamorphism processes discussed in Section 2.2, empirical equations might return more accurate results in some cases.

*Dry Snow*

Dry snow is considered to be a mixture of pure ice and air gaps. The permittivity of dry snow, $\epsilon_{ds}$, as a two-phase medium is calculated by (the subscript $pi$ denotes pure ice)

$$\epsilon_{ds} = 1 + \frac{3V_{pi}\epsilon_{ds}\left(\epsilon_{pi} - 1\right)}{\epsilon_{pi} + 2\epsilon_{ds}} \tag{2.27}$$

Since the dielectric of pure ice is only slightly temperature dependent, the dry snow dielectric is mainly dependent on the dry snow density (determining the volume fraction of pure ice within the snowpack by $V_{pi} = \rho_{ds}/0.916$ [32]). It is also common to calculate the dry snow permittivity based on empirical experiments as done in [32,33].

*Wet Snow*

Wet snow can be considered as dry snow with water inclusions [32]. Therefore, the wet snow permittivity, $\epsilon_{ws}$, can be determined by a two-phase mixture equation, as

$$\epsilon_{ws} = \epsilon_{ds} + \frac{m_v\epsilon_{ws}}{3}\left(\epsilon_w - \epsilon_{ds}\right)\sum_{u=a,b,c}\left[\epsilon_{ws} + (\epsilon_w - \epsilon_{ws})A_u\right]^{-1} \tag{2.28}$$

In (2.28), $m_v$ is the water content volume fraction which should be measured independently. Furthermore, $A_u$ has been defined in (2.15). There are also empirical equations for wet snow permittivity calculation as reported in [34].

*Brine-Wetted Dry Snow*

As the snowpack goes through the metamorphism process, brine might be ejected into the bottom of the snowpack[(12)]. This results in a brine-wetted snow, as explained in Section 2.2. Drinkwater and et al. in [35] suggests the following procedure to calculate the permittivity of brine-wetted dry snow, $\epsilon_{bds}$. First, the true volume fraction of brine

[(12)] Moreover, airborne deposition of sea salt can also lead to a saline surface.

within the snowpack, $v_b$, is calculated as

$$v_b = \frac{V_b \rho_b}{(1 - V_b)\,\rho_{pi} + V_b \rho_b} \frac{\rho_s}{\rho_b} \tag{2.29}$$

Then using the mixture formula, $\epsilon_{bds}$ will be

$$\epsilon_{bds} = X v_b \frac{\epsilon_b - \epsilon_{ds}}{1 + \left(\frac{\epsilon_b}{\epsilon_{ds}} - 1\right) A_\circ} \tag{2.30}$$

In (2.30), $A_\circ$ is the dominant depolarization factor, and $X$ is a coupling factor. For isotropically oriented oblate spheroids, the coupling factor is 2/3. In the pendular regime, depolarization factor is about 0.053. Finally, typical values for sea ice and brine-wetted dry snow for various temperature and salinity combinations versus frequency is depicted in Figure 2.2.

## *2.4 Snow-Covered Sea Ice Thermodynamics*

Snow-covered sea ice thermodynamics investigates the flow of energy through the snow and ice [10]. Therefore, thermodynamics governs the melt and growth process of snow-covered sea ice. In addition to the physical structure of the profile and its density, four thermal parameters, namely, thermal diffusivity $\kappa$ in $m^2.s^{-1}$, specific heat capacity $C^P$ in $J.Kg^{-1}.C^{-1}$, latent heat $L^T$ in $J.Kg^{-1}$, and thermal conductivity $k^T$ in $W.m^{-1}.C^{-1}$, determine the thermodynamic characteristics of the snow and ice. These parameters are defined in Section 2.4.1. Section 2.4.2 describes the heat transfer and energy balance applied to the snow-covered sea ice. Finally in Section 2.4.3, the relation of thermodynamics to sea ice geophysics and dielectric properties is explained.[13]

[13] As a reminder, throughout this thesis, the temperature is in $^\circ C$, the density is in $g/cm^3$, and the salinity is in *ppt*, unless mentioned specifically to be otherwise.

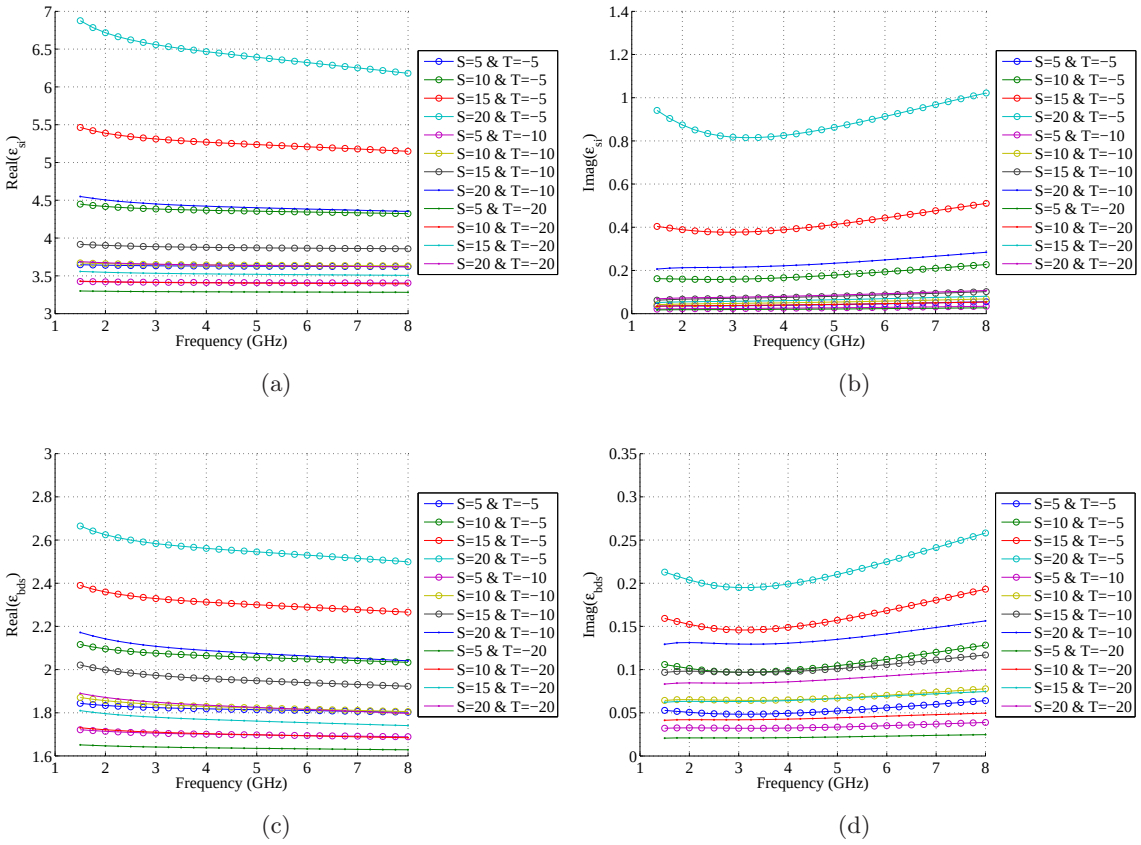


*Fig. 2.2:* Typical values for (a) real part of sea ice permittivity, (b) imaginary part of sea ice permittivity, (c) real part of brine-wetted dry snow permittivity, and (d) imaginary part of brine-wetted dry snow permittivity. ($T$ represents the temperature in $^{\circ}C$ and $S$ denotes the salinity in *ppt*.) PVS/de Loor method is utilized for mixture dielectric formula in this figure.

### *2.4.1 Thermodynamic Parameters*

Specific heat capacity, or thermal capacity, is the ratio of the heat added to an object to the resulting change in its temperature. The specific heat of snow or ice depends on $(i)$ specific heat of their components, and $(ii)$ the amount of water that changes state during a temperature change. For example, the specific heat of sea ice, $C_{si}^{P}$, is calculated by the following approximate equation [36]

$$C_{si}^{P} = C_{pi}^{P} + \gamma \frac{S}{MT^2} \tag{2.31}$$

In (2.31), $S$ is the salinity, $T$ is the temperature, and $C_{pi}^{P}$ is the specific heat of pure ice. We also have $\gamma = 1.72 \times 10^{7}\ J.K.m^{-3}.ppt^{-1}$, and $M = 900\ kg.m^{-3}$. The brine inclusions in sea ice is represented in (2.31) through the salinity. For dry snow specific heat, $C_{ds}^{P}$, there is only a temperature dependence as shown in [37],

$$C_{ds}^{P} = 92.88 + 7.364T_{k}^{2}. \tag{2.32}$$

In (2.32), $T_k$ is the temperature in $K$.

Latent heat is the heat released or absorbed per unit mass during phase change. This allows us to calculate the amount of energy when snow and ice form or melt. For instance, the latent heat of sea ice can be calculated as [38]

$$L_{si}^{T} = 333394 - 2113T - 114.2S + 18040\frac{S}{T} \tag{2.33}$$

The difficulty with latent heat modeling arises when a layer contains more than one phase; *e.g.*, having both solid and liquid such as a snowpack with liquid water and ice crystals.

Thermal conductivity is the ability of a material to conduct heat. In the case of snow and ice, this parameter may be expressed based on the components of the snow and ice and their thermal conductivity, shape, and arrangement. In the case of sea ice, the thermal conductivity may be formulated as [39]

$$k_{si}^{T} = k_{pi}^{T} + \beta\frac{S}{T} \tag{2.34}$$

In (2.34), $\beta$ is equal to 0.13 $W.m^{-1}$. It should be noticed that the thermal conductivity has a direct relation to salinity and an inverse one with temperature. A more complex formula which takes into account the effect of brine and air bubbles can be found in [38]. In the case of snow, an empirical formula is presented in [40] that relates the

thermal conductivity of dry snow to its density and temperature as

$$k_{ds}^{T} = 2.845 \times 10^{-6} \rho_{ds}^{2} + 2.7 \times 10^{-4} \times 2^{(T_{ds}-233)/5} \tag{2.35}$$

In (2.35), $T_{ds}$ is the temperature in $K$. Finally, it should be mentioned that the thermal conductivity of snow, despite a large variance, is on average seven times smaller than that of the ice [17]. Therefore, the snowpack can effectively act as a thermal insulator for the ice underneath.

Thermal diffusivity is the ability of heat conduction through a medium relative to its ability to store thermal energy as an indicator of heat conduction rate. Thermal diffusivity is therefore defined as

$$\kappa \triangleq k^{T} / \rho C^{P} \tag{2.36}$$

It can be seen from (2.36) that if snow-covered sea ice becomes thermally more conductive, the energy conduction rate increases. But if the temperature increases, this rate will be reduced.

### *2.4.2 Heat Transfer and Energy Balance*

Measurement of major Arctic system parameters such as the snow mass balance (*i.e.*, the mass difference between deposited and melted snow) and ice extent (*i.e.*, the area of open water covered with sea ice) over time is of great modeling significance. Since the melt and growth of sea ice is temperature dependent, retrieval of the temperature within the snow-covered sea ice profile will assist us in better modeling of the Arctic system [17]. One way to retrieve the temperature of the snow-covered sea ice is to use the heat equation which describes the distribution of heat (*i.e.*, variation in temperature) within the profile over time. If we consider the snow-covered sea ice to be

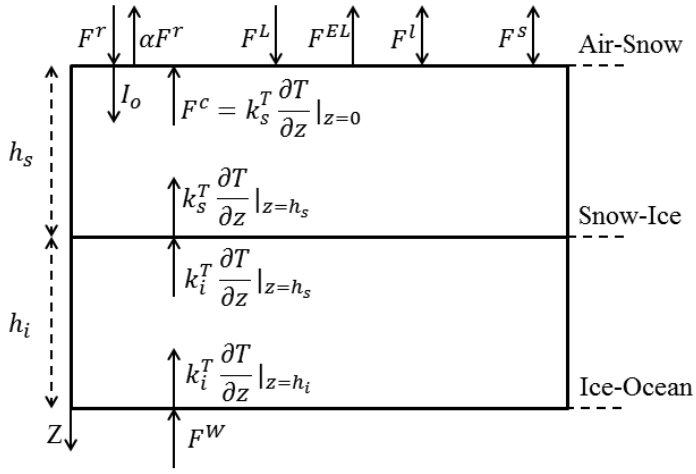


*Fig. 2.3:* Schematic of one dimensional heat transfer, surface energy balance, and boundary conditions. The air-snow interface is at $z = 0$.

homogenous within each layer of snow and ice, the three dimensional heat equation will be reduced to a one-dimensional heat diffusion equation as [41]

$$\rho C^P \frac{\partial T}{\partial t} = \frac{\partial}{\partial z}\left(k^T \frac{\partial T}{\partial z} \pm I_\circ\right) \tag{2.37}$$

whose schematic is depicted in Figure 2.3. In (2.37), $t$ is the time, $z$ is the profile depth, and $I_\circ$ is the internal heating due to an external source (*e.g.*, from penetrated solar energy flux). To solve this differential equation for both snow and ice layer, the boundary conditions should be satisfied. There are three boundaries, namely air-snow, snow-ice, and ice-ocean. For the air-snow interface, surface energy balance (*i.e.*, the first law of thermodynamics at the profile's surface) states that the summation of incoming and outgoing energy fluxes must be zero for temperatures below freezing as[14] [41]

$$(1-\alpha)\, F^r - I_\circ + F^L - F^{EL} + F^s + F^l + F^c = 0 \tag{2.38}$$

[14] For above freezing temperatures, there will be an imbalance of heat fluxes that causes the snow to melt. This melting is therefore represented by the right hand side of (2.38) to be equal to $-L_s^T \frac{(dh_s+dh_i)}{dt}$ *at* $z = 0$, where $L_s^T$ , $h_s$, and $h_i$ are the snow latent heat, snow thickness, and sea ice thickness respectively.

In (2.38), positive and negative signs denote incoming and outgoing heat flux densities[(15)]. Furthermore, in (2.38), fluxes are defined as follows [10]

- $F^r$ is the incoming short-wave radiation (*i.e.*, higher frequency) of the sun on the snow surface after traveling through the atmosphere.
- $F^L$ is the incoming long-wave radiation (*i.e.*, lower frequency) due to the atmosphere and cloud radiation warmed up by the solar radiation.
- $F^{EL}$ is the outgoing long-wave radiation of the profile's surface. This is calculated through the Stefan-Boltzmann law of radiation that describes the power radiated from a gray body in terms of its temperature as

$$F^{EL} = e_L \sigma T_k^4 \tag{2.39}$$

  In (2.39), $T_k$ is the surface temperature in $K$. Also, $\sigma$ is the Stefan-Boltzmann constant, and $e_L$ is the surface emissivity. For a perfect black body, $e_L = 1$. The emissivity is close to unity for snow, and is between 0.66 and 0.99 for sea ice [10].
- $F^s$ is the sensible heat flux that is the heat transfer between the surface of the profile and air through conduction. If the surface is warmer than air, $F^s$ is upwards and negative and vice versa.
- $F^l$ is the latent heat flux to the air that is due to sublimation (*i.e.*, solid snow grains turn into gas without going through a liquid stage).
- $F^c$ is the heat flux conducted through the body of snow (upwards or downwards, depending on the profile's temperature).
- $\alpha$ denotes the surface albedo, defined as the fraction of the reflected radiation

[(15)] Heat flux density is the rate of heat energy transfer through a given surface per unit area per unit time. Therefore, is has a unit of $W.m^{-2}$.

from the surface to the incident radiation on it[16].

For the snow-ice interface, we need to consider the conducted heat through this boundary that leads to a Neumann boundary condition as [10, 41]

$$k_s^T \frac{\partial T_s}{\partial z} = k_i^T \frac{\partial T_i}{\partial z}. \tag{2.40}$$

Finally, at the ice-ocean interface, the difference between conducted heat from the ice and the ocean heat flux, $F^w$, results in the melting/freezing rate of the snow-covered sea ice[17] denoted by $W^{m/f}$, as [10, 41]

$$F^w - k_i^T \frac{\partial T_i}{\partial z} = L_i^T W^{m/f}. \tag{2.41}$$

Knowing these three boundary conditions, the differential equation can be solved to obtain the temperature profile variations.

### *2.4.3 Thermodynamics in Relation to Sea Ice Geophysics and Dielectric*

In Section 2.2, the snow-covered sea ice geophysics was discussed. At different times of the year, the snow-covered sea ice goes through different stages of growth or melt and shows different characteristics. Most notably, three parameters, namely, temperature, salinity, and density profiles, change during snow-covered sea ice evolution. Also, from Section 2.3, it can be concluded that the complex permittivity of the snow and sea ice are primarily based on these three parameters. Moreover, in the same section, it was shown that the thermodynamic parameters of specific heat capacity, latent heat, and thermal conductivity, are also dependent on temperature, salinity, and density. Therefore, a change in these three latter parameters of snow-covered sea ice will affect

[16] For example, the new snow, bare first year sea ice, and open water albedo are approximately 0.87, 0.52, and 0.06 respectively [10].
[17] That is, $-L_{si}^T \frac{(dh_s + dh_i)}{dt}$ *at* $z = h_s + h_i$.

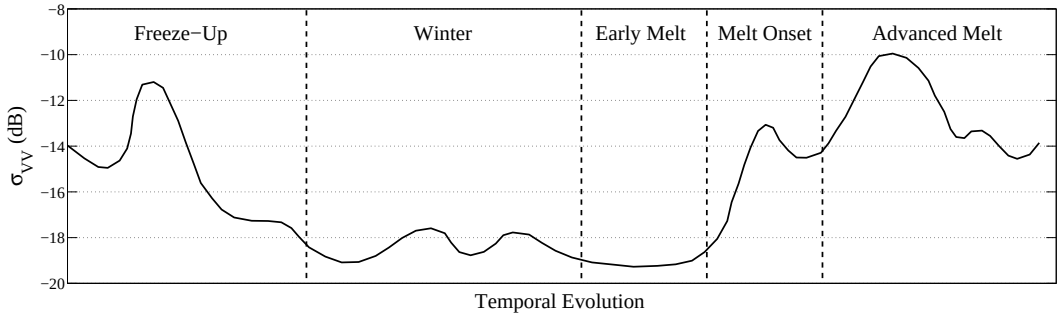


*Fig. 2.4:* Seasonal evolution of the normalized radar cross section data with vertical-sent vertical-receive polarization, denoted by $\sigma_{VV}$, for the first-year sea ice measured at 5.3 GHz, based on [42].

both the dielectric and thermodynamics of the profile. To track these changes for first-year sea ice, each stage of the profile's evolution is studied separately as follows.

#### *2.4.3.1 Freeze-Up*

The first stage is the freeze-up, happening after the summer and before the winter. As the temperature drops, the sea ice formation begins. As the sea ice grows, more brine is ejected out of the sea ice and therefore, its bulk salinity decreases[(18)]. Lower salinity then decreases the real and imaginary parts of the complex permittivity. On the other hand, as we progress towards the winter, the profile's temperature decreases. It is also shown that the brine volume fraction decreases as the temperature decreases. Since the permittivity is directly related to the brine volume fraction, the profile's dielectric value (both real and imaginary parts of the complex permittivity) will also decrease. In summary, the average dielectric decreases as we progress during the freeze-up. Moreover, as temperature decreases, both the density and the specific heat capacity decrease. In addition, thermal conductivity tends to decrease with temperature decrease and tends to increase with salinity reduction. Since both temperature and salinity decrease at

[(18)] It should be noted that, there is often a highly saline brine skim at the upper interface. This condition might continue to exist until the spring melt.

this stage, the prediction of thermal conductivity changes becomes difficult. The brine pockets also act as temperature capacitors, releasing and absorbing the latent heat. This further complicates the thermodynamic processes. Finally, frost flowers and brine skim also might appear at this stage of sea ice growth. These structures are highly saline, and therefore, increase the overall permittivity. It should be noted that the frost flowers are also insulators and reflect the solar radiation, thus, affecting the heat transfer.

#### *2.4.3.2 Winter*

Next, we move to the winter stage during which the sea ice growth continues with the dropping temperature. The reduction in salinity and temperature will further decrease the permittivity. Since the sea ice salinity reduction in winter has a considerably slower rate compared to the freeze up stage, the reduction rate in the permittivity will be slower as compared to the previous stage. The shortwave flux is at its lowest during this season and the temperature gradient within the profile is large. Winter is also marked by snow deposition on the ice layer. Storms often are associated with incursions of warm air and high winds that heat and pack the surface. Such periodic phenomena give rise to crusts on the snow, which often get buried. Early in the winter, the snow is at the beginning of its metamorphism process. It has a low salinity and the grains are not yet connected to each other. As a result, it has a low permittivity. The snow has a low thermal conductivity which results in a strong temperature gradient in the snowpack but a slightly lower one in the sea ice. Moreover, the snow albedo is considerably higher than sea ice which will significantly changes the surface energy balance. Therefore, the growth rate of ice and the thermodynamic processes are slowed down, and thus, the profile becomes more stable. The bulk density of the profile will also stay almost unchanged for most of the winter.

#### *2.4.3.3 Melt-Period*

The last stage is the melt period. The changes during this period are fast-paced and therefore, the melt period is divided into three sections: early melt, melt onset, and advanced melt. Starting with early melt, the shortwave radiation increases and affects the surface energy balance, resulting in temperature increase. The temperature increase of the profile is also due to a warmer climate and ocean currents. As a result of a high temperature gradient, the snow metamorphism speeds up and larger grains are formed within the snowpack. Also, the water content in the snowpack increases which increases the dielectric value. Moreover, the basal layer formation speeds up at the bottom of the snowpack with larger snow grains (lower densities) and higher salinities. Next, during the melt onset, the surface albedo of the snow will start to decrease further. The presence of clouds will also increase the longwave radiation which will further increase the temperature of the snowpack. Also, as the brine is further rejected from the profile, the dielectric value decreases. This reduction is not significant since the increase in liquid water present in the profile increases the dielectric value. This water is either due to rain or the melting of the snow. It can easily flow down to the the base of the snowpack and cause a slushy layer. Some of this water may freeze up during the night and create ice lenses. Later during the advanced melt, the melted snow on the snow creates puddles which will enlarge and create melt ponds. The excess water will go through the brine drainage channels and will flush out the remained brine within the sea ice eventually. This reduces the sea ice salinity further. The snow-covered sea ice will melt away completely later in summer in the case of a first year sea ice.

In summary, during the freeze-up and melt period, the geophysical and thermodynamic parameters change rapidly, thus, increasing the dielectric values. During the winter, on the other hand, the geophysical parameters are more stabilized and the thermodynamic

processes are slowed down. Dielectric values at this stage are stable but lower than those of both freeze-up and melt period. As a final note, it is interesting to follow the temporal change in the microwave back-scattering versus the snow-covered sea ice evolution as shown in [42], see Figure 2.4. Since the microwave back-scatterings are affected by the dielectric profile, the above discussion helps us understand the temporal change in micorowave back-scattering. Generally, microwave back-scattering increases as the dielectric values increase. It should also be noted that the microwave signature of the snow-covered sea ice is also dependent on the roughness of the profile. The rougher surfaces (*e.g.*, due to windy conditions) increase the monostatic back-scattering values.

## *2.5 Electromagnetic Inverse Scattering*

This Section investigates the electromagnetic inverse scattering. To this end, the definition of inverse problems and general approaches to solve these problems are presented in Section 2.5.1. Next, Sections 2.5.2 and 2.5.3 describe the forward and inverse solvers respectively, as two main components of an inversion algorithm.

### *2.5.1 Inverse Problem and Inversion*

Problems can be categorized into forward and inverse problems. When an input is applied to a physical system, a response is created based on the system's characteristics. A forward problem deals with the prediction of the system's response with the knowledge of its characteristics and input. On the other hand, an inverse problem deals with the prediction of system's characteristics or input when provided with the system's response. Broadly speaking, electromagnetic inverse problems can be classified into two categories: electromagnetic inverse source and electromagnetic inverse scattering problems. In electromagnetic inverse source problems, the unknown to be found is

the current distribution (*e.g.*, current distribution of a radiating element) that creates electromagnetic fields. In the electromagnetic inverse source problem, the response of the system (resulting electromagnetic fields) is known from measurements. In addition, the system's characteristics (*e.g.*, Green's function of free space) is also known. Therefore, the electromagnetic inverse source problem may then be formulated as finding the input to the system (current distribution) from the known system's response and characteristics. On the other hand, in the electromagnetic inverse scattering problem, we deal with an unknown medium. This unknown medium is interrogated by known incident electromagnetic fields (input to the system). The interaction of these known incident electromagnetic fields with this unknown medium results in scattered electromagnetic fields. These scattered electromagnetic fields, which are the response of the system, are then measured. The electromagnetic inverse scattering problem can then be formulated as finding the properties of this unknown medium (system's characteristics) from the knowledge of the system's input and response. The electromagnetic inverse scattering problem as applied to snow-covered sea ice is considered in this thesis. Therefore, within this thesis, we may use the electromagnetic inverse scattering problem and the electromagnetic inverse problem interchangeably.

As noted above, the inverse problem retrieves the parameters of a target (a medium) through utilizing the measured response. There are at least two approaches to retrieve the parameters of interest [43], which are to be explained below.

The first approach is empirical-based which does not depend on electromagnetic modeling. To explain the first approach, consider a set of $N$ different measurements, denoted by $D$ as

$$D = \{(x_i, y_i) \,|i = 1, 2, .., N\} \tag{2.42}$$

In (2.42), $x_i$ and $y_i$ are the measured data, and the parameter of interest, respectively, at the $i$th measurement. For example, $x_i$ can be the electromagnetic measured data

corresponding to an ice thickness of $y_i$. In this approach, the goal is to utilize $D$ to find an appropriate relation $f$ between the measured data and the parameter of interest. For example, finding an $f$ that minimizes the following norm

$$\left\| \underline{y} - f\left(\underline{x}\right) \right\| \tag{2.43}$$

where $\underline{y}$ and $\underline{x}$ denote the vectorized form of $y_i$ and $x_i$ respectively. There are different techniques to achieve this goal. One technique is the parametric regression. In this technique, it is assumed that the relation between $\underline{x}$ and $\underline{y}$ can be characterized in a parametric way (*e.g.*, with a multiple linear regression). In this statistical approach, it is essential to choose the right expression and have a large data set to minimize the fitting error. In summary, this technique requires a large data set containing different $x_i$ and $y_i$ measurements so as to find an appropriate relation between $x_i$ and $y_i$. Once this relation is found, the parameter of interest can be inverted for a given measured data through substitution into the equation.

Next technique within the first empirical-based approach is the non-parametric regression in which no assumption is made on the relation between $\underline{x}$ and $\underline{y}$. One example of this technique is the use of neural network as in [44]. The training strategy plays a major role in successful retrieval of this technique. Similar to the previous technique, a large data set is required to train the algorithm properly.

A majority of studies on parameter (*e.g.*, sea ice thickness, temperature, etc.) or characteristics (*e.g.*, sea ice type, extent, concentration, etc.) retrieval of snow and sea ice have been carried out using this empirical-based approach. Some of the important research studies within this framework are explained below. In [45], the sea ice concentration is retrieved through a linear interpolation of brightness temperature. In [46], the sea ice thickness is shown to be related to the radar signature of the profile through a linear regression. A similar work in [47] reported a significant logarithm

correlation between the sea ice thickness and the cross-polarized L-band radar data. Also in [48], the co-polarization to cross-polarization ratio was shown to have a linear relation with multi-year sea ice thickness. In [49], sea ice temperature is retrieved through an interpolation between the observed brightness temperature at 6.5 GHz, sea ice concentration, and sea ice emissivity. Furthermore, in [46], the type of sea ice is distinguished based on the back-scattering value thresholds defined for various ice types. Also neural networks have also shown to be a capable tool in sea ice classification. One example is in [50] where the algorithm could successfully distinguish different ice types using radarsat-1 ScanSAR data from the Baltic sea. For snow layer retrieval, the thickness has been retrieved utilizing a snow radar in [51]. The retrieval is based on the signal power thresholds and peaks defined based on the received time-domain scattered signal. A similar work for thickness retrieval is also presented in [52]. More recently, a novel method has been proposed in [53] that determines the fresh snow thickness through co-polarization phase difference of X-band SAR. Finally in [54], the snow-water-equivalent (SWE) is retrieved through a linear interpolation of brightness temperatures at different frequencies.

The second retrieval approach is physical-based which relies on electromagnetic modeling. In this approach, the characteristics of the system are predicted using an electromagnetic model. The mechanism to solve this inverse problem is formulated by the utilized electromagnetic inversion algorithm. Broadly speaking, inversion algorithms can be categorized into linear and nonlinear. Linear inversion algorithms approximates the physics of wave propagation through linearizing the scatterring problem, and then solve for the unknown. For example, the Born approximation, which is a famous linear inversion algorithm, approximates the total field within the scatterer to be equal to the incident field so as to linearize the scattering problem. The parameters of the scatterer (*e.g.*, sea ice thickness and dielectric properties) are then to be found from the measured data by assuming this simplified physics (linearization). As will be seen

later, as opposed to nonlinear approaches, linear inversion algorithms do not need to update the unknown parameters iteratively, nor find the new scattered fields. As a result, no forward solver is needed to be used in conjunction with linear inversion algorithms so as to simulate the scattered field. Consequently, simpler techniques compared to nonlinear inversion algorithms can be used to solve linearized inversion problems; *e.g.*, Fourier transformation-based techniques [55]. The linearization approximation mentioned above can result in low reconstruction accuracy for complex profiles. To alleviate this problem, the second category of physical-based retrieval approaches, which are nonlinear inversion algorithms, can be used.

In contrast to linear inversion algorithms, nonlinear inversion algorithms do not attempt to simplify the physics of wave propagation within the scatterer. That is, they attempt to converge to the actual wave propagation within the profile in an iterative fashion. During this iterative process, nonlinear inversion algorithms update the unknown parameters until convergence occurs. One approach to solve the nonlinear inversion problem is to formulate it through an optimization algorithm. Optimization algorithms as applied to the electromagnetic inverse scattering problem are iterative and often require repeated calls to inverse and forward solvers so as to minimize a cost function [56–58]. (There also exist some iterative inversion algorithms that do not require explicit calls to a forward solver [59].) At each iteration of the nonlinear inversion algorithm, the inverse solver calculates an estimated profile based on the measured scattered data and the available estimate for the profile at that iteration. The forward solver will then calculate the scattered data due to the newly estimated profile.[(19)] By iteratively minimizing the data misfit cost function between the measured and simulated data, the inversion algorithm attempts to converge to an estimated profile that is sufficiently close to the actual one. As noted before, the iterative nature of these reconstruction algorithms is to handle the nonlinearity of the mathematical formulation

[(19)] Typically, a forward solver calculates the fields inside the domain of interest as well as on the measurement domain.

associated with the electromagnetic inverse scattering problem. Finally, it should be noted that an optimization-based nonlinear electromagnetic inversion algorithm will be considered in this thesis.

There are very few studies cited in the literature on the electromagnetic inversion of snow and sea ice. Some of the important studies in this area are described below. It should be noted that the algorithms utilized in each study are suitable only for a specific profile and data set. In [56], a review on the earlier inversion algorithms for sea ice can be found. Most of the early work on sea ice inversion investigate considerably simplified profiles. These profiles are generally a one-layer medium with flat interfaces. For example in [60], the profile is simplified into a single sea ice layer with flat interfaces. Then, the thin saline ice thickness is retrieved using time-series back-scattered data, considering the penetration depth of electromagnetic waves. In this paper, a combination of radiative transfer equation and thermodynamic saline ice growth model acts as the forward solver. Also, the Levenberg-Marquardt scheme is utilized as the inverse solver. More advanced models are used with a one-layer ice having rough interfaces. For example in [61], a combined surface and volume scattering model for altimeter measurements is used to re-track individual waveforms scattered from the ice layer. Then a weighted least-squares fitting procedure is used to invert the data. Another example is brought in [62] where a combination of the radiative transfer theory and the dense medium phase and amplitude correction theory is utilized as the forward model. This model predicts the radar signature of a single sea ice layer with rough interfaces. Then, the Levenberg-Marquardt inverse solver scheme is utilized to retrieve the sea ice thickness. The research on the electromagnetic inversion of snow-covered sea ice is truly scarce. One such example is brought in [63] where geometric optics is used as the forward solver to predict the large-scale radar signature of the profile. Then, an automated steepest descent method, as the inverse solver, minimizes the cost function to retrieve three parameters: the power reflection coefficient at nadir[(20)], the

[(20)] Herein, nadir denotes the direction that is perpendicular to the profile; *i.e.*, 0° incidence angle with respect

root-mean-square surface slope, and the volume scattering albedo. Another example can be found in [64] where a helicopter-mounted coil induces electromagnetic fields as flying over snow-covered sea ice. A forward solver then calculates the magnetic field at the coil, and the thickness is then retrieved through the Levenberg-Marquardt inverse scheme.

We have now briefly described physical-based electromagnetic nonlinear inversion algorithms. As noted above, such inversion algorithms require the use of two different solvers: forward and inverse solvers. In what follows, these two solvers will be explained in more details.

### *2.5.2 Forward Solver*

The role of the forward solver is to solve the forward problem. In our framework, this translates into calculating the electromagnetic response of the profile, as well as the field in the profile, when provided with the system's input (*i.e.*, incident field) and characteristics (*i.e.*, dielectric profile). Ideally, the response calculated by the forward solver should be equal to the data measured in practice from the same profile. (We also note that the forward solver also calculates the fields within the profile.) It is assumed that the available data to be used in this research is the measured normalized radar cross section (NRCS) of the profile. Therefore, the forward solver to be utilized in this research needs to be able to calculate the NRCS so as to be compared with the measured NRCS. The NRCS data can be collected under different configurations; *i.e.*, having different incidence angles, receiving angles, frequencies of operation, and polarizations. To this end, let's assume a plane wave of frequency $f$ and polarization $q$ impinges at angles of $\psi_{\text{inc}} = (\theta_{\text{inc}}, \varphi_{\text{inc}})$ on the dielectric profile of interest, denoted by $\chi(\boldsymbol{r})$, where $\theta$ is the elevation angle, $\varphi$ is the azimuth angle. Also, $\psi$ is a placeholder

to the vertical direction.

for these two angles. Now, if the $p$-polarized component of the far-field scattered field is collected from angles of $\psi_{\text{scat}} = (\theta_{\text{scat}}, \varphi_{\text{scat}})$, the resulting NRCS is defined as

$$\sigma_{pq}\left(\chi(\boldsymbol{r}); \psi_{\text{inc}}, \psi_{\text{scat}}, f\right) \triangleq \frac{1}{A}\left\langle \lim_{R_r \to \infty}\left(4\pi R_r^2 \frac{S_s^p}{S_i^q}\right)\right\rangle \tag{2.44}$$

for a distributed target of surface $A$ area at a distance of $R_r$. Also, $S_i^q$ and $S_s^p$ are the power density illuminating the target at a linear $q$ polarization, and the power density scattered off the target at a linear $p$ polarization, respectively. The symbol $\langle\ \rangle$ is the ensemble average of a large number of independent measurements. The polarization is assumed to be either horizontal (H) or vertical (V); *i.e.*, $p, q \in \{\text{H}, \text{V}\}$. Finally, the incident electric field having $q$ polarization will be denoted by $E_{\text{inc}}^q$, and the scattered field with $p$ polarization will be denoted by $E_{\text{scat}}^p$.

The scattered field can be calculated through solving the Maxwell equations which govern the wave's behavior. Generally, various forward solvers are differentiated from one another through their approaches towards solving these equations. However, from the snow-covered sea ice remote sensing perspective, forward solvers can be divided into the models considering only the surface scattering, and the models that also incorporate the effects of volume scatterers. In Section 2.2, it was explained that the snow-covered sea ice profile is a layered medium with possible inclusions within each layer. Surface scattering models assign an effective permittivity to each layer, as described in Section 2.3, and simulate the scattered field arising from these homogeneous layers having rough boundaries in between. Volume scattering models do not assign an effective permittivity to each layer. Instead, they account for the scattering contributions due to inclusions and surface-volume interactions. It should also be noted that forward models have also different capabilities in handling the profile's characteristics such as the number of layers, inclusion of rough boundaries, and the volume scatterers' properties. Finally, we note that Chapters 3 to 6 of this thesis consider a surface scattering model; then, in Chapter 7, a volume scattering model is added to

this surface scattering model.

Some of the surface scattering models applied to geophysical profiles are the geometric optics approximation (GO) [65], the small perturbation theory (SPM) [66], the boundary perturbation theory (BPT) [67], and the integral equation method (IEM) [68]. Some volume scattering models are the polarimetric strong fluctuation theory (SFT) [69] , the dense medium radiative transfer theory (DMRT) [70], and a model introduced in [71] for scattering from a low-dielectric layer of Rayleigh scatterers with irregular boundaries. The disadvantages of volume scattering models are their limitations on the number of layers, the properties of the inclusions, and the permittivities of the background layers. Finally, there are numerical full-wave solvers which result in high precision in calculating the scattered fields, for example finite-difference and finite-volume time-domain methods [69, 72]. The main disadvantage of these methods is the high computational expense that makes their incorporation in inversion algorithms difficult.

### *2.5.3 Inverse Solver*

The role of the electromagnetic inverse solver is to reconstruct the parameters of interest, in our case the dielectric profile denoted by $\chi$. This reconstructed profile should be as similar as possible to the true profile. This is usually achieved through the iterative minimization of a misfit cost function, denoted by $\mathcal{F}(\chi)$, between the measured and simulated data, as depicted in Figure 2.5. However, this cost function is ill-posed; thus, its minimization may result in an unstable (oscillatory) solution. As noted earlier, this ill-posedness indicates that $(i)$ a small change in the measured data can result in significant changes in the reconstructed dielectric profile (instability), and $(ii)$ the uniqueness of the solution is not necessarily guaranteed [73, 74].[(21)] Therefore,

[(21)] As noted in Chapter 1, although a physical solution always exist for our problem, the mathematical problem (strictly speaking) may not support the existence of the solution. For example, the use of a model

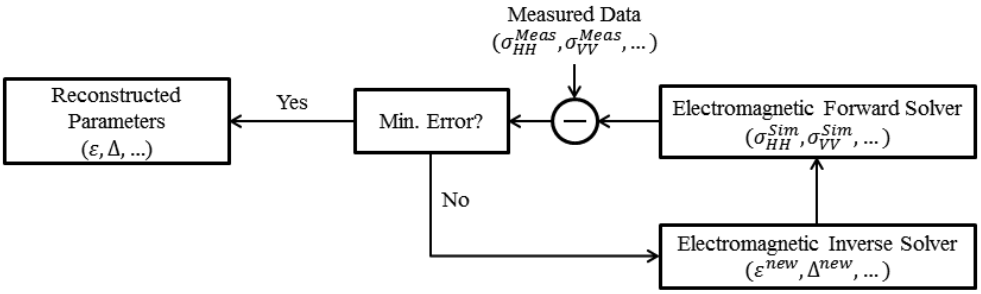


*Fig. 2.5:* The nonlinear inversion algorithm scheme.

due to this ill-posedness, the data misfit cost function needs to be regularized, which help to filter out those components of the measured data that can result in oscillatory solutions. This can be achieved by using several methods such as additive [75], projection-based [76], or multiplicative regularization methods [77]. For example in additive regularization, instead of minimizing the data misfit cost function, $\mathcal{F}(\chi)$, the regularized cost function, denoted by $\mathcal{C}(\chi)$, will be minimized as

$$\mathcal{C}(\chi) = \mathcal{F}(\chi) + \beta\mathcal{L}(\chi) \tag{2.45}$$

In (2.45), $\mathcal{L}(\chi)$ is the regularization cost function, and $\beta \in \mathrm{R}^{+}$ is the regularization weight. The regularization parameter $\beta$ needs to be chosen in such a way that is not too large to over-regularize, and not too small to under-regularize the problem. For linear ill-posed problems, there are some methods such as the $L$-curve [78] and generalized cross validation [79] techniques to properly determine the regularization weight. However, to the best of our knowledge, most of the techniques for choosing the regularization weight for nonlinear ill-posed problems are *ad hoc*.

Another common method of regularization is projection-based regularization. This regularization technique projects the solution space into a smaller subspace, and then

that assumes a flat interface with a homogeneous layer for an actual rough layered medium in conjunction with measured monostatic radar data can result in no solution. In practical cases, the model is chosen to be close to the actual problem, but of course is still not exact. In such cases, we usually formulate the problem based on cost function minimization as opposed to solving an exact equation.

attempts to reconstruct the solution in this subspace. For example, Krylov subspace and the truncated singular value decomposition regularization schemes fall into this category [8]. In some other inverse problems such as snow-covered sea ice remote sensing, the possible ranges of the parameters of interest might be known (*e.g.*, upper and lower levels for young sea ice real-part permittivity). In such cases, the inverse solver can attempt to reconstruct the unknown parameters within these ranges instead of blindly looking for any value. Such approaches, which will be used throughout this research, will also fall under the projection-based regularization scheme.

Another way to reduce the degree of ill-posedness is collecting "sufficient" scattering data. Except in some special cases (*e.g.*, see [80]), it is not currently known how we can determine whether or not sufficient scattering data has been collected for an electromagnetic inverse scattering problem. Therefore, at the current state-of-the-art, we need to rely merely on collecting as much scattering data as possible.[(22)] Moreover, the importance of increasing the number of measured data points can be mathematically justified as follows. Let's assume that the operator $\mathcal{M}$ maps the information within the snow-covered sea ice (imaging domain) to the NRCS data at the measurement site. The information that will be mapped to the NRCS data, denoted by $\sigma$, are often called contrast sources [82], which are the multiplication of the dielectric contrast of the snow-covered sea ice profile, denoted by $X$, and the induced electric field inside the profile ($E$). That is,

$$\sigma = \mathcal{M}(XE). \tag{2.46}$$

The challenge in finding $X$ from (2.46) lies in the fact that the inverse of the operator $\mathcal{M}$ does not exist since the null space of $\mathcal{M}$ is not trivial (due to non-radiating sources [83]). In inverse scattering, the issue of non-trivial null space of $\mathcal{M}$ is often handled by

[(22)] We note that such scattering data need to be reliable. If a non-reliable data point is added to a data set, this can deteriorate the performance of the inversion algorithm. In practical applications, we might know that (1) all data points are equally reliable, (2) some data points are not reliable, and (3) some data points are more reliable than the others. In case 1, we can utilize all data points equally. In case 2, we can discard not reliable data points. In case 3, we can use the concept of data covariance matrix [81] so as to modify the cost function to be minimized based on data points' uncertainties.

performing multiple measurements with the hope that the collective null space of all the measurements, which is the intersection of all individual null spaces, becomes trivial [83]. We note that in all these measurements, the induced electric field $E$ will be different. However, it is assumed that $X$ does not vary from one measurement to the other.

Now we can define the data misfit cost-function, $\mathcal{F}(\chi)$, for our snow-covered sea ice application. As explained above, the measured scattering data of our interest are the NRCS values. Therefore, $\mathcal{F}(\chi)$ can be defined as

$$\mathcal{F}(\chi(\boldsymbol{r})) \triangleq \sum_{i=1}^{nf} \gamma(f_i) \sum_{n=1}^{nRx} \sum_{m=1}^{nTx} \sum_{p=\mathrm{H,V}} \sum_{q=\mathrm{H,V}} \kappa_{pq}(\psi_{\mathrm{inc}}^{(m)}, \psi_{\mathrm{scat}}^{(n)}, f_i) \times \left| \sigma_{pq}^{\mathrm{meas}}(\psi_{\mathrm{inc}}^{(m)}, \psi_{\mathrm{scat}}^{(n)}, f_i) \; - \; \sigma_{pq}^{\mathrm{sim}}(\chi(\boldsymbol{r}), \psi_{\mathrm{inc}}^{(m)}, \psi_{\mathrm{scat}}^{(n)}, f_i) \right|. \tag{2.47}$$

In (2.47), $\gamma(f_i)$ and $\kappa_{pq}$ are the weighting factors, $\sigma^{\mathrm{meas}}$ is the measured NRCS data from the actual profile, and $\sigma^{\mathrm{sim}}$ is the simulated NRCS data due to the predicted dielectric profile $\chi(\boldsymbol{r})$. (The position vector within the domain of interest is denoted by $\boldsymbol{r}$.) The utilized expression for the frequency weighting factor is

$$\gamma(f_i) \; \triangleq \left( f_i^2 \sum_{\zeta=1}^{nf} \; f_\zeta^{-2} \right)^{-1}. \tag{2.48}$$

The frequency weighting factors in (2.48) have been already successfully used in geophysical inversion [84] in low frequencies. Herein, we use this weighting for snow-covered sea ice remote sensing. We only note that the choice of $\gamma(f_i)$ as presented in (2.48) lies in the idea that the smaller the frequency of operation is, the less nonlinear the associated mathematical problem will be. Therefore, based on (2.48), more weight is assigned to NRCS data of lower frequencies so as to help the inversion algorithm not be trapped in local minima due to the increased nonlinearity in higher frequencies. This frequency weighting can then help the convergence of the inversion algorithm to

an appropriate solution. As can be seen, the total numbers of frequencies, receiving angles, and incidence angles are $nf$, $nRx$, and $nTx$ respectively. Also, four different combinations of polarization components, namely, HH, HV, VH and VV, can be used. Therefore, when using all polarization combinations, the total number of data points to be used in reconstructing the unknown $\chi(\boldsymbol{r})$ will be $4 \times nTx \times nRx \times nf$.

In addition to the general challenges facing all electromagnetic inversions, there are specific challenges to snow-covered sea ice dielectric profile reconstruction. One is having limited measurement access (*e.g.*, measured data can be collected only above the domain of interest; not everywhere around it) that limits the number of data provided to the inverse solver. This limitation can potentially create an imbalance between the number of measured data points and the number of unknowns to be reconstructed. Below, two strategies are introduced (namely parametrization and use of prior information) to tackle this problem.

*Parametrization*

One way to handle the imbalance between the number of data points and unknowns is to increase the number of data points (*e.g.*, through the use of different polarizations and frequencies, several transmitting and receiving antennas). Another way is to reduce the number of unknowns. However, as noted above, microwave remote sensing of snow-covered sea ice merely permits performing limited-view one-sided measurements at limited frequencies and polarizations. It is, therefore, essential to parametrize the snow-covered sea ice dielectric profile to reduce the number of unknowns; thus, having a better balance between the number of unknown and known quantities. (We note that almost all the snow-covered sea ice inversion in the literature perform parametrization [56, 60–64].)

To set out parametrization for snow-covered sea ice under investigation in this research, it is assumed that the ice-formation process yields a layered medium with rough in-

terfaces and complex permittivity values with sphere-like or randomly oriented brine inclusions (note Sections 2.2 and 2.3). Therefore, we model the arctic snow-covered sea ice profile as a layered structure with air and ocean as upper and lower half-spaces. (This model has been shown to be in good agreement with experimental results for the snow-covered sea ice [72, 85].) Therefore, we begin our parametrization by assuming that the domain to be imaged is a layered medium, consisting of snow and ice layers, sandwiched between air and ocean half spaces. The next step in our parametrization assumes that the layers' properties do not vary in the horizontal plane ($xy$ plane). Now, let's focus on the vertical change (*i.e.*, change along the $z$ axis) of the dielectric properties within each layer. Electrically small inclusions within each layer, such as brine inclusions, cause each layer to have an inhomogeneous (and, possibly anisotropic) complex permittivity distribution. However, it is very difficult, if not impossible, to reconstruct these small inclusions individually merely based on the NRCS data, which is a far-field quantity. (This is due to the fact that super-resolution microwave inversion often requires capturing the information within evanescent waves, which is usually done by near-field measurements [86].) Therefore, we do not aim to reconstruct these individual electrically small inhomogeneities within each layer directly. In fact, in the cases where the existence of these inclusions is negligible, we assume that each layer has a homogeneous isotropic relative complex permittivity distribution as a simplifying assumption. This homogeneous isotropic relative complex permittivity is the effective relative complex permittivity of that layer. On the other hand, in the cases where the existence of these inclusions needs to be taken into account, parameters associated with the *collective* effect of these inclusions will be added as unknowns to the problem. In addition to the layers' relative complex permittivities, denoted by $\epsilon = \epsilon' + j\epsilon''$, parameters associated with the collective effect of non-negligible inclusions, thickness values of layers, denoted by $\Delta$, their surface roughness parameters have an important role in governing the interaction of electromagnetic waves with the profile. The surface roughness of a given layer is usually parametrized by two parameters [87]: $h$, which is

the root-mean-square (rms) height of roughness, and $l$, which is the roughness correlation length[23]. Therefore, the unknowns to be reconstructed are the parametrized form of $\chi(\boldsymbol{r})$.

To clarify this, let's consider an example in which we have a snow-covered sea ice profile with a single snow and a single ice layer. Based on the above parametrization, the unknown dielectric profile function $\chi(\boldsymbol{r})$ is parametrized into 12 unknowns for this example; namely,

$$\chi = \Big[\epsilon'_{\text{snow}} \quad \epsilon''_{\text{snow}} \quad \epsilon'_{\text{ice}} \quad \epsilon''_{\text{ice}} \quad \Delta_{\text{snow}} \quad \Delta_{\text{ice}} \quad h_{\text{air-snow}} \quad l_{\text{air-snow}} \quad h_{\text{snow-ice}} \quad h_{\text{snow-ice}} \quad h_{\text{ice-water}} \quad h_{\text{ice-water}}\Big] \in \mathtt{R}^{12} \tag{2.49}$$

where $\Delta_{\text{snow}}$ and $\Delta_{\text{ice}}$ denote the thickness of snow and ice layers respectively. Also, the subscripts used with roughness parameters indicate the interface between two layers. For example, $h_{\text{air-snow}}$ represents the rms height roughness at the interface of air and snow layer. Therefore, for this example, the inversion algorithm needs to reconstruct these 12 real unknowns. As will be discussed later, some of these unknown parameters can be assumed to be known for a given application. It is clear that if more layers are added to this model, the number of parameters increases accordingly. Finally, with the parameterization explained for the above example, the data misfit cost functional $\mathcal{F}(\chi)$ given in (2.47) will become a mapping from an $\mathtt{R}^{12}$ space to one single real number $\mathtt{R}$; *i.e.*, $\mathcal{F} : \mathtt{R}^{12} \rightarrow \mathtt{R}$. To further clarify our parametrization, let's consider the previous example but now with non-negligible inclusions in the snow layer; *e.g.*, having large snow grains. As will be discussed in Chapter 7, the snow grain size will now be added to the vector of unknowns to represent the collective effect of these inclusions on the volume scattering component.

[23] The height probability density function, denoted by $p(\zeta)$, is defined based on the probability of surface height occurrence, $\zeta(x, y)$, relative to the mean surface value (*i.e.*, $< \zeta >$). Based on this, the rms height is defined as $h =< \zeta^2 >^{1/2} = [\int_{-\infty}^{\infty} \zeta^2 p(\zeta) d\zeta]^{1/2}$. Moreover, denoting the surface correlation function by $C$, the correlation length of $l$ happens for $C(l) = e^{-1}$. Thus, the heights of two points on the surface separated by a distance greater than $l$ are considered to be uncorrelated [27].

*Use of prior Information*

Any extra information about the profile's characteristics that can be provided to the inverse solver will help the inversion algorithm converge to more accurate reconstruction. The use of prior information can be regarded as an attempt to make the null space of the problem as close as possible to trivial. There are different ways using which prior information can be incorporated into the inversion algorithm. In what follows, we present some of them which have been applied in this research. The most basic way is the case when the prior information provides exact information about an unknown, thus, removing that unknown from the list of the unknowns to be reconstructed. For example, as will be seen in this thesis, we can sometimes obtain the snow-air roughness parameters using lidar measurements, thus, removing $l_{\text{air-snow}}$ and $h_{\text{air-snow}}$ from the list of unknowns. Another way of using prior information is for the case when we know the possible ranges of the unknowns. In such cases, we may employ the projection-based regularization scheme as explained before, or use auxiliary unknowns [88]. Furthermore, a reasonable estimate for the vector of unknowns can be used as prior information to initialize[(24)] the inversion process. This is, in particular, useful for time-series data inversion [89]. Finally, different models such as the permittivity curve [52, 90] and thermodynamic ice growth model [60] can be incorporated into the inversion process as prior information. As will be seen later in this thesis, this may require the use of auxiliary unknowns.

[(24)] Nonlinear inversion algorithms require an initial guess to start the inversion process.

# 3

# Nonlinear Inverse Scattering Algorithm

## *3.1 Overview*

In Chapter 2, the background on the snow and sea ice geophysics, dielectric properties, thermodynamics, and the electromagnetic inverse scattering were explained. In this chapter, a nonlinear electromagnetic inverse scattering algorithm is developed and presented that reconstructs the snow-covered sea ice dielectric profiles using monostatic or bistatic, single or multiple-frequency, multi-polarimetric normalized NRCS data collected at any desired incidence angle. To this end, following an introduction in Section 3.2, the problem statement is brought in Section 3.3. Next in Section 3.4, the snow-covered sea ice profile is parametrized from an inverse scattering perspective. These profile parameters are the unknowns to be retrieved through the inversion algorithm.

As previously shown in Chapter 2, the electromagnetic inverse scattering algorithm

requires a forward and an inverse solver. Following this approach, in Section 3.5, the boundary perturbation theory is introduced as the forward solver utilized to simulate the normalized radar cross section data based on the simulated scattered field. Subsequently, the differential evolution as a global optimization inverse solver is presented in Section 3.6. This technique retrieves the complex permittivities, thickness values, and roughness parameters of the snow-covered sea ice. The inversion results for the so-called young ice are presented in Section 3.7. The parameters of the profile are retrieved utilizing the simulated data collected under the bistatic and monostatic configurations, as described in Sections 3.7.1 and 3.7.2, respectively. Next in Section 3.7.2, noise is added to the synthetic data to assess the robustness of the inversion algorithm. Finally, a conclusion is brought in Section 3.8. It is concluded that the achievable quantitative accuracy of the reconstructed profiles is reasonable as long as sufficient scattering data points are provided to the inversion algorithm.

The materials presented in this chapter are based on the paper published in the IEEE Geoscience and Remote Sensing Letters in 2015 [91][(1)].

## *3.2 Introduction*

This chapter is focused on the development of an appropriate electromagnetic inverse scattering algorithm that takes the microwave scattering data collected from a given snow-covered sea ice domain of interest, and then returns some important dielectric profile parameters of that domain. This nonlinear inversion algorithm consists of two main parts: forward solver and inverse solver. The utilized forward solver is the recently-developed boundary perturbation theory (BPT) solver [92], which has the same region of validity as the small perturbation method (SPM) [93]. To the best of

[(1)] © [2015] IEEE. Reprinted, with permission, from N. Firoozy, P. Mojabi, and D. Barber, "Nonlinear inversion of microwave scattering data for snow-covered sea-ice dielectric profile reconstruction," *Geoscience and Remote Sensing Letters, IEEE*, vol. 12, no. 1, pp. 209-213, Jan 2015.

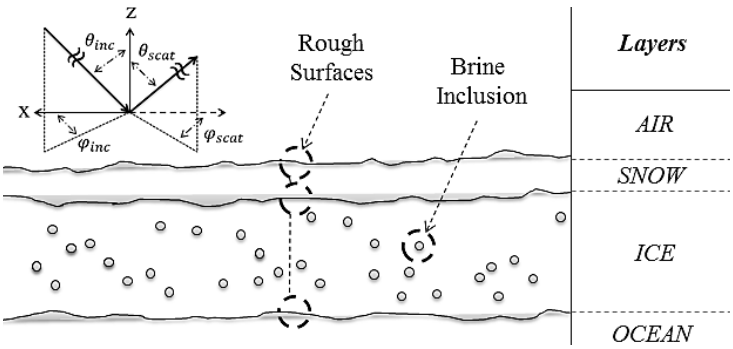


*Fig. 3.1:* Parameterization of the snow-covered sea ice profile into rough layered media.

our knowledge, this forward solver has not been used for snow-covered sea ice inversion. The inverse solver utilizes a global optimization algorithm to minimize a regularized data misfit cost functional.

The research on nonlinear inversion of snow-covered sea ice profile is scarce [57,60], and even less common when ice is covered with a snow layer [56,58]. The main contribution of this chapter is, therefore, the development of a nonlinear inversion algorithm that is capable of simultaneous reconstruction of the effective relative complex permittivity of snow and ice layers and their thickness values as well as their surface roughness parameters using multi-polarimetric multiple-frequency scattered data in both bistatic and monostatic configurations. Although the proposed algorithm assumes a simplified model for snow-covered sea ice and also utilizes idealized measurement scenarios, it is an important useful step towards developing strategies for reconstruction of snow-covered sea ice properties.

## *3.3 Problem Statement*

The unknown to be reconstructed is the snow-covered sea ice dielectric profile, which is denoted by $\chi(\boldsymbol{r})$ where $\boldsymbol{r}$ is the observation point. It is assumed that the available data to be used in this reconstruction is the measured normalized radar cross

section (NRCS) of the profile. To increase the number of data points, the NRCS can be collected under different configurations; *e.g.*, by having different incidence angles as shown in Figure 3.1 (*i.e.*, incidence angles of $\Psi_{\text{inc}} = (\theta_{\text{inc}}, \varphi_{\text{inc}})$ where $\theta_{\text{inc}}$ is the elevation and $\varphi_{\text{inc}}$ is the azimuth angle), receiving angles (*i.e.*, incidence angles of $\Psi_{\text{scat}} = (\theta_{\text{scat}}, \varphi_{\text{scat}})$), frequencies of operation $f$, and polarizations $q$. Therefore, an NRCS denoted as $\sigma_{pq}(\chi(\boldsymbol{r}); \Psi_{\text{inc}}, \Psi_{\text{scat}}, f)$. The polarization is assumed to be either horizontal (H) or vertical (V); *i.e.*, $p, q \in \{\text{H}, \text{V}\}$.

The inversion problem can be formulated as the minimization of the data misfit cost functional, defined as the discrepancy between the measured and simulated NRCS data, over the dielectric profile $\chi$. That is, the data misfit cost functional, $\mathcal{F}(\chi(\boldsymbol{r}))$, can be written as

$$\mathcal{F}(\chi(\boldsymbol{r})) \triangleq \sum_{i=1}^{n_f} \sum_{n=1}^{n_{Rx}} \sum_{m=1}^{n_{Tx}} \sum_{p=\text{H,V}} \sum_{q=\text{H,V}} \Big| \sigma_{pq}^{\text{meas}}(\Psi_{\text{inc}}^m, \Psi_{\text{scat}}^n, f_i) - \sigma_{pq}^{\text{sim}}(\chi(\boldsymbol{r}); \Psi_{\text{inc}}^m, \Psi_{\text{scat}}^n, f_i) \Big| \tag{3.1}$$

where $\sigma^{\text{meas}}$ is the measured NRCS data from the actual profile, and $\sigma^{\text{sim}}$ is the simulated NRCS data due to the predicted dielectric profile $\chi(\boldsymbol{r})$.

## *3.4 Parameterization of Snow-Covered Sea Ice Dielectric Profile*

Microwave remote sensing of snow-covered sea ice merely permits performing limited-view measurements in the sense that the scattering data can only be collected above the domain of interest. Due to this limitation, blind inversion (*i.e.*, inversion without the use of prior information) is more likely to fail for this application. It is, therefore, essential to parametrize the snow-covered sea ice dielectric profile to reduce the number of unknowns; thus, enhancing the quantitative accuracy of the reconstruction results.

To set out this parameterization, we model snow-covered sea ice as a layered media with rough surfaces having air and ocean as upper and lower half-spaces. (It was shown that this model is in good agreement with experimental results [72, 85].) This model is depicted in Figure 3.1. We further assume that each layer has a homogeneous isotropic relative complex permittivity distribution, denoted by $\epsilon = \epsilon' + j\epsilon''$. This homogeneous isotropic relative complex permittivity is, in fact, the effective relative complex permittivity of that layer taking into account the presence of inclusions such as brines. It should be noted that the assumption of having an isotropic permittivity distribution is based on the assumption that the brine cells are spherical inclusions. Although this might not be precise, this simplified model has been successfully used in literature [72]. The surface roughness of a given layer is parametrized by two parameters: $h$, which is the root-mean-square (rms) height of roughness, and $l$, which is the roughness correlation length. It should be mentioned that we will utilize $\Delta_{\text{snow}}$ and $\Delta_{\text{ice}}$ to denote the thickness of snow and ice layers respectively. Also, the subscripts used with roughness parameters will indicate the interface between two layers. For example, $h_{\text{air-snow}}$ represents the rms height roughness at the interface of air and snow layer. With the parameterization utilized in this chapter, the data misfit cost functional $\mathcal{F}(\chi)$ is now a mapping from an $\mathtt{R}^{12}$ space to one single real number $\mathtt{R}$. The minimization of $\mathcal{F}(\chi)$ will then reconstruct these 12 real unknowns.

## *3.5 Forward Solver*

The proposed nonlinear inversion algorithm requires calling a forward solver several times during dielectric profile reconstruction so as to evaluate the data misfit cost functional $\mathcal{F}(\chi)$; thus, the utilized forward solver needs to be sufficiently fast. Herein, the boundary perturbation theory (BPT) formalism, recently developed by Imperatore *et. al.* [92], is used. This method is a first-order approximation technique that provides polarimetric solution to the 3D scattering problem from rough layered media with

arbitrary numbers of layers. For this first-order approximation to be valid, the BPT algorithm only requires the classical gently roughness criterion at the interfaces of layers [92]. The logic of BPT is as follows. The BPT first assumes flat interfaces for the whole profile and then finds the so-called generalized reflection and transmission coefficients. It then considers the effects of roughness as equivalent current densities on flat interfaces to accommodate the incoherent scattering component. The tangential boundary condition is applied and these equivalent current densities are calculated based on the geometry of rough interfaces and the unperturbed field values. Since the roughness parameters of different layers, and subsequently their corresponding equivalent current densities, are considered to be uncoupled, a summation is utilized to find the total scattered field from the profile. Finally, the NRCS is derived from the calculated scattered field. Therefore, the formula to calculate the polarimetric NRCS for an $N$ layered medium with uncorrelated roughnesses for boundaries is as follows [94]

$$\sigma_{pq} = \pi k_0^4 \sum_{n=0}^{N-1} |\alpha_{pq}^{m,m+1}(\mathbf{k}_\perp^{\text{scat}}, \mathbf{k}_\perp^{\text{inc}})|^2 W_n(\mathbf{k}_\perp^{\text{scat}} - \mathbf{k}_\perp^{\text{inc}}) \tag{3.2}$$

Equation (3.2) takes into account contributions from individual rough surfaces within the layered media. The formulation to calculate $\alpha$ can be found in [94], and is based on the previously-calculated field values. Also $\mathbf{k}$ is the wavenumber times wave propagation direction vector and $\mathbf{k}_\perp$ is the perpendicular component of its projection on the surface. Also, $W_n$ denotes the spatial power density of surface $n$, defined as the Fourier transform (denoted by $\mathcal{F}$) of the auto-correlation function of the $n$th rough boundary $\zeta_n$ as [95]

$$W_n(\boldsymbol{\kappa}) = \mathcal{F}\{C_n(\boldsymbol{\rho})\} = \frac{1}{(2\pi)^2} \int\int < \zeta_n(\boldsymbol{r}_\perp + \boldsymbol{\rho})\zeta_n(\boldsymbol{r}_\perp) > e^{j\boldsymbol{\kappa}.\boldsymbol{\rho}} d\boldsymbol{\rho} \tag{3.3}$$

In (3.3), $C_n$ is the auto-correlation function associated with the $\zeta_n$ boundary, $\boldsymbol{r}_\perp$ denotes the position vector on the surface $\zeta_n$, and $<>$ denotes the statistical ensemble average. Two common forms of correlation functions are the exponential and Gaussian

functions, that result in the following spatial power densities [96]

$$W_{\text{Gaussian}}(\mathbf{k}_{\perp}^{\text{scat}} - \mathbf{k}_{\perp}^{\text{inc}}) = \frac{(hl)^2}{4\pi} \exp(\frac{-|\mathbf{k}_{\perp}^{\text{scat}} - \mathbf{k}_{\perp}^{\text{inc}}|^2 l^2}{4}) \tag{3.4}$$

$$W_{\text{exponential}}(\mathbf{k}_{\perp}^{\text{scat}} - \mathbf{k}_{\perp}^{\text{inc}}) = \frac{(hl)^2}{2\pi} \frac{1}{(1 + |\mathbf{k}_{\perp}^{\text{scat}} - \mathbf{k}_{\perp}^{\text{inc}}|^2 l^2)^{3/2}}. \tag{3.5}$$

Different ice and snow types exhibit various values for surface roughness parameters. Thus, one power density formulation might be more appropriate than the other depending on these values. Based on our experience and lidar measurements [97], the exponential distribution best fits the common new ice type. The region of validity for this method is similar to the small perturbation method [98]. We also note that due to its closed-form formulation, this forward model is computationally efficient. This is a vital property for our inversion algorithm scheme as it requires numerous calls to the BPT solver.

## *3.6 Inverse Solver*

The data misfit cost functional $\mathcal{F}(\chi)$ needs to be minimized so as to reconstruct the dielectric profile $\chi$. However, this cost functional is ill-posed; thus, its minimization may result in an unstable (oscillatory) solution. To handle this ill-posedness, we minimize the regularized cost functional $\mathcal{C}(\chi)$

$$\mathcal{C}(\chi) = \mathcal{F}(\chi) + \beta \mathcal{L}(\chi) \tag{3.6}$$

where $\mathcal{L}(\chi)$ is the regularization cost functional, and $\beta \in \mathrm{R}^+$ is the regularization weight. The regularization term is chosen to be the total variation regularizer. That

is,

$$\mathcal{L}(\chi) \triangleq \left|\epsilon'_{\text{snow}} + j\epsilon''_{\text{snow}} - \overbrace{\epsilon_{\text{air}}}^{=1}\right| + \left|\epsilon'_{\text{ice}} + j\epsilon''_{\text{ice}} - \epsilon'_{\text{snow}} - j\epsilon''_{\text{snow}}\right|. \tag{3.7}$$

The regularization parameter $\beta$ needs to be chosen in such a way that is not too large to over-regularize the problem, and is not too small to under-regularize the problem. In this chapter, to find an appropriate value for $\beta$, we perform reconstruction of a given reference true profile using several values of $\beta$. We then find the $\beta$ that provides the most accurate reconstruction. As long as the data collection procedure and noise level as well as the profile to be reconstructed do not change significantly as compared to this reference model, this $\beta$ can be used as a reasonable choice for other profile reconstruction.

We minimize this regularized cost functional via the differential evolution (DE) algorithm.[(2)] To this end, we have implemented the already developed algorithm introduced in the literature (*e.g.*, see [76, 99]). The DE algorithm is based on the evolution concept in which only the fittest elements get the chance to evolve to the next generation. Therefore, in the first generation, all elements are randomly distributed within a search space defined as prior information. Then their corresponding fitness values, $\mathcal{C}$, are calculated. Then three members of this generation are randomly chosen (denoted by $\mathcal{P}_1$, $\mathcal{P}_2$, and $\mathcal{P}_3$) and an off-spring is created as [76]:

$$\boldsymbol{x}_n^{\text{new}} = \begin{cases} \boldsymbol{x}_n^{\text{old}}|_{\mathcal{P}_1} + \xi \times (\boldsymbol{x}_n^{\text{old}}|_{\mathcal{P}_2} - \boldsymbol{x}_n^{\text{old}}|_{\mathcal{P}_3}) & \text{rand}(0,1) \leq \zeta \\ \boldsymbol{x}_n^{\text{old}} & \text{Otherwise} \end{cases} \tag{3.8}$$

[(2)] Several optimization algorithms such as derivative-based local optimizers, *e.g.*, Gauss-Newton and conjugate gradient algorithms, can be used to minimize our nonlinear data misfit cost function, each of which has its own advantages and disadvantages. Herein, we have chosen the DE algorithm due to the fact that it can easily (*i*) utilize phaseless (magnitude-only) data (NRCS data), (*ii*) accommodate different prior information, and (*iii*) incorporate physical/thermodynamic unknowns.

where $\xi$ and $\zeta$ are chosen to be 0.5 and 0.8 respectively [76]. This specific implementation is called the random DE algorithm. If the first parent, $\mathcal{P}_1$, is chosen as the one having the fittest value, as opposed to being chosen randomly, the algorithm is referred to as the DE/Best. Also, if $\xi$ is chosen randomly between 0 and 1, the algorithm may be called DE/ditter [100]. Herein, we use the DE/Best implementation. At this point, the data misfit cost functional is evaluated for each individual and that value is compared to the original parent. Either the off-spring or the parent with the lower fitness value is mutated to the next generation. This process is then repeated again till we get to an acceptable error level. The DE algorithm also requires the implementation of an appropriate boundary condition ensuring that the elements are within the search domain. In our implementation, if an element happens to exit the search domain, it will be randomly placed back somewhere within the search domain. Limiting the search space serves two purposes *(i)* as a projection-based regularization to tackle the inversion instability (ill-posedness) issue [75], and *(ii)* to act as prior information so as to achieve higher accuracy in parameter reconstruction. This limitation is based on our observation of typical permittivity or thickness values for snow and ice.

## *3.7 Inversion Results*

Herein, we attempt to reconstruct snow-covered young ice (YI) dielectric profiles using either microwave bistatic or monostatic synthetic data. For bistatic data collection, the domain of interest is illuminated by a unique incidence angle ($n_{Tx} = 1$); namely, $\Psi_{\text{inc}} = (45^\circ, 0^\circ)$. The scattered data is then collected at several scattered angles, all of which have the same azimuth angle, $\varphi_{\text{scat}} = 10^\circ$, but different elevation angles, $\theta_{\text{scat}}$. The elevation angle is varied from 25° to 65° with 10° increments (*i.e.*, measuring at 5 elevation angles). As far as monstatic data collection scheme is concerned, we use five different incidence angles, $\theta_{\text{inc}}$, from 25° to 65° with 10° increment; thus, having $n_{Tx} = 5$. Since, this is a monostatic setup, one scattered angle, which is the

same as the utilized incidence angle, is used to collect the NRCS data; thus, having, $n_{Rx} = 1$. For both monostatic and bistatic data collection schemes, all possible four polarization combinations are used toward reconstruction of the profile. All these data collection schemes are performed within the frequency range of 3 GHz to 4 GHz at 15 different frequencies equispaced in this frequency range (*i.e.*, $n_f = 15$). For the examples considered herein, this frequency range presents an appropriate trade-off between providing sufficient spatial resolution and penetration depth. Finally, the relative complex permittivity of the ocean is assumed to be $60 + j60$ for all these examples within the frequency range of interest. (Throughout this chapter, a time-dependency of $e^{-j\omega t}$ is implicitly assumed.)

To reconstruct these profiles, we first need to set the search space for the inversion algorithm based on the expected values. The inversion algorithm will then try to reconstruct the true values within the search domain. The search space for relative complex permittivity values is as follows: the real part of the snow permittivity from 2 to 3, the imaginary part of the snow permittivity from 0 to 1, the real part of the ice permittivity from 3 to 5, and the imaginary part of the ice permittivity from 0 to 1. The search space for thickness values is as follows: snow thickness from 0 to 20 cm, ice thickness from 0 to 40 cm. Finally, the search space for roughness parameters is as follows: $h$ and $l$ of the air-snow interface from 0.1 cm to 0.16 cm, and 1.20 cm to 1.60 cm respectively, $h$ and $l$ of the snow-ice interface from 0.12 cm to 0.25 cm, and 0.84 cm to 2.44 cm respectively, $h$ and $l$ of the ice-ocean interface from 0.22 cm to 0.33 cm and 1.00 cm to 5.50 cm respectively.

We finally note that when one deals with inversion of simulated data, *e.g.*, the data presented in Chapters 3 and 4, the simulated data needs to be contaminated with noise and collected on a different discretization grid as compared to that used in the inversion so as to avoid the so-called inverse crime. In our simulated data, we have considered noisy synthetic data sets. (We have also considered noiseless synthetic data

*Tab. 3.1:* Dielectric profile specifications used for snow-covered YI in Section 3.7.1. The complex permittivity values are assumed to be constant within the frequency range of 3 to 4 GHz.

| Snow-Covered YI Profiles | | Case I | Case II | Case III |
|---|---|---|---|---|
| Thickness [cm] | Snow | 5 | 10 | 12 |
| | Ice | 15 | 25 | 32 |
| Permittivity (averaged) | Snow | $2.3 + j0.2$ | | |
| | Ice | $3.6 + j0.5$ | | |
| Roughness Parameters [cm] | Air-Snow | $h = 0.15$ and $l = 1.3$ | | |
| | Snow-Ice | $h = 0.185$ and $l = 1.42$ | | |
| | Ice-Ocean | $h = 0.22$ and $l = 2.6$ | | |

sets for the sake of comparison.) However, since our utilized BPT forward solver does not discretize the imaging domain, *e.g.*, similar to the method of moments, change of the discretization grid is not applicable here. We also note that in Chapters 5, 6, and 7, we consider the inversion of experimental data; thus, there are no risks of committing inverse crime in these three chapters [101].

### *3.7.1 Snow-covered YI—Bistatic setup*

The specifications of the profile of interest are tabulated in Table 3.1 for three different cases with increasing snow/ice thickness values. As noted above, this profile is to be reconstructed using $4 \times 15 \times 5 = 300$ scattering data points. The results of this inversion, denoted by DE/Best, are depicted in Figure 3.2. The two horizontal lines in these plots represent the true snow-ice and ice-ocean interfaces. Also, the $y = 0$ line in these plots is the true air-snow interface. The true permittivity values are demonstrated in these plots by $\square$ (for the real part) and $\diamond$ (for the imaginary part). As can be seen, with the increase of snow/ice thickness, the retrieval of thickness values will degrade whereas the quantitative accuracy of the reconstructed complex permittivity values will not be affected that much. This might be due to the fact that as opposed to thickness retrieval, permittivity retrieval does not need full penetration all the way down to the ocean interface. Finally, Table 3.2 reports the reconstructed roughness parameters corresponding to Figure 3.2. As can be seen, the reconstructed

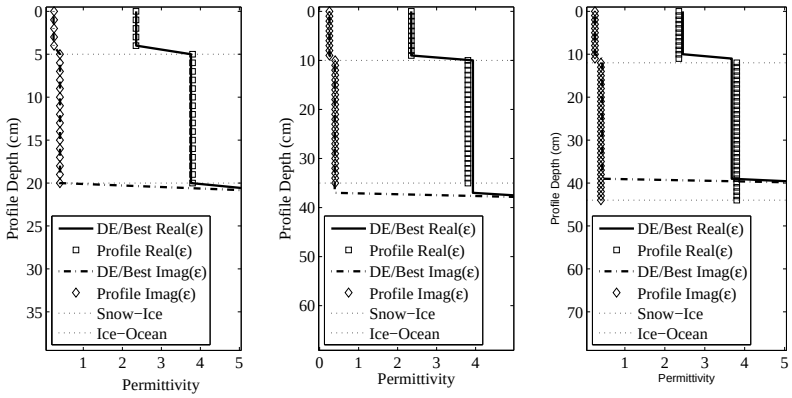


(a) Case I (b) Case II (c) Case III

*Fig. 3.2:* Reconstruction of the snow-covered YI for three different cases of Table 3.1 from bistatic data sets.

roughness parameters for the first interface, *i.e.*, air-snow interface, are more accurate than those for the other two interfaces.

### *3.7.2 Snow-covered YI—Monostatic setup*

Herein, we consider the same snow-covered YI as studied in Section 3.7.1. However, as opposed to Section 3.7.1 in which a bistatic data collection scheme was used, we now consider a monostatic data collection scheme. This is important as a monostatic configuration is more practical as it can be easily mounted on a single ship or an airplane. As described in the beginning of Section 3.7, the total number of data points to be inverted in the monostatic case is the same as the one in Section 3.7.1; *i.e.*, 300. Although the number of data points is the same in both monostatic and bistatic configurations, this does not mean that the amount of useful information is the same in these two different data sets. Based on our numerical trials, we have found that the bistatic data set is generally more suitable for our reconstruction algorithm. We speculate that this is due to the fact that the maximum NRCS usually occurs around the specular reflection angle. The reconstruction results for the monostatic

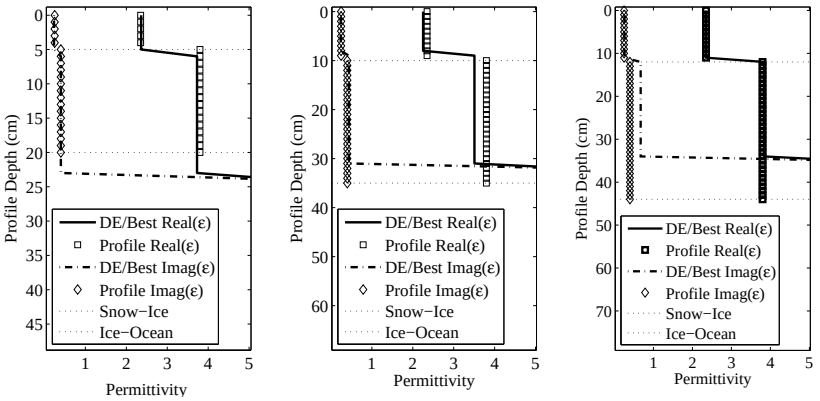


(a) Case I (b) Case II (c) Case III

*Fig. 3.3:* Reconstruction of the snow-covered YI for three different cases of Table 3.1 from monostatic data sets.

cases are shown in Figure 3.3. As can be seen, the inversion accuracy of the bistatic data sets outperform that of the monostatic data sets. However, since the number of data points is kept the same as the bistatic case, the inversion accuracy of the monostatic data sets does not suffer dramatically. Also, thanks to surface roughness, the amount of information within the monostatic data set is increased. Note that if there was no surface roughness, the received electromagnetic wave in monostatic case will be significantly reduced. Therefore, from this point of view, surface roughness is useful for monostatic data collection schemes. Finally, the reconstructed roughness parameters for this example are listed in Table 3.2. As can be seen, the reconstructed roughness parameters for the air-snow interface are more accurate compared to those of the other two interfaces.

### *3.7.3 Snow-covered YI–Noisy data set*

In all the above examples, we did not add synthetic noise to the collected data sets. We now consider the robustness of the inversion algorithm against noisy data sets. It should be noted that, in addition to thermal noise and radar speckle, some other

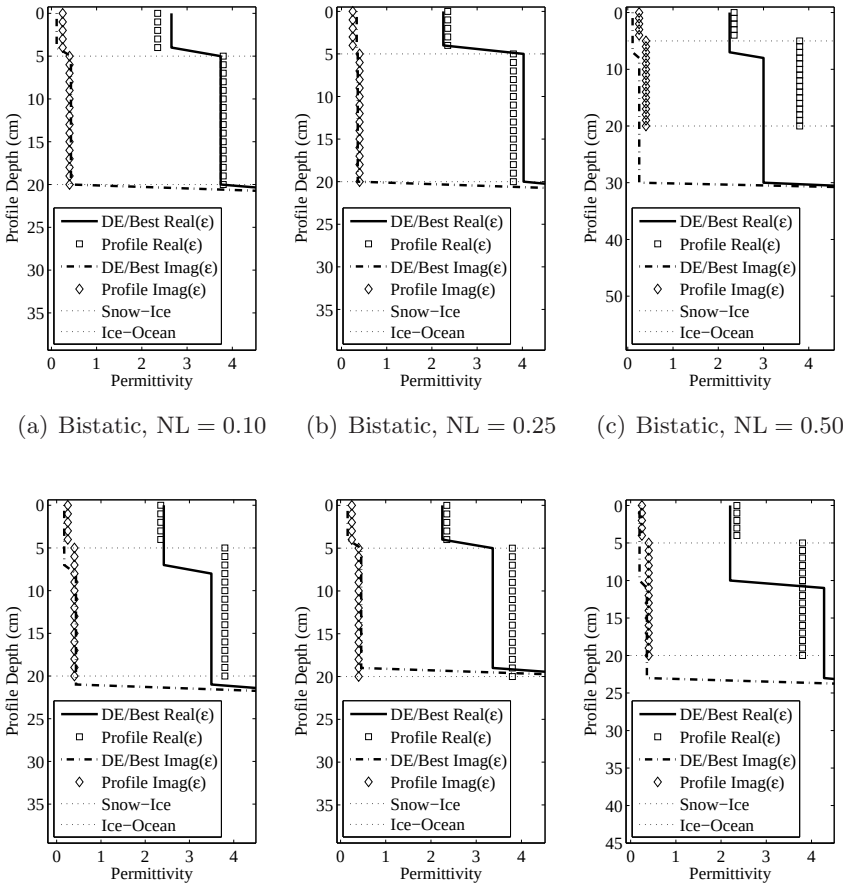


(a) Bistatic, NL = 0.10 (b) Bistatic, NL = 0.25 (c) Bistatic, NL = 0.50

(d) Mono, NL = 0.10 (e) Mono, NL = 0.25 (f) Mono, NL = 0.50

*Fig. 3.4:* Reconstruction of Case I Profile in Table 3.1 from noisy data sets, with varying noise level $NL$, in both bistatic and monostatic (mono) configurations.

interfering signals picked up by the antenna can contribute to the overall noise of the measured data. (The effect of some of these interfering signals may be minimized by using appropriate filtering techniques.) Also, in practice, the parameterization presented in Section 3.4 may not be accurate enough for an actual snow-covered sea ice profile. This simplification can then be regarded as a modelling error in the inversion algorithm. This modelling error can then be regarded as part of the manifest noise for the reconstruction algorithm.

The method used in this chapter to create a noisy data set is as follows. Let's assume

*Tab. 3.2:* Reconstruction of surface roughness parameters; all roughness parameters are in centimetres.

| Figure 3.2 | Case I | | Case II | | Case III | |
|---|---|---|---|---|---|---|
| | $h$ | $l$ | $h$ | $l$ | $h$ | $l$ |
| air-snow | 0.16 | 1.23 | 0.15 | 1.31 | 0.15 | 1.30 |
| snow-ice | 0.16 | 1.52 | 0.20 | 1.31 | 0.21 | 1.29 |
| ice-ocean | 0.22 | 3.86 | 0.28 | 1.83 | 0.24 | 3.41 |
| Figure 3.3 | Case I | | Case II | | Case III | |
| | $h$ | $l$ | $h$ | $l$ | $h$ | $l$ |
| air-snow | 0.15 | 1.30 | 0.15 | 1.30 | 0.15 | 1.30 |
| snow-ice | 0.19 | 1.31 | 0.22 | 1.81 | 0.25 | 1.52 |
| ice-ocean | 0.33 | 4.36 | 0.22 | 2.05 | 0.26 | 3.98 |
| Figure 3.4 | (a) | | (b) | | (c) | |
| | $h$ | $l$ | $h$ | $l$ | $h$ | $l$ |
| air-snow | 0.14 | 1.42 | 0.16 | 1.22 | 0.16 | 1.39 |
| snow-ice | 0.16 | 1.25 | 0.20 | 1.25 | 0.18 | 1.21 |
| ice-ocean | 0.33 | 3.05 | 0.35 | 2.75 | 0.33 | 2.76 |
| Figure 3.4 | (d) | | (e) | | (f) | |
| | $h$ | $l$ | $h$ | $l$ | $h$ | $l$ |
| air-snow | 0.12 | 1.20 | 0.15 | 1.28 | 0.16 | 1.45 |
| snow-ice | 0.22 | 1.22 | 0.21 | 1.77 | 0.21 | 1.45 |
| ice-ocean | 0.33 | 3.86 | 0.35 | 3.60 | 0.36 | 4.76 |

that the noise level is denoted by NL, which can vary from 0 to 1, then the noisy NRCS data will be $(1 \pm \text{NL}) \times \sigma$ where $\sigma$ is the dimensionless noiseless NRCS data. To evaluate the robustness of the inversion algorithm against noisy data, we consider Case I profile of Table 3.1. Two different data sets are then considered for this profile: a bistatic dataset as collected in Section 3.7.1, and a monostatic dataset as collected in Section 3.7.2. Then, three levels of noise are added to these two datasets. Inversion of these noisy datasets are shown in Figure 3.4. As can be seen, the quantitative accuracy of the inversion results corresponding to NL = 10%, and 25% is reasonable. However, for NRCS errors beyond $(max, min) = (1.76, -3.01)$ dB, which correspond to NL = 50%, the inversion results are no longer reliable. The reconstructed roughness parameters for this example are also shown in Table 3.2. As opposed to reconstructed thickness values which seem to suffer the most from increasing NL, this table shows that the reconstructed roughness parameters are not as much sensitive to the noise level.

## *3.8 Conclusion*

Forward and inverse scattering models of snow-covered sea ice hold promise in both the estimation of the geophysical and thermodynamic state of arctic. In this chapter, a nonlinear inversion algorithm was proposed to find the dielectric profile of a given snow-covered sea ice domain of interest from microwave NRCS data. Specifically, this algorithm simultaneously inverts multi-frequency multi-polarimetric bistatic (or, monostatic) datasets to reconstruct the relative complex permittivities, thickness values, and roughness parameters of snow and ice layers. The proposed algorithm has one main limitation: due to the use of the BPT forward solver, the roughness parameters of the interfaces cannot be beyond the validity region of the SPM. If needed, this issue can be handled by using another type of forward solver. It should also be noted that the quantitative accuracy achievable from this inversion algorithm depends on the amount of useful scattering information provided to the algorithm. Using this nonlinear inversion algorithm, three different forms of snow-covered young ice were investigated. It was shown that dielectric profile parameters associated with these cases can be reasonably retrieved as long as sufficient scattering data are available. It was also shown that the reconstruction accuracy, specially, accuracy of the reconstructed ice thickness, will be degraded in the presence of noise.

This chapter, therefore, contributes to the area of sea ice remote sensing, in places with snow-covered sea ice including the Arctic, Antarctic, Baltic Sea or the Sea of Okhotsk, by proposing an inverse scattering algorithm to extract more information from the normalized radar cross section data to be used to infer the dielectric profile. This can have several possible applications such as more accurate ice profile classification, detection of oil spills in sea ice, transport safety monitoring and more precise classification of both the geophysical and thermodynamic state of snow-covered sea ice.

# 4

# Balanced Inversion of Bistatic NRCS Data

## *4.1 Overview*

An electromagnetic inverse scattering algorithm that reconstructs the dielectric profile of the snow-covered sea ice was developed and presented in Chapter 3. In this algorithm, a misfit cost function calculates the discrepancy between the measured and simulated NRCS data associated with a predicted dielectric profile. To reconstruct the unknown profile, this cost function is iteratively minimized utilizing the differential evolution algorithm so as to achieve a minimum discrepancy. The weighting factor employed for this discrepancy in Chapter 3 was equal to unity for both monostatic and bistatic configurations. In this chapter, I introduce a weighting factor to be utilized in the cost function for the bistatic NRCS data, and compare its performance to three commonly-used weighting factors.

After an introduction in Section 4.2, the methodology utilized to perform the inver-

sion is presented in Section 4.3. As previously explained in Chapter 3, the inversion algorithm consists of a BPT forward solver that works in conjunction with DE inverse solver. This algorithm iteratively minimizes the NRCS data misfit cost function to reconstruct the snow-covered sea ice profile. In Section 4.4, four different cost functions (namely blind, normalized, constant, and balanced) are introduced. Subsequently, the reconstruction accuracy of the inversion algorithm utilizing these four cost functions are investigated in Section 4.5. Although these cost functions utilize the same synthetic bistatic NRCS data, their achievable reconstruction accuracy varies. In particular, the developed balanced weighting cost function results in the highest reconstruction accuracy compared to the rest. This weighting factor first normalizes the NRCS data discrepancies and then multiplies them by the measured horizontally-sent and horizontally-received NRCS data. This multiplication gives a larger weight to the data in the vicinity of the specular angle. Finally, the synthetic data is contaminated with noise to further assess the inversion performance. For this case, similar inversion results with respect to the working of the balanced weighting factor are obtained.

The materials of this chapter are based on the paper published in Taylor & Francis Remote Sensing Letters in 2015 [102][(1)].

## *4.2 Introduction*

This chapter, which builds on our abstract presented in [103], is focused on investigating four different cost functions for the inversion of simulated bistatic radar cross section data. Although the application of bistatic data in earth remote sensing is currently limited, it holds promise for accurate retrieval purposes. Such bistatic measurements are feasible via the use of bistatic ground-based scatterometers, two-aperture

[(1)] © [2015] Taylor & Francis Reprinted, with permission, from N. Firoozy, P. Mojabi, and D. G. Barber, "Balanced inversion of simulated bistatic radar cross-section data for remote sensing of snow-covered sea ice," *Remote Sensing Letters*, vol. 6, no. 5, pp. 399-408, 2015.

air-borne radar systems and tandem satellites.

In an inversion algorithm, the choice of the cost function to be minimized is important to properly account for the relative magnitude and importance of all data points. This is, in particular, very important in snow-covered sea ice dielectric profile inversion since the number of measured data points in snow-covered sea ice remote sensing applications is limited compared to the number of unknowns to be reconstructed. Therefore, the available data points need to be weighted with care in the minimization scheme so as to extract as much information as possible from the scattering ensemble. Based on this investigation, an appropriate balanced cost function, which can result in enhanced reconstruction accuracy, is proposed. Using three numerical examples, it will be shown that the proposed balanced inversion can enhance the reconstruction accuracy of dielectric profiles.

Throughout this chapter, we use simulated bistatic NRCS data to evaluate this balanced inversion algorithm. This simulated data is created with the BPT forward solver [94]. The three test cases are simplified models of rough layered snow-covered sea ice profiles. A time-dependency of $e^{-\mathrm{j}\omega t}$ where $\mathrm{j} = \sqrt{-1}$, $\omega$ is the angular frequency, and $t$ denotes the time, is implicitly assumed in this chapter.

## *4.3 Inversion Methodology*

We have recently developed an inversion algorithm for the reconstruction of unknown snow-covered sea ice dielectric profiles (denoted by $\chi$) from NRCS data (denoted by $\sigma$) as the algorithm's input [91]. To this end, this inversion algorithm iteratively minimizes

the following cost function over $\chi$,

$$\mathcal{C}(\chi(\boldsymbol{r})) \triangleq \sum_{i=1}^{\mathrm{F}} \sum_{n=1}^{\mathrm{R}} \sum_{m=1}^{\mathrm{T}} \sum_{p=\mathrm{H,V}} \sum_{q=\mathrm{H,V}} \left| \sigma_{pq}^{\mathrm{meas}}(\psi_{\mathrm{inc}}^{(m)}, \psi_{\mathrm{scat}}^{(n)}, f_i) \; - \; \sigma_{pq}^{\mathrm{sim}}(\chi(\boldsymbol{r}), \psi_{\mathrm{inc}}^{(m)}, \psi_{\mathrm{scat}}^{(n)}, f_i) \right|. \tag{4.1}$$

In the above cost function, $\sigma_{pq}^{\mathrm{meas}}(\psi_{\mathrm{inc}}^{(m)}, \psi_{\mathrm{scat}}^{(n)}, f_i)$ is the NRCS data when the domain of interest is illuminated from the $\psi_{\mathrm{inc}}^{(m)}$ direction with the $(p)$ polarization at the $f_i$ frequency, and then the resulting scattered field is measured from the $\psi_{\mathrm{scat}}^{(n)}$ direction with the $(q)$ polarization at the same frequency. (Polarizations $(p)$ and $(q)$ can be horizontal or vertical, denoted by H and V respectively. Also, the number of frequencies of operation, receiving angles, and incidence angles are F, R, and T respectively.) Within the scope of this chapter, $\sigma_{pq}^{\mathrm{meas}}$ is generated by simulating the profile using the BPT forward solver. Therefore, we choose to refer to $\sigma_{pq}^{\mathrm{meas}}$ as the reference NRCS data, and not the measured NRCS data, for more clarity. In addition, $\sigma_{pq}^{\mathrm{sim}}(\chi(\boldsymbol{r}), \psi_{\mathrm{inc}}^{(m)}, \psi_{\mathrm{scat}}^{(n)}, f_i)$ is the predicted NRCS data corresponding to the predicted dielectric profile $\chi$ at a position vector $\boldsymbol{r}$ under the same measurement configuration. We also note that each of the incident and scattered directions is characterized by two angles: the elevation angle $\theta$, and the azimuth angle $\varphi$. It should also be noted that if the measurement uncertainties at each data point are unknown, (4.1) can be modified as proposed in [104]. However, in this chapter, we assume we do not have access to this prior information. Therefore, the effect of measurement uncertainties will not be considered in the cost function.

At each iteration of the inversion algorithm, the BPT forward solver [94] is used to calculate the predicted NRCS data of a given predicted dielectric profile. Based on the discrepancy between this predicted NRCS data with the reference NRCS data, the differential evolution (DE) algorithm [100] will update the predicted dielectric profile through the minimization of (4.1). This iterative scheme continues until a

convergence is achieved. Herein, the unknown dielectric profile, $\chi(\boldsymbol{r})$, is assumed to be a rough layered medium consisting of a snow pack above sea ice, sandwiched between air and ocean. The inhomogeneities within the layers, such as the presence of brine pockets, are not included in this simplified model. However, the collective effect of these inhomogeneities will be accounted for by assigning an effective complex permittivity to each layer. We also assume that brine pocket is randomly oriented or is of spherical shape, and therefore, each layer has an isotropic complex permittivity. Since our algorithm is capable of modeling the stair-casing within both ice and snow layers, the utilized snow-covered sea ice models can consist of several layers, each of which has a different effective complex permittivity. Finally, to handle the ill-posedness of this problem [105], we have utilized a projection-based regularization scheme [91, 106] that limits the search space for the unknowns to be reconstructed to an appropriate subspace.

## *4.4 Balanced Inversion*

The cost function, presented in (4.1), treats the discrepancy values corresponding to different measurement scenarios equally. (That is, it is an unweighted summation of all discrepancies.) This is not necessarily a proper approach since the inversion algorithm may then favor minimizing certain discrepancy values over the others merely due to their larger magnitudes. If this happens, it is very likely that the inversion algorithm will not be able to utilize all the available information within the measured NRCS data toward dielectric profile reconstruction. As a result, the final solution will not be the most accurate reconstruction that could have been achieved from the given measured data set.

To address this issue, we consider the following cost function that utilizes two sets of

*Tab. 4.1:* Specifications of the snow-covered sea ice numerical model studied in Section 4.5 (Example 1). All length values are in (cm). Here, Half-Space refers to a medium with a boundary at infinity.

| | Snow | Ice | Ocean |
|---|---|---|---|
| Thickness | 4 | 18 | $Half - Space$ |
| Relative Permittivity | $2.50 + \text{j}0.10$ | $3.75 + \text{j}0.40$ | $60.00 + \text{j}60.00$ |
| rms Height ($h$) | 0.14 | 0.20 | 0.30 |
| Correlation Length ($l$) | 1.50 | 1.80 | 2.00 |

weighting factors, $\gamma(f_i)$ and $\kappa_{pq}$,

$$\mathcal{F}(\chi(\boldsymbol{r})) \triangleq \sum_{i=1}^{\text{F}} \gamma(f_i) \sum_{n=1}^{\text{R}} \sum_{m=1}^{\text{T}} \sum_{p=\text{H,V}} \sum_{q=\text{H,V}} \kappa_{pq}(\psi_{\text{inc}}^{(m)}, \psi_{\text{scat}}^{(n)}, f_i) \times \left| \sigma_{pq}^{\text{meas}}(\psi_{\text{inc}}^{(m)}, \psi_{\text{scat}}^{(n)}, f_i) \; - \; \sigma_{pq}^{\text{sim}}(\chi(\boldsymbol{r}), \psi_{\text{inc}}^{(m)}, \psi_{\text{scat}}^{(n)}, f_i) \right|. \tag{4.2}$$

Comparing (4.1) with (4.2), it can be seen that $\gamma(f_i)$ and $\kappa_{pq}$ are set to unity in our original cost function. Before considering $\kappa_{pq}$, let's present the utilized expression for the frequency weighting factors

$$\gamma(f_i) \; \triangleq \left( f_i^2 \sum_{\zeta=1}^{\text{F}} f_\zeta^{-2} \right)^{-1}. \tag{4.3}$$

The above frequency weighting factors have been already successfully used in geophysical inversion [84] in low frequencies; thus, we do not elaborate on the use of these frequency weights in this chapter. We only note that the choice of $\gamma(f_i)$ as presented in (4.3) lies in the idea that the smaller the frequency of operation is, the less nonlinear the associated mathematical problem will be. Therefore, based on (4.3), more weight is assigned to NRCS data of lower frequencies so as to help the inversion algorithm not be trapped in local minima due to the increased nonlinearity in higher frequencies. This frequency weighting can then help the convergence of the inversion algorithm to an appropriate solution.

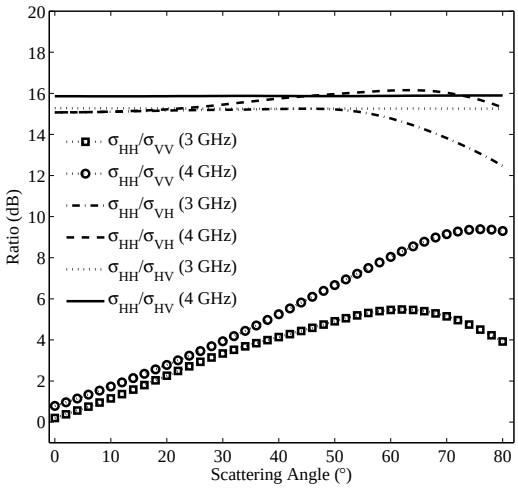


*Fig. 4.1:* NRCS ratios when the profile of Table 4.1 is irradiated from $\psi_{\text{inc}} = (45°, 0°)$ direction, and the emanating scattered data is collected at different scattering angles.

We now consider four different expressions for $\kappa_{pq}$ to be used in (4.2). In the first one, the weights $\kappa_{pq}$ are chosen to be unity. Therefore, in this form, the discrepancy values between all data points at one operational frequency are blindly summed. In the results to be presented, we refer to this cost function as "blind". Before moving on to the next choice of $\kappa_{pq}$, we first note that the NRCS data has different ranges of values for different polarization combinations. This has been illustrated in Figure 4.1 which shows different synthetic polarimetric NRCS ratios for the snow-covered dielectric profile of Table 4.1 for the frequencies of 3 and 4 GHz, when the profile is illuminated from $\psi_{\text{inc}} = (\theta, \varphi) = (45°, 0°)$. From this figure, it can be seen that the scale of NRCS values for various polarizations can be very different. Similar trends were observed from numerous other simulations for bistatic data from simplified snow-covered sea ice profiles, including those described in Section 4.5. It is speculated that this is partly due to the absence of the Brewster angle effect in HH polarization as noted in [107]. Therefore, in the blind cost function, the contribution of the smaller NRCS values may be lost, which indicates that the scattering information within these smaller NRCS values has not been fully utilized in the reconstruction. Thus, based on our numerical experience that shows that $\sigma_{\text{HH}}$ is often the dominant NRCS value in bistatic

measurements from the snow-covered sea ice, we consider the following $\kappa_{pq}$,

$$\kappa_{pq}(\psi_{\text{inc}}^{(m)}, \psi_{\text{scat}}^{(n)}, f_i) \triangleq \frac{\max\{\sigma_{\text{HH}}^{\text{meas}}(\psi_{\text{inc}}^{(m)}, \psi_{\text{scat}}^{(n)}, f_i)\}}{\max\{\sigma_{pq}^{\text{meas}}(\psi_{\text{inc}}^{(m)}, \psi_{\text{scat}}^{(n)}, f_i)\}}, \tag{4.4}$$

which presents a constant weight for each polarization combination, thus, resulting in four different $\kappa_{pq}$ values in total. In fact, the use of these four $\kappa_{pq}$ values in (4.2) classifies all the data points into four clusters, each of which corresponds to a specific polarization combination, and then attempts to equalize these four clusters of data points. In our results, we refer to this cost function as "constant". On the other hand, as opposed to equalizing these four clusters, we can normalize the discrepancy value corresponding to each data point individually by using the following $\kappa_{pq}$,

$$\kappa_{pq}(\psi_{\text{inc}}^{(m)}, \psi_{\text{scat}}^{(n)}, f_i) \triangleq \frac{1}{\sigma_{pq}^{\text{meas}}(\psi_{\text{inc}}^{(m)}, \psi_{\text{scat}}^{(n)}, f_i)}, \tag{4.5}$$

which will then result in the so-called "normalized" cost function.

The development of the last $\kappa_{pq}$, to be described below, is inspired by the observation that the receiving angles that are closer to the specular scattered angles often exhibit higher sensitivities with respect to the parameters to be reconstructed [108]. Based on this, we speculate that these receiving sites might provide more "informative" scattering data, and might then deserve to receive higher weights during the optimization. The expression for $\kappa_{pq}$ that implements this idea is given as

$$\kappa_{pq}(\psi_{\text{inc}}^{(m)}, \psi_{\text{scat}}^{(n)}, f_i) \triangleq \frac{\sigma_{\text{HH}}^{\text{meas}}(\psi_{\text{inc}}^{(m)}, \psi_{\text{scat}}^{(n)}, f_i)}{\sigma_{pq}^{\text{meas}}(\psi_{\text{inc}}^{(m)}, \psi_{\text{scat}}^{(n)}, f_i)}. \tag{4.6}$$

To understand the effect of these weights, note that the denominator of (4.6) when multiplied by the discrepancy in (4.2) will result in the normalized cost function. However, the numerator of (4.6) will emphasize the information measured at the specular angles as the $\sigma_{\text{HH}}$ value at these angles has often larger values. The use of these weights

in conjunction with (4.2) will then be referred to as the "balanced" cost function.

## *4.5 Synthetic Data Reconstruction Results*

To compare the effectiveness of the four cost functions presented in the above section with respect to the achievable reconstruction accuracy, numerous inversion scenarios were studied. Generally, all the cases investigated followed the same trend and therefore, only three scenarios are presented here. As the first example, let's consider the snow-covered sea ice profile of Table 4.1. This profile is irradiated from $\psi_{\text{inc}} = (45^\circ, 0^\circ)$ direction, and the polarimetric NRCS is synthetically created at 8 different directions having $\theta$ from 30° to 65° with the step of 5° and a fixed $\varphi = 10^\circ$ at 11 equispaced frequencies starting with 3 GHz, and ending at 4 GHz. In this example, the inversion algorithm retrieves 12 unknowns (namely, the roughness parameters of root mean square (rms) height, $h$, and correlation length, $l$, for the snow-ice and ice-ocean interfaces, height of snow and ice and finally, real and imaginary parts of the effective complex permittivity of snow and ice). Four different inversions, each of which utilizes one of the four cost functions described in the previous section, are applied to this synthetic bistatic NRCS data set. The error in the reconstruction of the twelve unknowns for each of these four cost functions is depicted in Figure 4.2. The profiles to be reconstructed in Figure 4.2(a) and (b) are presented in Table 4.1 and 4.2, respectively. A four percent noise is also added to the input data used to reconstruct the profile of Table 4.2(b) to further assess the algorithm's reconstruction ability in the presence of noise. Also, in part (b), as opposed to part (a), the roughness parameters are given to the inversion algorithm as prior information to keep the number of unknowns the same as part (a). In this figure, the lower the plot value, the lower the retrieval error, thus, the more accurate the reconstruction. This error is calculated based on the absolute value of the difference between the final predicted value and the true value, divided by the true value (*i.e.*, the relative error). We also note that the differential evolution

*Tab. 4.2:* Specifications of the snow-covered sea ice numerical model studied in Section 4.5 (Example 2). All length values are in (cm). Here, Half-Space refers to a medium with a boundary at infinity.

| | Snow | Ice Layer I | Ice Layer II | Ice Layer III | Ocean |
|---|---|---|---|---|---|
| Thickness | 2 | 2 | 5 | 2 | $Half - Space$ |
| Relative Permittivity | $2.10 + \text{j}0.20$ | $4.00 + \text{j}0.40$ | $3.60 + \text{j}0.15$ | $3.80 + \text{j}0.30$ | $60.00 + \text{j}60.00$ |
| rms Height ($h$) | 0.15 | 0.10 | 0.01 | 0.01 | 0.15 |
| Correlation Length ($l$) | 1.50 | 1.00 | 0.50 | 0.50 | 1.50 |

algorithm incorporates a partly-random step in each element's evolution [100] so as to be able to investigate the search space of each unknown parameter thoroughly for the universal minimum of the cost function after all iterations. Therefore, for every separate complete run of the DE algorithm, the final reconstructed profile might vary very slightly. To compensate for this effect and report a general trend, each of the four inversion algorithms is run a few times with the same input NRCS data for the same profile. Five runs is found sufficient since averaging beyond that did not change the reconstruction accuracy results considerably. (These average reconstructed values are the ones reported in this section.) As can be seen from both plots in Figure 4.2, the retrieval error associated with the balanced cost function is almost constantly bellow all others; therefore, the balanced inversion outperforms the others with respect to the achievable reconstruction accuracy. It should also be noted that the addition of noise to the input data has degraded the reconstruction accuracy and yet the balanced form has kept its advantage over other three cost functions.

To consider more practical scenarios, we next study the reconstruction of two more elaborate numerical models. These two models are a snow-covered thin New Ice (NI) model as specified in Table 4.2, and a thicker NI model as presented in Table 4.3. In these two numerical models, we consider three inner layers within the ice layer. This is done to represent the varying permittivity within the ice layer. As noted in [109], the plot of permittivity versus sea ice depth can have a C-shaped curve, with higher permittivity values for top and bottom layers, and lower permittivity value for the

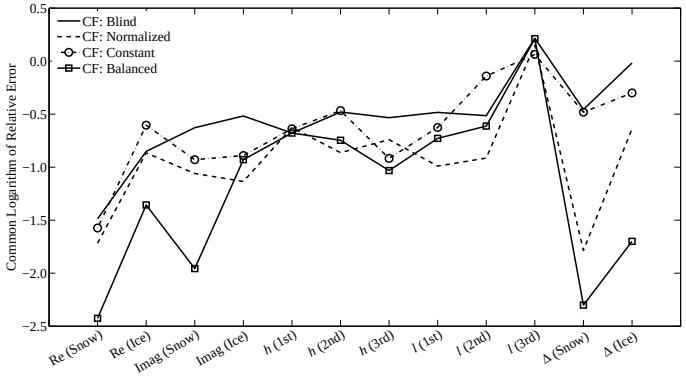


(a)

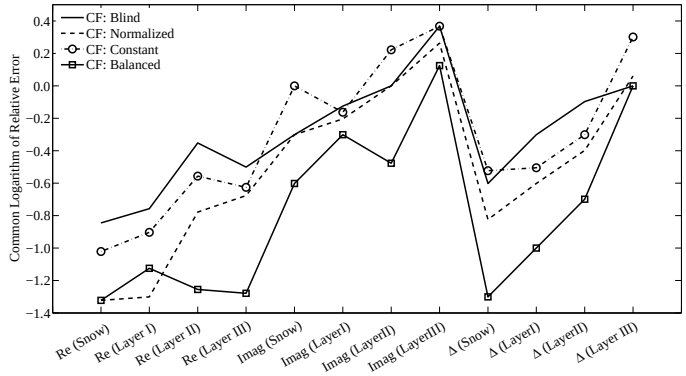


(b)

*Fig. 4.2:* The common logarithm ($\log_{10}$) of relative error in the reconstruction of the 12 unknowns using four different cost functions (CF) of the profiles of (a) Table 4.1, and (b) Table 4.2. The horizontal axis shows the parameter of interest, and the vertical axis is its corresponding error. Re and Imag denote the real-part and imaginary-part of the permittivity for the corresponding layer. $\Delta$ denotes the thickness parameter. In (a), 1st, 2nd, 3rd refer to as air-snow, snow-ice and ice-ocean interfaces. In (b), Layer I, Layer II, and Layer III refer to the layers within the ice as in Table 4.2.

middle layer. As can be seen in Tables 4.2 and 4.3, the interfaces for these inner layers within NI are almost flat. These very small roughness parameters associated with the inner NI layers are taken as known roughness parameters for the inversion algorithm. Therefore, each of these two numerical models has a total of 16 unknown parameters (namely, the roughness parameters of rms height, $h$, and correlation length, $l$, for the air-snow, snow-ice top layer and ice bottom layer-ocean interfaces, height of snow and ice and finally, real and imaginary parts of the permittivity for snow and three ice layers). It should also be noted that although the total thickness of the NI

*Tab. 4.3:* Specifications of the snow-covered sea ice numerical model studied in Section 4.5 (Example 3). All length values are in (cm). Here, Half-Space refers to a medium with a boundary at infinity.

| | Snow | Ice Layer I | Ice Layer II | Ice Layer III | Ocean |
|---|---|---|---|---|---|
| Thickness | 4 | 3 | 8 | 4 | $Half - Space$ |
| Relative Permittivity | $2.20 + \text{j}0.10$ | $4.20 + \text{j}0.60$ | $3.60 + \text{j}0.40$ | $3.90 + \text{j}0.50$ | $60.00 + \text{j}60.00$ |
| rms Height ($h$) | 0.16 | 0.04 | 0.01 | 0.01 | 0.16 |
| Correlation Length ($l$) | 1.60 | 0.40 | 0.50 | 0.50 | 1.60 |

layer is an unknown to the inversion algorithm, the relative thickness of each inner NI layer with respect to the total thickness of the NI layer is taken to be known, thus, serving as prior information to the inversion algorithm.

Before presenting the inversion results of these two profiles, let's note that the reference NRCS data to the inversion algorithm in these two examples are synthetically created using the same setup as used in the first example. For each profile, the unknown parameters are retrieved first through the inversion of the blind cost function and next by the inversion of the proposed balanced cost function. The inversion results for these two examples using both noiseless and noisy NRCS data are depicted in Figure 4.3. (To create the noisy data sets, 4% noise has been added to the noiseless data sets.) The closer the plotted reconstructed lines are to the true profile, the more accurate the reconstruction is. It is evident that the proposed balanced inversion outperforms the blind inversion in achieving enhanced reconstruction accuracy for both noiseless and noisy data sets. Therefore, as can be seen in Figure 4.3, the balanced inversion is still important when the noise is present in the NRCS data. For example, the achievable accuracy of the reconstructed real-part of the permittivity for the profile of Table 4.2 when using balanced inversion of noisy data, see Figure 4.3(f), is higher than that when using blind inversion of the same noisy data, see Figure 4.3(e). Note that as the noise in the NRCS data increases, the reconstruction accuracy decreases. However, the balanced inversion still manages to outperform the blind inversion, indicating its appropriate use of the information contents available in the NRCS data.

It should also be noted that the balanced inversion results for the last two examples (Tables 4.2 and 4.3) are not as good as the balanced inversion result for the first example (Table 4.1). This could be attributed to the increase of the number of unknown parameters in the last two examples as compared to the first example while having the same number of reference NRCS data points as compared to the first example. Also, the limitation on the penetration depth of irradiating electromagnetic waves degrades the inversion accuracy for lower profile depth. The effect of attenuation is even worse if the top layer is wet or brine-wetted [110].

Finally, we note that the reconstruction accuracy of the roughness parameters for the profile of Table 4.1, denoted by $h$ and $l$ in Figure 4.2(a), are generally better when the balanced cost function has been used. When the profile to be reconstructed becomes more complex, assuming all the parameters to be unknown will result in poor performance of the inversion algorithm due to the large imbalance between the number of unknowns and the number of known NRCS data points. Therefore, for the examples considered in Figures 4.2(b) and 4.3, we decided to give the roughness parameters as prior information to the inversion algorithm. (Otherwise, we have to increase the number of data points; *e.g.*, by adding more frequencies or incidence/scattered angles.) It would be instructive to investigate the performance of the inversion algorithm when provided by wrong prior information; *e.g.*, assuming that the inner interfaces are flat for the profile of Table 4.2. (For the top interface, we still consider a known rough interface, and use this as prior information since this roughness can be obtained by the use of lidar in practice.) Based on this wrong surface flatness assumption, the inversion algorithm was run for each cost function. The balanced cost function resulted in 78% error; however, the error of the three other cost functions exceeded 100%. Therefore, as can be seen, the balanced approach still outperforms; however, due to the use of wrong prior information (significant modelling error), the error level is high. Of course, as opposed to the profile of Table 4.2, if we consider a profile whose inner roughness

parameters are sufficiently smooth, the assumption of flat interfaces will be acceptable, thus, resulting in satisfactory reconstruction accuracy.

## *4.6 Conclusion*

We have investigated the formulation of an appropriate cost function, which we refer to as the balanced cost function, for dielectric reconstruction of simplified snow-covered sea ice profiles from simulated bistatic NRCS data sets. This balanced cost function is a weighted discrepancy between the reference NRCS data and the NRCS data of a given predicted dielectric profile. The minimization of this cost function over the dielectric profile will result in the final reconstructed dielectric profile. This balanced cost function was compared with three other cost functions. The inversion of the proposed balanced cost function achieved the best retrieval accuracy as compared to the reconstruction accuracy obtained by inverting the other three cost functions. The weighting scheme utilized in the balanced cost function normalizes the discrepancy and also emphasizes the data points in the vicinity of the bistatic specular angle. The latter is achieved through a multiplication with the HH polarized NRCS data. We speculate that the NRCS data of these data points are more sensitive to the profile unknowns, thus, being more informative to the inversion algorithm [108]. Numerous simulated scenarios have been studied, three of which have been presented in this chapter. The trend in all these scenarios were similar, supporting our claim on the advantage of the balanced inversion algorithm. As a further step in this research, the synthetically created bistatic NRCS data sets used in this chapter should be replaced by the measured bistatic NRCS data to further assess the reconstruction accuracy achievable from the proposed balanced inversion algorithm against experimental data.

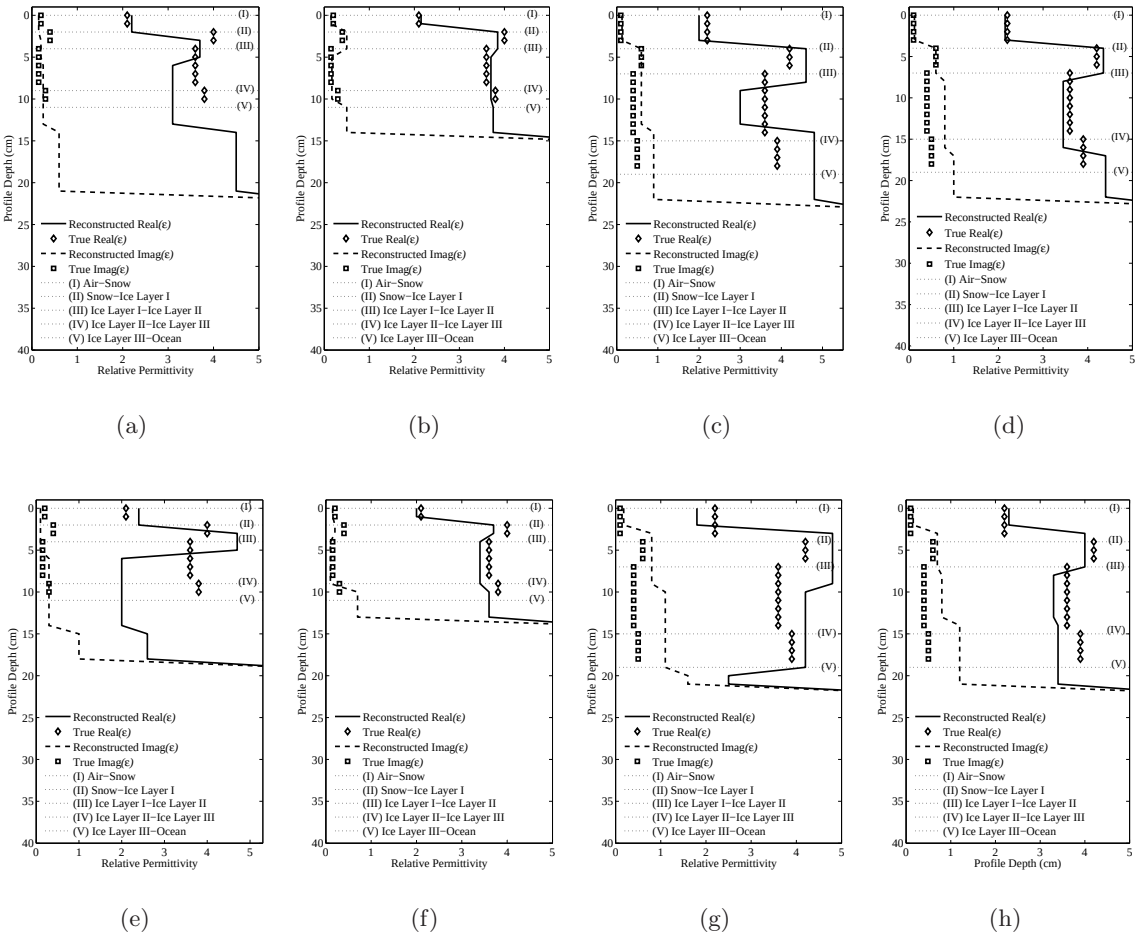


*Fig. 4.3:* Reconstructed permittivity and thickness values using (a) blind inversion of noiseless NRCS data for the profile shown in Table 4.2, (b) balanced inversion of noiseless NRCS data for the profile shown in Table 4.2, (c) blind inversion of noiseless NRCS data for the profile shown in Table 4.3, (d) balanced inversion of noiseless data for the profile shown in Table 4.3, (e) blind inversion of noisy NRCS data for the profile shown in Table 4.2, (f) balanced inversion of noisy NRCS data for the profile shown in Table 4.2, (g) blind inversion of noisy NRCS data for the profile shown in Table 4.3, and (h) balanced inversion of noisy data for the profile shown in Table 4.3. The horizontal lines in each figure represent the named interfaces (numbered from top to bottom). Real and Imag indicate the real and imaginary parts of the reconstructed relative permittivity (denoted by $\epsilon$).

# 5

# SERF Experiment I: Inversion and Sensitivity Analysis

## *5.1 Overview*

In Chapters 3, an electromagnetic inverse scattering algorithm was developed, and its reconstruction accuracy for the snow-covered sea ice profile was assessed utilizing synthetic data for various scenarios. Also in Chapter 4, it was shown that emphasizing the role of the NRCS data collected in the vicinity of the specular angle in a bistatic configuration results in higher reconstruction accuracy. Utilizing the same inversion algorithm in this chapter, our objectives are to (*i*) find the NRCS data which are more sensitive to the profile's parameters of interest and assess their role in inversion, (*ii*) employ the experimental NRCS data instead of synthetic NRCS data, and (*iii*) introduce a further profile parametrization scheme based on prior information. In particular, the use of this prior results in enhanced reconstruction. As will be described in this chapter, the experimental data have been collected in the SERF during Winter

2014.

This chapter is structured as follows. After an introduction, the problem statement is outlined in Section 5.3. Next, a preview of the BPT solver is brought in Section 5.4. Subsequently, the NRCS sensitivity analysis from a forward scattering perspective is presented in Section 5.5. To calculate these sensitivity values, the derivatives of the NRCS data with respect to the profile parameters are calculated utilizing the finite difference formulation. From the sensitivity analysis results, it is concluded that the NRCS data collected at incidence angles in the vicinity of $(i)$ nadir for the monostatic configuration, and $(ii)$ specular reflection for the bistatic configuration, are more sensitive compared to the NRCS data collected at other incidence angles.

In Section 5.6, the reconstructed profiles are presented when synthetic NRCS data are inverted. Based on the reconstruction results, it is concluded that the inclusion of more sensitive NRCS data results in higher retrieval accuracy. Subsequently, the speculation on the role of more sensitive NRCS data is investigated in Section 5.8, utilizing the experimental data. To this end, the data are divided into two cases, one with the NRCS data collected close to the nadir, and the other case with the NRCS data set excluding the latter.

In addition, a C-shaped curve is fitted to the complex permittivity model of the profile to reduce the number of problem unknowns. This will take advantage of prior information regarding the complex permittivity distribution of the profile, thus, reducing the number of unknowns, and guiding the inversion algorithm toward the true solution. The inversion results using this prior information are then presented. These results further confirm the speculation that utilizing more sensitive data achieves better reconstruction results for the monostatic case. Finally, a conclusion ends this chapter in Section 5.9.

At the end, it should be noted that the monostatic NRCS data were collected at the

Sea-ice Environmental Research Facility (SERF), located at University of Manitoba, Winnipeg, Canada, during Winter 2014. During one phase of this experiment, the polarimetric NRCS data were collected at frequencies ranging from 5.3 GHz to 5.7 GHz through a C-band scatterometer. The air-snow interface was also scanned through a lidar to calculate the roughness parameters. Moreover, physical samplings of snow and sea ice (*i.e.*, temperature, salinity, and density measurements) were carried out to determine the true permittivity of the profile.

The materials of this chapter are based on the paper published in the IEEE Journal of Selected Topics in Applied Earth Observations and Remote Sensing in 2015 [90][(1)].

## *5.2 Introduction*

Two general challenges in solving any electromagnetic inverse scattering problem are how to deal with the nonlinearity and ill-posedness of the associated mathematical problem. Herein, the nonlinearity of the problem is treated by the use of an iterative inversion algorithm, and the ill-posedness of the problem is handled by the use of a projection-based regularization technique. Also, in the case of snow-covered sea ice microwave remote sensing, which is the focus of this chapter, at least two other challenges exist. First, there exist vertical heterogeneous characteristics in the ice-snow profile as well as possible horizontal inhomogeneities within the imaging domain. Second, the inversion algorithm often have access to only limited measured data points [111]. To address the first issue, full-wave forward solvers are available which consider both volume and surface scattering mechanisms. Such solvers can also take into account different inclusion shapes within a rough-layered medium [72]. Unfortunately, the profile's large electrical size and the complexity of such models make it difficult to use

[(1)] © [2015] IEEE. Reprinted, with permission, from N. Firoozy, A. Komarov, J. Landy, D. Barber, P. Mojabi, and R. Scharien, "Inversion-based sensitivity analysis of snow-covered sea ice electromagnetic profiles," *Selected Topics in Applied Earth Observations and Remote Sensing, IEEE Journal of*, vol. 8, no. 7, pp. 3643-3655, July 2015.

these full-wave forward solvers in conjunction with inversion algorithms due to their high computational complexities. (This can be better understood by noting that a forward solver will be called several times in an iterative inversion algorithm.) One way to handle this challenge, which will be used throughout this chapter, is to simplify and parametrize the structure of the domain under study, and then use non full-wave forward solvers [112, 113]. To tackle the lack of access to sufficient measured data points, appropriate data collection schemes need to be utilized so as to collect more informative data points to help the inversion algorithm converge to more accurate reconstruction. Also, the development of efficient inverse scattering algorithms which can fully utilize the information within the measured data points should also be considered.

This chapter addresses the issue of having access to only limited data points by investigating which data points can possibly present the most useful information for the reconstruction of the dielectric profile of the domain of interest. In fact, this chapter attempts to set some guidelines for an appropriate data collection configuration for the purpose of optimal dielectric profile reconstruction of snow-covered sea ice profiles. These guidelines are derived based on the sensitivity analysis of the scattering data with respect to the unknowns which are to be reconstructed. To derive these sensitivity values, we utilize the recently-developed boundary perturbation theory (BPT) as our forward scattering solver [94] in conjunction with a finite difference derivative formulation. The effectiveness of these guidelines will be first investigated by the inversion of synthetically collected data, and then through the inversion of the experimental data collected in the Sea-ice Environmental Research Facility (SERF) at the University of Manitoba, Winnipeg, MB, Canada [114].

This chapter is a contribution to the J-STARS Special Issue that builds on our conference paper at IGARSS 2014 [108] by presenting our experimental data collection procedure and the experimental data inversion. Throughout this chapter, the term "snow" is used in its general form which is taken to include all states of dry, wet,

brine-wetted and slush [115]. Also, a time-dependency of $\exp(-j\omega t)$ has been implicitly assumed in this chapter.

## *5.3 Problem Statement*

Our goal is to investigate the sensitivity of different measured data points with respect to the unknowns to be reconstructed. We then study the role of these sensitivity values in the achievable reconstruction accuracy. Our speculation is that the inversion of data points of higher sensitivity values results in more precise reconstruction results as compared to the reconstruction results obtained by inverting the same number of data points that correspond to smaller sensitivity values. We will then attempt to support this speculation by inverting synthetically and experimentally collected data sets having different sensitivity values. This study is important as it provides insight on how to perform data collection in a practical measurement system so as to achieve enhanced reconstruction accuracy.

In this chapter, the measured quantity is the normalized radar cross section (NRCS) data, denoted by $\sigma_{pq}$. The NRCS data can be collected from different incidence and scattered angles. Herein, we are interested in studying the sensitivity of the NRCS data collected from different angles with respect to the layers' complex permittivities and their thickness values. To this end, we utilize an electromagnetic forward solver in conjunction with a finite difference formulation to calculate these sensitivities. We finally consider inverting different synthetic and experimental data sets, having the same number of data points but different sensitivity values to assess our speculation on the role of more sensitive NRCS data in inversion.

## *5.4 Forward Scattering Solver*

To calculate the sensitivities, we first need to be able to calculate the NRCS value for given incidence and scattered angles from a given snow-covered sea ice profile. Herein, the boundary perturbation theory (BPT) is utilized as our forward solver to calculate the NRCS values. (This forward solver will also be utilized in our inversion algorithm to evaluate how close the calculated NRCS due to a predicted profile is with respect to the measured NRCS data.) In this section, we first briefly explain the structure of snow-covered sea ice profile and its evolution, and then briefly describe the simplified electromagnetic models that will be used in this chapter. The description of the BPT forward solver then follows.

### *5.4.1 Snow-covered sea ice evolution and electromagnetic model*

Herein, we study the snow-covered new ice (NI) developed in a calm condition. Therefore, it is only slightly rough and the brine pockets are either randomly positioned or spherical.Therefore the layer posses an isotropic complex permittivity [116]. A simplified profile under a monostatic measurement configuration is depicted in Figure 5.1. Note that this chapter assumes almost flat interfaces for layers within the ice layer. However, other interfaces, particularly the air-snow one, are generally rough. As will be seen later, for all synthetic data sets, we assume that we have rough layers of snow and ice sandwiched between air and ocean half spaces. We then assume homogeneous complex permittivity and thickness values for these layers. The assumption of having a homogeneous complex permittivity value for a given layer can be justified by assuming an effective complex permittivity value for that layer. This effective complex permittivity will also serve the purpose of reducing the number of unknowns associated with an inhomogeneous complex permittivity distribution. Another type of model simplification is presented in the experimental data section of this chapter in which

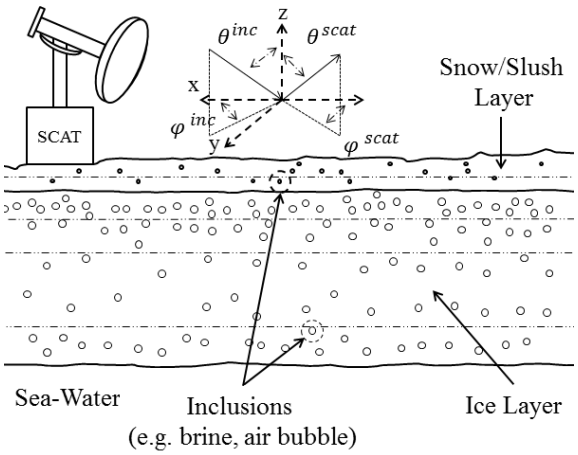


*Fig. 5.1:* Schematic of radar cross section measurements of a simplified snow-covered sea ice profile with rough interfaces through a scatterometer. As can be seen the incident direction $\Psi^{\text{inc}}$ is characterized by two angles; i.e., $\Psi^{\text{inc}} = (\theta^{\text{inc}}, \varphi^{\text{inc}})$. Also, the scattered direction $\Psi^{\text{scat}}$ is characterized by two angles; i.e., $\Psi^{\text{scat}} = (\theta^{\text{scat}}, \varphi^{\text{scat}})$. In the case of a monostatic setup, $\theta^{\text{scat}} = \theta^{\text{inc}}$, and $\varphi^{\text{scat}} = 180^{\circ} - \varphi^{\text{inc}}$.

the inhomogeneous complex permittivity distribution is modeled by the superposition of two exponential functions. This will be based on using prior information about the inhomogeneous complex permittivity distribution of the actual profile.

### *5.4.2 NRCS calculation using the BPT forward solver*

The BPT forward solver [94] is utilized to calculate the NRCS values, $\sigma_{pp}$. Also based on our experience and lidar measurements [97], the exponential distribution for the spatial power density best fits the common new ice type. We also note that due to BPT closed-form formulation, this forward model is computationally efficient. This makes it suitable to be used in global optimization inversion algorithm (as used in our earlier work [91]), and also to be called repetitively to perform sensitivity analysis using a finite-difference differentiation scheme (as will be shown in Section 5.5).

In what follows, we consider a numerical example, in which we calculate the NRCS of a snow-covered sea ice profile described in Table 5.1 with the orientation notation

*Tab. 5.1:* Dielectric profile specifications of the snow-covered ice profile considered in Section 5.4.2. $h$ and $l$ are the surface roughness parameters of rms height and correlation length, respectively.

| Snow (wet) | Ice Layer I | Ice Layer II | Ice Layer III | Ocean |
|---|---|---|---|---|
| THICKNESS (cm) | | | | |
| 3 | 5 | 8 | 5 | $Half - Space$ |
| PERMITTIVITY | | | | |
| $2.0 + 0.3j$ | $4.5 + 0.4j$ | $3.7 + 0.2j$ | $4.0 + 0.3j$ | $58.0 + 41.0j$ |
| ROUGHNESS PARAMETERS (cm) | | | | |
| $h = 0.15$ | $h = 0.05$ | $h = 0.01$ | $h = 0.01$ | $h = 0.05$ |
| $l = 1.50$ | $l = 0.50$ | $l = 0.50$ | $l = 0.50$ | $l = 0.50$ |

used in Figure 5.1 at the frequencies of 5 GHz and 6 GHz with the Horizontal-sent Horizontal-receive (HH) polarization. As can be seen, this snow-covered sea ice profile has been parametrized as a rough-surface multi-layered medium in which each layer has a homogeneous complex permittivity value. For the monostatic configuration, with $\Psi^{\text{inc}} = (\theta^{\text{inc}}, \phi^{\text{inc}}) = (15°{:}75°, 0°)$ and $\Psi^{\text{scat}} = (\theta^{\text{scat}}, \phi^{\text{scat}}) = (\theta^{\text{inc}}, 180°)$, and the bistatic configuration, with $\Psi^{\text{inc}} = (\theta^{\text{inc}}, \phi^{\text{inc}}) = (45°, 0°)$ and $\Psi^{\text{scat}} = (\theta^{\text{scat}}, \phi^{\text{scat}}) = (15°{:}75°, 0°)$, the BPT forward solver returns the NRCS results shown in Figure 5.2. (These two frequencies of operation are chosen as the lower and upper frequencies of the C-band spectrum commonly used in space-borne SARs such as radarsat.) From many NRCS simulations of different ice types for the purpose of inversion, we recommend that measurements in high incidence angles (*i.e.*, usually above 60°) should be generally avoided as they might return too small NRCS values which could be lost in the noise floor of the system or environmental interferences. Also, we can induce that in bistatic configuration, unlike the monostatic, NRCS values for $HH$ is higher than $VV$. Moreover, although in the case of Figure 5.2, the increase of frequency leads to higher values for NRCS (due to more comparable size of wavelength to surface roughness), a more complex medium might not follow this trend due to multiple scattering events between its various layers.

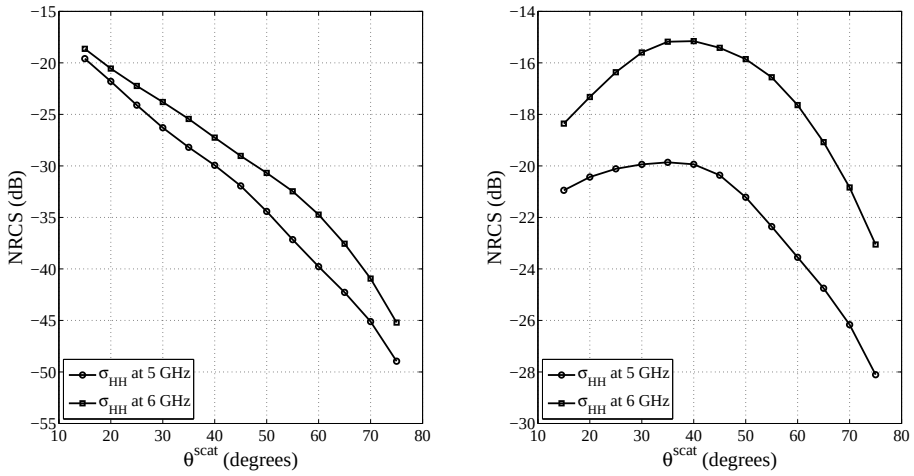


(a) Monostatic (b) Bistatic

*Fig. 5.2:* NRCS (denoted by $\sigma$) for HH polarizations at 5 and 6 GHz for values of Table I in (a) Monostatic, and (b) Bistatic configurations.

## *5.5 Sensitivity Analysis*

Sensitivity analysis for remote sensing applications can be performed from different viewpoints. For example, it can be carried out to investigate the ability of the inverse solver to accurately differentiate between two similar profiles. For sea ice applications, this has been previously investigated to evaluate the reconstruction abilities of various inversion algorithms; *e.g.*, see [117, 118]. Herein, we look at the sensitivity analysis from a forward scattering viewpoint. That is, we utilize a forward scattering solver (*i.e.*, the BPT) to calculate the change in the NRCS value due to a small change of one of the profile parameters.

The sensitivity of the NRCS data with respect to the model parameters of each layer's permittivity and thickness can then be calculated through the following fourth-order finite-difference derivative formulation as

$$\frac{\partial \sigma_{pq}}{\partial \chi_i} \approx \frac{-\sigma_{pq}|_{\chi_i+2\Delta\chi_i} + 8\sigma_{pq}|_{\chi_i+\Delta\chi_i} - 8\sigma_{pq}|_{\chi_i-\Delta\chi_i} + \sigma_{pq}|_{\chi_i-2\Delta\chi_i}}{12\Delta\chi_i} \tag{5.1}$$

In (5.1), $\chi_i$ is the unknown parameter (e.g., the real part of the snow complex permittivity) with respect to which the sensitivity is being calculated. Also, $\Delta\chi_i$ is the perturbation of the model parameter $\chi_i$ used to calculate the sensitivity. To find an appropriate value for the perturbation of each of the profile's parameters, we iteratively reduce the magnitude of $\Delta\chi_i$ and calculate the corresponding sensitivity until it converges to a stable value.

Figures 5.3 and 5.4 depict the sensitivity values of the NRCS data with $HH$ polarization for the profile of Table 5.1. The monostatic configuration has a look angle of $\Psi^{\text{inc}} = (\theta^{\text{inc}}, \phi^{\text{inc}}) = (15°{:}70°, 0°)$ and $\Psi^{\text{scat}} = (\theta^{\text{scat}}, \phi^{\text{scat}}) = (\theta^{\text{inc}}, 180°)$ and the bistatic configuration has a look angle of $\Psi^{\text{inc}} = (\theta^{\text{inc}}, \phi^{\text{inc}}) = (45°, 0°)$ and $\Psi^{\text{scat}} = (\theta^{\text{scat}}, \phi^{\text{scat}}) = (15°{:}70°, 0°)$. The sensitivities are calculated with respect to each layer's permittivity and thickness values at 5.5 GHz, at different angles for both monostatic and bistatic setups. Since, for this case, the sensitivity trend for $HH$ and $VV$ polarizations proved to be the same, only the sensitivity for $HH$ polarization is shown here. Also, since the sensitivity with respect to real and imaginary parts of the complex permittivity proved to have the same pattern for this case, only the sensitivity with respect to the real part of the complex permittivity is shown here. For the monostatic configuration, it is obvious that the closer the observation angle is to the nadir, the higher the sensitivity is. In the case of the bistatic configuration, the sensitivity is generally highest within the vicinity of the specular angle, though not necessarily exactly at that angle. The reason for this shift is linked to the multiple scattering events between the layers. Finally, for both the monostatic and bistatic configurations, the magnitude of the sensitivity decreases as the depth increases, since only a smaller portion of the illuminating wave can penetrate to deeper locations within the profile and also make it back to the observation point. We also note that herein we do not investigate the sensitivities with respect to the roughness parameters ($h$ and $l$) since these roughness parameters are taken as prior information in the utilized inversion

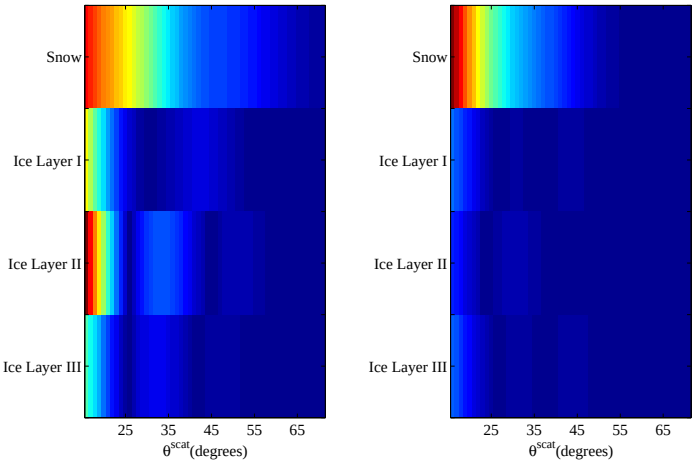


(a) $\frac{\partial \sigma_{\mathrm{HH}}}{\partial \epsilon}$ (b) $\frac{\partial \sigma_{\mathrm{HH}}}{\partial \Delta}$

*Fig. 5.3:* Monostatic sensitivity analysis for the HH polarizations at 5.5 GHz for the profile of Table 5.1 (a) NRCS sensitivity with respect to permittivity, (b) NRCS sensitivity with respect to thickness. Here, $\Delta$ denotes the thickness values.

algorithm. It should also be noted that when we calculate the sensitivity values, *e.g.*, with respect to the real part of the snow complex permittivity, we keep the rest of the parameters constant. (These constant values are chosen to be close to the typical values.) Therefore, we do not claim that the sensitivity results presented here are true for all rough multi-layer profiles. However, we tried different rough snow-covered sea ice profiles, and similar results were obtained for them.

We speculate that higher sensitivity values with respect to a parameter translates into more accurate reconstruction accuracy with respect to that parameter. If this speculation is correct, the data collection setup should attempt to collect data points having higher sensitivity values for the inversion algorithm to provide enhanced reconstruction accuracy. Therefore, for the bistatic configuration, an appropriate margin of measurements around the specular angle should be provided. Also, for the monostatic configuration, an appropriate margin around the nadir should be utilized. In what follows, we attempt to support this speculation by applying our inversion algorithm to synthetic and experimental data sets.

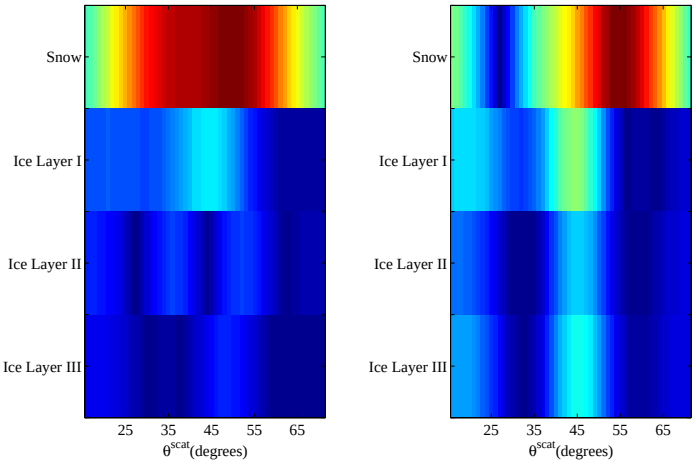


(a) $\frac{\partial \sigma_{\mathrm{HH}}}{\partial \epsilon}$ (b) $\frac{\partial \sigma_{\mathrm{HH}}}{\partial \Delta}$

*Fig. 5.4:* Bistatic sensitivity analysis for the HH polarizations at 5.5 GHz for the profile of Table 5.1 at 45° incidence angle (a) NRCS sensitivity with respect to permittivity, (b) NRCS sensitivity with respect to thickness. Here, $\Delta$ denotes the thickness values.

## *5.6 Inversion Algorithm*

The inversion algorithm utilized in this chapter has been presented in [91]. The differential evolution (DE) algorithm [99] in conjunction with the BPT forward solver constitute the two main components of this inversion algorithm. Using an iterative scheme between these two components, this inversion algorithm reconstructs the unknown parameters of snow-covered sea ice from the NRCS data by minimizing a data misfit cost functional. Moreover, a projection-based regularization algorithm handles the ill-posedness of the mathematical problem by limiting the search space of the unknown parameters. Finally, a band of 0 to 2 for the imaginary part of the complex permittivity and 2 to 8 for the real part of the complex permittivity is considered. For the synthetic data inversion, layer thickness is also set between 0 to 30 cm. The roughness parameters are provided to the algorithm to reduce the number of unknowns in both synthetic and experimental data inversion.

## *5.7 Synthetic Results*

In this section, we will present the snow-covered sea ice profile reconstruction results considering the data sensitivity discussed previously.

### *5.7.1 Synthetic data sets*

To investigate the importance of using data points having high sensitivity values in the inversion algorithm, we consider two synthetic data sets, referred to as Case I and Case II, per monostatic and bistatic configurations for the profile of Table 5.1. The scattering data sets for both cases are collected at 10 equispaced frequencies between 5 and 6 GHz and an incidence angle illuminating the profile at $(\theta^{\text{inc}}, \varphi^{\text{inc}}) = (\theta^{\text{scat}}, 0^\circ)$ for the monostatic and $(\theta^{\text{inc}}, \varphi^{\text{inc}}) = (45^\circ, 0^\circ)$ for the bistatic configuration. The scattered data is measured at the azimuth angle of $\varphi^{\text{scat}} = 180^\circ$ for the monostatic case and $\varphi^{\text{scat}} = 5^\circ$ for the bistatic case. In both configurations, the elevation measurement (scattered) angles are $(i)$ $15^\circ$ to $35^\circ$ with $5^\circ$ steps for Case I data set, and $(ii)$ $40^\circ$ to $60^\circ$ with $5^\circ$ steps for Case II.

### *5.7.2 Inversion results*

The inversion of these synthetic data sets are shown in Figure 5.5. As it is evident from the reconstruction results, the inversion of Case I returns more accurate reconstruction results for the monostatic configuration and the inversion of Case II returns more accurate reconstruction results for the bistatic one (with mean-square-root of relative error of 0.9448, 1.0674, 1.4164 and 0.5266 for part (a) to (d), respectively). This confirms the speculations of Section 5.5 as Case I data set is within the region of high sensitivity for the monostatic case and Case II data set is within the region of high

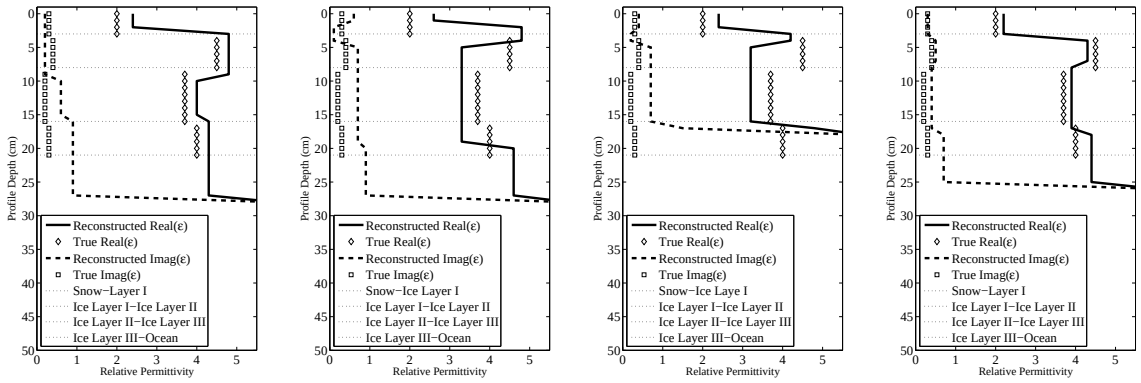


*Fig. 5.5:* Reconstruction of the snow-covered sea ice dielectric profile of interest using two different synthetic data sets, Case I and Case II. The $y = 0$ line indicates the air-snow interface, (a) monostatic configuration, Case I, (b) monostatic configuration, Case II, (c) bistatic configuration, Case I, and (d) bistatic configuration, Case II

sensitivity for the bistatic case. It should be noted that various other profiles of snow-covered new ice were investigated under the same scheme and they all follow the same trend in inversion accuracy as the case studied above.

## *5.8 Experimental Results*

In this section, we present our measurement setup that has been used to collect experimental NRCS data. It should be noted that our equipment is only capable of measuring monostatic NRCS data. Therefore, this section is entirely focused on the monostatic experimental data measurements and inversion.

### *5.8.1 Measurement Setup and Equipment*

The measurements were performed at the Sea-ice Environmental Research Facility (SERF) located at the University of Manitoba, Winnipeg, MB, Canada. The SERF

was constructed in 2011 as the first experimental sea-ice facility in Canada. In this facility, the sea ice is developed within a pool 18.3 meters long, 9.1 meters wide, and 2.4 meters deep. The pool is equipped with in-situ sensors, *e.g.*, a temperature logger, and external instruments, *e.g.*, a met station, for time-series monitoring as the ice in the pool develops. There is also a platform constructed at the end of the pool for scatterometer and lidar placement so as to perform NRCS and surface roughness parameter measurements respectively.

The scatterometer in this experiment is a polarimetric, solid-state frequency-modulated continuous-wave radar working in the frequency band of 5.25 to 5.75 GHz (C-band). This frequency band was chosen as a tradeoff between the achievable resolution and the penetration depth. Also, models evaluated through the C-band scatterometer measurements may be scaled up to measurements by same-band satellites, *e.g.* current Canadian radarsat-2 and European Sentinel-1 as earth observation satellites. The radar system is equipped with a parabolic solid dish antenna of 61 cm diameter and a nominal 25 dB gain. This results in a half-power beam-width of about 5.5° for various polarizations. For polarimetric measurements, the scatterometer RF signal consists of polarization tooth-saw sections, with a polarization delay between them, and finally a calibration and noise segment. Sensitivity of the system is measured to be -40 dB which defines the system noise floor. A lidar system is used to scan the surface for roughness parameter calculations. The lidar system used in this research is a Leica Scanstation C10 terrestrial laser scanner [97]. The minute laser wavelength of the lidar pulse makes 3D mapping of the surface feasible, which in turn enables us to calculate the roughness parameters. The Scanstation C10 emits pulses of light at a repetition frequency up to 50 Hz and records both the trajectory and time-of-flight for each pulse to be reflected by the surface of the target and return to the scanner. At a wavelength of 532 nm, the laser pulses are consistently reflected by the surface.

(a) (b)

*Fig. 5.6:* SERF facility (a) The initial stage of sea-ice growth, (b) Calibration setup using a trihedral corner reflector at the last day of measurement.

### *5.8.2 Measurement Procedure*

The SERF pool was filled with a salt mixture to simulate the sea-water (*i.e.*, $Cl^-$ with 568.32 mmol/kg, $SO_4^{2-}$ with 20.77 mmol/kg, $Na^+$ with 510.36 mmol/kg, $K^+$ with 10.52 mmol/kg, $Mg^{2+}$ with 57.99 mmol/kg and $Ca^{2+}$ with 11.73 mmol/kg) with an overall salinity of 33.8 ppt. As one of the project's phases, in January 2014, ice growth started from open-water under the natural cold weather of Winnipeg, as shown in Figure 5.6a. A monostatic configuration was chosen in which polarimetric (*i.e.*, $HH$, $VV$ and $VH$ linear polarization) NRCS of the domain was measured. The C-band scatterometer was placed on the platform facing the pool, with the antenna-base height of about 5 m from the pool's surface. The scatterometer is capable of measuring NRCS at frequencies from 5.25 to 5.75 GHz in a 100 MHz step. The elevation and azimuth scanning angles range from 20° to 60° and from -15° to +15° with 5° steps respectively. The scanning in azimuth plane is averaged for each elevation incidence angle as we assume azimuthal homogeneity for the domain of interest for each elevation angle. Also each identical scan is repeated 5 times and the scan results are averaged to produce a single scattering matrix so as to reduce the effect of random noise in the measurement, by a minimum ratio of $1/\sqrt{5}$.

### *5.8.3 Calibration*

Two calibrations were carried out: (*i*) a sky calibration (cold source) for the system noise temperature, and (*ii*) a polarimetric calibration using a metallic trihedral corner reflector for each sampling frequency, as shown in Figure 5.6b. Due to the excellent cross-polarization (more than 30 dB in the peak of every polarization) between channels of this specific scatterometer, a single target calibration was sufficient for polarimetric calibration. It should be noted that the application of new calibration files resulted in an almost constant shift for NRCS values for all scattering angles when compared with both simulation and previous calibration files for similar configurations. Therefore, the measured values were corrected for this shift. Finally, since the scatterometer was not in the far-field for all incidence angles, a correction factor was applied to all NRCS measurements.

### *5.8.4 Lidar Measurements*

The scatterometer measurement was followed by a lidar scan on the 4th of February 2014 to measure the small-scale roughness of the surface. Roughness parameters are assumed unchanged compared to previous days as there was no significant weather incidence. The lidar scanner was mounted on the scaffold directly below the C-band scatterometer as shown in Figure 5.7a, at a height of 2.8 m above the SERF pool. The scanner was configured to obtain samples at a spatial resolution of less than 2 mm from an area of the snow surface enclosing almost the entire scatterometer measurement footprint. The final scan contained more than 15 million surface measurements.

After the scan was taken, the data were post-processed following the procedure outlined in [97] to extract the relevant surface roughness parameters with two approaches. In one approach, rms height $h$ and correlation length $l$ are measured alongside the

estimated scatterometer scanning arc at 5° intervals with incidence angles from 25° to 60°. For each incidence angle, a series of square 1m × 1m sections were extracted from the full scan at 0.2 m intervals along the scatterometer swath. Each square section was aligned parallel to the scatterometer beam and contained more than 200,000 surface measurements. A few sections of lidar data contained outlying samples located well above the true pool surface, caused by laser reflections from precipitation, which were removed using a simple height-threshold algorithm. The samples within each section were interpolated to a regular grid made up of 5mm × 5mm cells (*i.e.*, less than one tenth of the utilized scatterometer's wavelength of 5.5 cm) using a linear interpolation scheme. This method of interpolation was chosen, rather than a more sophisticated method such as kriging, because the sampling interval between raw samples was smaller than 2 mm. Therefore, the linear interpolation helped to the information from the original data while re-sampling to a grid with cells larger than the sampling interval of the raw samples. In the other approach to calculate $h$ and $l$, sampling was carried out within a rectangular mesh over the surface, instead or the scatterometer arc scan path, with sampling of 2 mm and a window size of 1m × 1m.

The scanned surface contained a larger scale of surface topography. This was possibly caused by irregular deposition of snow at the pool surface or, alternatively, redistribution of snow by wind across the pool in previous days. Including this larger scale of topography in the surface roughness measurements would bias $h$ and $l$. An FFT-based detrending algorithm was therefore used to remove low-frequency surface topography above a wavelength of 0.5 m within each section, leaving only the high-frequency (radar-relevant) roughness components. Surface roughness parameters were calculated for each detrended section using two-dimensional auto-correlation. Mean values for $h$ and $l$ were obtained for each scatterometer incidence angle from the average of all 1m × 1m sections in a swath. For instance in the first approach, five sections were used to calculate roughness parameters for the narrow-swath 25° incidence angle, whereas

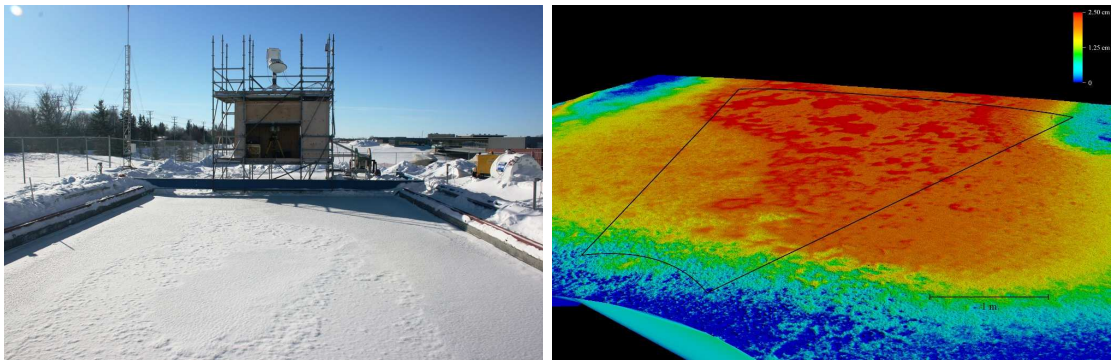

(a) (b)

*Fig. 5.7:* Surface roughness measurement at SERF (a) Lidar placement under scatterometer in the shed, (b) Oblique view of the profile's surface. The scatterometer scanning area on the surface is outlined in black lines.

eighteen sections were used for the wider-swath 60° incidence angle.

### *5.8.5 Profile Description*

By the 3rd of February 2014, the ice in the SERF pool had grown to a thickness of about 26 cm. An early snow-fall that happened at the beginning of the ice formation created a top layer on ice of about 1.5 cm thickness. This top layer is highly saline; we speculate the reason to be a combination of brine expulsion to the surface from the ice bellow and a process of melt-refreeze over past days.

To have a reference for our electromagnetic modeling evaluation, we need to measure the thickness and complex permittivity value for each layer of the profile. A direct in-situ complex permittivity measurement method of snow and upper layer of ice at the C-band frequencies using a dielectric probe was not successful. The reasons are speculated to be (*i*) melting snow/ice at the probe surface, and (*ii*) imperfect contact of the probe with the surface due to the roughness (in case of ice) or air-bubbles (in case of snow). Therefore, semi-empirical methods were chosen to calculate the complex permittivity as follows. For ice, the brine permittivity is first calculated from the ice temperature

and the frequency of operation [4]. Then, its volume fraction from ice salinity [5] and finally a mixture model is used to calculated the sea ice permittivity [116]. To this end, an ice-core was extracted from the pool and a temperature profiling was carried out with 2.5 cm steps when the scatterometer was measuring the NRCS. It was then cut into 5 cm slices which were later melted and salinity measured. It was not initially clear what the geophysical composition and structure of the top layer was. Therefore, four different formulations are tested in our data: dry snow [32, 119], wet snow [32], brine-wetted dry snow [110, 115], and slush [72, 120]. To extract the input variables, temperature was measured every 0.75 cm and a cutter was used to sample it every 1 cm (0.5 cm overlapping). The snow samples were first weighted for density and later melted for salinity measurements. Possible top layer middle permittivity is brought in Table 5.2 for each scenario (mixture formula for ice and brine was used to calculate the slush permittivity [27]). To use the right formulation for the permittivity of the top layer, each state was simulated by the forward solver and the resulting simulated NRCS values were compared to the NRCS measurements. The assumption of the slush state proved to provide the best match between the simulation and measurement results. This conclusion is also in line with our physical observations during the experiments. The occurrence of such high salinity and slush was also recorded in SERF in the previous year [72]. We should note that the top layer seems too saline to have formed only through brine rejection during ice formation. Therefore, we speculate that the thin ice sheet was depressed by the snow cover and seawater percolated up through to the base of the snow layer, or the ice was not in freeboard but rather frozen to the pool edge, so the seawater was under pressure causing hydrostatic pumping of water to the ice surface at some point. This condition is not generally observed in the Arctic. (*i.e.*, the snow is typically much less saline with lower permittivity.) The true profile of the complex permittivity is thus calculated and depicted in Figure 5.8 for the middle frequency of 5.5 $GHz$.

*Tab. 5.2:* Four possible states of top layer and their corresponding physical/chemical properties permittivity at the middle point.

| TOP LAYER PROPERTIES | | | |
|---|---|---|---|
| Temperature ($C$) | Density ($g/cm^3$) | | Salinity ($ppt$) |
| -8.81 | 0.39 | | 60.30 |
| PERMITTIVITY | | | |
| Dry Snow | Wet Snow | Brine-Wetted Snow | Slush |
| 1.54 | 3.68+1.12j | 3.62+1.42j | 7.81+1.44j |

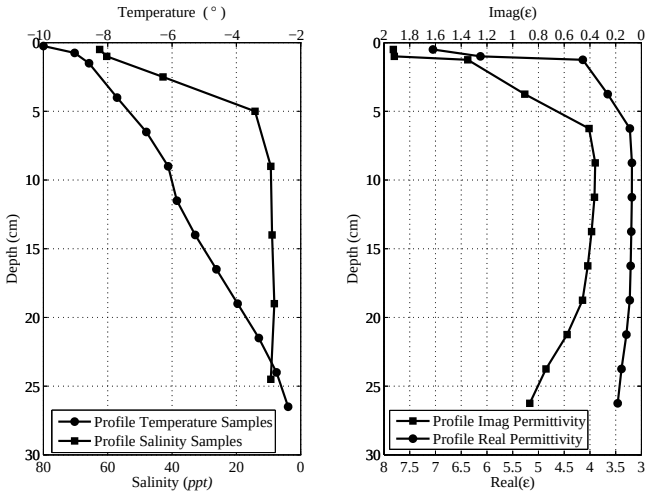


(a) (b)

*Fig. 5.8:* True profile (a) salinity and temperature measurements, (b) calculated permittivity.

### *5.8.6 Profile Parametrization*

As apparent from Figure 5.8b, both real and imaginary parts of the complex permittivity profile follow an exponential pattern with depth, showing a significant decrease within the first few centimeters. Therefore to reduce the number of parameters which define the dielectric profile of the domain, and thus reducing the number of unknowns for the inversion algorithm, a curve is fitted to the real and imaginary parts of the complex permittivity as

$$\epsilon(\mathbf{z}) = a \times \exp(c\mathbf{z}) + b \times \exp(d\mathbf{z}) \tag{5.2}$$

where $\epsilon$ can be the real or the imaginary parts of the complex permittivity. In (5.2), $\mathbf{z}$ is the depth from the snow top and $a$, $b$, $c$ and $d$ are the real-valued unknowns. Therefore, the whole domain's complex permittivity profiled is parametrized by 8 unknowns. It should be noted that the choice of such exponential form to fit the permittivity profile, comes from the knowledge of its true profile's $C$ shape. Therefore, the use of (5.2) in the inversion algorithm is considered as another prior information in the inversion process.

### *5.8.7 Discussion on the Measured Values*

Polarimetric measurements of the *HH*, *VV*, and *VH* NRCS of the profile were carried out at the frequency samples of 5.3, 5.4, 5.5, 5.6 and 5.7 GHz. Figure 5.9 shows the measured $\sigma_{VV}$ for all sample frequencies. Four issues should be addressed here. First, the NRCS is not an ever-decreasing pattern. This can be traced back to the inhomogeneity in the roughness parameter values for each elevation angle, confirmed by the lidar measurements. Second, unlike a simple half-space, the NRCS does not equally increase by stepping up the frequency for all incidence angles. This is due to the layered nature of this medium which causes multiple reflections. Third, an error margin of up to 0.5 dB exists in each measurement, defined as the NRCS variation in repetitive measurements. Fourth, sampling frequencies, due to the scatterometer limitation, are only 100 MHz away from each other. Therefore, it is expected that the the information at some data points might be lost as the NRCS difference to be due to the frequency change or the error margin. Such incidents will contribute to the reconstruction error of the inversion algorithm. Moreover, the BPT as a multi-layered rough media surface scattering forward solver follows the measured NRCS accurately. We trace it to our speculation that the surface scattering component is overwhelmingly larger than the volume scattering component. The justifications for this are ($i$) first few layers have a very high permittivity with high interface electromagnetic reflection,

*Tab. 5.3:* Roughness parameters of rms height and correlation length (*i*) Approach A: along rectangular, with sampling interval scale of 2 $mm$, $1m \times 1m$ window (*ii*) Approach B: along arc, with sampling interval scale of 5 $mm$, $1m \times 1m$ window (*iii*) Chosen Values: based on lidar suggestions and electromagnetic modeling result comparison with measurement. *NA* refers to not available data. Values are in *cm*

| APPROACH A | | | APPROACH B | | | CHOSEN VALUES | | |
|---|---|---|---|---|---|---|---|---|
| $\theta^\circ$ | $h$ | $l$ | $\theta^\circ$ | $h$ | $l$ | $\theta^\circ$ | $h$ | $l$ |
| 60 | 0.12 | 1.20 | 60 | 0.11 | 1.7 | 60 | 0.120 | 1.200 |
| 57 | 0.10 | 1.41 | 55 | 0.13 | 1.0 | 55 | 0.100 | 2.100 |
| 53 | 0.10 | 2.50 | 50 | 0.11 | 2.8 | 50 | 0.130 | 2.300 |
| 49 | 0.12 | 3.67 | 45 | 0.10 | 1.7 | 45 | 0.115 | 1.700 |
| 44 | 0.12 | 4.17 | 40 | 0.12 | 1.9 | 40 | 0.215 | 1.900 |
| 37 | 0.10 | 3.57 | 35 | 0.18 | 1.8 | 35 | 0.180 | 1.300 |
| 29 | 0.24 | 1.40 | 30 | 0.28 | 1.3 | 30 | 0.250 | 1.400 |
| 25 | *NA* | *NA* | 25 | *NA* | *NA* | 25 | 0.105 | 1.800 |
| 20 | *NA* | *NA* | 20 | *NA* | *NA* | 20 | 0.105 | 1.800 |

(*ii*) the slush-covered sea ice in the SERF is new, thus, lacking more complex volume scatterers (*e.g.*, lenses), and *(iii)* the measured values for the cross-polarized NRCS components are very small.

Table 5.3 shows the calculated roughness parameters resulting from the lidar scans. To examine the certainty of these values, two approaches were considered: (*i*) measurements along vertical rectangular grids with sampling interval scale of 2 mm, 1m × 1m windows, and (*ii*) measurements along arcs corresponding to the scatterometer elevation measurement angles with the sampling interval scale of 5 mm, 1m × 1m windows. As can be seen, the subjective approach in the roughness parameter calculation method can result in different values, more noticeably for the correlation length, for even the same incidence angles. Furthermore, what is considered here as "scattering angle arc" for lidar off-setting, is merely resulted from simple geometry calculation as $H\tan(\theta) \times (\cos(\phi)\hat{x} + \sin(\phi)\hat{y})$ in which $H$ is considered to be the distance between the tube on which antenna bracket is mounted to the profile's surface. This value is not exactly the same as the actual incidence angle from the scatterometer's antenna, as the complex antenna's bracket movement in this calculation is ignored.

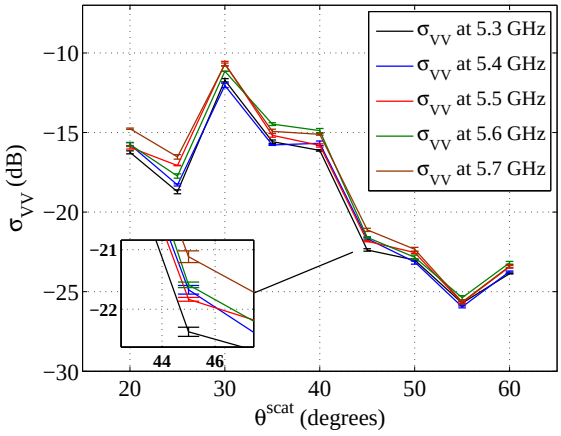


*Fig. 5.9:* Measured $\sigma_{VV}$ at sampling frequencies of 5.3, 5.4, 5.5, 5.6 and 5.7 GHz with error margin at each measurement. The inner box is a magnifier for more detailed view. (b) Comparison of $\sigma_{VV}$ between the simulated, denoted by Sim, and measured, denoted by Meas, at 5.5 GHz.

Moreover, the antenna has a Gaussian field distribution which does not incorporate roughness effects uniformly. Therefore, instead of using the exact values of the roughness parameters provided by the lidar calculation in our electromagnetic modeling, we use them as a reference and tweak them in a way that the resulting NRCS from the forward solver resembles the measured NRCS data the most. Final values chosen on this assumption are shown in the last column of Table 5.3. This model-based judgment on roughness parameters was possible since we had the true permittivity of the profile through direct physical measurements. This shortcoming in independently choosing the right roughness parameters can be partially solved if a completely objective method in roughness parameter calculation is developed. Other interfaces are taken to be almost smooth in accordance with our observations and previous studies at the SERF [72]. Moreover, to make sure that these roughness values are within the validity region of the BPT forward solver, an NRCS comparison with improved integral equation method ($I^2EM$) [27], was carried out for a simplified profile of half space with the same roughness parameters as reported in Table 5.3. The results varied only about 0.15 dB in most data points which is within the tolerance of the algorithm. Finally, a comparison between simulated and measured data at 5.5 GHz for the SERF profile is depicted in Figure 5.10.

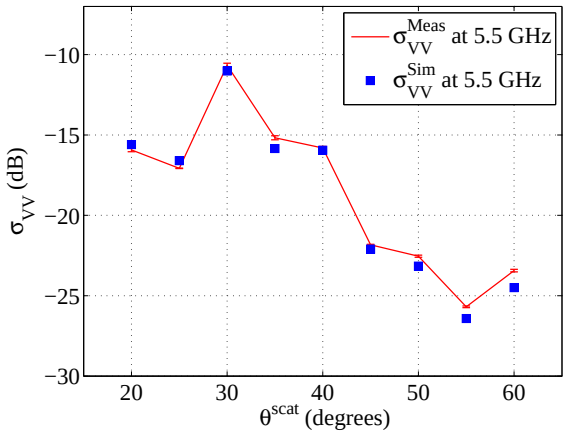


*Fig. 5.10:* Comparison of $\sigma_{VV}$ between the simulated, denoted by Sim, and measured, denoted by Meas, at 5.5 GHz.

### *5.8.8 Inversion results*

In this section, we apply our inversion algorithm to the NRCS data measured at the SERF. The inversion results can then be used to evaluate the role of the sensitivity in the achievable reconstruction accuracy. Due to the large number of the profile unknowns and limited number of NRCS data points, the surface roughness parameters are taken to be as prior information. Also a height position griding based on measurement points on the snow-covered sea ice provides the algorithm with the profile's freeboard. Therefore, the total number of unknowns to be reconstructed is 8 (4 as the coefficients of (5.2) for the real part of the profile's complex permittivity and the other 4 as the coefficients of (5.2) for the imaginary part of the profile's complex permittivity). Two different measured data sets are then considered, and named as Case I and Case II. For Case I, the input data of $\sigma_{VV}$ and $\sigma_{HH}$ belonging to the look angles of 20°, 25°, 30°, 35°, and 40° at the sampling frequencies of 5.3, 5.4, 5.5, 5.6 and 5.7 GHz are considered. Therefore, a total number of 50 input data points is available for Case I. For Case II, the input data of $\sigma_{VV}$ and $\sigma_{HH}$ belonging to the look angles of 40°, 45°, 50°, 55°, and 60° at the sampling frequencies of 5.3, 5.4, 5.5, 5.6, and 5.7 GHz are considered. Therefore, similar to Case I, a total number of 50 data points is available

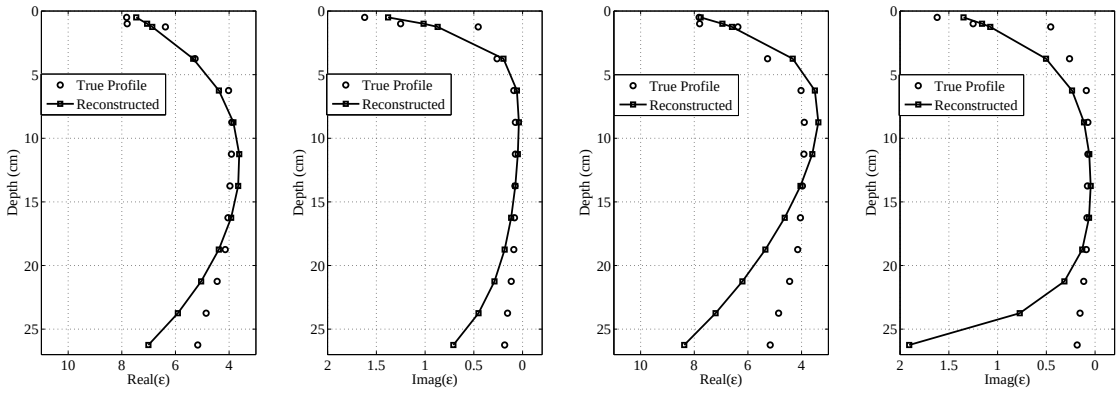


*Fig. 5.11:* Reconstruction of the snow-covered sea ice dielectric profile of interest using two different data sets, Case I and Case II through monostatic configuration experimental data. (a) real permittivity profile, Case I, (b) imaginary permittivity profile, Case I, (c) real permittivity profile, Case II, (d) imaginary permittivity profile, Case II

for Case II. The profile is then reconstructed using these two different data sets. The result of the reconstruction is shown in Figure 5.11. It is obvious that the inversion of the data set of Case I returns more accurate reconstructions, with mean square relative error of at least two times smaller than that of Case II (*i.e.*, for the first 9 points permittivity, with mean-square-root of relative error of 0.0649, 0.4196, 0.1091 and 0.8139 for part (a) to (d), respectively). This verifies our speculation that the NRCS data collected at the angles close to the nadir in a monostatic configuration provide more sensitive data to the dielectric profile of the domain of interest, thus, helping the inversion algorithm to converge to a more accurate reconstruction. Also, it is evident that due to the penetration depth, the illuminating wave interrogates deeper layers of the profile less efficiently. Therefore, the retrieval accuracy deteriorates in deeper layers.

## *5.9 Conclusion*

In this chapter, we have (*i*) investigated the sensitivity of the NRCS data in both monostatic and bistatic configurations with respect to the dielectric profile parameters of snow-covered sea ice, and (*ii*) demonstrated through synthetic and experimental data that enhanced reconstruction accuracy can be obtained if more sensitive NRCS data is used for inversion. To calculate the sensitivity of the NRCS data at different look angles, we have used the BPT forward solver in conjunction with the fourth-order finite-difference derivative formulation. The choice of the BPT forward solver was beneficial as its closed-form recursive formulation results in efficient computational time. It was then shown that the NRCS data collected close to the nadir in monostatic setups is more sensitive to the dielectric profile parameters. Also, it was shown that the NRCS data collected close to the specular angle in bistatic setups exhibit high sensitivity values with respect to the dielectric profile parameters. It should be noted that in the case of a bistatic configuration, the maximum sensitivities for all the profile parameters do not necessarily happen at the specular angle. This could be due to multiple scattering events from rough interfaces. Therefore, it was recommended that an angular margin in the vicinity of the specular angle should be included in measurements.

Based on these observations, we then speculated that the inversion of the data sets corresponding to higher sensitivity values should result in enhanced dielectric profile reconstruction accuracy as compared to the inversion of the data sets corresponding to smaller sensitivity values. To verify this speculation, we created two different NRCS data sets for each profile of interest. These two different data sets are distinguished by their corresponding look angles towards the profile. The difference between the look angles transforms into different NRCS sensitivity values. It was then shown that the inversion of more sensitive data set results in enhanced reconstruction accuracy, thus,

confirming our speculation.

For the monostatic configuration, we investigated inverting both experimentally and synthetically collected data sets of different sensitivity values. In particular, for the experimental NRCS data inversion, we used a parametrization technique to lower the number of profile unknowns to deal with the imbalance between the number of known and unknown quantities. In this parametrization, prior information regarding the shape of the dielectric profile curve, based on physical observations, was utilized. For the bistatic configuration, we only showed the inversion of synthetically collected data sets of different sensitivity values. This is due to the fact that experimental bistatic NRCS data was not available. As a future work, inversion of experimentally collected bistatic NRCS data should be carried out. This will further evaluate our speculation on bistatic inversion of the more sensitive NRCS data in the vicinity of the specular angle. Such bistatic data may be measured through tandem satellites, dual-apertured airborne radars, and bistatic ground-based scatterometers. In addition, it will be useful and practical to assess similar scenarios to those studied in this chapter using single-frequency data sets. The use of single-frequency data sets, as opposed to multiple-frequency data sets, may then require incorporating more prior information about the profile to be reconstructed.

This chapter, therefore, contributes to better understanding the importance of the sensitivity of the measured NRCS data points with respect to the parameters to be reconstructed in microwave remote sensing of snow-covered sea ice dielectric profiles. The framework presented above can then be a useful tool in selecting more informative data points for the microwave inversion process.

# 6

# SERF Experiment II: Temporal Evolution Retrieval

## *6.1 Overview*

In the previous chapter, the use of sensitive NRCS data with respect to the unknown parameters of the profile for a multi-frequency monostatic configuration was investigated. Furthermore, a profile parametrization technique was employed based on prior information about the permittivity profile of the snow-covered sea ice. These two techniques allowed an appropriate treatment of the ill-posedness associated with the inverse scattering of the snow-covered sea ice. Herein, we consider the case in which we do not have access to multi-frequency data sets; instead we have access to time-series NRCS data. To address this scenario, I develop another strategy in this chapter to invert single-frequency time-series monostatic NRCS data. Within this framework, the inversion algorithm reconstructs the vertical temporal profiles of temperature, salinity, and density of the snow-covered sea ice. The time-series single-frequency NRCS data

utilized in this chapter have been collected at the SERF during Winter 2014.

Herein, the structure of this chapter is described. A brief introduction is brought in Section 6.2 and is followed by the problem statement in Section 6.3. Afterwards in Section 6.4, the general strategy utilized for inversion is outlined as below. It is expected that when the number of measured NRCS data points is small, the employment of prior information about the profile can increase the accuracy of the reconstruction by tackling the ill-posedness. Thus to take advantage of this concept, it is proposed to utilize the reconstructed profile at a given time step as prior information for the profile reconstruction at the subsequent time step. Next in Section 6.5, the measurement procedure is explained. The measurement procedure is similar to that explained in Chapter 7 (*i.e.*, physical sampling, lidar, and scatterometer measurements), except that the NRCS data collected through the scatterometer are single frequency and in time-series. The physical sampling is also carried out throughout the temporal NRCS measurements.

The utilized inversion algorithm is briefly described in Section 6.6. This inversion algorithm employs a normalizing weighting factor for the misfit cost function to retrieve the temperature, salinity, and density profiles of the snow-covered sea ice. It should be noted that these geophysical and thermodynamic parameters of snow and sea ice are related to their dielectric properties through the proxy formulas presented in Chapter 3. In Section 6.7, the use of prior information is further explained. This includes ($i$) an appropriate parameterization of the snow-covered sea ice profile, and ($ii$) taking advantage of the reconstructed profile at one time step to reconstruct the profile at the next time step. The latter allows us to minimize the search space for the problem unknowns assuming that the profile goes through no abrupt changes. Finally, the retrieved temporal evolution of the temperature, salinity, and density profiles are presented in Section 6.8. These retrieved parameters are in good agreement with the true values. Furthermore, a relation between the evolution of the retrieved temperature and

salinity profiles and their complex permittivities is established. Some specifications of the retrieved results are also deciphered considering the physical state of the measurement setup (*e.g.*, air temperature at the time of measurements). Subsequently, various sources of error due to the utilized non-ideal physical sampling procedure are outlined. At the end, a conclusion in Section 6.9 highlights the findings of this chapter.

The materials of this chapter are based on the paper accepted for publication in IEEE Journal of Oceanic Engineering in 2015 [89][(1)].

## *6.2 Introduction*

Herein, we use the normalized radar cross section (NRCS) data as the measured quantity to characterize the snow-covered young sea ice profile. Young sea ice is a transition ice between earlier nilas and later first year ice, with a typical thickness varying from 10 to 30 cm. It is known that the NRCS data collected from a given snow-covered sea ice profile is nonlinearly related to its dielectric profile. On the other hand, the dielectric profile of snow-covered sea ice is linked to its temperature, salinity, and density profiles. Therefore, the temperature, salinity, and density profiles are associated with the measured NRCS data. This chapter aims to reconstruct the temperature and salinity profiles of the snow-covered sea ice from time-series monostatic single-frequency (C-band) NRCS data. The inversion algorithm considered herein is an electromagnetic inverse scattering solver that iteratively reconstructs the temperature and salinity profiles from NRCS data. This chapter shows how time-series NRCS data can provide prior information for the utilized inversion algorithm so as to monitor the evolution of temperature and salinity profiles during the time interval of interest.

[(1)] © [2015] IEEE. Reprinted, with permission, from N. Firoozy, A. Komarov, P. Mojabi, D. Barber, J. Landy, and R. Scharien, "Retrieval of young snow-covered sea-ice temperature and salinity evolution through radar cross-section inversion," *Oceanic Engineering, IEEE Journal of*, vol. 41, no. 2, pp. 326-338, 2016.

## *6.3 Problem Statement*

The profile under study in this chapter is a new ice (NI) rapidly-grown from sea water in the Sea Ice Environmental Research Facility (SERF) under cold condition. This facility is a unique Arctic Ocean mesocosm [121] located on the University of Manitoba campus. The profile under investigation in this chapter is a simulation of young sea ice that would form in polynya or lead areas. In such areas, similar to the experiment presented herein, when the ice sheet diverges in cold conditions, the open water freezes into new ice with a high growth rate resulting in high brine rejection. These forms of young ice are becoming increasingly important physically, biologically, and geochemically due to climate change [11].

The ice in SERF was covered with a thin layer of snow for almost the entire period of study. Based on the true properties of the profile under study, it can be modeled as a multi-layered medium with rough interfaces, as depicted in Figure 6.1. A single complex permittivity was assigned to the top snow layer and a changing complex permittivity to the ice layer. The imaginary part of the complex permittivity is mostly due to the presence of brine which is taken to be of spherical shape in this chapter. Due to the assumption of the spherically-shaped brine inclusions, the complex permittivity of the ice will be isotropic. It should also be noted that, throughout this chapter, slush is referred to as a special case of snow.

The unknown properties of the above profile, which are to be retrieved, are its temperature and salinity at different depths as well as the density of the top layer (snow layer). On the other hand, the known quantity, from which the unknowns are to be retrieved, is the single-frequency NRCS data, $\sigma_{pq}$. In this chapter, we consider monostatic NRCS in which one antenna serves as both the transmitter and receiver.

The unknowns are then to be reconstructed from the knowledge of the single-frequency

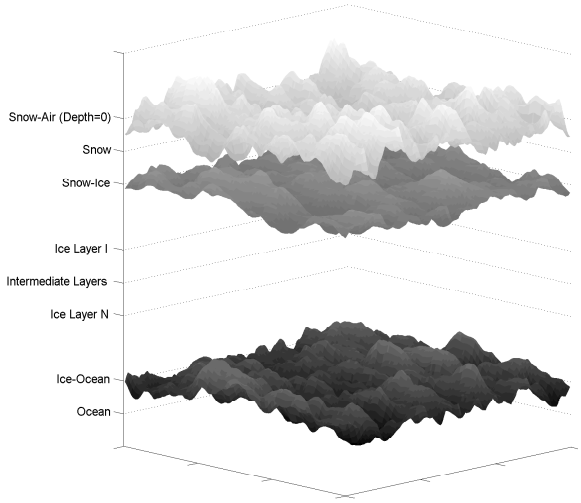


*Fig. 6.1:* Simplified stair-cased snow-covered sea ice profile with rough interfaces. The top thin snow layer is assumed to have a homogeneous complex permittivity. The ice layer is assumed to have varying complex permittivity.

(C-band) monostatic NRCS data. In this chapter, the NRCS data are collected as a time-series data, thus, enabling us to quantitatively reconstruct the salinity and temperature profiles at different time steps within the time period of interest. This provides us with the ability to quantitatively monitor the thermodynamic evolution of the sea ice. In the next section, we briefly describe our strategy; more details will be presented in the rest of the chapter.

## *6.4 General Strategy*

As noted earlier, we aim to reconstruct the unknown profiles within the framework of electromagnetic inverse scattering. It is well-known that electromagnetic inverse scattering is an ill-posed problem [105, 122]. Consequently, the accuracy of the reconstructed profile depends on the ratio of the number of (independent) measured data points to the number of unknown parameters of the profile. The number of measured data points can be increased by performing data collection at different angles, frequencies, and polarizations.

When the number of measured data points is not sufficient to achieve a reasonable reconstruction accuracy, prior information about the profile to be reconstructed can be employed. Similar to the above discussion, the use of prior information can be regarded as an attempt to make the null space of the problem as close as possible to trivial. To this end, different methods such as the incorporation of thermodynamic ice growth model [60] and permittivity curve parameterization [90] have been previously used.

In this chapter, the NRCS data are only measured at 5.5 GHz. Although being limited to a single-frequency NRCS data set, we collect a time series of these NRCS data. To take advantage of the fact that we do have a time-series data set, we propose to use the reconstructed profile at a given time step as prior information for the reconstruction of the profile at the subsequent time step. This strategy is implemented assuming that there is no extreme abrupt changes in the profile under investigation. The details of our implementation are presented in Section 6.7. To the best of our knowledge, this method has not been previously applied to an electromagnetic inverse scattering algorithm for snow-covered sea ice.

## *6.5 Measurements*

In what follows, different aspects of our measurements have been classified into six different parts, as described below.

### *6.5.1 Measurement Setup*

Time-series NRCS measurements were carried out at the University of Manitoba SERF mesocosm located in Winnipeg, Canada, spanning from 25th of January 2014 to 10th of February 2014. In this phase of the SERF project, the pool, see Figure 6.2a, was

filled with a salt combination of $Cl^{-}$, $SO_4^{2-}$, $Na^{+}$, $K^{+}$, $Mg^{2+}$, and $Ca^{2+}$, resulting in an approximate salinity of 33.8 ppt. The sea-water grew into thick new ice (NI) under the natural cold weather of Winnipeg. The weather conditions were stable with no precipitation during the experiment except a snow-fall on the late evening of January 25th with drifting snow condition which left a layer of about 1.5 cm thick snow on the surface. A meteorological station located beside the pool at the SERF measured the air temperature. As can be seen in Figure 6.3, this temperature shows a small deviation from manual air temperature measurements at the snow-covered sea ice due to the difference in the height of measurements.

### *6.5.2 Scatterometer Setup*

During most of the measurement period (25th of January 2014 to 10th of February 2014), a C-band solid-state frequency-modulated continuous-wave (FMCW) scatterometer, with an antenna height of approximately 5m from the profile's surface, was continuously measuring the polarimetric NRCS at elevation angles of 20° to 60° with 5° intervals and at azimuth angles of -15° to 15°. Continuous measurements along the azimuth plane for each incidence angle were averaged to account for a horizontally symmetric medium assumption. At the end of the measurements, a trihedral metallic corner reflector was used for polarimetric scatterometer NRCS calibration, as shown in Figure 6.2b. Also, a sky measurement was performed for each scan separately as a part of system's calibration procedure. (A detailed report on the calibration errors and procedures for this scatterometer is presented in [90].) On one occasion, a Leica Scanstation C10 terrestrial laser scanner (light detection and ranging; lidar) was also employed for detailed surface roughness characterization.

(a) (b)

*Fig. 6.2:* Measurements at the SERF (a) Scaffolding setup on which the scatterometer (on the roof of the scaffolding) and lidar (located on a tripod) are mounted. Both Scatterometer and lidar are looking toward the pool and scanning the snow-covered sea ice; (b) Scatterometer calibration through a trihedral corner reflector mounted on a tripod in the middle of the pool.

### *6.5.3 Physical Sampling Procedure*

To be able to evaluate the accuracy of the retrieval results, physical sampling of the snow-covered sea ice profile was also performed with a temporal resolution between one and three times per day. In each physical sampling session for the snow layer, whose total average thickness is 1.5 cm, a cutter of 1 cm thickness was used to extract two samples: one from 0 cm to 1 cm and the other from 0.5 cm to 1.5 cm. These samples were later weighted to calculate their densities. Next, they were melted; and, the salinity of each sample was measured through a salinity meter. We averaged the values of the two salinity and the two density measurements to assign homogenous salinity and density properties to the snow layer. For the ice layer, an ice core was extracted in each physical sampling session. The ice core was then cut into different samples. Starting from the ice surface, the first and second samples had a thickness of 2 cm and 3 cm respectively; the rest of the samples were then of 5 cm thickness. Each sample was later melted and the bulk salinity was measured through a salinity meter. Finally, a manual temperature profiling of snow and ice was carried out. For the snow layer, these temperature measurements were performed at the air-snow interface,

middle of snow and snow-ice interface. For the ice core, holes were drilled at 2.5 cm intervals for temperature probe insertion. In addition to the manual temperature profiling, a temperature string, installed in the SERF pool, also measured the vertical temperature every 2 cm. (The first temperature sensor is located at the depth of 1.5 cm.) The temperature measurements obtained through this string are shown in Figure 6.4. As seen in this Figure, the temperature data from this string was not available during some time periods. Therefore, the available string readings are only shown here for comparative purposes. As can be seen later, we have used the manual temperature data to model the dielectric properties of the snow-covered sea ice. We also note that the thickness of ice across the pool may vary slightly. This affects the sampling at different locations in the pool; *e.g.*, the small reduction of the measured ice thickness on the 31st of January.

As also noted in [90], a top layer of slush with an average thickness of 1.5 cm covers the ice. The presence of a highly saline slush may be explained by one of the following scenarios, or a combination thereof: (1) the melt-down of early snow on very young ice, (2) possible breaks at the edges of the pool that might have expelled some sea-water on the young ice at an early stage, and (3) brine migrating towards the surface. This might happen particularly in case of a high ice growth rate resulting in a high brine expulsion rate. However, as can be seen from Figure 6.3, the air temperature during the period of this experiment was consistently below $-10$ °C; therefore, the possibility of a direct thermodynamic melt of the snow is small. On the other hand, a high rate of brine expulsion is more likely due to the consistently cold temperatures.

### *6.5.4 In-situ Indirect Permittivity Extraction*

Enabled by this sampling, the permittivity of slush layer was then calculated based on its density, salinity and temperature as a mixture of ice and brine [120]. Calculation of

sea ice permittivity was also performed based on each measurement point's salinity and temperature. Brine salinity was calculated through formulation in [123]. Similarly, we calculated brine permittivity following [4], pure ice permittivity following [3], brine and pure ice density following [30]. The Polder-van Santen/de Loor mixture formulation with spherical inclusion was also applied based on the formulation presented in [27]. In this formulation, we considered an effective dielectric constant equal to the host medium (*i.e.*, ice), or inclusion (*i.e.*, brine), for the region immediately surrounding the inclusion if the brine fraction volume was smaller, or greater than 0.1 respectively. Further details on these proxy formulations are brought in Appendix B. Figure 6.5 depicts the manually measured temperature of the profile at the surface and at depths 0.75 cm, 2.5 cm, 5 cm, 9 cm, 14 cm, 19 cm, 24 cm, and 29 cm away from the surface. Figure 6.6 shows the measured salinity from snow/ice samples for the aforementioned points. When the data for a specific point were not available, an interpolation technique was applied between the neighboring points to extract the expected value. From Figure 6.6a, a large salinity for the top layer is evident. The jump in salinity, starting after the first sampling, is an indication of the early surface slush layer formation.

Regarding the assignment of the salinity values to the above measurement heights, the following protocol was followed. The extracted profile sample was staircased at the depths of 1.5 cm, 3.5 cm, 6.5 cm, 11.5 cm, etc. The salinity within each separate section of the profile was then measured. This measured salinity was then assigned to the middle point of this layer. For example, the salinity values for the first, second, third, and fourth layers were assigned to 0.75 cm, 2.5 cm, 5 cm, and 9 cm respectively. As will be seen later in Section 6.7.1, the salinity (and, temperature) values at these points are taken to be the unknowns of the inversion algorithm. (The reconstructed values can then be compared with the measured values at these points.)

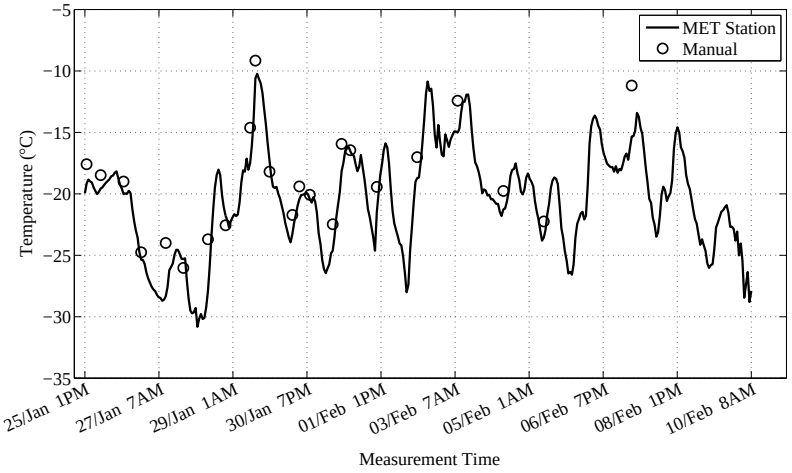


*Fig. 6.3:* Air temperature measurements at the SERF through the MET station and the manual temperature meter.

### *6.5.5 Time-Series NRCS Data*

The C-band (5.5 GHz) polarimetric NRCS measurements were performed in a time-series manner from 1pm on January 25th (2014) to 8am on February 10th (2014), capturing the evolution of snow-covered sea ice from open water to almost 30 cm thick ice. To reduce the effect of the measurement random error, the NRCS measurements for a given incidence angle and polarization within one hour of continuous measurements are averaged into one number. Therefore for each hour within the measurement period, we have one $\sigma_{HH}$, one $\sigma_{VH}$, and also one $\sigma_{VV}$ per incidence angle.

Figure 6.7 shows this time-series NRCS data. As can be seen in this figure, five different measurement periods can be identified for this time-series experiment.

#### *6.5.5.1 Initial formation of ice*

In the first period from 1pm on January 25th to 7am on January 27th, ice forms from open sea water. After the initial formation, the ice grew to 3.5 cm after which,

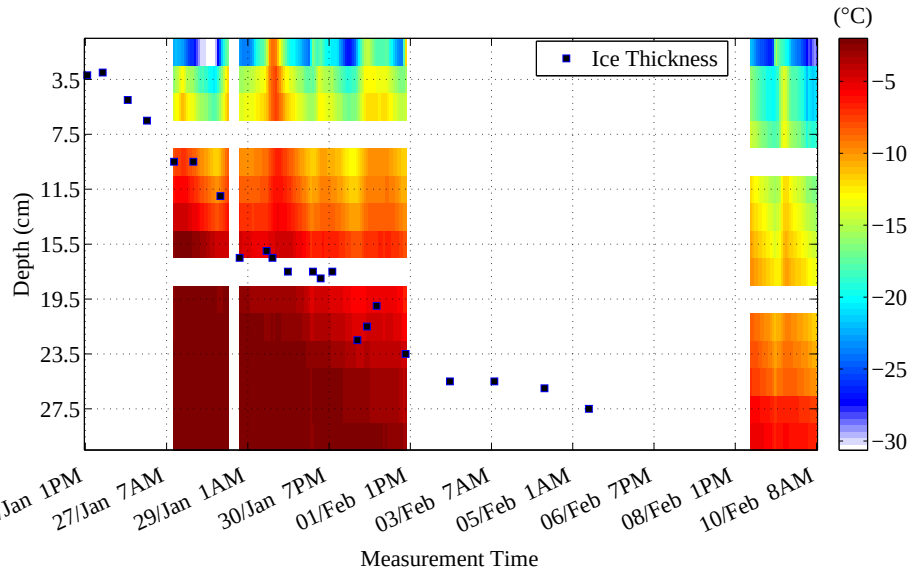


*Fig. 6.4:* Temperature string color map. First sensor is at the depth of 1.5 cm, and the rest of the sensors are placed with an interval of 2 cm. The colorbar represents the temperature in °C. The manually measured (total) ice thickness is projected on the plot as squares.

there was a snow-fall event. We speculate that the significant increase in the NRCS value, compared to its initial value, is either due to the complex effect of this snow-fall or the expulsion of sea water on the newly-formed ice surface. The spectrogram (*i.e.*, the Fourier-domain data within a moving window with time) of the time-series NRCS data also showed the presence of higher-order frequency components for this time interval compared to the rest of the measurements. We speculate that this is an indication of dealing with a rapidly-changing nonlinear system for this interval. The complexity of this time interval prohibits its electromagnetic inversion through our utilized electromagnetic solver; therefore, this time interval is only presented as an observational case.

#### *6.5.5.2 Stabilization period*

In the next stage of the profile's evolution, the system goes into a transition state till 12am on January 30th, during which the system behavior stabilizes (*i.e.*, moving

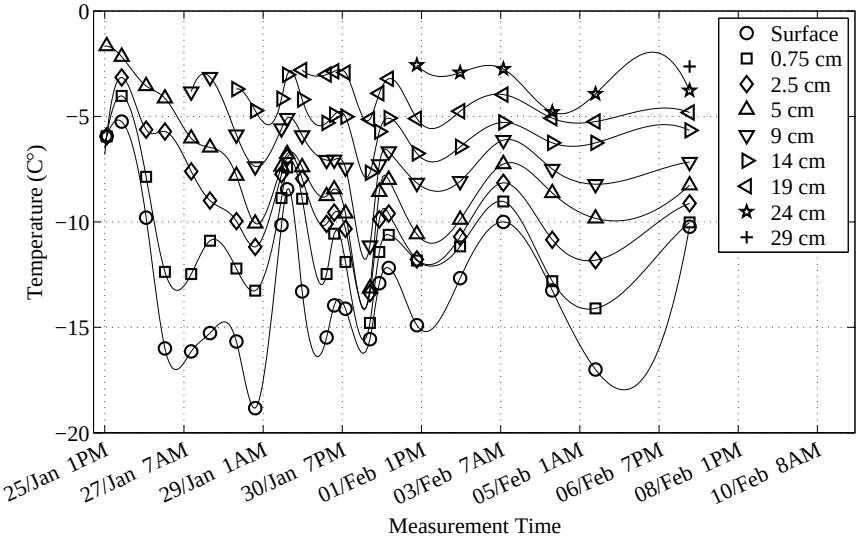


*Fig. 6.5:* Manual ice temperature profiling. The solid line is only to connect the measurement points of the same profile height.

towards a stable NRCS.) Similar to the previous measurement period, this period will not be investigated for inversion, and is only presented for context. Finally, regarding these two measurement periods, it should be noted that from 11am on January 26th to 10.30am on January 27th, NRCS measurements were not carried out for the angles of 20°, 25°, 30°, 35° and 40°, due to human operator's error. An interpolation technique was then used to plot the missing data as follows. The NRCS curve as a function of time at 45° is taken as the reference plot. Then, its deviation from a direct line connecting the start and the end points within the missing time slot is calculated. Next, this deviation is weighted by the ratio of the NRCS standard deviation of the intended missing angle to that of 45°. These weighted values are finally added to a direct line connecting the start and the end points within the missing time slot for each angle of interest. It should be reminded that the interpolated data have not been utilized in the inversion algorithm, and have been presented only for show purposes.

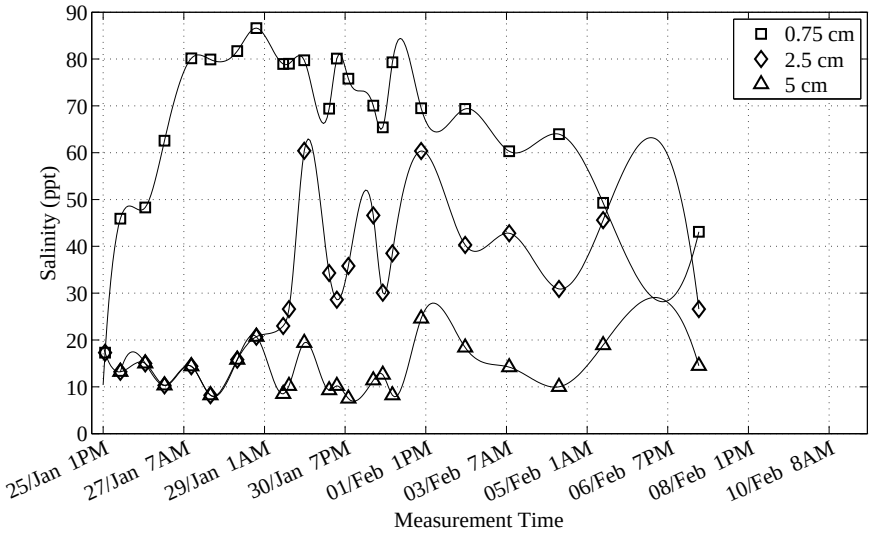


(a)

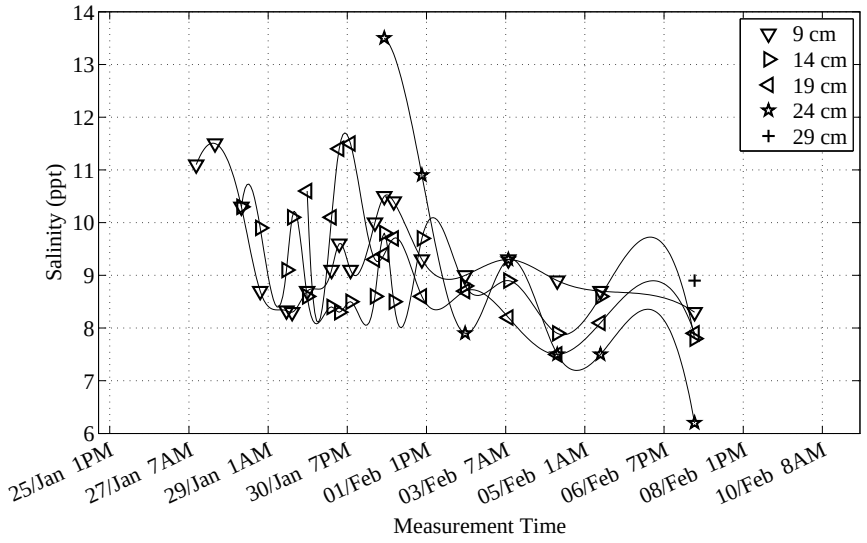


(b)

*Fig. 6.6:* Manual salinity profiling (a) 0.75 cm up to 2.5 cm; (b) 9 cm up to 29 cm.

#### *6.5.5.3 Period of interest*

From 12am on January 30th to 2pm on February 3rd, no significant meteorological event occurred and the measured NRCS behavior agreed with our electromagnetic modeling expectation. Thus, we designate this interval as the period of interest. That is, our electromagnetic inversion, to be presented later, will be performed on the time-series NRCS data within this measurement period. (We note that the necessary condition for a successful inversion is that the utilized modeling should be sufficiently close to the actual scenario.)

#### *6.5.5.4 Measurement halt period*

There was no NRCS measurements performed from 12pm on February 4th to 2pm on February 7th. We note that this missing data, and also the aforementioned missing data in the second measurement period are both outside the period of interest. Therefore, they do not affect our inversion process.

#### *6.5.5.5 Last measurement period*

The last measurement interval happened from 2pm on February 7th to 8am on February 10th. Due to the changes on the profile's surface and the lack of the lidar data, the inversion of the NRCS data within this interval is not investigated. (The lidar data, to be described later, serves as prior information for the inversion algorithm.)

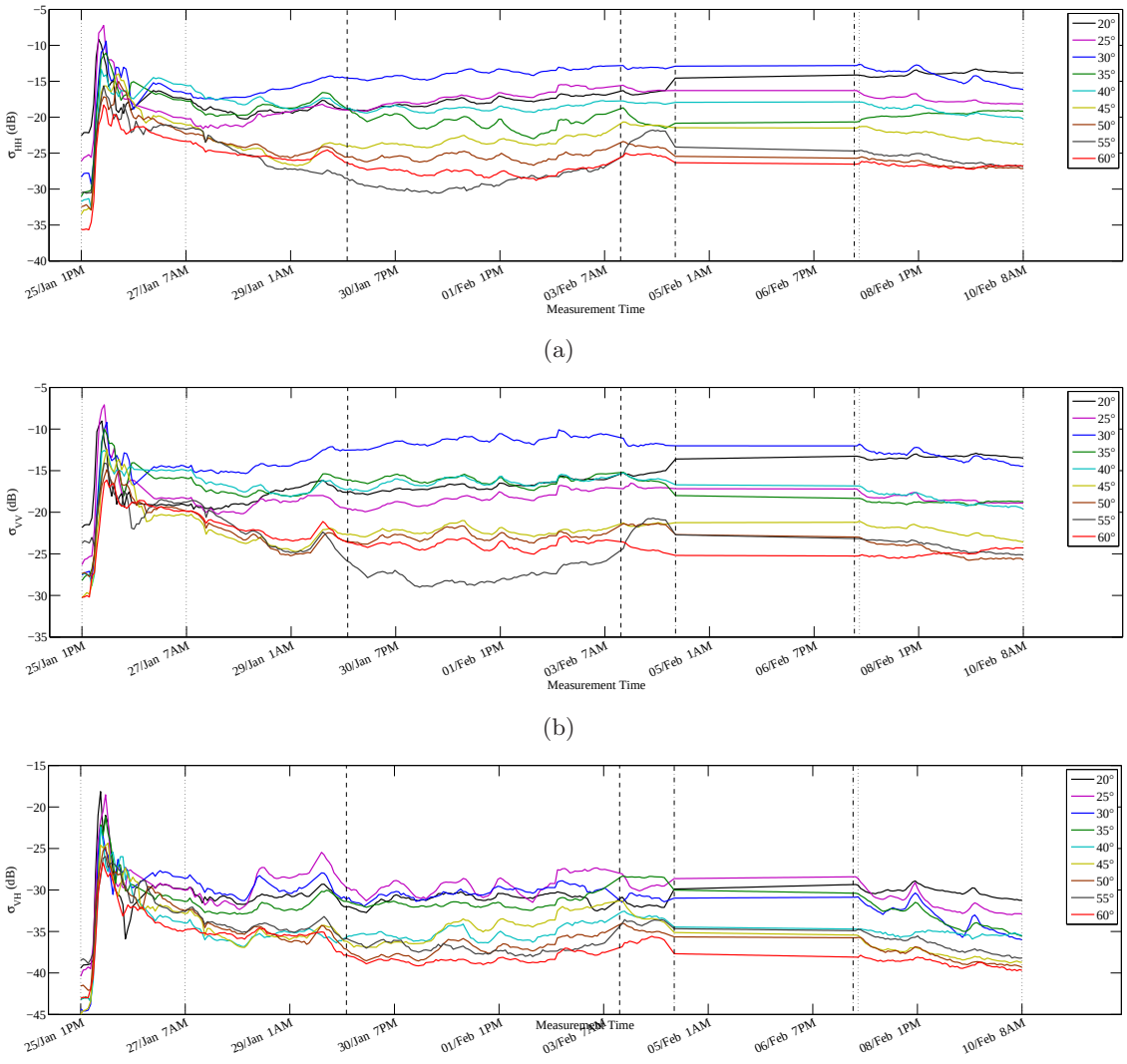


(a)

(b)

(c)

*Fig. 6.7:* Time-series measured NRCS (denoted by $\sigma$) at 5.5 GHz for (a) HH polarization; (b) VV polarization; (c) VH polarization. The vertical lines denote the time intervals for (1) period of initial ice formation and rapid changes due snow-fall from January 25th 13pm to January 27th 7am, (2) period of stabilization from January 27th 7am to 30th 12am, (3) period of interest from January 30th 12am to February 3rd 2pm, (4) period of measurement halt, and (5) period of post measurement from February 7th 2pm to February 10th 8am.

*Tab. 6.1:* The rms height, $h$, and correlation length, $l$, regarding the roughness parameters of the air-snow interface at 9 different incidence angles

| $\theta^\circ$ | 20 | 25 | 30 | 35 | 40 | 45 | 50 | 55 | 60 |
|---|---|---|---|---|---|---|---|---|---|
| *h (cm)* | 0.105 | 0.105 | 0.250 | 0.180 | 0.215 | 0.115 | 0.130 | 0.100 | 0.120 |
| *l (cm)* | 1.800 | 1.800 | 1.400 | 1.300 | 1.900 | 1.700 | 2.300 | 2.100 | 1.200 |

### *6.5.6 Lidar Data*

A lidar scan was carried out on 4th of February so as to determine the roughness parameters: the rms height, $h$, and the correlation length, $l$. Figure 6.8 shows the result of the surface scan in terms of the surface height and variation. The investigation domain is stable in the period of interest; thus, the surface roughness parameters estimated on the date of lidar measurements are used for the whole period of interest. A Gaussian height distribution best fits the data and an exponential distribution has been used to determine the correlation length. The resulting surface roughness parameters ($h$ and $l$) for the first interface at each incidence angle are presented in Table 6.1. For other interfaces, we assumed very small roughness. This assumption was confirmed with both our physical observation for this profile, and also the comparison of simulated with measured NRCS values. A detailed description on our lidar data acquisition and interpretation can be found in [90, 124].

## *6.6 Inversion Algorithm*

We have previously used our inversion algorithm for snow-covered sea ice permittivity profile reconstruction successfully [90, 91]. This inversion algorithm consists of two main parts; namely, forward solver and inverse solver. The utilized forward solver is the Boundary Perturbation Theory (BPT) solver [94]. The BPT is a non full-wave solver which uses a closed-form formulation to calculate the polarimetric NRCS of a multi-layer medium with rough interfaces. Moreover, the BPT forward solver provides

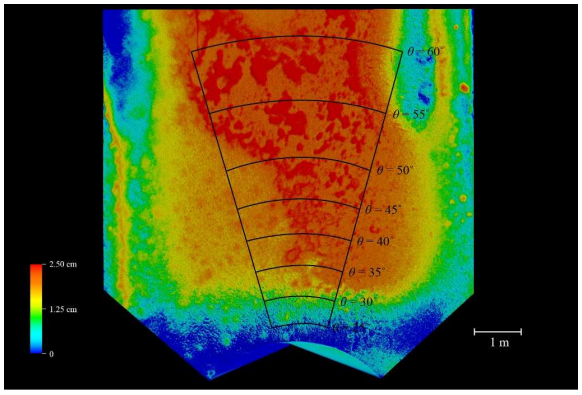


(a)

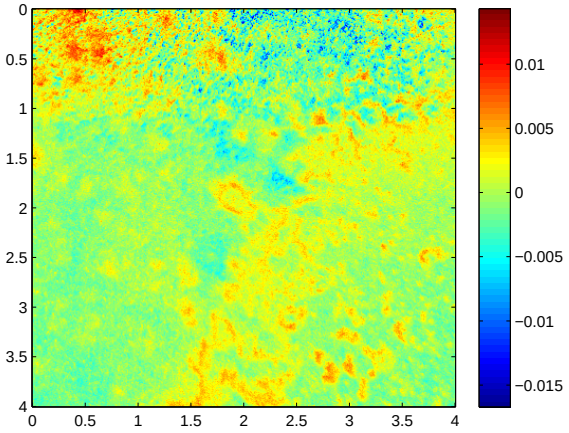


(b)

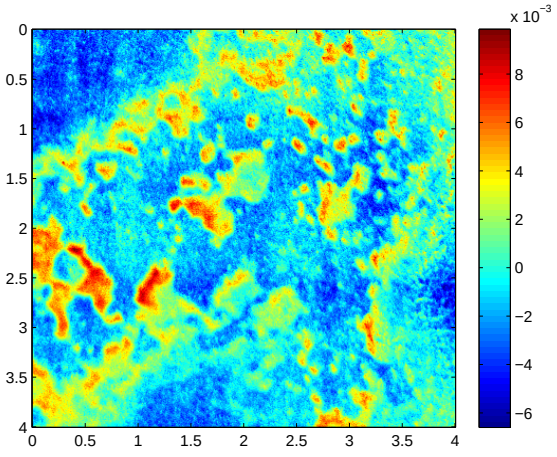


(c)

*Fig. 6.8:* Lidar scan of SERF's pool surface at 12pm on February 4th showing surface height for (a) the whole pool surface; (b) near detrended; and (c) far detrended. The colorbar scale is in [cm] in (a), and is in [m] in (b) and (c).

flexibility in parameterization of the profile of interest since it is capable of simulating an arbitrary number of layers. Therefore, it is suitable to be used with snow-covered sea ice profiles which are modelled as a multi-layer medium with rough interfaces. Finally the utilization of the BPT forward solver as a surface scattering model is assumed to be sufficient for our profile of interest since the volume scattering component contributing to NRCS values are negligible. This condition is due to the high permittivity contrast between the first few layers, and also due to the early stage of profile metamorphism that lacks large multifaceted grains or volume scatterers like lens. The very small measured values for NRCS cross polarization components also serve as an indication for this condition. The inverse solver utilizes the Differential Evolution (DE) algorithm [76], in conjunction with an appropriate regularization scheme, to minimize a data misfit cost functional. The DE algorithm is a global optimization method based on the evolution in which only the fittest elements evolve to the next generation. As a global optimization, the DE algorithm calls the forward solver during many iterations and, therefore, the forward solver run-time needs to be very small. The BPT solver is capable of providing this fast run-time through its use of closed-form formulations. The fitness is evaluated based on a cost functional defined as the weighted discrepancy between the measured NRCS value and the simulated NRCS value due to a candidate profile using the BPT. This data misfit cost functional can be written as

$$\mathcal{F}(\chi(\boldsymbol{r})) \triangleq \sum_{n=1}^{N} \sum_{pq=\mathrm{HH,VV}} \kappa_{pq}(\Psi^n_{\mathrm{inc}}, \Psi^n_{\mathrm{scat}}, f) \times \left| \sigma^{\mathrm{meas}}_{pq}(\Psi^n_{\mathrm{inc}}, \Psi^n_{\mathrm{scat}}, f) \; - \; \sigma^{\mathrm{sim}}_{pq}(\chi(\boldsymbol{r}); \Psi^n_{\mathrm{inc}}, \Psi^n_{\mathrm{scat}}, f) \right| \tag{6.1}$$

In (6.1), the superscripts "meas" and "sim" represent measured and simulated NRCS data respectively. The parameter $N$ denotes the number of the measurement (incident) angles. (Herein, $N = 9$ since the incidence angles change from 20° to 60° with the step of 5°.) As can be seen in the summation index of (6.1), only two polarization combinations, namely, HH and VV, are used for this experiment. The reason that the

cross-polarized NRCS data has not been included in the cost functional is associated with the inaccurate prediction of the BPT forward solver for the cross-polarized data due to its inability to take into account more complex monostatic second-order surface scattering and volume scattering events within the dielectric profile. Also, $\Psi^n_{\text{inc}}$ denotes the $n$th incident azimuth and elevation angles and $\Psi^n_{\text{scat}}$ denotes the $n$th scattering azimuth and elevation angles respectively. Note that herein, we consider a monostatic setup; thus, the incident and scattered angles are co-located. The constant $f$ stands for the frequency of operation, which is 5.5 GHz for our C-Band scatterometer. The properties of the profile to be reconstructed are represented by the unknown $\chi$. Finally, the weight $\kappa_{pq}$ in (6.1) is a normalization factor defined as

$$\kappa_{pq}(\Psi^n_{\text{inc}}, \Psi^n_{\text{scat}}, f) \triangleq \frac{1}{\sigma^{\text{meas}}_{pq}(\Psi^n_{\text{inc}}, \Psi^n_{\text{scat}}, f)} \tag{6.2}$$

This inversion algorithm attempts to solve this electromagnetic inverse scattering problem by iterative minimization of (6.1). To handle the instability of the solution associated with this inverse scattering problem, a projection-based regularization scheme is used to stabilize the mathematical formulation [91]. This projection-based regularization limits the search space of the DE algorithm to those values which are reasonable and physically meaningful. This will be explained in more details in Section 6.7.

As will be discussed in Section 6.7, the unknowns to be reconstructed are the salinity, temperature, and density profiles. However, our BPT forward solver requires the knowledge of the dielectric profile to calculate the simulated NRCS data. To handle this, at each iteration of the inversion algorithm, the predicted salinity, temperature and density are fed into semi-empirical formula (see Section 6.5.4) to calculate the slush and sea ice permittivities. This calculated permittivity profile will then be fed to the BPT solver to calculate the corresponding NRCS values.

## *6.7 Use of prior Information in Inversion*

As noted in Section 6.4, the greater the number of measured data points, the more accurate the reconstructed profile. In the research presented in [90], a multiple-frequency (5 frequencies) polarimetric NRCS data set enabled us to reconstruct the snow-covered sea ice profile of SERF accurately. However, the time-series polarimetric NRCS data being considered in this chapter were carried out only at a single frequency of operation; *i.e.*, 5.5 GHz. Of course, a single-frequency scattering data set provides the inversion algorithm with less information compared to a multiple-frequency data. To compensate for this lack of information associated with our single-frequency time-series NRCS data, the following two-step strategy was developed.

### *6.7.1 Parameterization of the unknown properties*

As shown in [90], our inversion algorithm was unable to reconstruct deeper sections of the profile with sufficient accuracy even with the use of a multiple-frequency data set including five frequencies within the C-band. This is partly due to the attenuation of electromagnetic waves at C-band within a lossy dielectric medium. Considering a half space lossy dielectric medium, having a relative complex permittivity of $\epsilon' + j\epsilon''$, the amplitude of the electric field drops off to 36.8% of its surface value after traveling the distance given below [21]

$$\delta = \frac{c_0}{\omega\sqrt{\epsilon'}}\left\{\frac{1}{2}\left(\sqrt{1+\left(\frac{\epsilon''}{\epsilon'}\right)^2}-1\right)\right\}^{-1/2} \tag{6.3}$$

where $c_0$ is the speed of light in vacuum, and $\omega$ is the angular frequency. (For example, for a half space dielectric medium having a permittivity close to that of ice, say,

$3.7 + j0.4$, the value of $\delta$ will be about 8 cm.) Moreover, based on the intrinsic impedance of the profile, surface roughness values, and the incidence angle, only a portion of the incident power makes it into the profile [21], thus, resulting in less penetration. (Of course, the achievable imaging depth is also related to the ability of the radio-frequency receiver of the scatterometer to detect weak scattered signals.)

Based on the above discussion, we do not expect that a single-frequency inversion at the C-band, which is considered in this chapter, can reconstruct these deeper sections. Also, as noted in [90, 125], the permittivity changes in the middle section of the NI is small. Based on this observation and also the limited penetration of the wave deeper in the profile, we assume that the complex permittivity below 6.5 cm is homogeneous in inversion algorithm. (Note that this is assumed to implicitly guide the inversion algorithm that there is minimal scattering contributions received from anywhere below 6.5 cm.) It should finally be mentioned that once the salinity and temperature of upper layers are reconstructed, they can be used to infer the properties of the profile below the imaging depth using thermodynamic models [126]. This is due to the fact that the surface brine volume and temperature changes are a function of the thermodynamic balance between the ocean and the atmosphere.

To be able to compare the reconstruction results with the measured profile parameters obtained by physical sampling, we assume that the profile to be imaged is staircased in the same way as described in Section 6.5.4. The thickness of each layer in the inversion process is taken to be consistent with the one used in the staircasing procedure employed in the physical sampling. This enables us to compare the reconstructed results with the measured ones. Based on this staircasing, the unknowns to be reconstructed will be the salinity and temperature values at the following depths: 0.75 cm, 2.5 cm, 5 cm and 9 cm. Based on our sampling procedure, the actual profile's layers, starting from the top of the profile, are located between 0 to 1.5 cm, 1.5 to 3.5 cm, 3.5 to 6.5 cm, 6.5 to 11.5 cm, etc. Each of these individual layers is then taken to be homogenous.

Therefore, the properties at the middle points of each layer, which will be located at 0.75, 2.5, 5, 9 cm, etc., are chosen as the unknowns to be reconstructed. Since the utilized C-band scatterometer barely sees the profile bellow 6.5 cm (due to having a limited $\delta$, and the overall signal-to-noise ratio of the measured data), we assume the the profile under study is homogeneous for depth bellow 6.5 cm. Thus, based on our labeling protocol explained above, the salinity and temperature at the depth of 9 cm will be the same as those reconstructed from the information of the interface located at 6.5 cm. In addition, the density of the profile at the top layer (*i.e.*, at the depth of 0.75 cm) is the other unknown. Noting that the roughness parameters are assumed to be known, the inversion algorithm is left with 9 real-valued parameters to retrieve. Mathematically speaking, this results in the parameterization of the unknown $\chi$ into a real vector of size 9; *i.e.*, $\chi \in \mathtt{R}^9$. Therefore, the cost functional to be minimized, $\mathcal{F}$, will be a mapping from $\mathtt{R}^9$ to $\mathtt{R}$.

### *6.7.2 Use of time-series data*

Instead of reconstructing the profile independently at each measurement time, we take advantage of the nature of the time-series data as prior information. That is, we use the reconstructed profile at a given measurement time (say, $t_{i-1}$) to provide prior information for the inversion of the NRCS data at the subsequent measurement time ($t_i$). This idea can be extremely helpful for the utilized inversion algorithm. To understand this, the expected variations in the unknown parameters in the whole period of interest have been listed in Table 6.2. (These values are obtained by physical sampling as described in Section 6.5.3.). From this table, it is clear that an independent reconstruction at a given time step (*i.e.*, reconstruction at that time step without using the reconstructed values at the previous time steps) requires the definition of a large search space for both salinity and temperature parameters in the inversion algorithm. For example, the changes in salinity and temperature for the 0.75 cm

layer is 69.3 ppt and 9.24 °C. However, based on our time-series physical sampling, we know that the changes of salinity and temperature for all measurement points between two consecutive measurements (*i.e.*, $t_{i-1}$ and $t_i$), are less than $\pm 7$ ppt and $\pm 4$ °C respectively. Therefore, by knowing the reconstructed parameters at a given time step, the search space for the unknown parameters in the subsequent time step can be significantly reduced. Mathematically speaking, a more limited search space can filter out spurious solutions for this electromagnetic inverse scattering problem, thus, guiding the inversion algorithm toward the correct solution.

Therefore, to reduce the search space significantly and increase the resulting reconstruction accuracy, the retrieved salinity, temperature, and density at time $t_{i-1}$ are used as prior information for the inversion of the NRCS data at time $t_i$. That is, when inverting the NRCS data at time $t_i$, the inversion algorithm looks for parameter values in the proximity of the reconstructed values at the previous time step. The range of this proximity is $\pm 7$ ppt for salinity and $\pm 4^\circ$ C for temperature respectively. The process of limiting the search space of our inversion algorithm is done in two different fronts. First, when the agents of the DE algorithm are distributed, we make sure that they lie within the limited search space. Second, the boundary condition of the DE algorithm also needs to be modified. This is implemented by utilizing a damping boundary condition [76] in the DE algorithm to ensure that each evolved agent stays within both the limits of Table 6.2 and those that are based on prior information from the reconstructed parameters at the previous time step.

As can be seen, this scheme requires the reconstruction of the profile at the first time step (*i.e.*, for $t_i = t_0$) to be sufficiently accurate. (Otherwise, the error in the first reconstruction may propagate to other reconstructions.) To have accurate reconstruction for the first time step, we have at least two options. In the first option, we collect more scattering data only for the first time step; *e.g.*, performing multiple-frequency measurements as presented in [90]. Collecting more scattering data will then result in

*Tab. 6.2:* Salinity and temperature changes for the top four measurement reference points withing the time of interest interval

| $Depth(cm)$ | 0.75 | 2.5 | 5 | 9 |
|---|---|---|---|---|
| $Salinity(max)$ | 86.6 | 60.4 | 20.7 | 11.5 |
| $Salinity(min)$ | 17.3 | 8.2 | 8.2 | 8.3 |
| $Temperature(max)$ | -4.02 | -3.15 | -1.66 | -3.13 |
| $Temperature(min)$ | -13.26 | -11.185 | -10.07 | -7.37 |

accurate reconstruction of the profile at the first time step. The second option uses physical sampling of the profile only at the first time step. In other words, it performs the procedure outlined in Section 6.5.3 only for the first time step. In this chapter, we used the second option. That is, we used physical sampling to extract the properties of the profile at time $t_0$ (11am on January 30th). Using this prior information, we then inverted the single-frequency NRCS data at the next time step $t_1$. Then, the reconstructed profile at $t_1$ was used to invert the NRCS data at time $t_2$. This procedure continued until the NRCS data at all time steps were inverted.

Finally, it should be mentioned that we assume to have no knowledge of the measurement uncertainties corresponding to different data points. When there is no such prior information, the cost function presented in (6.1) implicitly assumes that the measurement noise is identical at each measurement point, and is also uncorrelated. That is, the so-called data covariance matrix [81] is an identity matrix in (6.1).

## *6.8 Results*

As an initial attempt, the inversion algorithm was applied to the time-series data without utilizing the reconstructed profile at the previous time step as prior information for reconstructing the profile at the next time step. Under this condition, the inversion algorithm was not able to converge to an accurate reconstruction. Next, time-series prior information was added to the inversion algorithm. The reconstructed profile

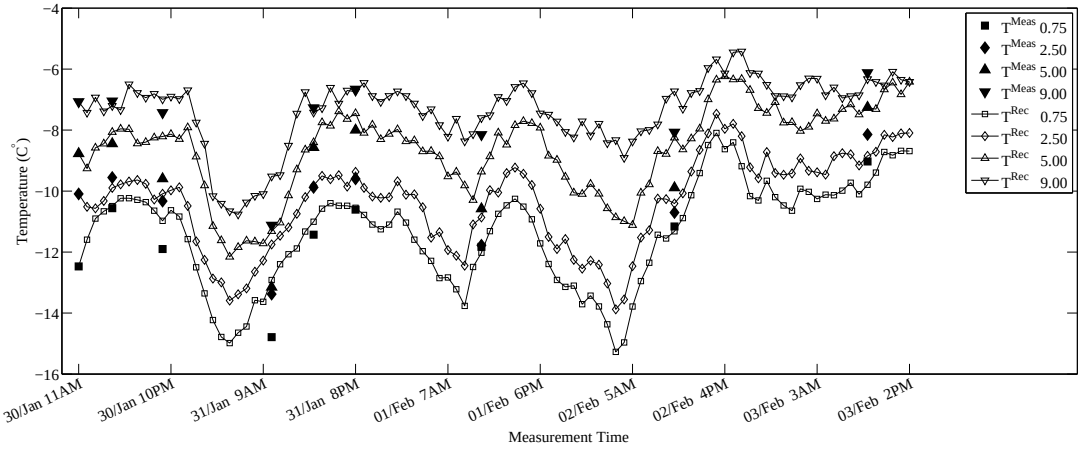


(a)

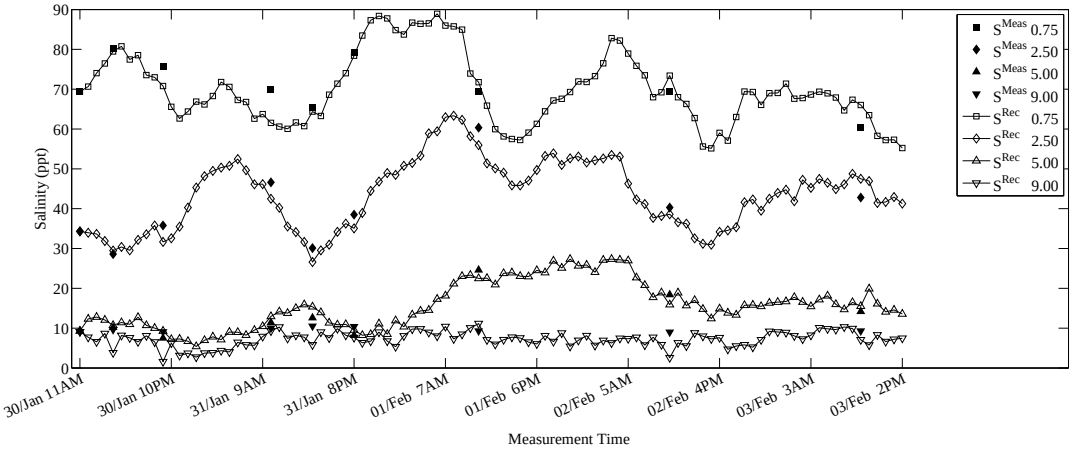


(b)

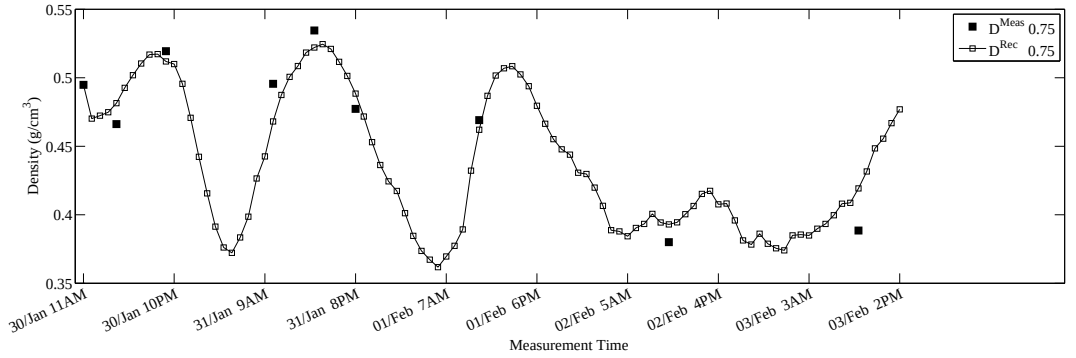


(c)

*Fig. 6.9:* Time-series reconstruction results from January 30th 11am to February 3nd 2pm for the (a) Temperature profile; (b) Salinity Profile; and (c) Top layer (slush) density profile. Depth is given in cm. *Rec* and *Meas* stand for reconstructed and measured data.

for both salinity and temperature at 0.75 cm, 2.5 cm, 5 cm, and 9 cm depth within the profile is shown in Figure 6.9a and b. As can be seen in these two figures, the reconstructed temperature and salinity values, denoted by $T^{Rec}$ and $S^{Rec}$ respectively, are close to the physically measured temperature and salinity values, denoted by $T^{Meas}$ and $S^{Meas}$ respectively. We also note that the density value of the top layer (snow) was also reconstructed by the inversion algorithm. The time-series reconstructed density values, shown in Figure 6.9c, are also close to the measured ones and the diurnal variability of the retrievals make sense physically for a very thin young snow cover over sea ice. The oscillation in the retrieved snow density can be partially due to the performance of the inversion algorithm. It should be noted that the amplitude of this oscillation is small (*i.e.*, 0.15 g/cm$^3$), and might also be reasonably due to the temporal temperature changes of the top layer.

Moreover, to demonstrate the relations between the retrieved temperature and salinity with respect to the complex permittivity of the profile, the temporal reconstructed values at different depths are plotted against the profile's permittivity in Figure 6.10. As can be seen, the temporal changes in permittivity are reduced within the ice as we move deeper into the profile. Also, there is no linear relation between temperature and permittivity at 2.5 cm, while such relations are more evident for other plots. Finally, the average of reconstructed profile's permittivity is $5.22 + j0.31$ with a standard deviation of $1.56 + j0.99$.

To further verify the overall accuracy of the reconstruction results, the following argument is presented. Based on the heat exchange, we expect to see a resemblance between the air temperature variations and the profile's temperature variations. Figure 6.11a confirms this expectation by demonstrating that the variations of the reconstructed temperature at the depth of 0.75 cm follows a similar trend as the variations of the measured air temperature within the time period of interest. Moreover, it is interesting to notice that the local minima/maxima trend of the NRCS data resembles

the temperature variations as shown in Figure 6.11a for the incidence angles of 30°. (Since NRCS variations for different incidence angles are generally similar, as shown in Figure 6.7, hence comparison with only 30° is demonstrated.) Also temperature variations for different depths are similar (with some time delay); thus, the depth of 0.75 cm is only considered in Figure 6.11a.

Another interesting observation is the trend in the order (not exact alignment) of NRCS local minima/maxima occurrences which resembles that of the reconstructed salinity at 0.75 cm (with some time lag), as shown in Figure 6.11b for the incidence angle of 30°. Among several parameters that affect the NRCS data, the complex permittivity of this top layer, due to the presence of slush (highly saline), is an important parameter. The salinity at the depth of 0.75 cm is an important indication of the complex permittivity of this top layer. That's why the effect of its variations is reflected in the time-series NRCS data.

It should be noted that there are a few error sources in the physical sampling of the profile that might affect the measured true parameters. For example, the ice-core extraction is an invasive method which can result in brine leakage from ice cores. Also, once extracted, the ice-core temperature starts decreasing quickly as it has a higher temperature compared to the air temperature. Therefore, a deviation might exist between the actual *in-situ* ice temperature and its measured value from the ice-core. Noting that the reconstructed temperature, in fact, represents the *in-situ* temperature, this might explain some of the discrepancies observed between $T^{Meas}$ and $T^{Rec}$ in Figure 6.9a. Moreover, a few physical sampling sessions took more than one hour, and therefore the measured values in these experiments will represent the average of temperature or salinity for a longer period of time. Finally, it should be noted that the accuracy of the time-series reconstruction is greatly dependent on the accurate measurement of the initial density, salinity, and temperature. To test the resilience of the utilized inversion algorithm with respect to non-accurate initial data,

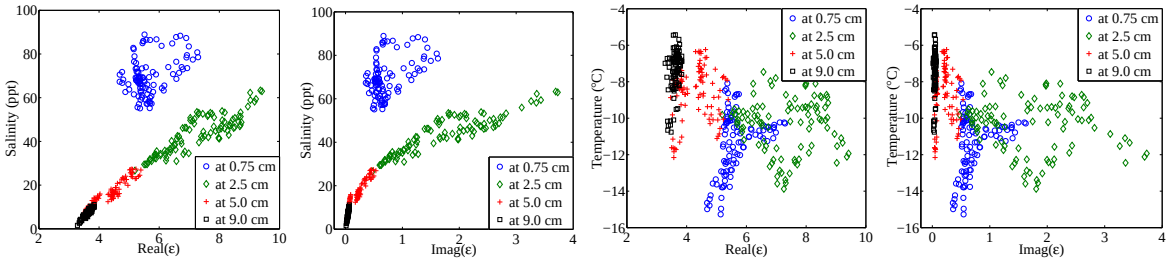


*Fig. 6.10:* The relationship of reconstructed points from 30th of January 11am to 3rd of February 2pm between (a) salinity and real part of the permittivity; (b) salinity and imaginary part of the permittivity; (c) temperature and real part of the permittivity; and (d) temperature and imaginary part of the permittivity. *Real* and *Imag* stand for real and imaginary part respectively.

same percentage of white additive Gaussian noise was synthetically added to each of the measured initial values of density, temperature, and salinity. When the added synthetic noise to the measured initial data exceeded 7%, the inversion algorithm was not able to converge.

## *6.9 Conclusion*

This chapter investigated the time-series NRCS data inversion within the electromagnetic inverse scattering framework for artificially-grown snow-covered sea ice profile reconstruction. In particular, the temperature and salinity of the snow/sea ice profile and the density of the surface slush (wet snow) layer were reconstructed. The reconstruction results matched well with the measured values obtained via physical sampling. The main feature of this inversion algorithm is its ability to use time-series NRCS data to provide prior information for the inversion at different time steps. This prior information is incorporated in the inversion algorithm by limiting the search space associated with the DE algorithm. Enabled by this feature, we were able to quantitatively reconstruct the temperature and salinity profiles of the investigation domain, and observe their evolutions within the time period of interest.

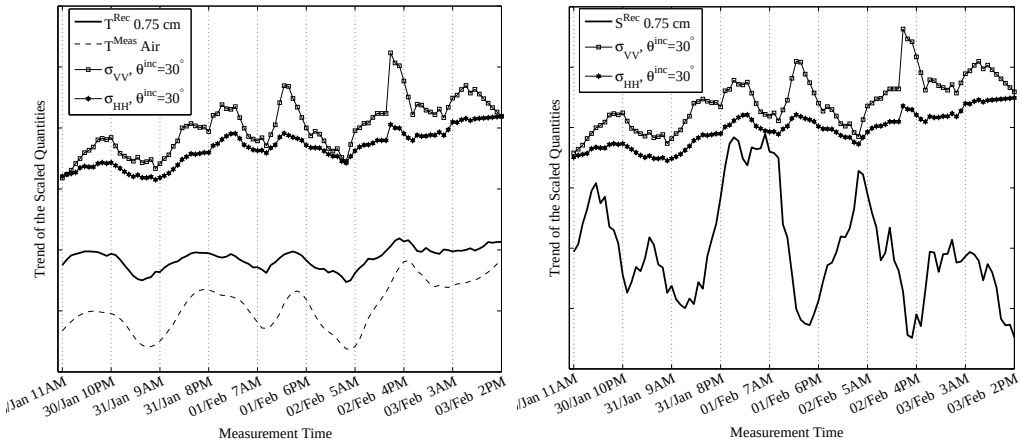


(a) (b)

*Fig. 6.11:* (a) Trend comparison between the reconstructed temperature profile at 0.75 cm and the measured air temperature as well as the measured NRCS at 30°; (b) Trend comparison between the reconstructed salinity profile at 0.75 cm and the measured NRCS at 30°. *Rec* and *Meas* stand for reconstructed and measured data. The vertical axis is not to scale to accommodate comparison of data having different dimensions.

Since the proposed algorithm only utilizes a single-frequency time-series monostatic NRCS data, it has the potential to be extended to time-series SAR data inversion for quantitative monitoring of a given investigation domain. To this end, it needs to be ensured that an accurate retrieval at the first time step is available to the inversion algorithm. In practice, this might be achieved by employing ground truth exploration, or inverting more informative data at the first time step (*e.g.*, the data collected from an air-borne multi-frequency multi-polarization SAR platform).

# 7

# Cambridge Bay Experiment: Enhanced Electromagnetic Modeling for Inversion

## *7.1 Overview*

In previous chapters, I introduced an electromagnetic inverse scattering algorithm that retrieves the parameters of the snow-covered sea ice profile. The input data to the inversion algorithm were the synthetic NRCS data in Chapters 3 and 4, and the experimentally measured NRCS data collected at the SERF using a C-band scatterometer in Chapters 5 and 6. Furthermore, various techniques were utilized and developed to enhance the reconstructions. These include the use of ($i$) more sensitive NRCS data with respect to the problem unknowns, ($ii$) multi-frequency NRCS data, ($iii$) temporal reconstruction, ($iv$) further parametrization, and ($v$) various prior information. In this chapter, the profile reconstruction of the first-year snow-covered sea ice utilizing an enhanced inverse scattering algorithm is presented. The measurements were carried out

in Cambridge Bay, Nunavut, located within the Arctic Circle. The data to be inverted are the combination of the NRCS data collected by an on-site C-band scatterometer, and the radarsat-2 SAR satellite. Furthermore, a profile averaging technique is introduced that reduces the number of problem unknowns. Finally, the forward solver utilized in conjunction with the inversion algorithm is enhanced to consider the effects of the so-called volume scattering.

This chapter is structured as explained below. The background of the research and the problem statement are presented in Section 7.2. In Section 7.3, the measurement procedure is described. The experiments were carried out during May 2014 in Cambridge Bay, located in the Canadian High Arctic. The measurements include (*i*) the temporal physical sampling of snow and sea ice, (*ii*) time-series single-frequency monostatic NRCS data collection through an on-site C-band scatterometer over a period of one month, (*iii*) cross-sectional single-frequency monostatic NRCS data collection through radarsat-2 satellite in different days, and (*iv*) laser scans of the air-snow interface utilizing a lidar for roughness parameter estimation.

As previously discussed in Chapter 2, our inversion algorithm consists of a forward and an inverse solver. Forward solver attempts to model the electromagnetic scattering fields associated with the irradiated rough multi-layered dielectric profile. The BPT forward solver utilized in the previous chapters considers homogenous layers, assuming each of which has an effective permittivity; *i.e.*, only the so-called surface scattering component is considered in NRCS calculation. In the case of the snowpack under investigation in this chapter, large snow grains in the brine-wetted dry snow layers contribute to the so-called volume scattering component (not considered in the BPT formulation used in the previous chapters). Therefore, in this chapter, a volume scattering model is developed and added to the current BPT surface scattering model to predict the NRCS of the profile more accurately. This model is a variation of the existing heuristic single scattering cloud-model that is modified to

consider multiple reflections in a multi-layered medium. The utilized forward scattering model is introduced in Section 7.4. In Appendix C, the ray-tracing technique is used for a single-layer medium to put the formulas associated with the forward solver introduced in Section 7.4 into perspective. The implementation of this forward solver significantly improved the agreement between the experimentally measured and the simulated NRCS data.

The inversion algorithm employed to retrieve the profile parameters through electromagnetic inverse scattering is briefly explained in Section 7.5. This is followed by the description of the inversion strategy in Section 7.6. This strategy includes the parametrization of the snow-covered sea ice and profile averaging. The former leads to the formation of the vector of unknown whose dimension is reduced through the utilization of prior information. In the case of profile averaging, it should be noted that the snow-covered sea ice profile under investigation is considered to change minimally within the period of interest during the temporal measurements. Therefore, an averaging technique is utilized to represent the snow-covered sea ice by a single profile during the period of interest. The reconstructed profiles through this framework are presented in Section 7.7. Three inversion scenarios are considered in this section based on the NRCS data set to be inverted. These scenarios include the NRCS data collected by the (*i*) satellite, (*ii*) scatterometer, and (*iii*) satellite and scatterometer. Based on the reconstruction accuracy in each scenario, it is concluded that increasing the number of measurement points (*e.g.*, data provided by satellites with higher re-visit rates) can improve the retrieval accuracy. Finally, a conclusion in Section 7.8 summarizes the findings in this chapter.

The materials of this chapter are based on the paper accepted for publication in IEEE Journal of Selected Topics in Applied Earth Observations and Remote Sensing [127][(1)].

[(1)] © [2016] IEEE. Reprinted, with permission, from N. Firoozy, P. Mojabi, J. Landy, and D. Barber, "Landfast First-Year Snow-Covered Sea Ice Reconstruction via Electromagnetic Inversion," *Selected Topics in Applied Earth Observations and Remote Sensing, IEEE Journal of*, 2016, *Early Access*.

## *7.2 Introduction*

To extract a profile's parameters of interest, say the complex permittivity profile of the snow-covered sea ice, from the measured scattering data, an inverse scattering algorithm is needed to work in conjunction with an appropriate forward scattering model so as to reconstruct (retrieve) these parameters. The final choice of a specific forward model depends greatly on the profile under investigation. The choice of inverse scattering algorithm also affects the choice of the forward model. For instance, although full-wave forward solvers are generally the most accurate methods, they require the discretization of the snow-covered sea ice profile, which results in large matrices due to the large electrical size and roughness associated with the profile, thus, being computational expensive. Since inverse scattering algorithms are often iterative techniques to handle the nonlinearity of the associated mathematical problem, they require the call of the forward solver at each iteration, which might not be practical if the forward solver is computationally expensive. Furthermore, since the number of measured data points in the arctic microwave remote sensing application is limited and the measured data are often amplitude-only (phaseless), the profile under investigation cannot be reconstructed with too many detailed features. Thus, the forward solvers that rely on knowing subwavelength properties of the profile may not be even practical for this application.

Previously, we have developed an inverse scattering (inversion) algorithm utilized to reconstruct the snow-covered sea ice dielectric profile from the simulated normalized radar cross section (NRCS) data [91]. This algorithm was then successfully applied to the measured NRCS data collected at the sea ice environmental research facility at the University of Manitoba. Specifically, in [90], we showed that the use of multiple-frequency NRCS dataset can provide sufficient information for accurate reconstructions. Also in [89], reconstruction was achieved through a time-series measurement

and utilization of the retrieved profile at each time step as prior information for reconstruction at the next time step. In all of these previous works, the boundary perturbation theory (BPT) [94] was used as our forward solver. The use of this forward solver, which does not take into account the volume scattering phenomena within each layer of the profile, was justified since the volume scattering effect within those profiles were negligible compared to surface scattering arising from the rough layered medium. In [128], we applied this inversion algorithm to the measured NRCS data collected at Cambridge Bay, Canada. However, the reconstruction results were not successful due to the fact that the volume scattering component was not negligible anymore. Herein, we improve our inversion algorithm by advancing our forward solver to take into account the volume scattering as well as the cross-polarized surface scattering components. We then apply this inversion algorithm to the monostatic NRCS data collected by radarsat-2 satellite, on-site C-band scatterometer, and the combination thereof to reconstruct the temperature, salinity, density, and snow grain size associated with landfast snow-covered sea ice in Cambridge Bay, Canada. (As will be described below, the measurements were performed in May 2014.) The world-map and magnified view of the measurement area is shown in Figure 7.1. Finally, it should be noted that this chapter is a contribution to the J-STARS Special Issue based on our conference paper presented at the IGARSS 2015 [128]. Throughout this chapter, a time-dependency of $\exp(-j\omega t)$ has been implicitly assumed.

## *7.3 Measurements*

The measurement process consisted of four main components. The first component was the in-situ physical sampling of the snow and ice. The time-series polarimetric monostatic NRCS measured data, which were collected by utilizing an on-site C-band scatterometer, was the second component. The third component was the satellite imagery of the measurement area. The last component was the in-situ lidar scans of

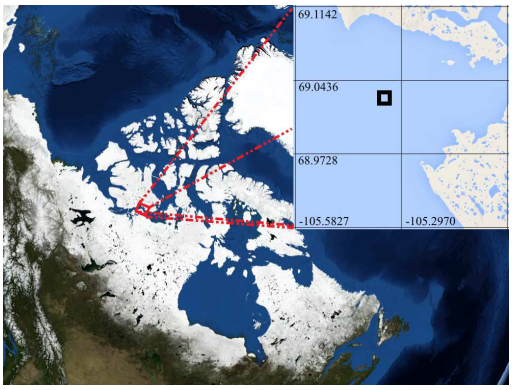


*Fig. 7.1:* The measurement location (black square) at Cambridge Bay, Nunavut, Canada, both on a world-map and a magnified view.

the snow surface which were used to extract the roughness parameters of the air-snow interface. As will be described later, the physical sampling and lidar data are used either as prior information to the inversion algorithm, or for reconstruction accuracy assessment. The measured NRCS data are then utilized as the input to the inversion algorithm to retrieve the parameters of interest.

### *7.3.1 Physical sampling*

A series of physical sampling of snow and ice was carried out in Cambridge Bay, Nunavut, Canada, starting 12th of May 2014, and with continuous measurements from 20th to 28th of May 2014. In each physical sampling session, snowpack temperature and density were measured with a resolution of 2 cm. To later estimate the snow grain size at different depths, we spread the snow over a grid and took photos for visual assessment; see Figures 7.2. The snow samples were eventually melted to measure the bulk salinity of the snow at different depths of the profile. Ice cores were also extracted each time. After drilling holes in each core at every 5 cm (except for the first two points that have a 2.5 cm spatial resolution), a temperature probe was utilized for temperature profiling of the ice. Next, the ice core was cut in blocks with a thickness of 5 cm (except for the top 5 cm which was cut into two 2.5 cm blocks). These ice

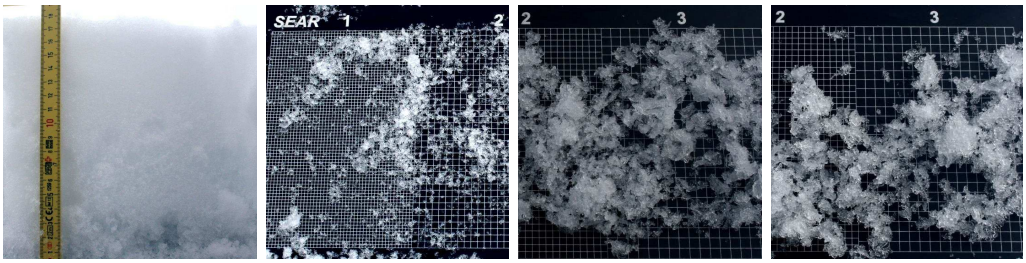

(a) Snow Profile (b) New snow layer (c) Original snow layer (d) Basal snow layer

*Fig. 7.2:* Snowpack on May 22nd, 2014 at 4 pm.

samples were later carried to the laboratory, and were then melted to measure their bulk salinity. The temporal in-situ measured temperature, salinity, and density of the profile are shown in Figure 7.3 to Figure 7.5 from 20th of May to 28th of May, with two or three times sampling carried out daily, usually at 9 am, 4 pm, and 10 pm.

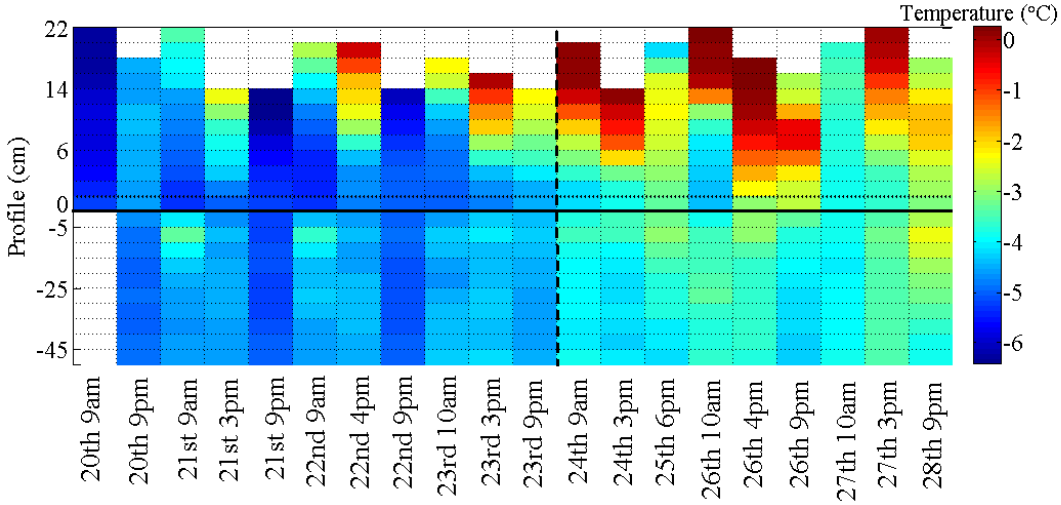


(a) Temperature profile

*Fig. 7.3:* Physical sampling data (temperature) from 9 am on May 20th, 2014 to 9 pm on May 28th, 2014. The solid horizontal line (*i.e.*, $y = 0$ line) is the snow-ice interface and the vertical dashed line mark the measurements performed at 6 pm on May 25th, 2014.

### *7.3.2 Scatterometer measurements*

Time-series monostatic polarimetric C-band NRCS measurements were carried out from May 20th to May 28th, 2014. To achieve the minimum recommended height

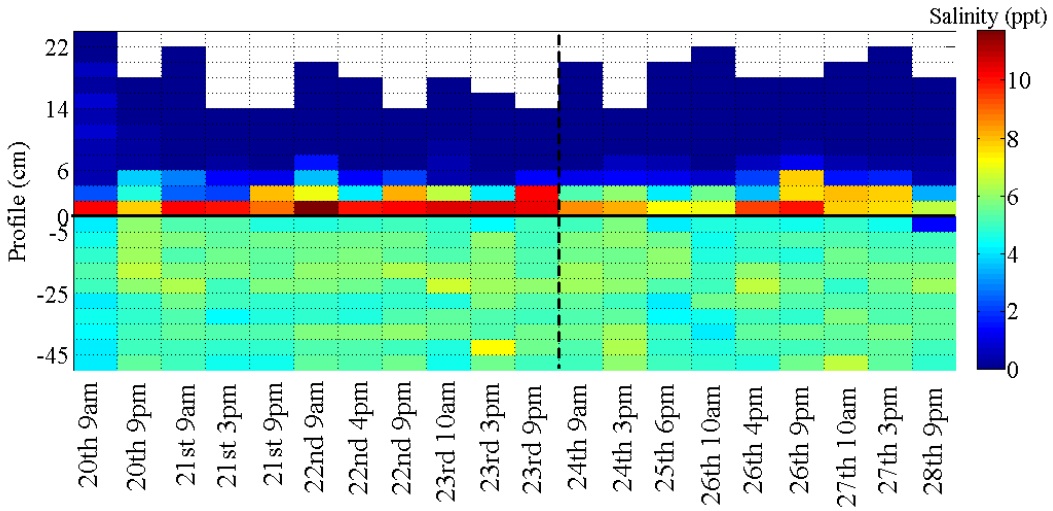


(a) Salinity profile

*Fig. 7.4:* Physical sampling (salinity) data from 9 am on May 20th, 2014 to 9 pm on May 28th, 2014. The solid horizontal line (*i.e.*, $y = 0$ line) is the snow-ice interface and the vertical dashed line mark the measurements performed at 6 pm on May 25th, 2014.

for scatterometer measurements, a setup was constructed to mount the equipment on, as shown in Figure 7.6 (a). A near-field to far-field correction factor were applied to obtain the far-field scattered wave [129]. Also, to reduce the effect of random noise, the NRCS data measured within each hour were averaged into a single NRCS data point per hour. The scatterometer measured the NRCS for the incidence angles ranging from 20° to 65° with 5° intervals in the elevation plane. Also for each incidence angle, the scatterometer swept 30° in azimuth plane and averaged the measured scattered field. This technique helps reduce the effects of local profile inhomogeneity at each incidence angle on the measured NRCS. The measured NRCS data were later calibrated against the calibration data collected from a metallic trihedral in the field as depicted in Figure 7.6 (b). Further details on this calibration procedure can be found in [129]. The excellent channel isolation of the scatterometer (greater than 30 dB) allows a single object calibration, resulting in equal values for $\sigma^{\mathrm{HV}}$ and $\sigma^{\mathrm{VH}}$. The noise floor of the scatterometer system is measured at $-40$ dB. The measured co-polarized NRCS data for select incidents are shown in Figure 7.7. The gaps in the time-series data represent no measurement periods due to either logistic (*e.g.*, generator failure) or

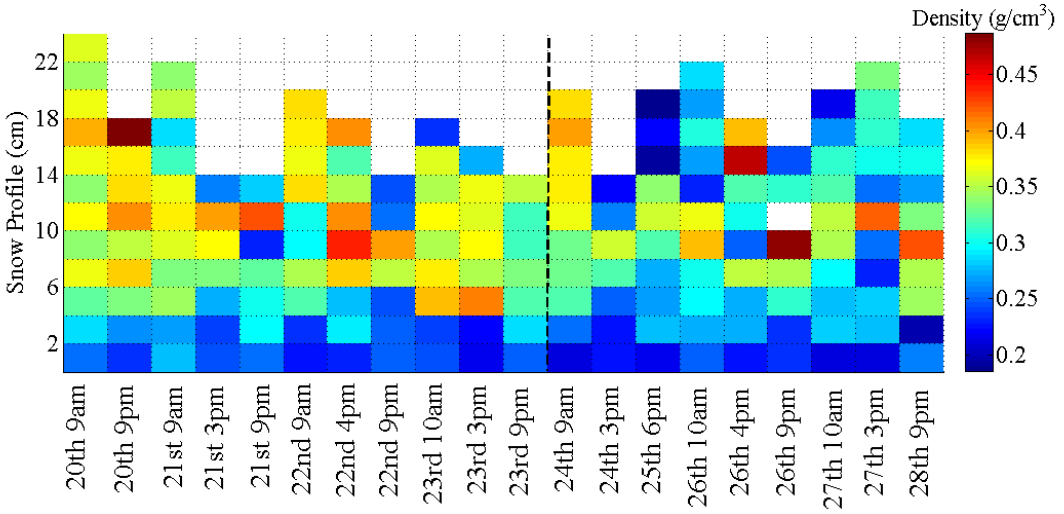


(a) Snow density profile

*Fig. 7.5:* Physical sampling (density) data from 9 am on May 20th, 2014 to 9 pm on May 28th, 2014. The horizontal line $y = 0$ is the snow-ice interface and the vertical dashed line mark the measurements performed at 6 pm on May 25th, 2014.

environmental obstacles (*e.g.*, whiteout periods). From the NRCS trend in Figure 7.7, the NRCS measurement period can be divided into two main periods: (1) 9 am on May 20th to 4 pm on May 24th when the measured NRCS was stable and almost constant for each incidence angle, and (2) 5 pm on May 25th to 12 am on May 28th in which the measured NRCS data started to change rapidly, went through an unstable period, and then seemed to stabilize again. In the first period, no significant meteorological events occurred during the NRCS measurements, and the NRCS data were stable, thus, being appropriate to be used in our model-based inversion algorithm. On the other hand, from the beginning of the second period, a short series of drizzle, snow, and ice pellet occurred. These events seemed to have altered the snow-covered sea ice profile, thus, resulting in a complex NRCS behavior in the second period. To be more specific with respect to the observed physical changes in the profile, the average temperature of the snowpack increased and the density showed a more erratic nature. Consequently, the measured NRCS was not constant anymore, but experienced sudden variations for both channels that might be related to daily melt and freeze of the snowpack due to warmer conditions approaching the end of May.

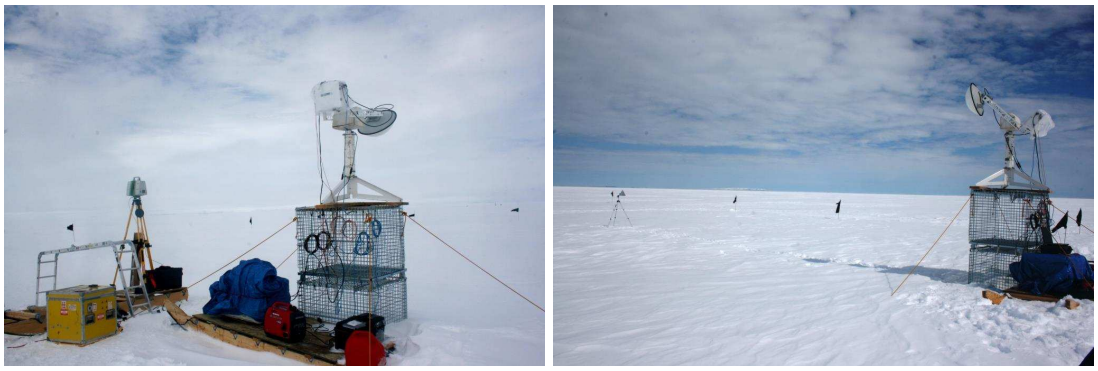

(a) (b)

*Fig. 7.6:* On-site measurements of snow-covered sea ice at Cambridge Bay, Nunavut. (a) Scatterometer NRCS measurement along side lidar on 23rd of May, 2014, (b) Scatterometer calibration using a metallic trihedral on 28th of May, 2014.

### *7.3.3 Satellite imagery*

We also obtained the NRCS data of the snow-covered sea ice under investigation from the ScanSAR Wide Beam mode (dual HH–HV polarization) images of SAR Georeferenced Fine type from the Canadian radarsat-2 (active SAR operating in the C-band). The images are available for various days within May 2014, but the selected dates are the 3rd, 4th, 11th, 17th, 18th, 24th, and 25th for the reasons to be explained later. To extract the NRCS from the satellite images, they were first calibrated. Then, to reduce the speckle noise and yet retain the NRCS value integrity, a simple mean-box filter was applied to the images. As an example, Figure 7.8 shows the processed products for 17th and 18th of May, with measurement location within the yellow rectangular. The ScanSAR images were zoomed in and cropped out in the vicinity of Cambridge Bay for a better view of the measurement location.

### *7.3.4 Lidar measurements*

A lidar laser scanner was employed on the measurement site to scan the height topography of the air-snow surface on the 23rd of May. These collected data were later

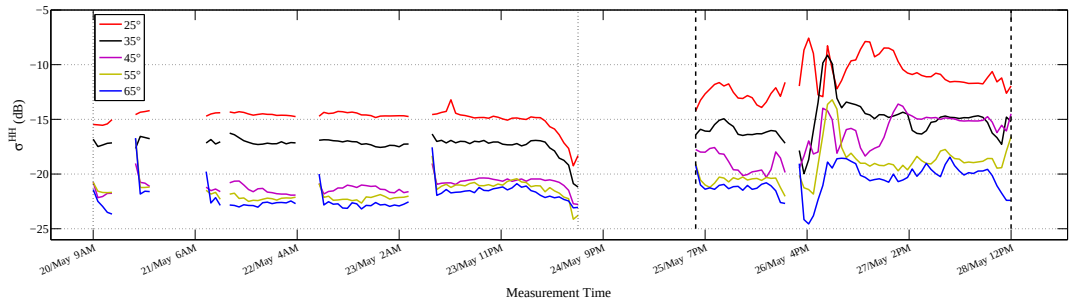


(a) HH polarization

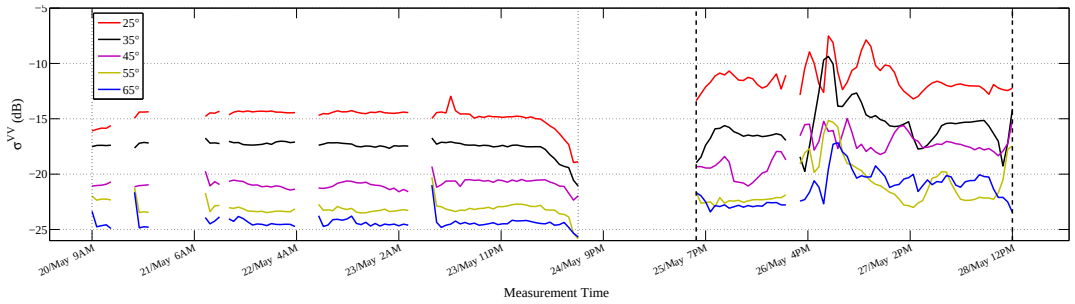


(b) VV polarization

*Fig. 7.7:* Measured time-series NRCS data (denoted by $\sigma$) at 5.5 GHz. The vertical lines represent (*i*) first period from 9am on May 20th to 4pm on May 24th, (*ii*) measurement halt from 4pm on May 24th to 5pm on May 25th, and (*iii*) second period of NRCS measurement from 5pm on May 25th to 12am on May 28th.

utilized to calculate the roughness parameters of rms height and correlation length as shown in Figure 7.9 and reported in Table 7.1. As can be seen in this table, two sampling interval grids were used for the extraction of the roughness parameters. The average of these two different sets of roughness parameters will be provided to the inversion algorithm as prior information. The procedure to calculate these roughness parameters is as follows. We first corrected for the offset between scatterometer and lidar position. Then, we filtered out anomalous returns (*e.g.*, due to precipitation, blowing snow, or multi-path reflections). Then, we selected subsections of the scan area using $0.5 \times 0.5$ m$^2$ moving window with one section every 0.2 m along each radial scat profile for scatterometer looking angles of 25° to 60°. It should be noted that the size of this window is approximately equal to the scatterometer footprint on the snow surface. Each subsection was detrended using a FFT-based algorithm to remove

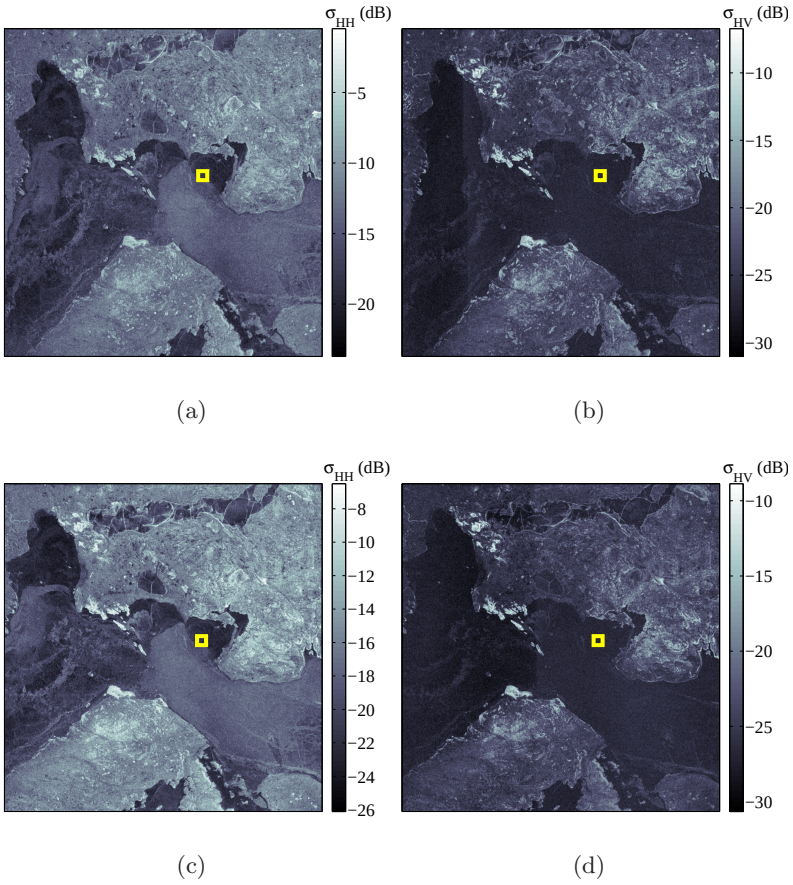


*Fig. 7.8:* Radarsat-2 ScanSAR images cropped around Cambridge Bay area (approximately 115 × 115 $km^2$). The measurement area is marked by the yellow rectangles. (a) May 17th, HH Polarization. (b) May 17th, HV Polarization. (c) May 18th, HH Polarization. (d) May 18th, HV Polarization. Radarsat-2 Data and Products MacDonald, Dettwiler and Associates Ltd. 2014 - All Rights Reserved. Radarsat is an official mark of the Canadian Space Agency.

low-frequency topography which does not affect surface scattering of the radar but biases the calculation of the roughness parameters. Next, we calculated the rms height and correlation length within each subsection using the method applied in. We then averaged those values for each inclination angle. Finally, we adjusted the roughness parameters using calibration functions [130].

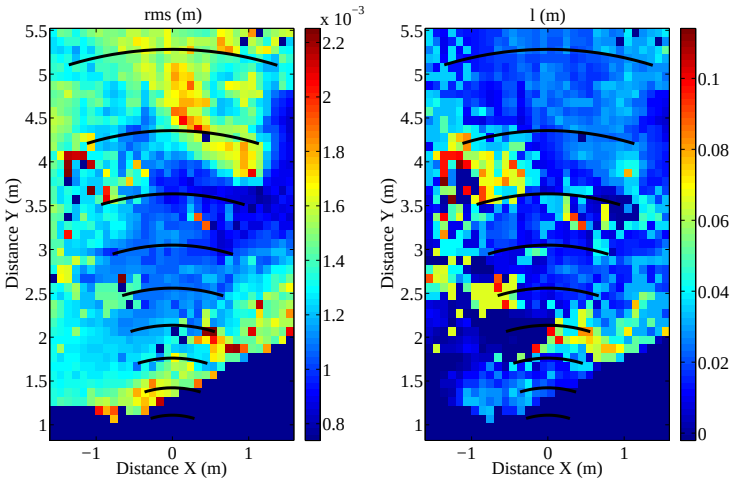


(a) (b)

*Fig. 7.9:* Lidar scan of the snow-covered sea ice profile measured through scatterometer on May 23rd. (a) The calculated rms height. (b) The calculated correlation length. The black arcs represent the scanning path of scatterometer.

*Tab. 7.1:* The rms height, $h$, and correlation length, $l$, for the air-snow rough interface for different incidence angles $\theta$. The subscripts 1 and 2 denote two different sampling intervals having 0.2 cm and 0.5 cm grids respectively. NA refers to not available data.

| $\theta^\circ$ | 20 | 25 | 30 | 35 | 40 | 45 | 50 | 55 | 60 | 65 |
|---|---|---|---|---|---|---|---|---|---|---|
| $h_1$ *(cm)* | NA | 0.16 | 0.13 | 0.10 | 0.10 | 0.10 | 0.10 | 0.14 | 0.15 | NA |
| $l_1$ *(cm)* | NA | 2.6 | 1.7 | 2.6 | 2.3 | 2.4 | 2.8 | 3.1 | 2.0 | NA |
| $h_2$ *(cm)* | NA | 0.15 | 0.13 | 0.10 | 0.10 | 0.10 | 0.10 | 0.14 | 0.14 | NA |
| $l_2$ *(cm)* | NA | 2.8 | 2.2 | 1.9 | 1.2 | 2.3 | 2.5 | 3.4 | 2.4 | NA |

## *7.4 Forward Solver*

As noted earlier, our inversion algorithm requires the use of an electromagnetic forward scattering solver. The role of this solver is to calculate the scattered field or scattering parameters associated with a profile that is illuminated by an incident field. (This profile is, in fact, the predicted profile at each iteration of the inversion algorithm.) Herein, the scattering parameter of interest is a phaseless quantity known as the normalized radar cross section (NRCS), denoted by $\sigma^{p/q}$. From one perspective, the scattered field from a rough layered profile, and consequently its NRCS, consists of

two main components that are due to the so-called surface and volume scattering, each containing coherent and incoherent components [131,132]. Surface scattering is related to the interfaces between homogenous layers with different dielectric values, and volume scattering is related to the effects of the individual scatterers within each layer. Therefore, the total NRCS for rough layered media may be written as summation of surface and volume scattering contributions [133]

$$\sigma_{\text{tot}}^{p/q} = \sigma_s^{p/q} + \sigma_v^{p/q} \tag{7.1}$$

where the subscripts $s$ and $v$ denote the surface and volume scattering components. Also $p/q$ denotes $p$-sent and $q$-received polarizations where $p$ and $q$ represent vertical or horizontal polarizations. In what follows, we first introduce the method applied to calculate the surface scattering component. The calculation of the volume scattering component will then follow. For the discussion presented below, it is assumed that we have a rough multi-layered medium consisting of $(N+1)$th layers, numbered from 0 to $N$. As a result, we will have $N$ interfaces, numbered from 0 to $(N-1)$. The layer 0 is consider to be the measurement half space, which is air. The layer $(N+1)$ is considered to be the termination layer, which is also a half space. The $z$ direction is assumed to be perpendicular to the layers' interfaces. Finally we define a number of parameters. $k_0$ is the wavenumber in free space, $h_m$ is the rms height, and $l_m$ is the correlation length associated with the roughness of the $m$th interface.

### *7.4.1 Surface scattering*

To calculate the co-polarized component of the surface scattering $\sigma_s^{pp}$ of a multi-layered media with rough interfaces, the boundary perturbation theory (BPT) is utilized. We now present the calculation procedure for the cross-polarized component of the surface scattering.

#### *7.4.1.1 Cross-polarized component*

The BPT is a first-order approximation solution. Therefore, the cross-polarized NRCS calculated through the BPT will be zero in a monostatic configuration [94]. Since we are planning to use the measured cross-polarized NRCS data in our inversion, the following procedure is considered to estimate the cross-polarization component $\sigma_s^{pq}$. To this end, we first start by noting that the cross-polarized NRCS of a rough interface between two half spaces, the first one being air and the second one being a dielectric medium having a complex permittivity of $\epsilon_1$, can be obtained as [134]

$$\sigma_s^{pq,(0)} = \frac{S(\theta_0)k_0^4}{8\pi}\int\int\Bigg[\sum_{f=1}^{\infty}\sum_{l=1}^{\infty} e^{-2k_{z0}h_0^2}\times \frac{k_{z0}h_0^{2f+l}}{f!l!}S(\theta_0)|F_{pq}^{(0)}(v,\phi)|^2 W_0^{(f)}W_0^{(l)}\Bigg]d\phi dv. \tag{7.2}$$

In (7.2), the general form of $F_{pq}$ can be found in [134, 135]. Furthermore, for $S$, a Smith shadowing function is considered to calculate the back-scattering [136].

The next step will be how to adapt the above relation, which considers two half spaces, to a multi-layered medium. To this end, we treat the layers $m$ and $(m+1)$ as two half spaces with a rough interface. Using (7.2), we then calculate its corresponding $\sigma_s^{pq,(m)}$. We will then use the concept of the generalized transmission coefficients [137] to transfer this $\sigma_s^{pq,(m)}$ to the measurement half plane (air, or the 0th layer). As will be seen below, we will utilize two generalized transmission coefficients; namely, $\mathfrak{T}_{0|m}^{p}$ and $\mathfrak{T}_{m|0}^{q}$. The first one is utilized to bring the power down to the outset of $m$th layer, and the second one is used to transfer the power from the outset of $m$th layer to the measurement half space (the 0th layer). We then incorporate the effect of loss within the $m$th layer into the formulation through the complex wavenumber of this medium. Finally, the summation of all the transferred components from each interface to the measurement half-plane results in the total cross-polarized surface

NRCS. It should be noted that this proposed procedure provides an approximation for the cross-polarized surface scattering for multi-layered medium, and is not an exact solution. Also, in [134], the coefficients $F_{pq}$ are provided for an air-dielectric interface. To adapt this formulation to our problem, these coefficients were slightly modified to accommodate a dielectric-dielectric interface.

To put the above discussion into mathematical formulation, the approximated cross-polarized surface scattering can be written as

$$\sigma_s^{pq} = \sum_{m=0}^{N-1} |e^{jk_{zm}\Delta_m}|^4 |\mathfrak{T}_{0|m}^p|^2 |\mathfrak{T}_{m|0}^q|^2 \sigma_s^{pq,(m)} \tag{7.3}$$

where $\sigma_s^{pq,(m)}$ can be found from (7.2) by substituting the 0th and 1st layers with the $m$th and $(m+1)$th layers. In (7.3), $\mathfrak{T}_{m|0}^q$ is calculated based on $\mathfrak{T}_{0|m}^p$ using the reciprocity of the generalized transmission coefficient, as brought in [138]. Also, $\mathfrak{T}_{m|m}^{p/q} = 1$, and $\Delta_m$ is the thickness of the $m$th layer ($\Delta_0$, which corresponds to the measurement half space, is taken to be zero). Finally, $k_{zm} = k_m \cos\theta_m$ where the angle $\theta_m$ is the refraction angle in the $m$th layer with respect to nadir assuming a flat interface, and $k_m$ is equal to $k_0$ for $m = 0$, and is equal to $k_0\sqrt{\epsilon_m}$ otherwise. Finally, we note that the generalized transmission coefficients, $\mathfrak{T}$, can be obtained as [137, 138]

$$\mathfrak{T}_{0|m}^p = \frac{\exp\left[j \sum_{n=1}^{m-1} k_{zn}\Delta_n\right] \prod_{n=0}^{m-1} T_{n|n+1}^p}{\prod_{n=1}^{m} \left[1 + R_{n-1|n}^p \mathcal{R}_{n|n+1}^p e^{j2k_{zn}\Delta_n}\right]} \tag{7.4}$$

where $\mathcal{R}$ is the generalized reflection coefficient that is recursively calculated [138], and $R$ and $T$ are the Fresnel reflection and transmission coefficients.

As can be seen, the above procedure for estimating the cross-polarized surface scattering NRCS does not take into account the presence of surface roughness. This is as opposed to the co-polarized surface scattering component calculated by the BPT that

does take into account the presence of rough surfaces. In an attempt to incorporate the effect of surface roughness into cross-polarized surface scattering NRCS estimation, we substitute the Fresnel field reflection coefficient in (7.4) with the following coherent field reflection coefficient based on [139]

$$R^{p,\mathrm{coh}}_{n|n+1} = R^{p}_{n|n+1} e^{-2(k_n h_n \cos\theta_n)^2} \tag{7.5}$$

By considering this assumption, which is usually referred to as the quasi-specular reflection, the mechanism of reflection will be the same as Fresnel reflection, but the attenuation factor $e^{-2k_n^2 h_n^2 \cos^2\theta_n}$ will incorporate the loss due to the roughness of the interface. Similarly, we substitute the Fresnel field transmission coefficient in (7.4) with the following coherent field transmission coefficient based on [140]

$$T^{p,\mathrm{coh}}_{n|n+1} = T^{p}_{n|n+1} e^{-2\left(0.5 k_n h_n \left|\sqrt{\epsilon_n}\cos\theta_n - \sqrt{\epsilon_{n+1}}\cos\theta_{n+1}\right|\right)^2} \tag{7.6}$$

Finally, we note that the utilization of the generalized transmission coefficients instead of Fresnel transmission coefficients allows us to take into account the multiple reflections due to the layered nature of the profile. This concludes our discussion on the calculation of the co-polarized and cross-polarized NRCS due to surface scattering.

### *7.4.2 Volume scattering*

Let's now consider how the volume scattering component of the NRCS is estimated in this work. To calculate $\sigma_v^{pp}$, the volume scattering in each layer, $\sigma_v^{pp,(m)}$, is approximately calculated, and then transferred into the measurement half-space (*i.e.*, air) using a similar procedure explained in the previous section as

$$\sigma_v^{pp} = \sum_{m=1}^{N-1} |\mathfrak{T}^{p}_{0|m}|^2 |\mathfrak{T}^{p}_{m|0}|^2 \sigma_v^{pp,(m)}. \tag{7.7}$$

It should be noted that the above formulation assumes that the volume scattering occurs in the layers sandwiched between the two half spaces, and not the half spaces themselves. The volume scattering $\sigma_v^{pp,(m)}$ within each layer $m$ is calculated by a heuristic single scattering model, which is equivalent to a single scattering radiative transfer model as [27, 119]

$$\sigma_v^{pp,(m)} = \sigma_{v1}^{pp,(m)} + \sigma_{v2}^{pp,(m)} + \sigma_{v3}^{pp,(m)} \tag{7.8}$$

where $\sigma_{v1}^{pp,(m)}$, $\sigma_{v2}^{pp,(m)}$, and $\sigma_{v3}^{pp,(m)}$ are due to the direct volume contribution of particles (*e.g.*, ice or brine inclusions), particle-interface interactions, and interface-particle-interface interactions respectively. To calculate $\sigma_{v1}^{pp,(m)}$, a cloud model is utilized as [27]

$$\sigma_{v1}^{pp,(m)} = \sigma_V^{pp,(m)} \times \left| \frac{\cos\theta_m}{2\kappa_m}(1 - (\mathfrak{L}^{(m)})^2) \right| \tag{7.9}$$

In (7.9), $\mathfrak{L}^{(m)}$ is the power loss factor, and $\kappa_m = 2\mathrm{Im}\{k_m\}$ is the extinction coefficient approximated as inverse of the half of the skin-depth as [141]

$$\kappa_m = 2\frac{\omega}{c}\left\{ \frac{1}{2}\left(\sqrt{1 + \left(\frac{\epsilon_m''}{\epsilon_m'}\right)^2} - 1\right) \right\}^{1/2} \tag{7.10}$$

Furthermore in (7.9), $\sigma_V^{pp,(m)}$ is the volume back-scattering coefficient defined as [119]

$$\sigma_V^{pp,(m)} = \sum_{i=1}^{U} N_i \sigma_{bi} = \sum_{i=1}^{U} \frac{V_i}{\frac{4}{3}\pi r_i^3} \times \sigma_{bi} \tag{7.11}$$

In (7.11), $U$ is the number of different types of spherical scatterers within each layer of snow (*e.g.*, water, brine, ice particles, etc.), and $N_i$ is the number of scatterer of type $i$. Moreover, $r_i$ is the radius of a single scatterer and $V_i$ is its respective volume fraction [142]. Also, $\sigma_{bi}$ is the scattering cross section of a single scatterer, and can be

calculated as [143]

$$\sigma_{bi} = \begin{cases} \frac{64\pi^5 r_i^6}{\lambda_o^4} |\frac{\epsilon_i - \epsilon_b}{\epsilon_i + 2\epsilon_b}|^2 & |k_i r_i| \ll 1 \\ \frac{2\pi}{k_i^2} \sum_{n=1}^{\infty} (2n+1)(|a_{(n),i}|^2 + |b_{(n),i}|^2) & \text{Otherwise} \end{cases} \tag{7.12}$$

In (7.12), $\epsilon_i$ and $\epsilon_b$ are the permittivity values of the scatterer and its background respectively. Depending on the size of each scatterer, we either use the Rayleigh approximation (*i.e.*, the first condition) or the Mie scattering (*i.e.*, the second condition) in (7.12). The unknown coefficients $a_{(n),i}$ and $b_{(n),i}$ are defined in [27, 143], and are calculated recursively.

Next, the particle-interface contribution, $\sigma_{v2}^{pp,(m)}$, is calculated as [27]

$$\sigma_{v2}^{pp,(m)} = \sigma_V^{pp,(m)} \times \left| 4\Delta_m (\mathfrak{L}^{(m)})^2 (R^p_{m|m+1})^2 \right|. \tag{7.13}$$

We note that in (7.13), we use the quasi-specular reflection assumption; *i.e.*, (7.5) is used to calculate the reflection coefficient.

The last volume scattering component in (7.8), $\sigma_{v3}^{pp,(m)}$, considers a double reflection from the bottom interface and double loss for the direct volume contribution as [27]

$$\sigma_{v3}^{pp,(m)} = \sigma_V^{pp,(m)} \times \left| \frac{\cos(\theta_m)}{2\kappa_m} (R^p_{m|m+1})^4 (\mathfrak{L}^{(m)})^2 (1 - (\mathfrak{L}^{(m)})^2) \right| \tag{7.14}$$

Similar to the above, the quasi-specular reflection assumption is used to calculate the reflection coefficient. This concludes our discussion on the calculation of the co-polarized volume scattering component of the NRCS. We also note that the limitation of this method lies in the fact that its calculated cross-polarized volume scattering component of the NRCS becomes zero for the monostatic configuration. For better understanding and further discussion on the above forward solver, please see Appendix ch:Appendix3.

Now that our forward solver has been described, let's consider Figure 7.10 that shows the comparison of the simulated and measured NRCS data at 2 pm on 24th of May 2014. This time was chosen due to concurrent NRCS measurements by both the on-site scatterometer and the satellite. For the co-polarized $\sigma^{\mathrm{HH}}$ in Figure 7.10(a), we have shown the surface scattering component and the volume scattering component as well as their summation (total component). As can be seen, the summation of the simulated surface and volume scatting components follows the NRCS measured by the scatterometer closely. It should be mentioned that we speculate the unexpected variations in the NRCS measured by the scatterometer is caused by local inhomogeneities at some incidence angles. On the other hand, the NRCS measured by the satellite is calculated by averaging an area of few kilometers, thus, tending to cancel out the effects of any local inhomogeneity. Therefore, the NRCS data from the satellite is closer to the simulated NRCS. It is also worthwhile to note that the large value of volume scattering component in comparison with the surface scattering component for the profile under study, may explain the similar values observed for the measured $\sigma^{\mathrm{HH}}$ and $\sigma^{\mathrm{VV}}$ as shown in Figure 7.7.

In addition, Figure 7.10(b) compares the simulated and measured cross-polarized NRCS data, namely, $\sigma^{\mathrm{HV}}$. As noted above, our forward solver only estimates the surface scattering component of the cross-polarized NRCS. This could be the reason for the large discrepancy between the measured and simulated $\sigma^{\mathrm{HV}}$. Therefore, to crudely compensate for the absence of the cross-polarized volume scattering component in our forward solver, a calibration factor is introduced based on the mean difference of the measured and simulated data. Under the speculation that the cross-polarized volume scattering component varies slightly for different incidence angles, we obtain the calibrated simulated $\sigma^{\mathrm{HV}}$ as

$$\sigma^{\mathrm{HV}}_{(sim-cal)} = \sigma^{\mathrm{HV}}_{s,(sim)} + A_0. \tag{7.15}$$

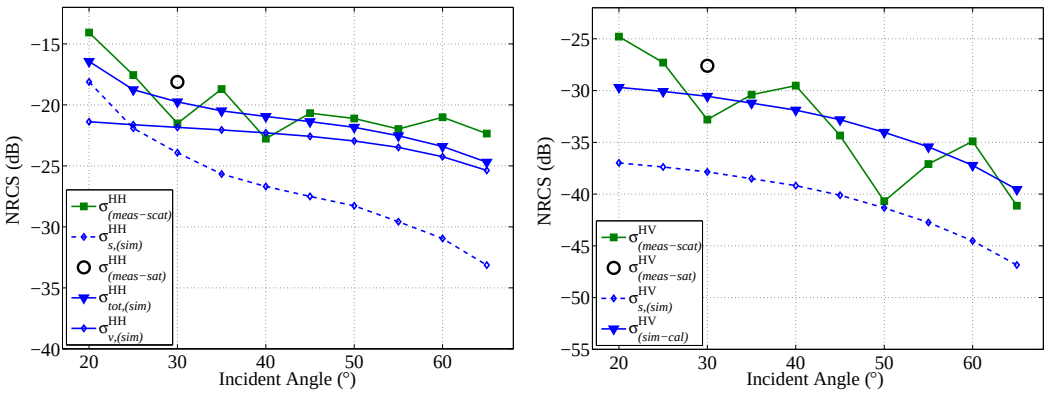


(a) (b)

*Fig. 7.10:* Comparison of measured and simulated NRCS for 2pm on 24th of May. Subscripts *(sim)*, *(sim-cal)*, *(meas-scat)*, and *(meas-sat)* refer to simulated, calibrated simulated, measured by scatterometer, and measured through satellite respectively. Also subscripts $s$ and $v$ refer to surface and volume components.

In (7.15), the calibration coefficient, $A_0$, is taken to be 7.3 dB. Of course, this calibration factor is for the profile under study in this chapter, and can vary for other profiles of interest. Furthermore, the accuracy of this forward scattering model was assessed by comparing with the measured NRCS data reported in [144]. Our simulated NRCS values are in agreement when compared to the reported values, with lower accuracy for the cross-polarization component. Finally, it should be noted that we acknowledge that the proposed framework for cross-polarization calculation is based on a crude model, and requires further development. Also more comparisons with different measured data sets will be part of the future work. Nonetheless, this method lays the ground work for more accurate models to better simulate the cross-polarization component. Within the framework of this chapter, we speculate that the use of the above calibration method alleviates some errors associated with the cross-polarized component calculation.

## *7.5 Inversion Algorithm*

The inversion algorithm reconstructs the parameters of interest from the measured NRCS data. To this end, the inversion algorithm iteratively updates these parameters by minimizing a data misfit cost functional. This process, which requires repeated calls to a forward solver, continues until the inversion algorithm converges to a solution. This solution will then serve as the reconstructed parameters associated with the snow-covered sea ice profile of interest. In our case, the data misfit cost functional to be minimized is the difference between the measured NRCS and the simulated NRCS due to a set of unknown parameters. However, due to the ill-posedness of this problem, the minimization may result in an unstable (*i.e.*, oscillatory) solution, and also the uniqueness of the solution is not necessarily guaranteed [73, 74]. To treat the ill-posedness of the problem, the data misfit cost functional needs to be regularized. In this chapter, the utilized regularization is a projection-based regularization scheme [76]. In our implementation, this regularization technique defines the possible range of values for each unknown parameter to be retrieved, thus projecting the solution space into a smaller subspace. To further treat the ill-posedness issue, it is recommended to increase the number of measurements as much as possible. The reason behind this idea can be explained as follows. For every measurement, there is an operator that maps the snow-covered sea ice information to the NRCS data. Thus, the collective nullspace associated with the problem can be thought as the intersection of all these individual operators' nullspaces. It is, therefore, expected that the collective null space will be minimized as the number of operators increases.

Our inversion algorithm utilizes a global optimization method, known as the differential evolution (DE) algorithm [99], to iteratively minimize the following data misfit cost

functional

$$\mathcal{C}(\chi) \triangleq \sum_{n=1}^{M} \sum_{p/q} \frac{1}{\sigma_{\text{meas}}^{p/q}(\Psi_{\text{inc}}^{n}, \Psi_{\text{scat}}^{n}; f)} \times \left| \sigma_{\text{meas}}^{p/q}(\Psi_{\text{inc}}^{n}, \Psi_{\text{scat}}^{n}; f) \; - \; \sigma_{\text{sim}}^{p/q}(\chi; \Psi_{\text{inc}}^{n}, \Psi_{\text{scat}}^{n}; f) \right| \tag{7.16}$$

In (7.16), $\chi$ is the vector containing the unknown parameters of interest which will be described in the next section, $M$ denotes the number of the measurements at various incidence angles, and $p/q$ denotes different utilized polarization configurations. Also, $\Psi_{\text{inc}}^{n}$ and $\Psi_{\text{scat}}^{n}$ denote the $n$th azimuth and elevation for incident and scattering angles respectively. Finally, $f$ is the frequency of operation, which is a fixed frequency at the C-band. The weighting factor in (7.16) normalizes the discrepancies to the measured NRCS, thus balancing the data for each incidence angle. In this chapter, we consider a monostatic configuration, thus, $\Psi_{\text{inc}}^{n} = \Psi_{\text{scat}}^{n}$. Also, two combinations of $p/q$ will be considered herein: HH and HV.

## *7.6 Inversion Strategy*

Herein, we present the assumptions made in our inversion algorithm in the following four subsections.

### *7.6.1 Snow-covered sea ice parameterization*

Based on our field observations and the physical sampling results, we divide the snow cover into three distinct layers; namely, (1) new snow layer, (2) original snow layer, and (3) basal layer. The new snow layer is due to the recent snow falls, has zero salinity, and is considered dry (no water in liquid phase)[(2)]. Next comes the older original snow

[(2)] We acknowledge that an error associated with the dry snow assumption exists, since the temperature of the top layer of snowpack approaches zero for the end part of the period of interest.

layer that is due to previous snow falls. This layer has gone through metamorphism, thus, having larger grain size. It is also slightly saline due to its adjacency to the third layer, which is the oldest snow layer. The third layer is the basal layer, which is highly saline. This layer is due to the first snow fall on the sea ice. The metamorphism has led to the presence of depth hoars in this layer. Herein, the second and third layers are taken to be brine-wetted dry snow. The presence of brine might be due to the upward movement of brine from the sea ice into the snow, or initial snowfall over frost flowers. These values are typical of many measurements of snow covered smooth first year sea ice [145, 146]. Figure 7.2 depicts the snow samples associated with each of these layers. Finally, we note that the ice layer is assumed to be a half space in the inversion algorithm.

### *7.6.2 Temporal average*

Our physical sampling demonstrates that the profile under study has changed minimally in May up to the 25th, in particular for the parameters of interest that play a key role in profile's back-scattering[(3)]. Therefore, we propose to consider a single temporally-averaged profile to represent the snow-covered sea ice for the aforementioned time period. This can be further verified considering the NRCS measured by the scatterometer as shown in Figure 7.7. It is evident that the NRCS values are fairly unchanged for each incidence angle since the beginning of scatterometer measurements on 20th till the end of the observation period. Therefore, we calculate the temporal averages of the measured salinity, temperature, and density for each layer within the snow as well as the ice (Table 7.2). We then take these averages as our reference snow-covered sea ice profile. Also, we note that in Table 7.2, the snow grain size is reported based on in-situ visual evaluation of snow grains using a mm-grid etched plate. In addition, Figure 7.11 shows these calculated average values with the uncertainty bars

[(3)] These parameters are defined in Section 7.6.3.

*Tab. 7.2:* The averaged parameters for each layer within the reference snow-covered sea ice profile.

| | Snow New Layer (18 cm – 6 cm) | Snow Original Layer (6 cm – 2 cm) | Snow Basal Layer (2 cm – 0 cm) | Sea Ice (Half-Space) |
|---|---|---|---|---|
| *Salinity* $(ppt)$ | 0.12 | 3.47 | 9.58 | 4.93 |
| *Temperature* $(°C)$ | -3.63 | -4.62 | -4.73 | -4.34 |
| *Density* $(g/cm^3)$ | 0.30 | 0.29 | 0.24 | 0.84 |
| *Grain Radius* $(cm)$ | 0.10 | 0.20 | 0.50 | NA |

representing the standard deviation values. Concerning this plot, it should be noted that although the average snow depth is assumed to be 18 cm, the actual snow depth varied in each measurement session within a standard deviation of about 3 cm; thus, there exists a larger uncertainty bar for the top layer in Figure 7.11. Consequently, the values for the upper two points show unrealistic standard deviations, leading to an artificial lower density. Although it should be noted that the averaging of the values associated with the top six measurement points in our simulation mostly corrects this effect. Also, it is expected that the temperature of the top snow layer to be be more affected by hourly air temperature and solar radiation changes. Therefore, a larger variation is present for this top layer. (Temperature of the top layer will not be used in the permittivity calculation of the top layer since the top layer is assumed to be dry snow.) Finally, we note that we did not have access to physical sampling for the 3rd and 4th of May; however, no significant meteorological event took place from these dates up to the start of our physical sampling. Therefore, the whole period from May 3rd to May 25th is assumed to have minimal changes. In addition, although the air mean temperature difference between 4th and 11th is about 13.8 degrees, we expect that the deviation of temperature in lower snow layers between these dates is minimal due to snow's small thermal conductivity. Also, as noted above, the top layer of snow is considered to be dry; thus, its contribution to the NRCS will be only density-dependent[(4)].

[(4)] It should be note that the snow might also be heated from below by the ocean heat conducted through the sea ice, based on the average temperature variation represented in Table 7.2.

### *7.6.3 Formation of the vector of unknowns*

The choice of the vector of unknowns is mainly affected by our measured data, which is the NRCS. That is, we are interested in parameters that affect the NRCS in our utilized physical model. These parameters are the complex permittivity of each layer as well the grain size. In our inversion algorithm, the complex permittivity is obtained through proxy formulations to be explained in the next subsection. To this end, for the top snow layer (new snow), only the density will be retrieved, since this layer is assumed to be dry snow; thus, having its density will be sufficient to calculate its corresponding permittivity. For the third snow layer (basal layer), the salinity, temperature, density, and radius of the snow grain are treated as unknowns to be retrieved. As noted above, the middle original layer is labeled as a transitional layer. (This is from a modeling point of view, and not necessarily from a physical perspective.) Therefore, we calculate its parameters based on the properties of the top new snow and bottom basal layer. Specifically, the density of this layer is taken to be the average of the new snow and basal layer, its salinity is taken to be one-third of the basal layer's salinity, and its temperature is approximated to be the same as that of the basal layer. These assumptions are based on our physical observations and the thickness of the middle and bottom snow layers. All other parameters are considered to be prior information that are available through methods such as in-situ physical sampling, lidar measurements, and the general knowledge of the typical seasonal snow-covered sea ice in the area. For example, all the roughness parameters are provided to the inversion algorithm as prior information. Based on the lidar measurements reported in Table 7.1, the average rms height and correlation length of the air-snow interface are taken to be 0.12 cm and 2.34 cm respectively. Moreover, for the inner snow interfaces, we assume a roughness based on the grain size in an ad hoc manner. Therefore, an rms height and correlation length of 0.20 cm and 2.00 cm, and 0.50 cm and 5.00 cm, are assumed for the new-original and original-basal layer interfaces respectively. For snow-ice interface,

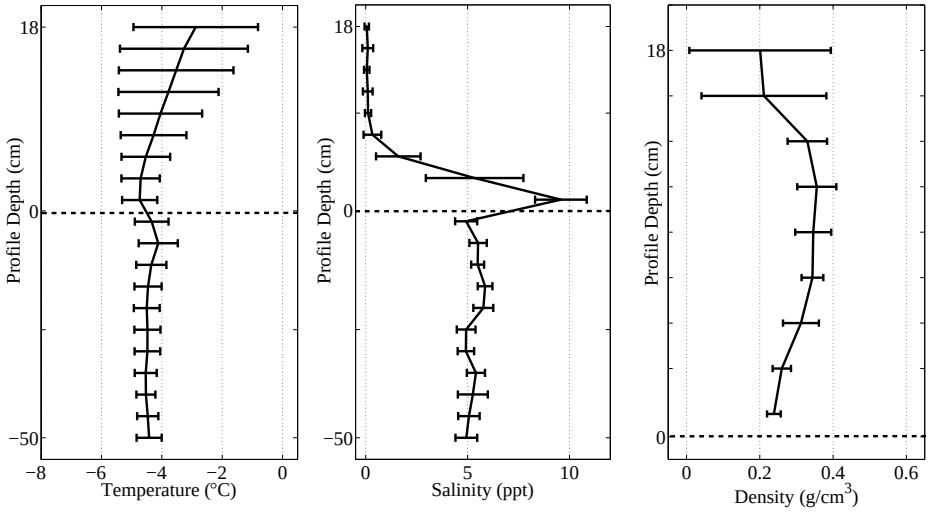


*Fig. 7.11:* The temporally-averaged physically measured values of snow-covered sea ice for (a) temperature, (b) salinity and (c) density, all of which up to 26th of May 2014. The uncertainty bars are their respective standard deviation values. (The top two points have large bars due to considering snowpack thickness (average) to be 18 cm for what is actually a variable thickness.) The horizontal dashed line at zero is the snow-ice interface.

an almost smooth condition is assumed based on field observations with a typical rms height and correlation length of 0.15 cm and 8.50 cm respectively, which is similar to previously reported values [142].

### *7.6.4 Use of proxy formulations*

After updating the unknowns, introduced above, at each iteration of the inversion algorithm, we need to obtain the complex permittivity profile associated with the predicted profile so as to find its corresponding simulated NRCS. To this end, the proxy formulations introduced in [27, 119, 142] are utilized to calculate the permittivities of dry snow, brine-wetted dry snow, and sea ice based on these retrieved parameters.

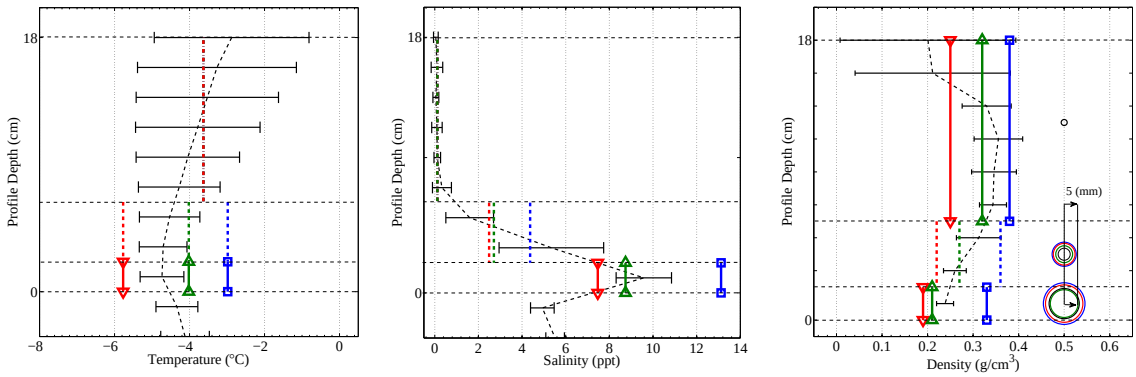


(a) (b) (c)

*Fig. 7.12:* The reconstructed (a) temperature, (b) salinity, and (c) density & snow grain size. The solid colored vertical lines are the retrieved parameter, the dashed colored vertical lines are the parameters derived based on the retrieved parameter, and the vertical colored dash-dot lines are the extra information (*i.e.*, not used in inversion). The colors blue (square), red (downside triangle), and green (upside triangle) represent the inversion in Scenario (I) (using satellite data), Scenario (II) (scatterometer data), and Scenario (III) (satellite plus scatterometer data) as inversion algorithm input. Circles in (c) are the reference (black) and reconstructed (colored) relative snow grain sizes for the basal snow layer, following the same color coding scheme.

## *7.7 Inversion Results*

Herein, we first present the three scenarios that we consider for inversion. The inversion results associated with each scenario will then be presented and discussed.

### *7.7.1 Three scenarios*

Herein, we investigate the reconstruction of the snow-covered sea ice whose reference profile is reported in Table 7.2 by utilizing the inversion algorithm introduced in Section 7.5 in conjunction with the forward solver presented in Section 7.4. To this end, we consider three different inversion scenarios distinguished by the measured data available to the algorithm. In Scenario (I), the NRCS given to the inversion algorithm is the NRCS data collected by the satellite on the seven dates mentioned in Section 7.3.3. Given that we are using a dual polarization data (HH and HV), and we have seven

different incidence angles, the number of data points will be 14 in this scenario. In Scenario (II), the dual-polarized (HH and HV) NRCS measured by the on-site scatterometer is given to the inversion algorithm. Noting that we have 10 incidence angles in this scenario, the total number of data points will be 20. (Note that each data point in Scenario (II) is the temporal average of the NRCS data collected over the period of interest.) Finally, in Scenario (III), we utilize the NRCS measured by both the scatterometer and satellite. Since the incidence angles in Scenarios (I) and (II) are not exactly the same, Scenario (III) will have more information regarding the profile of interest.

### *7.7.2 Results and Discussion*

The reconstructed salinity, temperature, density, and snow grain size for these three scenarios are depicted in Figure 7.12. These reconstructions are color-coded: blue, red, and green represent Scenarios (I), (II), and (III) respectively. For example, in Figure 7.12(a), the three reconstructed temperatures at the basal layer, shown by colored solid vertical lines, correspond to these three scenarios. These reconstructions can then be compared with the reference temperature at this layer, which is shown by the dashed black curve. Also, as noted in Section 7.6.3, the parameters of the original snow layer (middle snow layer) are found based on the reconstructed properties of the first and third snow layers. That's why in Figure 7.12(a), the temperature of the original snow layer (three dashed colored vertical lines) coincide with the reconstructed temperature of the basal layer. Finally, we note that the colored dash-dot line is the temperature of the new snow layer, which is not used in the inversion algorithm for the reasons explained in Section 7.6.3, and is brought here for demonstration purposes.

Figure 7.12(b) shows the reconstructed salinity at the basal layer for these three scenarios, see colored solid vertical lines. Similar to Figure 7.12(a), the salinity of the

original snow layer can be obtained from these reconstructed salinity values, and is presented by dashed colored vertical lines. (The salinity of the new snow layer is not used in the inversion algorithm.) Finally, Figure 7.12(c) represents two different parameter reconstruction: the density and the snow grain size. As can be seen, the reconstructed density values at the new snow layer as well as the basal snow layer are shown with colored solid vertical lines. Based on Section 7.6.3, the density of the original snow layer can then be found by knowing the reconstructed density values at the new and basal snow layers. Furthermore, Figure 7.12(c) shows the reconstructed snow grain size for the basal layer. The black circle is the reference size, and the colored concentric circles represent the reconstructed snow grain size for these three scenarios. The snow grain size for new snow layer has been taken as prior information, and that of the original snow layer has been obtained based on the reconstructed snow grain size of the basal layer.

The calculated average of the reconstruction relative errors for Scenarios (I), (II), and (III) for the 5 problem unknowns outlined in Section 7.6.3, are 32%, 18%, and 13% respectively. These reconstruction results confirm our speculation that with an increase in the number of measurements (*i.e.*, NRCS data points), the reconstruction accuracy increases. Finally, as can be seen in Figure 7.12 (c), it is interesting to note that for all the three scenarios, the accuracy of density retrieval is higher for the top layer compared to the basal layer. When comparing Scenario (II) to Scenario (I), we should bear in mind that the area scanned by the scatterometer is a few meter squares while that of the satellite is a few kilometer squares. On the other hand, the reference profile for the reconstruction accuracy was also calculated based on the in-situ physical measurements around the scatterometer area. Therefore, the accuracy of the reconstruction results are slightly biased towards Scenario (II). Nevertheless, the nature of the landfast snow-covered sea ice in the measurement area and our field observations both confirm the validity of the assumption of a homogenous profile for the area used

for satellite NRCS extraction. A further confirmation of the homogeneity assumption is the higher reconstruction accuracy of Scenario (III) compared to Scenario (II), which would have not happened if the reference profile was not representative enough for the area under investigation. Finally, it is worthwhile to note that the inclusion of volume scattering in our forward solver was critical in successful inversion for the snow-covered sea ice profile studied in this chapter. In fact, a sole surface scattering model failed to accurately retrieve the unknown parameters as shown in [128].

## *7.8 Conclusion*

We have considered the inversion of the monostatic NRCS data collected from landfast snow-covered sea ice in Cambridge Bay, NU, Canada, in May 2014. The NRCS data were collected using an on-site C-band scatterometer as well as radarsat-2 satellite. It was shown that the inclusion of the volume scattering component in the electromagnetic forward solver is crucial for accurate NRCS modeling for the profile under study. Thus, it is also crucial for obtaining accurate inversion results. To this end, the concept of the generalized transmission coefficients in conjunction with the volume scattering component of a single layer was utilized to model the volume scattering component of our multi-layered rough medium. In addition to the co-polarized NRCS data, the cross-polarized NRCS data were used in the inversion process to increase the number of data points.

The developed inversion algorithm retrieves the temperature, salinity, density, and snow grain size of the snow-covered sea ice profile through iterative minimization of a normalized data misfit cost functional. This cost functional is associated with a discrepancy between the NRCS data simulated by our proposed forward solver and the measured NRCS data. Moreover, a projection-based regularization was utilized to tackle the inversion ill-posedness. Based on the measured NRCS dataset provided

to the inversion algorithm, we studied three different inversion scenarios in which satellite data (Scenario (I)), scatterometer data (Scenario (II)), and finally the combination thereof (Scenario (III)) were fed to the inversion algorithm. There were 14 data points available through satellite and 20 data points available through scatterometer measurements (HH and HV polarizations for each incidence angle). Based on the reconstruction results, it was shown that the reconstructed profile became more accurate as the number of input data increased; with the best reconstruction achieved through Scenario (III) (mean relative reconstruction error of 13%).

Based on the comparison of these three scenarios, it can be concluded that if satellites with shorter re-visit times are to be employed for this application, the reconstruction accuracy may be enhanced. This may be particularly pertinent as the new 'sentinel' series and the constellation missions of ESA and CSA come online. In addition, the inversion algorithm utilized some prior information to reconstruct the unknown parameters. Assuming that more NRCS data points become available, *e.g.*, through more incidence angles, bistatic NRCS data, and more frequencies of operation, the inversion algorithm may be able to treat some of these prior information as the actual unknowns in the inversion process.

8

# Conclusion and Future Work

In this chapter, I present the conclusions of my thesis and the proposed future work. Firstly, the summary of the thesis and the contributions made towards the thesis objectives (as outlined in Chapter 1) are brought in Section 8.1. Next in Section 8.2, the proposed new research direction and the future work based on the findings of this research are introduced.

## *8.1 Conclusion*

The main objective of this thesis was to retrieve the parameters of interest associated with the snow-covered sea ice profile from NRCS data. These parameters can be the geophysical, thermodynamic, or dielectric properties of the snow and sea ice. To this end, an electromagnetic inverse scattering algorithm was developed that consists of forward and inverse solvers. The performance of this electromagnetic inverse scattering algorithm was then investigated against both synthetic and experimentally-collected

NRCS data. It is concluded that for more accurate parameter retrieval, it is necessary to (*i*) add more measured data, and (*ii*) utilize appropriate prior information. The addition of more measured data points is limited due to the structure of the snow-covered sea ice profile (*e.g.*, data collection only on one side of the profile), specifications of the available electromagnetic sensors (*e.g.*, single-frequency monostatic satellites with limited re-visit rates), and the location of the profile (*e.g.*, in remote and hazardous Arctic environment). Therefore, various techniques were developed in this thesis to take advantage of the prior information to add extra data to the inversion algorithm. In addition to enriching the information content via performing more measurements and the use of prior information, we need to ensure that the modeling error in the inversion algorithm is as low as possible. To this end, the utilized forward solver was enhanced so as to simulate the NRCS data associated with snowpacks containing large snow grains more accurately. In summary, it has been shown that the electromagnetic inverse scattering framework provides a promising tool to retrieve the dielectric (complex permittivity), geophysical (*e.g.*, snow grain size), and thermodynamic (*e.g.*, temperature) properties of snow-covered sea ice.

### *8.1.1 Contributions*

Herein, I outline the specific contributions made towards achieving the objectives of the thesis.

1. A nonlinear electromagnetic inverse scattering algorithm is developed that reconstructs the dielectric profile of the snow-covered sea ice. This reconstruction is achieved through iterative minimization of a misfit cost function that represents the discrepancy between the measured and simulated data. The measured data are the normalized radar cross section (NRCS) values collected from various snow-covered sea ice types under different measurement configurations. The

simulated data are produced utilizing the boundary perturbation theory and the heuristic single scattering multiple reflection cloud model. The differential evolution method is utilized as the inverse solver to reconstruct a candidate profile at each iteration most similar to the true profile. It should be noted that in addition to the dielectric profile of the snow-covered sea ice, this algorithm retrieves some geophysical (*e.g.*, snow grain size), and thermodynamic (*e.g.*, temperature profile) properties of the snow and sea ice through the previously established proxy formulas. The proxy formulas relate the geophysical and thermodynamic properties of the snow and sea ice to their dielectric properties. Moreover, a projection-based regularization is utilized to tackle the ill-posedness of the inversion problem. This translates into setting limits for the search space of each unknown parameter in the inverse solver. These limits act as prior information, and are based on our knowledge of the specific profile under investigation (*e.g.*, setting the search space for the sea ice permittivity based on the experimentally-determined expected variations).

2. The inversion of experimental data sets collected from two types of snow-covered sea ice profiles are investigated within the framework of electromagnetic inverse scattering. The first type, is the slush-covered artificially-grown sea ice in the sea-ice environmental research facility (SERF) located in Winnipeg, studied in Winter 2014. This type of profile represents the young sea ice that would form in polynya or lead areas. The second type, is the first-year snow-covered sea ice located in Cambridge Bay in the Canadian High Arctic, studied in May 2014. In each of these two experiments, the time-series NRCS data are collected utilizing a C-band scatterometer. Temporal physical sampling of snow and sea ice (*i.e.*, temperature, salinity, and density profiling) are also performed concurrently with the NRCS measurements, utilized to later verify the accuracy of the reconstructed profiles through inversion.

3. The formulation for the forward solver in the proposed electromagnetic inverse scattering algorithm is expanded to include the effects of the non-negligible volume scatterers within the snowpack. This is achieved through the addition of a volume scattering component to the surface scattering component simulated by the BPT. The volume scattering component is calculated via a heuristic single scattering cloud-model that sums the scattering effects of randomly distributed scatterers. I expanded this model for multi-layered mediums to consider multiple reflections from the rough boundaries through the use of the generalized reflection and transmission coefficients. It should be noted that under the introduced inversion scheme, which utilizes this enhanced forward solver, the collective effect of volume scatterers is considered. Therefore, a collective characteristic for all scatterers is retrieved in contrast to each scatterer being individually reconstructed.

4. The following algorithms and techniques are developed and implemented to better regularize the problem, and to add extra information to the problem (or, use more sensitive information) so as to help the nonlinear inversion algorithm converge to an appropriate solution.

   – It is shown that the utilization of more sensitive NRCS data with respect to the unknown parameters of the profile to be retrieved results in higher reconstruction accuracy. Therefore for the purpose of inversion, the NRCS data that are considered to be more sensitive are collected and inverted (*i.e.*, NRCS data measured at incidence angles closer to the nadir or specular angle for the monostatic or bistatic configurations respectively).

   – An appropriate weighting factor for the misfit cost function is introduced for the case of bistatic NRCS data collection configuration. This weighting factor normalizes the discrepancy between the measured and simulated NRCS data and assigns a higher weight to those collected at angles in the vicinity

of the specular reflection. The employment of this weighting factor is shown to increase the reconstruction accuracy utilizing the synthetic bistatic NRCS data.

– A further parametrization technique for the sea ice permittivity profile is developed that reduces the number of inverse problem unknowns. This parametrization is based on prior information about the shape of the sea ice permittivity curve versus the profile depth. This curve is known to have a C-shape for specific sea ice types as a result of their growth process.

– An inversion strategy is introduced that takes advantage of the time-series nature of the temporally collected NRCS data. This is achieved through utilization of the reconstructed profile at each time step, to set the search space for the profile unknowns in the next time step. The assumptions considered in this strategy are that (*i*) no abrupt changes occur in snow-covered sea ice profile status during the period of the NRCS measurements, and (*ii*) the true profile at the first time step is known either via physical sampling or other inversion schemes (*e.g.*, a multi-frequency scheme).

– A combination of the time-series NRCS data collected through a C-band scatterometer and a C-band spaceborne SAR satellite (*i.e.*, radarsat-2) are utilized for the first time to retrieve the parameters of interest from the snow-covered sea ice profile through an electromagnetic inverse scattering algorithm. A profile averaging technique is introduced to reduce the number of inversion problem unknowns. The reconstruction results for different scenarios utilizing this approach confirmed that the deployment of satellite platforms with higher re-visit rates (*i.e.*, satellites that would provide more measured NRCS data points) can lead to higher reconstruction accuracy within the electromagnetic inverse scatting framework.

## *8.2 Future Work*

My research presented in this thesis can be further developed on three fronts (*i*) the electromagnetic inverse scattering algorithm improvements, (*ii*) application expansion, and (*iii*) multi-physics inversion.

1. Electromagnetic inverse scattering algorithm improvements.– The proposed inversion algorithm consists of two main components, namely, forward and inverse solvers. Each of these solvers can then be further developed to achieve better retrieval accuracy for specific snow-covered sea ice types. In the case of forward solver, there are always promising opportunities to enhance the utilized forward solver (*e.g.*, use of higher order approximations), or use more sophisticated forward solvers (*e.g.*, dense medium radiative transfer theory). However, it should be noted that the forward solver within this inversion framework is not used in isolation. It is, in fact, used in conjunction with an inverse solver applied to a given measured data set. Therefore, the choice of the forward solver can affect the number of unknowns to be recovered, and thus, can affect the performance of the inverse solver. For example, in a practical scenario in which the number of measured data points are limited, if the use of a forward solver results in too many unknowns, that might lead to reconstruction failure due to the significant imbalance between the number of known and unknown quantities. Finally, we should always consider the computational complexity of the forward solver as the forward solver is often called several times during the inversion process.

   On the other hand, the data used in this thesis for parameter retrieval of the snow-covered sea ice profile were the phaseless NRCS data. It is expected that the addition of other data extracted from the measurements to the inverse problem can improve the reconstruction accuracy. This is particularly noticeable in the case of the data provided by polarimetric images of spaceborne SAR satel-

lites (*e.g.*, radarsat-2 and sentinel-1). Based on these data, various polarimetric parameters can be calculated (*e.g.*, target entropy), and then used (solely, or in conjunction with the NRCS data) for parameter retrieval and classification. In such scenarios, the inverse solver should be modified to take into account multiple forms of data.

2. Application expansion.– Various applications for the developed inversion algorithm can be considered depending on the profiles and parameters to be retrieved. One application is the oil detection in the snow-covered sea ice profile. The ever-increasing development in oil and gas exploration and shipping throughout the Arctic translates into possible future oil spills. In the case of such oil spill occurrences, detection of the spill is a prerequisite to any subsequent endeavors for cleanup and recovery. The electromagnetic inverse scattering algorithm developed in my thesis can be further expanded for oil detection. The oil can manifest itself as (*i*) a separate distinguishable layer above, within, or below the snow-covered sea ice profile, or (*ii*) inclusions within the snow or sea ice layer. The dielectric contrast of the oil layer versus snow and sea ice layers in the former case, and the change in the overall permittivity of the snow-covered sea ice profile in the latter case, can lead to the oil retrieval utilizing the framework of the developed inversion algorithm.

3. Multi-physics inversion.– It should be noted that new technologies proposed for parameter retrieval from various types of snow and sea ice in the Arctic focus on multi-physics methods. In such technologies, various types of data (*e.g.*, electromagnetic, hyperspectral, acoustic, etc.) are collected from the profile to be reconstructed. There are at least two approaches to invert these multi-physics data sets. In the first inversion approach, the measured electromagnetic data are inverted by an electromagnetic inverse scattering algorithm while the rest of data are processed through other inversion algorithms (*e.g.*, use of an acoustic

inversion algorithm for the acoustic data set). Consequently, the intersection of the retrieved parameters by each algorithm will form the final reconstruction. In the second inversion approach, the multi-physics data are all fed to a single inversion algorithm that reconstructs a single profile. This simultaneous inversion approach can reduce the chance for the inversion algorithm to be trapped in wrong solutions. The author believes that multi-physics methods will be the key tool in future strategies for parameter retrieval through remote sensing.

This concludes my Ph.D. dissertation on radar cross section data inversion for snow-covered sea ice remote sensing.

# APPENDIX

A

# Appendix A

In this thesis, the boundary perturbation theory (BPT) developed by Imperatore et. al. [92, 94, 138] was implemented as the forward solver to calculate the NRCS data associated with a layered medium with rough interfaces. The details on the derivation of BPT formulation by Imperatore are presented in [94]. (We later enhanced this forward solver as described in Chapter 7.) In this appendix, I briefly describe the concept behind the BPT. Next, I will describe the details on how I have implemented the BPT formulation to calculate the NRCS data associated with the snow-covered sea ice profile having rough interfaces. Finally, the simulation results of the implemented BPT code are verified via comparisons against simulation results of other forward solver codes. (The details of the enhancement are not repeated here, and can be found in Chapter 7.)

To explain the concept of the BPT, I initially introduce the generalized reflection and transmission coefficients for flat interfaces as described in [137]. To this end, let's first consider a three-layer profile with flat boundaries as shown in Figure A.1. The total

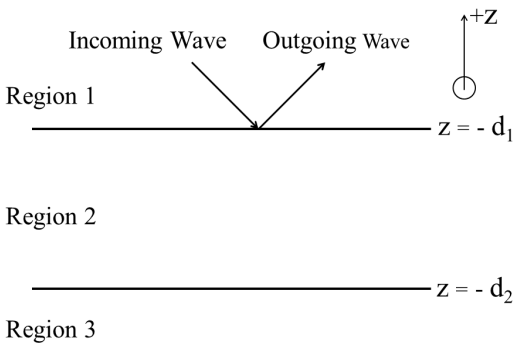


*Fig. A.1:* Three-layer medium with flat surfaces (based on a figure in [137]).

field (*i.e.*, the superposition of the down-going and up-going waves) in each of the layers can be written as[(1)] [137]

$$E_{1y} = A_1 \left[ e^{-jk_{z1}z} + \mathcal{R}_{1|2} e^{2jk_{z1}d_1 + jk_{z1}z} \right] \tag{A.1}$$

$$E_{2y} = A_2 \left[ e^{-jk_{z2}z} + R_{2|3} e^{2jk_{z2}d_2 + jk_{z2}z} \right] \tag{A.2}$$

$$E_{3y} = A_3 e^{-jk_{z3}z} \tag{A.3}$$

In (A.1), $\mathcal{R}_{1|2}$ is the reflection coefficient parameter that considers the effect of multiple reflections due to Region 2 and Region 3 interface. Also in (A.2), $R_{2|3}$ is the Fresnel reflection coefficient between Region 2 and Region 3. Moreover $k$ is the wave number and $A$ is the wave amplitude. (Different subscripts denote different layers.) Knowing that the down-going wave in Region 2 at $z = -d_1$ is equal to the transmission of the down-going wave from Region 1 plus the reflection of the up-going wave in Region 2, we have[(2)] [137]

$$A_2 e^{jk_{z2}d_1} = T_{1|2} A_1 e^{jk_{z1}d_1} + R_{2|1} A_2 R_{2|3} e^{2jk_{z2}d_2 - jk_{z2}d_1} \tag{A.4}$$

[(1)] The example considers the transverse electric (TE) polarization.
[(2)] To be precise, this translates to $z = -d_1 - \epsilon$ where $\epsilon$ is a very small positive number.

Furthermore, the up-going wave in Region 1 at $z = -d_1$ is equal to the reflection of down-going wave in Region 1 plus a transmission of the up-going wave in Region 2. This can be written as

$$\mathcal{R}_{1|2}A_1e^{jk_{z1}d_1} = R_{1|2}A_1e^{jk_{z1}d_1} + T_{2|1}A_2R_{2|3}e^{2jk_{z2}d_2-jk_{z2}d_1} \tag{A.5}$$

Next, we solve (A.4) for $A_2$ to be

$$A_2 = \frac{T_{1|2}A_1e^{j(k_{z1}-k_{z2})d_1}}{1 - R_{2|1}R_{2|3}e^{2jk_{z2}(d_2-d_1)}} \tag{A.6}$$

and use $A_2$ in (A.5) to find $\mathcal{R}_{1|2}$ as

$$\mathcal{R}_{1|2} = R_{1|2} + \frac{T_{1|2}R_{2|3}T_{2|1}e^{2jk_{z2}(d_2-d_1)}}{1 - R_{2|1}R_{2|3}e^{2jk_{z2}(d_2-d_1)}} \tag{A.7}$$

The above procedure represents the concept of the generalized reflection coefficients for a three-layer medium with flat interfaces. Based on this, we can then understand that if a new layer is added below the profile in Figure A.1, the Fresnel reflection coefficient of $R_{2|3}$ will be replaced by $\mathcal{R}_{2|3}$ [137]. Such reflection coefficients are referred to as the generalized reflection coefficients. Therefore, for an $N$-layered medium, we have the following generalized reflection coefficients where the index $i$ denotes the layer number [137]

$$\begin{aligned}\mathcal{R}_{i|i+1} &= R_{i|i+1} + \frac{T_{i|i+1}\mathcal{R}_{i+1|i+2}T_{i+1|i}\ e^{2jk_{z(i+1)}(d_{i+1}-d_i)}}{1 - R_{i+1|i}\mathcal{R}_{i+1|i+2}\ e^{2jk_{z(i+1)}(d_{i+1}-d_i)}} \\ &= \frac{R_{i|i+1} + \mathcal{R}_{i+1|i+2}\ e^{2jk_{z(i+1)}(d_{i+1}-d_i)}}{1 + R_{i|i+1}\mathcal{R}_{i+1|i+2}\ e^{2jk_{z(i+1)}(d_{i+1}-d_i)}}\end{aligned} \tag{A.8}$$

Similar to (A.6) which shows the transmission between two successive layers in a three-layer medium, we can arrive at a similar transmission formula between two successive

layers in an $N$-layered medium as follows [137]

$$A_i e^{jk_{zi}d_{i-1}} = \frac{T_{i-1|i}A_{i-1}\ e^{jk_{z(i-1)}d_{i-1}}}{1 - R_{i|i-1}\mathcal{R}_{i|i+1}\ e^{2jk_{zi}(d_i - d_{i-1})}} \tag{A.9}$$

The above equation establishes a transmission relation between two successive layers. Since $A_1$ is known (incident field), $A_2$ can be obtained. Then, from $A_2$, $A_3$ can be found, and so on. This enables us to define the so-called generalized transmission coefficient, $\mathfrak{T}_{1|m}$, that establishes a transmission relation between layers 1 and $m$ as follows

$$A_m e^{jk_{zm}d_{m-1}} = \mathfrak{T}_{1|m}A_1 e^{jk_{z1}d_1} \tag{A.10}$$

Noting (A.10) and (A.9), the generalized transmission coefficient $\mathfrak{T}_{1|m}$ can be recursively obtained as [137]

$$\mathfrak{T}_{1|m} = \prod_{i=1}^{m-1} \frac{T_{i|i+1}\ e^{jk_{zi}(d_i - d_{i-1})}}{1 - R_{i+1|i}\mathcal{R}_{i+1|i+2}\ e^{2jk_{z(i+1)}(d_{i+1} - d_i)}} \tag{A.11}$$

This concludes our description of the generalized transmission and generalized reflection coefficients.

Now let's define $S_m^{\pm p(0)}$ as the zero-order complex amplitudes of the spectral representation of the field at $m$th layer[(3)]. (The superscript zero refers to the zero-order field, *i.e.*, the unperturbed field.) Therefore the amplitude of the up-going (+) and down-going (-) field components at the interface between layers $m$ and $m+1$, *i.e.*, $z = -d_m$, can be combined into a matrix, denoted by $\boldsymbol{S}_m^{p(0)}$, as[(4)] [94]

$$\mathbf{S}_m^{p(0)}(k_\perp, d_m) = \begin{bmatrix} S_m^{+p(0)}(k_\perp)e^{-jk_{zm}d_m} \\ S_m^{-p(0)}(k_\perp)e^{+jk_{zm}d_m} \end{bmatrix} \tag{A.12}$$

[(3)] We note that $\boldsymbol{E}_m^{\pm(0)}(\boldsymbol{r}) = \sum_{p=h,v} e^{j\boldsymbol{k}_\perp^i \cdot \boldsymbol{r}_\perp} \hat{p}_m^{\pm}(\boldsymbol{k}_\perp^i) S_m^{\pm p(0)}(k_\perp^i) e^{\pm jk_{zm}^i z}$, where $\hat{p}_m^{\pm}(\boldsymbol{k}_\perp^i)$ is the unit vector indicating the horizontal/vertical (TE/TM) polarization [94]. Note that based on Imperatore's notation [94], $\boldsymbol{k}_\perp$ is the wavenumber vector projected on the interfaces; *i.e.*, $\boldsymbol{k}_\perp^i = k_x\hat{x} + k_y\hat{y}$.

[(4)] From this point on, the region indexing starts from 0.

Employing a recursive approach, and applying the continuity of the tangential fields across each interfaces, Imperatore finds [94]

$$\begin{aligned}\boldsymbol{S}_m^{p(0)}(k_\perp^i, d_m) &= \boldsymbol{N}_{m|m+1}^p(k_\perp^i)\boldsymbol{S}_{m+1}^{p(0)}(k_\perp^i, d_m) \\ &= \boldsymbol{N}_{m|m+1}^p(k_\perp^i)\boldsymbol{\Pi}_{m+1}(k_\perp^i)\boldsymbol{S}_{m+1}^{p(0)}(k_\perp^i, d_{m+1})\end{aligned} \tag{A.13}$$

In (A.13) we have [94]

$$\boldsymbol{N}_{m|m+1}^p(k_\perp) = \frac{1}{T_{m|m+1}^p}\begin{bmatrix} 1 & R_{m|m+1}^p \\ R_{m|m+1}^p & 1 \end{bmatrix}; \tag{A.14}$$

$$\boldsymbol{\Pi}_{m+1}(k_\perp) = \begin{bmatrix} e^{jk_{zm}\Delta_m} & 0 \\ 0 & e^{-jk_{zm}\Delta_m} \end{bmatrix} \tag{A.15}$$

Noting that the matrices $\boldsymbol{N}$ and $\boldsymbol{\Pi}$ create a transfer function formulation between the field values at different layers, and that the very last layer is a half space[(5)], we can utilize the generalized transmission and reflection coefficients to arrive at [94]

$$\mathbf{S}_m^{p(0)}(k_\perp^i, d_m) = \begin{bmatrix} \mathcal{R}_{m|m+1}^p(k_\perp^i) \\ 1 \end{bmatrix} \mathfrak{T}_{0|m}^p(k_\perp^i) e^{jk_{zm}\Delta_m} S_0^{-p(0)}(k_\perp^i) \tag{A.16}$$

The above equation relates the unperturbed field at the $m$th layer on $z = -d_m$ to the incident field.

We now consider a profile with slightly rough interfaces. To this end, we write the Taylor series expansion of the field jump at the $m$th interface, denoted by $\Delta\boldsymbol{E}_m(z)$[(6)], as

$$\Delta\boldsymbol{E}_m(z) = \Delta\boldsymbol{E}_m\Big|_{z=-d_m} + \frac{\partial\Delta\boldsymbol{E}_m}{\partial z}\Big|_{z=-d_m}(z+d_m) + \frac{1}{2}\frac{\partial^2\Delta\boldsymbol{E}_m}{\partial z^2}\Big|_{z=-d_m}(z+d_m)^2 + \ldots \tag{A.17}$$

(5) The up-going field will be zero at this half space.
(6) Similar equations can be written for $\Delta\boldsymbol{H}_m(z)$.

If the interface roughness shape is characterized by $\zeta_m(x,y)$, from the tangential boundary condition $\hat{n}_m \times \Delta E_m\Big|_{z=\zeta_m(x,y)-d_m} = 0$ and keeping only the first orders of $\zeta_m$ and $\boldsymbol{\upsilon}$, we arrive at[7] [94]

$$\hat{z} \times \Delta \boldsymbol{E}_m\Big|_{z=-d_m} = \nabla_\perp \zeta_m \times \Delta \boldsymbol{E}_m\Big|_{z=-d_m} - \zeta_m \hat{z} \times \frac{\partial \Delta \boldsymbol{E}_m}{\partial z}\Big|_{z=-d_m} \tag{A.18}$$

The field solution can be approximated as $\boldsymbol{E}_m \approx \boldsymbol{E}_m^{(0)} + \boldsymbol{E}_m^{(1)}$ [94] (*i.e.*, the unperturbed solution with superscript (0) plus the correction due to the first-order roughness with superscript (1)). Utilizing this field expansion in (A.18) gives [94]

$$\hat{z} \times \Delta \boldsymbol{E}_m^{(1)}\Big|_{z=-d_m} = \nabla_\perp \zeta_m \times \Delta \boldsymbol{E}_m^{(0)}\Big|_{z=-d_m} - \zeta_m \hat{z} \times \frac{\partial \Delta \boldsymbol{E}_m^{(0)}}{\partial z}\Big|_{z=-d_m} \tag{A.19}$$

It should be noted that the left hand side of (A.19) can be thought as an effective (magnetic) current density.[8] The spectral representation of this left hand side will then be

$$\hat{z} \times \Delta \boldsymbol{E}_m^{(1)}\Big|_{z=-d_m} = \int\int d\boldsymbol{k}_\perp e^{j\boldsymbol{k}_\perp \cdot \boldsymbol{r}_\perp} \tilde{\boldsymbol{J}}_{Hm}^{p(1)}(\boldsymbol{k}_\perp, \boldsymbol{k}_\perp^i) \tag{A.20}$$

In (A.20), the spectral surface equivalent current density $\tilde{\boldsymbol{J}}_{Hm}^{p(1)}$ is the Fourier transform of the RHS of (A.19), which is dependent only on the unperturbed field component $\boldsymbol{E}_m^{(0)}$ (*i.e.*, the field component associated with the flat-interface assumption), and the roughness $\zeta_m$. Similar treatment of tangential boundary condition for magnetic field results in an additional spectral surface equivalent current density of $\tilde{\boldsymbol{J}}_{Em}^{p(1)}$. As can be noticed, the roughness effect can be thought as a flat boundary, plus the equivalent current densities due to the roughness. Thus, Imperatore considers the effect of these current densities by adding them as a perturbation matrix $\boldsymbol{\Theta}$ to the field equations in

[7] We note that the normal vector at $m$th interface, denoted by $\hat{n}_m$, is defined as $\hat{n}_m = \frac{\hat{z} - \boldsymbol{\upsilon}_m}{\sqrt{1+\upsilon_m^2}}$. The slope vector, denoted by $\boldsymbol{\upsilon}_m$, is defined as $\boldsymbol{\upsilon}_m = \nabla_\perp \zeta_m$.

[8] A similar equation can also be found for $\hat{z} \times \Delta \boldsymbol{H}_m^{(1)}\Big|_{z=-d_m}$, which can be thought as an effective electric current density.

(A.13) at the $m$th boundary as [94]

$$\boldsymbol{S}_m^{q(1)}(\boldsymbol{k}_\perp, d_m) + \overbrace{\begin{bmatrix} -\frac{k_o Z_o \mu_m}{2k_{zm}}(\hat{k}_\perp \times \hat{z}).\tilde{\boldsymbol{J}}_{Em}^{p(1)} + \frac{1}{2}\hat{k}_\perp.\tilde{\boldsymbol{J}}_{Hm}^{p(1)} \\ +\frac{k_o Z_o \mu_m}{2k_{zm}}(\hat{k}_\perp \times \hat{z}).\tilde{\boldsymbol{J}}_{Em}^{p(1)} + \frac{1}{2}\hat{k}_\perp.\tilde{\boldsymbol{J}}_{Hm}^{p(1)} \end{bmatrix}}^{\Theta} = \boldsymbol{N}_{m|m+1}^{q}(k_\perp)\boldsymbol{S}_{m+1}^{q(1)}(\boldsymbol{k}_\perp, d_m) \tag{A.21}$$

Based on the above, $S_0^{+q(1)}$ (the up-going $S$ in the first half-space on the very first interface) can be calculated [94].

The field in the first half-space (*i.e.*, in the measurement domain) due to the medium under investigation can be written as [94]

$$\boldsymbol{E}_0^{(1)}(\boldsymbol{r}) = \sum_{q=h,v} \int\int d\boldsymbol{k}_\perp e^{j\boldsymbol{k}_\perp.\boldsymbol{r}_\perp} \hat{q}_0^+(\boldsymbol{k}_\perp) S_0^{+q(1)}(\boldsymbol{k}_\perp) e^{jk_{z0}z} \tag{A.22}$$

Employing the method of stationary phase, we find the scattered field in the direction of interest [94]

$$\boldsymbol{E}_0^{(1)}(\boldsymbol{r}).\hat{q}_0^+(\boldsymbol{k}_\perp^s) \cong -j2\pi k_0 \cos(\theta_0^s)\frac{e^{jk_0 r}}{r} S_0^{+q(1)}(k_\perp^s) \tag{A.23}$$

The normalized radar cross section of an area, denoted by $A$, is calculated by ensemble averaging, denoted by $<>$, of the statistically identical interfaces as [94]

$$\sigma_{qp} = \lim_{r\to\infty}\lim_{A\to\infty} \frac{4\pi r^2}{A} < \left|\boldsymbol{E}_0^{(1)}(\boldsymbol{r}).\hat{q}_0^+(\boldsymbol{k}_\perp^s)\right|^2 > \tag{A.24}$$

By utilizing (A.23) in (A.24) and replacing $S_0^{+q(1)}$ with its solution we have[(9)] [94]

$$\sigma_{qp} = \pi k_0^4 |\tilde{\alpha}_{qp}^{m,m+1}(\boldsymbol{k}_\perp^{\boldsymbol{s}}, \boldsymbol{k}_\perp^{\boldsymbol{i}})|^2 W_m(\boldsymbol{k}_\perp^{\boldsymbol{s}} - \boldsymbol{k}_\perp^{\boldsymbol{i}}) \tag{A.25}$$

[(9)] The solutions of $S_0^{+q(1)}$ are directly proportional to $\tilde{\zeta}(\boldsymbol{k}_\perp^s - \boldsymbol{k}_\perp^i)$, that is $S_0^{+q(1)} \propto \tilde{\zeta}(\boldsymbol{k}_\perp^s - \boldsymbol{k}_\perp^i)$. Therefore we have $\sigma_{qp} \propto < |S_0^{+q(1)}|^2 > \propto < |\tilde{\zeta}(\boldsymbol{k}_\perp^s - \boldsymbol{k}_\perp^i)|^2 > \propto W(\boldsymbol{k}_\perp^s - \boldsymbol{k}_\perp^i)$. (Note the definition of $W$ in (3.3).) This explains the appearance of the spatial power density, that is dependent on the perpendicular wave numbers, in the final formulation for $\sigma_{qp}$.

In (A.25), we have used $\tilde{\alpha}_{qp}^{m,m+1}$ notation to represent the following [94]

$$\begin{aligned}\tilde{\alpha}_{hh}^{m,m+1} &= \frac{k_{z0}^{s}}{k_{zm}^{s}}(\epsilon_{m+1}-\epsilon_{m})(\hat{k}_{\perp}^{s}.\hat{k}_{\perp}^{i}) \\ &\times e^{jk_{zm}^{s}\Delta_{m}}\mathfrak{T}_{m|0}^{h}(k_{\perp}^{s})[1+\mathcal{R}_{m|m+1}^{h}(k_{\perp}^{s})] \\ &\times e^{jk_{zm}^{i}\Delta_{m}}\mathfrak{T}_{0|m}^{h}(k_{\perp}^{i})[1+\mathcal{R}_{m|m+1}^{h}(k_{\perp}^{i})]\end{aligned} \tag{A.26}$$

$$\begin{aligned}\tilde{\alpha}_{vh}^{m,m+1} &= -\frac{k_{z0}^{s}}{k_{0}}(\epsilon_{m+1}-\epsilon_{m})\hat{z}.(\hat{k}_{\perp}^{s}\times\hat{k}_{\perp}^{i}) \\ &\times e^{jk_{zm}^{s}\Delta_{m}}\mathfrak{T}_{m|0}^{v}(k_{\perp}^{s})[1-\mathcal{R}_{m|m+1}^{v}(k_{\perp}^{s})] \\ &\times e^{jk_{zm}^{i}\Delta_{m}}\mathfrak{T}_{0|m}^{h}(k_{\perp}^{i})[1+\mathcal{R}_{m|m+1}^{h}(k_{\perp}^{i})]\end{aligned} \tag{A.27}$$

$$\begin{aligned}\tilde{\alpha}_{hv}^{m,m+1} &= \frac{k_{z0}^{s}k_{zm}^{i}}{k_{0}k_{zm}^{s}\epsilon_{m}}(\epsilon_{m+1}-\epsilon_{m})\hat{z}.(\hat{k}_{\perp}^{i}\times\hat{k}_{\perp}^{s}) \\ &\times e^{jk_{zm}^{s}\Delta_{m}}\mathfrak{T}_{m|0}^{h}(k_{\perp}^{s})[1+\mathcal{R}_{m|m+1}^{h}(k_{\perp}^{s})] \\ &\times e^{jk_{zm}^{i}\Delta_{m}}\mathfrak{T}_{0|m}^{v}(k_{\perp}^{i})[1-\mathcal{R}_{m|m+1}^{v}(k_{\perp}^{i})]\end{aligned} \tag{A.28}$$

$$\begin{aligned}\tilde{\alpha}_{vv}^{m,m+1} &= \frac{k_{z0}^{s}}{k_{0}^{2}k_{zm}^{s}\epsilon_{m}}(\epsilon_{m+1}-\epsilon_{m}) \\ &\times e^{jk_{zm}^{s}\Delta_{m}}\mathfrak{T}_{m|0}^{v}(k_{\perp}^{s})e^{jk_{zm}^{i}\Delta_{m}}\mathfrak{T}_{0|m}^{v}(k_{\perp}^{i}) \\ &\times\{[1+\mathcal{R}_{m|m+1}^{v}(k_{\perp}^{s})][1+\mathcal{R}_{m|m+1}^{v}(k_{\perp}^{i})] \\ &\times\frac{\epsilon_{m}}{\epsilon_{m+1}}k_{\perp}^{i}k_{\perp}^{s}-[1-\mathcal{R}_{m|m+1}^{v}(k_{\perp}^{s})] \\ &\times[1-\mathcal{R}_{m|m+1}^{v}(k_{\perp}^{i})]k_{zm}^{s}k_{zm}^{i}(\hat{k}_{\perp}^{s}.\hat{k}_{\perp}^{i})\}\end{aligned} \tag{A.29}$$

In (A.25), we also used the notation $W_m$ defined as the spatial power spectral density of $m$th corrugated interface, that is equal to [94]

$$W_{m}(\boldsymbol{\kappa}) =< \tilde{\zeta}_{m}(\boldsymbol{\kappa}), \tilde{\zeta}_{m}^{*}(\boldsymbol{\kappa}) >= \frac{1}{(2\pi)^{2}}\int\int < \zeta_{m}(\boldsymbol{r}_{\perp}+\boldsymbol{\rho})\zeta_{m}(\boldsymbol{r}_{\perp}) > e^{j\boldsymbol{\kappa}.\boldsymbol{\rho}}d\boldsymbol{\rho} \tag{A.30}$$

Furthermore, to consider the contribution of all uncorrelated rough interfaces, the effects of equivalent currents on all $N$ rough interfaces are summed, resulting in the

total NRCS value as [94]

$$\sigma_{qp} = \pi k_0^4 \sum_{m=0}^{N-1} |\tilde{\alpha}_{qp}^{m,m+1}(\boldsymbol{k}_\perp^{\boldsymbol{s}}, \boldsymbol{k}_\perp^{\boldsymbol{i}})|^2 W_m(\boldsymbol{k}_\perp^{\boldsymbol{s}} - \boldsymbol{k}_\perp^{\boldsymbol{i}}) \tag{A.31}$$

It should be noted that based on roughness measurements on random and isotropical surfaces, two popular forms of spatial power spectral density are determined to be exponential and Gaussian, defined as [27]

$$W_{\text{gaussian}}(\boldsymbol{k}_\perp^{\boldsymbol{s}} - \boldsymbol{k}_\perp^{\boldsymbol{i}}) = \frac{(hl)^2}{4\pi} e^{-|\boldsymbol{k}_\perp^{\boldsymbol{s}} - \boldsymbol{k}_\perp^{\boldsymbol{i}}|^2 l^2/4} \tag{A.32}$$

$$W_{\text{exponential}}(\boldsymbol{k}_\perp^{\boldsymbol{s}} - \boldsymbol{k}_\perp^{\boldsymbol{i}}) = \frac{(hl)^2}{2\pi} \frac{1}{(1 + |\boldsymbol{k}_\perp^{\boldsymbol{s}} - \boldsymbol{k}_\perp^{\boldsymbol{i}}|^2 l^2)^{3/2}} \tag{A.33}$$

In both (A.32) and (A.33), $h$ is the root-mean-square height (*i.e.*, the height standard deviation of $\zeta$), and $l$ is the so-called correlation length, as defined in Chapter 2.

After presenting an overview on the derivation of BPT formulas by Imperatore, I outline my methodology to implement the BPT formulation to calculate the NRCS data associated with a multi-layered snow-covered sea ice with rough interfaces. As can be seen in (A.31), the NRCS can be calculated if the $\tilde{\alpha}_{qp}^{m,m+1}$ and $W_m$ for each boundary is determined. To this end, the following steps must be traversed.

1. The snow-covered sea ice vertical profile is stratified into homogenous layers, each layer being assigned with a complex effective permittivity[(10)]. Moreover, the thickness values of each layer, the rms height, and the correlation length of each boundary are also assigned. Furthermore, the frequency of operation, and the azimuth and the elevation angles of the incident and scattered waves are set.

2. The values of basic parameters including $k_m$, $k_\perp^i$, $k_\perp^s$, $k_\perp^s - k_\perp^i$, $\hat{k}_\perp^s.\hat{k}_\perp^i$, $\hat{k}_\perp^s \times \hat{k}_\perp^i$, $k_{zm}^i$, $k_{zm}^s$ for the $m$th layer are calculated.

[(10)] Under the BPT scheme, the profile is not further discretized within each layer, nor on the boundaries.

3. The Fresnel reflection and transmission coefficients are calculated through [94]

$$R^h_{m|m+1} = \frac{\mu_{m+1}k_{zm} - \mu_m k_{z(m+1)}}{\mu_{m+1}k_{zm} + \mu_m k_{z(m+1)}} \tag{A.34}$$

$$R^v_{m|m+1} = \frac{\epsilon_{m+1}k_{zm} - \epsilon_m k_{z(m+1)}}{\epsilon_{m+1}k_{zm} + \epsilon_m k_{z(m+1)}} \tag{A.35}$$

$$T^h_{m|m+1} = \frac{2\mu_{m+1}k_{zm}}{\mu_{m+1}k_{zm} + \mu_m k_{z(m+1)}} \tag{A.36}$$

$$T^v_{m|m+1} = \frac{2\epsilon_{m+1}k_{zm}}{\epsilon_{m+1}k_{zm} + \epsilon_m k_{z(m+1)}} \tag{A.37}$$

4. The generalized reflection coefficients for each boundary are recursively calculated, utilizing (A.8) and the Fresnel reflection coefficients. We should note that $\mathcal{R}_{(N-1)|N} = R_{(N-1)|N}$.

5. The generalized reflection coefficients for each boundary are calculated through [94]

$$\mathfrak{T}^p_{0|m}(k_\perp) = exp[j\sum_{n=1}^{m-1} k_{zn}\Delta_n]\prod_{n=0}^{m-1} T^p_{n|n+1}[\prod_{n=1}^{m}(1 - R^p_{n|n-1}\mathcal{R}^p_{n|n+1}e^{j2k_{zn}\Delta_n})]^{-1} \tag{A.38}$$

$$\mathfrak{T}^p_{m|0}(k_\perp) = \begin{cases} \mathfrak{T}^p_{0|m}(k_\perp)\frac{\mu_0 k_{zm}}{\mu_m k_{z0}} & \text{for } p = h \\ \mathfrak{T}^p_{0|m}(k_\perp)\frac{\epsilon_0 k_{zm}}{\epsilon_m k_{z0}} & \text{for } p = v \end{cases} \tag{A.39}$$

6. The $\tilde{\alpha}^{m,m+1}_{pq}$ values are calculated utilizing (A.26) to (A.29).

7. The spatial power spectral densities for each boundary are calculated via (A.32) or (A.33), depending on the choice of the Gaussian or Exponential distribution for the roughness respectively.

8. The total NRCS associated with the profile is calculated through (A.31).

Imperatore has evaluated the consistency and validity of perturbative formulations derived for the scattering from a medium with rough boundaries in [92]. Further-

*Tab. A.1:* Dielectric profile specifications of the multi-layered profile with rough boundaries introduced in [94]. NA, $k_0$, and $\lambda$ denote not applicable, wave number in air, and wavelength in air. The looking angles are $\theta_{inc} = 45°$, $\phi_{inc} = 0°$, and $\phi_{scat} = 45°$.

| | *Region 1* | *Region 2* | *Region 3* | *Region 4* |
|---|---|---|---|---|
| *thickness* | half-space | $1.15\lambda$ | $2.80\lambda$ | half-space |
| *permittivity* | 1 | 3 | 9.5+j0.00055 | 20.5+j2.55 |
| *rms height* | NA | $0.15/k_0$ | $0.15/k_0$ | $0.15/k_0$ |
| *correlation length* | NA | $1.50/k_0$ | $1.50/k_0$ | $1.50/k_0$ |

more, an in-depth discussion on the physical meaning of the perturbative solutions for the scattering associated with such a medium can be found in [147]. In what follows, I initially investigate the validity of my implementation of the BPT algorithm through the comparison of my NRCS results with that of Imperatore's. Next, comparisons with another approximation formulation introduced by Sarabandi to calculate the NRCS associated with layered medium with rough interfaces is presented. Finally, the implemented BPT simulation results are compared to those of the finite-volume time-domain (FVTD) and method of moment (MoM) for rough layered media. To verify our implementation of BPT, the example layered medium with rough boundaries introduced in [94] by Imperatore is revisited here. The profile and simulation specifications are listed in Table A.1. The NRCS values calculated via the implemented BPT in this thesis are compared to the values reported in [94] for the profile in Table A.1 are reported in Figure A.2. As can be seen, the NRCS results are almost identical and this confirms the correct implementation of BPT. The small discrepancies between the two values are due to the error associated with visual reading of the NRCS values off the graphs brought in [94]. In the next step, we compare the simulation results of the implemented BPT with another approximation method developed for layered media with rough boundaries. To this end, the formula introduced by Sarabandi in [148] is considered. The profile in Table A.2 is investigated, and the simulated NRCS values through both methods are depicted in Figure A.3. It can be seen that both result in matching NRCS values. Indeed, Imperatore shows in [149] that BPT is consistent with the formula introduced by Sarabandi in [148], Yarovoy in [150], and Fuks in [151].

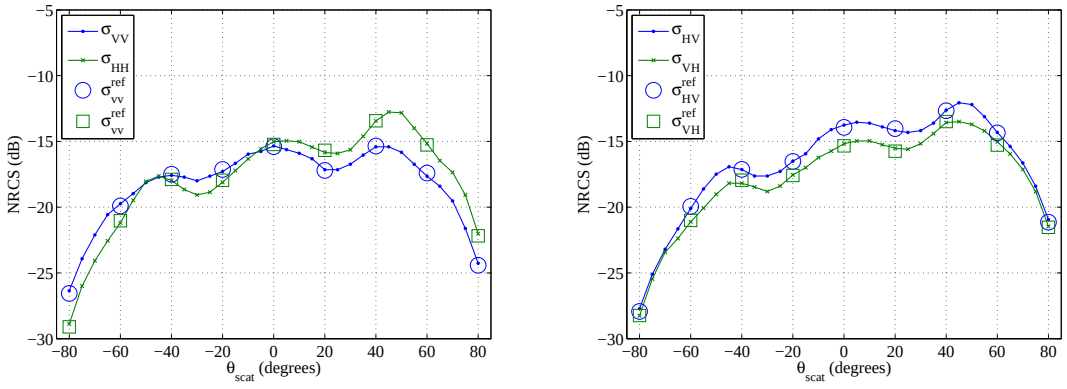


*Fig. A.2:* The NRCS values associated with the profile of Table A.1 utilizing the implemented BPT. The superscript $ref$ denotes the NRCS values for the aforementioned profile, as reported in [94].

*Tab. A.2:* Dielectric profile specifications of the multi-layered profile with rough boundaries introduced in [148]. NA, $k_0$, and $\lambda$ denote not applicable, wave number in air, and wavelength in air. The looking angles are $\theta_{inc} = 45°$, $\phi_{inc} = 0°$, and $\phi_{scat} = 0°$.

| | *Region 1* | *Region 2* | *Region 3* |
|---|---|---|---|
| *thickness* | half-space | $3.33\lambda$ | half-space |
| *permittivity* | 1 | 2 | 25+j10 |
| *rms height* | NA | 0 | $0.20/k_0$ |
| *correlation length* | NA | 0 | $2.00/k_0$ |

Finally, the consistency between the NRCS values calculated through BPT and SPM has been investigated in [152]. To further investigate the NRCS simulation accuracy via BPT as an approximate method, I present two cases of comparison with the so-called full-wave methods of ($i$) method of moment (MoM), ($ii$) and finite volume time domain (FVTD). For the first case, we consider a profile introduced by Demir in [153], with specifications as described in Table A.3. The NRCS results are reported in Figure A.4(a). It can be seen that the NRCS values for look angles close to the nadir are more accurate than those with higher incidence angles values. The observed discrepancies in NRCS values are tolerable for our application, considering the inevitable error associated with in-situ measurements, dielectric modeling inaccuracies, and the requirement for fast NRCS calculations[(11)].

[(11)] In [153], Demir reports that the problem under investigation had approximately two million unknowns. Utilizing supercomputing resources (512 processors) with parallelized implementation, it took 10 CPU hours

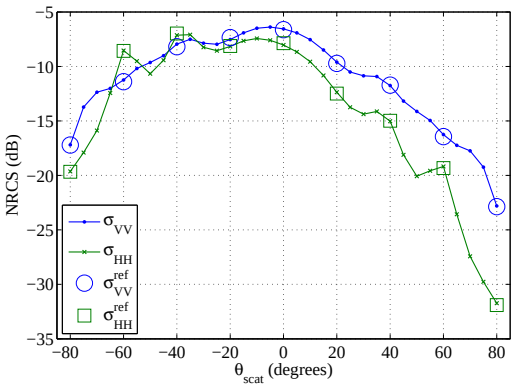


*Fig. A.3:* The NRCS values associated with the profile of Table A.2 utilizing the implemented BPT. The superscript $ref$ denotes the NRCS values for the aforementioned profile, calculated through Sarabandi method, as reported in [148].

*Tab. A.3:* Dielectric profile specifications of the multi-layered profile with rough boundaries introduced in [153]. NA and $\lambda$ denote not applicable, wave number in air, and wavelength in air. The looking angles are $\theta_{inc} = 40°$, $\phi_{inc} = 0°$, and $\phi_{scat} = 0°$.

| | *Region 1* | *Region 2* | *Region 3* |
|---|---|---|---|
| *thickness* | half-space | $0.20\lambda$ | half-space |
| *permittivity* | 1 | 5.4+j0.44 | 11.27+j1 |
| *rms height* | NA | $0.02\lambda$ | $0.02\lambda$ |
| *correlation length* | NA | $0.50\lambda$ | $0.50\lambda$ |

Finally, I present the comparison results between my implemented BPT and FVTD reported in [72]. The profile under investigation is a sea ice layer covered with a rough layer of slush, as characterized in Table A.4. The NRCS values associated with this profile are depicted in Figure A.4(b). It should be noted that only HH and VH polarizations are calculated in [72] through FVTD method for a monostatic setup. Due to zero cross-polarization component for the NRCS that is simulated through the BPT, only a comparison of NRCS with HH polarization is presented in Figure A.4(b). Furthermore, the in-situ measured NRCS values associated with this profile are also shown in this figure. As can be seen, the BPT results are following both FVTD and measurement points closely. This concludes our appendix on verification of the

per incident polarization for a single surface realization. Furthermore, Demir adds that a tapered wave incident field to reduce the edge truncation effects was utilized that introduces numerical errors.

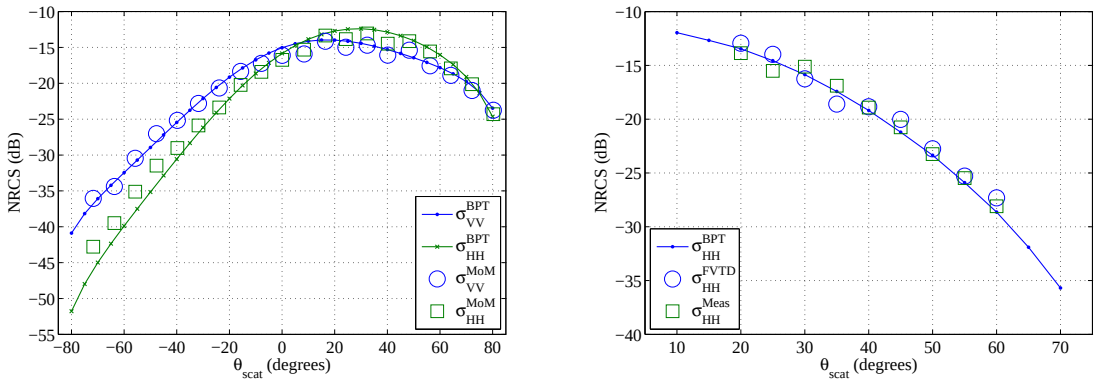


*Fig. A.4:* The NRCS values associated with the profile of (a) Table A.3 for comparison through MoM, as reported in [153], and (b) Table A.4 for comparison through FVTD, as reported in [72].

*Tab. A.4:* Dielectric profile specifications of the multi-layered profile with rough boundaries introduced in [72]. NA denotes not applicable. The looking angles are $\theta_{inc} = \theta^{\circ}_{scat}$, $\phi_{inc} = 0^{\circ}$, and $\phi_{scat} = 0^{\circ}$.

| | *Region 1* | *Region 2* | *Region 3* |
|---|---|---|---|
| *thickness (m)* | half-space | 0.0065 | half-space |
| *permittivity* | 1 | 7.2173+j1.7059j | 4.1711+j0.1726 |
| *rms height (m)* | NA | 0.00153 | 0 |
| *correlation length (m)* | NA | 0.01406 | 0 |

implemented BPT.

B

# Appendix B

In this appendix, I present the procedure utilized in Chapter 6 to calculate the complex permittivity value of the sea ice. Furthermore, I describe the procedure for calculating the permittivity of dry snow, and brine-wetted dry snow, as utilized in Chapter 7. The permittivity values are calculated utilizing the thermodynamic parameters of the profile. As will be seen, in the case of sea ice, these parameters are the temperature, denoted by $T$, and salinity, denoted by $S$. In the case of dry snow, only the density of the snow, denoted by $\rho$, is utilized. Finally, in the case of brine-wetted dry snow, the temperature, salinity, and density of the snow are used to calculate its permittivity. All these thermodynamic parameters can be measured through in-situ measurements along with snow and sea ice sample analysis. This enables us to compare the reconstructed and calculated permittivities and also enables us to indirectly reconstruct thermodynamic parameters.

As described in Chapter 2, the sea ice is considered to be a mixture of pure ice and brine. Therefore, the sea ice permittivity can be calculated from the permittivity

of these two constituents, their volume fractions, and the shape of brine inclusions. Herein, I outline the procedure to calculate the sea ice permittivity as follows

1. The permittivity of the pure ice, denoted by $\epsilon_i = \epsilon_i' + j\epsilon_i''$, is calculated through [3]

$$\epsilon_i' = 3.1884 + 9.1 \times 10^{-4} T \tag{B.1}$$

$$\epsilon_i'' = \frac{\alpha_0}{f} + \beta_0 f \tag{B.2}$$

In (B.1), $T$ is in °C. Also in (B.2), the frequency $f$ is in GHz, and $\alpha_0$ and $\beta_0$ are defined as [27]

$$\alpha_0 = (0.00504 + 0.0062(\frac{300}{T_k} - 1)) \times \exp\left(-22.1(\frac{300}{T_k} - 1)\right) \tag{B.3}$$

$$\begin{aligned}\beta_0 = \frac{0.0207}{T_k} \frac{\exp\left(335/T_k\right)}{[\exp\left(335/T_k\right) - 1]^2} + \\ (1.16 \times 10^{-11}) f^2 + \exp\left[-9.963 + 0.0372(T_k - 273.16)\right]\end{aligned} \tag{B.4}$$

where $T_k$ is the temperature in °K.

2. Brine salinity, denoted by $S_b$, as a temperature dependent parameter is calculated through the following empirical equations [123]

$$S_b = \begin{cases} 1.725 - 18.756T - 0.3964T^2 & \text{for} -8.2 \leq T < -2°C \\ 57.041 - 9.929T - 0.16204T^2 - 0.002396T^3 & \text{for} -22.9 \leq T < -8.2°C \\ 242.94 + 1.5299T + 0.0429T^2 & \text{for} -36.8 \leq T < -22.9°C \\ 508.18 + 14.535T + 0.2018T^2 & \text{for} -43.2 \leq T < -36.8°C \end{cases} \tag{B.5}$$

3. The permittivity of brine, denoted by $\epsilon_b = \epsilon_b' + j\epsilon_b''$, is calculated as follows [154]

$$\epsilon_b' = \epsilon_{w\infty} + \frac{\epsilon_{b0} - \epsilon_{w\infty}}{1 + (2\pi f \tau_b)^2} \tag{B.6}$$

$$\epsilon_b'' = (2\pi f\tau_b)\frac{\epsilon_{b0} - \epsilon_{w\infty}}{1 + (2\pi f\tau_b)^2} + \frac{\sigma_b}{2\pi f\epsilon_0} \tag{B.7}$$

The parameters in (B.6) and (B.6) are calculated through the following equations [27, 154]

$$\epsilon_{w\infty} = 4.9 \tag{B.8}$$

$$\begin{aligned}\epsilon_{b0} = [88.045 - 0.4147T + 6.295 \times 10^{-4}T^2 + 1.075 \times 10^{-5}T^3]\times \\ [1 - 0.255N_b + 5.15 \times 10^{-2}N_b^2 - 6.89 \times 10^{-3}N_b^3]\end{aligned} \tag{B.9}$$

$$\begin{aligned}2\pi\tau_b = [1.1109 \times 10^{-10} - 3.824 \times 10^{-12}T + 6.938 \times 10^{-14}T^2 - 5.096 \times 10^{-16}T^3]\times \\ [1 + 0.146 \times 10^{-2}TN_b - 4.89 \times 10^{-2}N_b - 2.97 \times 10^{-2}N_b^2 + 5.64 \times 10^{-3}N_b^3]\end{aligned} \tag{B.10}$$

$$\begin{aligned}\sigma_b = [N_b(10.36 - 2.378N_b + 0.683N_b^2 - 0.135N_b^3 + 1.01 \times 10^{-2}N_b^4)]\times \\ [1 - 1.96 \times 10^{-2}\Delta + 8.08 \times 10^{-5}\Delta^2 - N_b\Delta[3.02 \times 10^{-5} + 3.92 \times 10^{-5}\Delta \\ + N_b(1.72 \times 10^{-5} - 6.58 \times 10^{-6}\Delta)]\end{aligned} \tag{B.11}$$

$$N_b = S_b[1.707 \times 10^{-2} + 1.205 \times 10^{-5}S_b + 4.058 \times 10^{-9}S_b^2] \tag{B.12}$$

$$\Delta = 25 - T \tag{B.13}$$

4. The brine volume fraction, denoted by $v_b$, in the sea ice under investigation is calculated based on the sea ice temperature and salinity, denoted by $S_i$, through the empirical expression brought below [31]

$$v_b = 10^{-3}S_i(\frac{-49.185}{T} + 0.532) \tag{B.14}$$

5. The effective permittivity of the sea ice can now be calculated through the so-called Polder-van Santen/de Loor mixture formula for spherical brine inclusions

through [155]

$$\epsilon_{\text{sea ice}} = \epsilon_i + 3v_b\epsilon^* \frac{\epsilon_b - \epsilon_i}{\epsilon_b + 2\epsilon^*} \tag{B.15}$$

In (B.15), $\epsilon^*$ is the effective dielectric constant for the region immediately surrounding an inclusion particle, determined as [27]

$$\epsilon^* = \begin{cases} \epsilon_{\text{sea ice}} & \text{for} \quad v_b > 0.1 \\ \epsilon_i & \text{for} \quad v_b \leq 0.1 \end{cases} \tag{B.16}$$

This concludes the procedure that we used to calculate the permittivity of sea ice. Finally, it should be noted that another common mixing formula utilized for sea ice is the Tinga-Voss-Blossey (TVB), that is simplified to the following for spherical brine inclusions [156]

$$\epsilon_{\text{sea ice}} = \epsilon_i + \frac{3v_b\epsilon_i(\epsilon_b - \epsilon_i)}{(2\epsilon_i + \epsilon_b) - v_b(\epsilon_b - \epsilon_i)} \tag{B.17}$$

I now present the method to calculate the permittivity of dry snow, denoted by $\epsilon_{ds}$, utilized in this thesis. This method only requires the knowledge of the dry snow density, denoted by $\rho_{ds}$, through the following empirical equation as [119]

$$\epsilon_{ds} = 1 + 1.7\rho_{ds} + 0.7\rho_{ds}^2 \tag{B.18}$$

As can be seen in (B.18), the imaginary part of the dry snow permittivity is negligible.

Finally, I describe the methodology utilized to calculate the permittivity of the brine-wetted dry snow, denoted by $\epsilon_{bds}$, in this thesis. This requires the knowledge of the snow's temperature, salinity, and density. To this end, the following steps are considered:

1. The so-called true volume fraction of the brine, denoted by $V_b$, within the snow

is calculated as [142]

$$V_b = \frac{v_b \rho_b}{(1 - v_b)\rho_i + v_b \rho_b} \times \frac{\rho_s}{\rho_b} \tag{B.19}$$

In (B.19), $\rho_i$ is the density of pure ice that is equal to 0.934 $g/cm^3$. Also, the brine density, denoted by $\rho_b$, can be calculated via $\rho_b = 1 + 0.01T$. Moreover, the brine volume fraction, $v_b$, is calculated using (B.14).

2. The permittivity of the brine-wetted dry snow is calculated via [142]

$$\epsilon_{bds} = \frac{2}{3} V_b \frac{\epsilon_b - \epsilon_{ds}}{1 + 0.053(\frac{\epsilon_b}{\epsilon_{ds}} - 1)} \tag{B.20}$$

In (B.20), the brine permittivity $\epsilon_b$ is calculated via (B.6) and (B.7).

This concludes our appendix on methodologies utilized to relate the thermodynamic properties of snow and sea ice to their permittivity values as utilized in Chapters 6 and 7.

C

# Appendix C

In this appendix, the enhanced forward solver introduced in Chapter 7 is explained for a three-layered medium with rough interfaces. To this end, the volume and surface scattering components are investigated in Sections C.1 and C.2, respectively.

## *C.1 Volume Scattering*

Herein, we demonstrate how single volume scattering with multiple boundary reflections can be formulated based on the concept of the generalized transmission coefficients. To demonstrate this, we assume a three layer medium (numbered as 0, 1, and 2) containing volume scatterers within the middle layer. The middle layer is sandwiched between two homogeneous half-spaces. This direct calculation provides insight into the role of the generalized transmission coefficient as utilized in Section 7.4.2 for multi-layered medium. To take into account multiple reflections within this three-layer medium, we utilize a ray tracing technique as introduced in [137]. Since the discussion

here is focused on co-polarized scattering, we drop the $p/q$ superscripts for simplicity.

To begin the discussion, let's assume that the field within the middle layer experiences volume scattering due to a differential volume. The tube shown in Figure C.1 contains the differential volumes over which the effect of volume scattering is integrated so as to find the collective volume scattering due to that tube. This volume scattering can be of two types: back-scattering and bi-scattering. Based on [27], the scattered power, $P_s^{\text{tube}}$, due to the interaction of the incident power, $P_i^{\text{tube}}$, with a volume scattering tube can be found as

$$\frac{P_s^{\text{tube}}}{P_i^{\text{tube}}} = \begin{cases} \sigma_V \frac{\cos(\theta)}{2\kappa}(1 - |e^{4jk_z\Delta}|), & \text{back-scattering} \\ \sigma_V \Delta |e^{2jk_z\Delta}|, & \text{bi-scattering} \end{cases} \tag{C.1}$$

where $k_z$ and $\Delta$ belong to the middle layer. (This notation holds for the rest of this appendix.) To complete our list of notations, we assume that $P_s^{\text{tube}}/P_i^{\text{tube}}$ is equal to $|\mathcal{V}|^2$ where $\mathcal{V}$ represents the field volume scattering due to the tube. In the case of back-scattering, we denote this as $\mathcal{V}^b$, and in the case of bi-scattering, it is denoted as $\mathcal{V}^{bi}$. As noted above, the collective volume scattering can be due to back-scattering and bi-scattering from the tubes. Let's now consider the back-scattering. As will be explained, back-scattering can occur under two scenarios. In the first scenario, the wave enters the tube from the above, and will then be scattered back. To understand this scenario, let's consider Figure C.1(a). As can be seen, the tube can be at position (i), (ii), etc. The field will be transferred to each position with a coefficient of $T_{0|1}$, $T_{0|1}R_{1|2}R_{1|0}e^{2jk_z\Delta}$, etc. respectively. Furthermore, for any of these positions, the scattered field will be transferred to the first half-space by $T_{1|0}$, $T_{1|0}R_{1|2}R_{1|0}e^{2jk_z\Delta}$, and etc., as depicted in

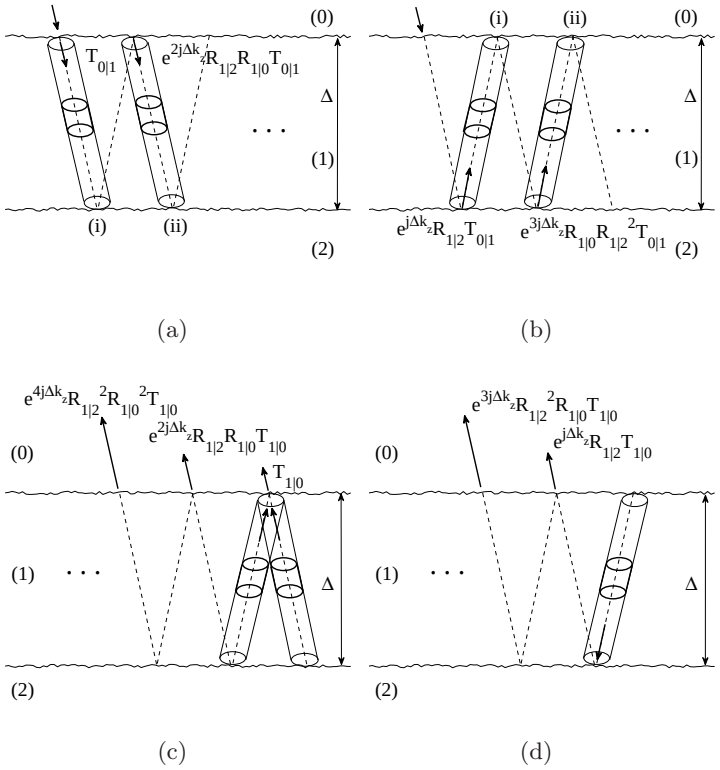


*Fig. C.1:* Different wave configurations for (a) into the back-scattering tube from above, (b) into the back-scattering tube from below and bi-scattering tube, (c) exiting the back-scattering tube from above and bi-scattering tube, and (d) exiting the back-scattering tube from below.

Figure C.1(c). Therefore, the total effect will be

$$\begin{aligned}
\frac{A_s^{b1}}{A_i} &= T_{0|1} \times \mathcal{V}^b \times \\
&(T_{1|0} + T_{1|0}R_{1|2}R_{1|0}e^{2jk_z\Delta} + ...) + \\
&(T_{0|1}R_{1|2}R_{1|0}e^{2jk_z\Delta}) \times \mathcal{V}^b \times \\
&(T_{1|0} + T_{1|0}R_{1|2}R_{1|0}e^{2jk_z\Delta} + ...) + \\
&... \\
&= (T_{0|1} + T_{0|1}R_{1|2}R_{1|0}e^{2jk_z\Delta} + ...) \times \\
&(T_{1|0} + T_{1|0}R_{1|2}R_{1|0}e^{2jk_z\Delta} + ...) \times \mathcal{V}^b. \qquad \text{(C.2)}
\end{aligned}$$

Each of the last two parenthesis in (C.2) contains an infinite geometric series. Therefore, they simplify as

$$\frac{A_s^{b1}}{A_i} = \mathcal{V}^b \overbrace{\frac{T_{0|1}}{1 - R_{1|2}R_{1|0}e^{2jk_z\Delta}}}^{=\mathfrak{T}_{0|1}} \times \overbrace{\frac{T_{1|0}}{1 - R_{1|2}R_{1|0}e^{2jk_z\Delta}}}^{=\mathfrak{T}_{1|0}} \tag{C.3}$$

We note that $R_{i|j} = -R_{j|i}$. In (C.3), $\mathfrak{T}$ represents the generalized transmission coefficient introduced in (7.4). Now let's calculate the corresponding NRCS as

$$\sigma = \frac{4\pi R_r^2}{C_0}\frac{S^s}{S^i} = \frac{4\pi R_r^2}{C_0}\frac{|A_s|^2/4\pi R_r^2}{|A_i|^2/C_0} = \frac{|A_s|^2}{|A_i|^2} \tag{C.4}$$

where $C_0$ and $R_r$ are the cross-section area of the tube and the observation distance from the profile, respectively. Therefore, this NRCS will be

$$\begin{aligned}\sigma_1 &= |\mathcal{V}^b|^2 |\mathfrak{T}_{0|1}|^2 |\mathfrak{T}_{1|0}|^2 \\ &= \underbrace{\sigma_V \frac{\cos(\theta)}{2\kappa}(1 - |e^{4jk_z\Delta}|)}_{=\sigma_{v1}^{(1)}} |\mathfrak{T}_{0|1}|^2 |\mathfrak{T}_{1|0}|^2\end{aligned} \tag{C.5}$$

where $\sigma_1$ is the NRCS observed at the first half space (layer 0), and $\sigma_{v1}^{(1)}$ is the NRCS corresponding to the middle layer (layer 1) associated with this scenario whose effect is transferred to the 0th layer via $\mathfrak{T}_{1|0}$ and $\mathfrak{T}_{0|1}$ coefficients. To link this to the three mechanisms presented in Section 7.4.2, we note that this scattering is associated with the particle back-scattering. This concludes our discussion on the first scenario for back-scattering.

Now, let's consider the second scenario for volume scattering due to back-scattering, as shown in Figure C.1(b). In this scenario, the field enters the tube from the bottom due to reflection(s) at the interface of layer 1 and layer 2. The field is then back-scattered by the tube, and will then reach the 0th layer. This can be better understood by noting Figure C.1(b) in which the tube could be at position (i), or (ii), etc. The field will be

transferred to each position with a coefficient of $T_{0|1}R_{1|2}e^{jk_z\Delta}$, $T_{0|1}R_{1|2}{}^2R_{1|0}e^{j3k_z\Delta}$, etc. Furthermore, for any of these positions, the scattered field will be transferred to the first half-space by $T_{1|0}R_{1|2}e^{jk_z\Delta}$, $T_{1|0}R_{1|2}{}^2R_{1|0}e^{3jk_z\Delta}$, etc., as depicted in Figure C.1(d). Therefore, the total effect will be

$$\begin{aligned}
&\frac{A_s^{b2}}{A_i} = (T_{0|1}R_{1|2}e^{jk_z\Delta}) \times \mathcal{V}^b \times \\
&(T_{1|0}R_{1|2}e^{jk_z\Delta} + T_{1|0}R_{1|2}{}^2R_{1|0}e^{3jk_z\Delta} + ...) + \\
&(T_{0|1}R_{1|2}{}^2R_{1|0}e^{3jk_z\Delta}) \times \mathcal{V}^b \times \\
&(T_{1|0}R_{1|2}e^{jk_z\Delta} + T_{1|0}R_{1|2}{}^2R_{1|0}e^{3jk_z\Delta} + ...) + \\
&... \\
&= (T_{0|1}R_{1|2}e^{jk_z\Delta} + T_{0|1}R_{1|2}{}^2R_{1|0}e^{3jk_z\Delta} + ...) \times \\
&(T_{1|0}R_{1|2}e^{jk_z\Delta} + T_{1|0}R_{1|2}{}^2R_{1|0}e^{3jk_z\Delta} + ...) \times \mathcal{V}^b
\end{aligned} \tag{C.6}$$

The last two parenthesis in (C.6), each has an infinite geometric series. Therefore, they simplify as

$$\frac{A_s^{b2}}{A_i} = (R_{1|2}e^{jk_z\Delta})^2\mathcal{V}^b \overbrace{\frac{T_{0|1}}{1 - R_{1|2}R_{1|0}e^{2jk_z\Delta}}}^{=\mathfrak{T}_{0|1}} \overbrace{\frac{T_{1|0}}{1 - R_{1|2}R_{1|0}e^{2jk_z\Delta}}}^{=\mathfrak{T}_{1|0}} \tag{C.7}$$

Consequently utilizing (C.4), the NRCS respective to this scenario is calculated as

$$\begin{aligned}
\sigma_2 &= |R_{1|2}|^4|e^{4jk_z\Delta}||\mathcal{V}^b|^2|\mathfrak{T}_{0|1}|^2|\mathfrak{T}_{1|0}|^2 \\
&= \underbrace{|R_{1|2}|^4|e^{4jk_z\Delta}|\sigma_V \frac{\cos(\theta)}{2\kappa}(1 - |e^{4jk_z\Delta}|)}_{=\sigma_{v3}^{(1)}} |\mathfrak{T}_{0|1}|^2|\mathfrak{T}_{1|0}|^2
\end{aligned} \tag{C.8}$$

where $\sigma_2$ is the NRCS observed at the first half space (layer 0), and $\sigma_{v3}^{(1)}$ is the NRCS corresponding to the middle layer (layer 1) associated with this scenario whose effect

is transferred to the 0th layer via $\mathfrak{T}_{1|0}$ and $\mathfrak{T}_{0|1}$ coefficients. To link this to the three mechanisms presented in Section 7.4.2, we note that this scattering is associated with the interface-particle-interface scattering mechanism. This concludes our discussion on the second scenario for back-scattering.

We will now consider the volume scattering due to bi-scattering effects of the scatterers within the middle layer. This bi-scattering can happen under two scenarios. The first scenario involves an incoming field as shown in Figure C.1(b). Upon reflection(s) from the interface of layer 1 and layer 2, this field enters the tube. The volume scattering then occurs in a bi-static fashion, and the resulting scattered field enters the half space (layer 0) as depicted in Figure C.1(c). Therefore, following the same procedure, we will have

$$\begin{aligned}
&\frac{A_s^{bi}}{A_i} = (T_{0|1}R_{1|2}e^{jk_z\Delta}) \times \mathcal{V}^{bi}\times \\
&(T_{1|0} + T_{1|0}R_{1|2}R_{1|0}e^{2jk_z\Delta} + ...)+ \\
&(T_{0|1}R_{1|2}^2R_{1|0}e^{3jk_z\Delta}) \times \mathcal{V}^{bi}\times \\
&(T_{1|0} + T_{1|0}R_{1|2}R_{1|0}e^{2jk_z\Delta} + ...)+ \\
&... \\
&= (T_{0|1}R_{1|2}e^{jk_z\Delta} + T_{0|1}{R_{1|2}}^2R_{1|0}e^{3jk_z\Delta} + ...)\times \\
&(T_{1|0} + T_{1|0}R_{1|2}R_{1|0}e^{2jk_z\Delta} + ...) \times \mathcal{V}^{bi}
\end{aligned} \tag{C.9}$$

Again, the last two parenthesis in (C.9), each contains an infinite geometric series. Therefore, they simplify into

$$\frac{A_s^{bi}}{A_i} = (R_{1|2}e^{jk_z\Delta})\mathcal{V}^{bi}\overbrace{\frac{T_{0|1}}{1 - R_{1|2}R_{1|0}e^{2jk_z\Delta}}}^{=\mathfrak{T}_{0|1}}\overbrace{\frac{T_{1|0}}{1 - R_{1|2}R_{1|0}e^{2jk_z\Delta}}}^{=\mathfrak{T}_{1|0}} \tag{C.10}$$

The second scenario for volume scattering due to bi-scattering is simply the mirror of

the first scenario. This would give a multiple of two to the right hand side of (C.10). Therefore utilizing (C.4), the NRCS due to this configuration is calculated as

$$\begin{aligned}\sigma_3 &= 4|R_{1|2}|^2|e^{2jk_z\Delta}||\mathcal{V}^b|^2|\mathfrak{T}_{0|1}|^2|\mathfrak{T}_{1|0}|^2 \\ &= \underbrace{4|R_{1|2}|^2|e^{2jk_z\Delta}|\sigma_V\Delta|e^{2jk_z\Delta}|}_{=\sigma_{v2}^{(1)}}|\mathfrak{T}_{0|1}|^2|\mathfrak{T}_{1|0}|^2 \end{aligned} \tag{C.11}$$

where $\sigma_3$ is the NRCS observed at the first half space (layer 0), and $\sigma_{v2}^{(1)}$ is the NRCS corresponding to the middle layer (layer 1) associated with this bi-scattering configuration whose effect is transferred to the 0th layer via $\mathfrak{T}_{1|0}$ and $\mathfrak{T}_{0|1}$ coefficients. Similarly, to link this to the three mechanisms presented in Section 7.4.2, we note that this scattering is associated with the particle-interface scattering mechanism.

To account for the effect of all different configurations, we utilize a summation as in [27] to calculate the total NRCS, $\sigma_v$. Thus, from (C.5), (C.8), and (C.11) it follows

$$\begin{aligned}\sigma_v = \sum_{i=1}^{3}\sigma_i =&(\sigma_{v1}^{(1)} + \sigma_{v2}^{(1)} + \sigma_{v3}^{(1)})|\mathfrak{T}_{0|1}|^2|\mathfrak{T}_{1|0}|^2 \\ =&\sigma_v^{(1)}|\mathfrak{T}_{0|1}|^2|\mathfrak{T}_{1|0}|^2 \end{aligned} \tag{C.12}$$

As can be seen, the above equation is identical to (7.7) for a three-layered medium considered here. In addition, (C.12) may be re-written as

$$\sigma_v = \sigma_v^{(1)}|\mathfrak{T}_{0|1}|^2\frac{\eta_0\cos(\theta)}{\eta\cos(\theta_0)}|\mathfrak{T}_{1|0}|^2\frac{\eta\cos(\theta_0)}{\eta_0\cos(\theta)} = \sigma_v^{(1)}\mathtt{T}_{0|1}\mathtt{T}_{1|0} \tag{C.13}$$

where we refer to $\mathtt{T}$ as the generalized transmittivity. If we consider only one reflection (*i.e.*, Fresnel reflection and transmission coefficients instead of generalized coefficients), (C.13) will be identical to the expression presented in [27] for a similar profile.

## *C.2 Surface Scattering*

Herein, we consider the same profile as presented above. The goal is to show how the cross-polarized surface scattering is calculated. Let's assume that the surface scattering component due to the first interface is $\sigma_s^{pq,(1)}$, which can be found from (7.2). For the second interface, following the same procedure presented in the previously, we have

$$\begin{aligned}
&\frac{A_s}{A_i} = (T_{0|1}e^{jk_z\Delta}) \times \mathcal{S}\times \\
&(T_{1|0}e^{jk_z\Delta} + T_{1|0}e^{jk_z\Delta}R_{1|0}R_{1|2}e^{2jk_z\Delta} + ...)+ \\
&(T_{0|1}e^{jk_z\Delta}R_{1|0}R_{1|2}e^{2jk_z\Delta}) \times \mathcal{S}\times \\
&(T_{1|0}e^{jk_z\Delta} + T_{1|0}e^{jk_z\Delta}R_{1|0}R_{1|2}e^{2jk_z\Delta} + ...)+ \\
&... \\
&= (T_{0|1}e^{jk_z\Delta} + T_{0|1}e^{jk_z\Delta}R_{1|0}R_{1|2}e^{2jk_z\Delta} + ...)\times \\
&(T_{1|0}e^{jk_z\Delta} + T_{1|0}e^{jk_z\Delta}R_{1|0}R_{1|2}e^{2jk_z\Delta} + ...) \times \mathcal{S}
\end{aligned} \tag{C.14}$$

where $\mathcal{S}$ represents the field cross-polarized surface scattering effect at the interface of the layers 1 and 2 assuming that these layers are half spaces. Again, utilizing the formulation for an infinite geometric series, we simplify (C.14) as

$$\frac{A_s}{A_i} = (e^{jk_z\Delta})^2\mathcal{S}\overbrace{\frac{T_{0|1}}{1 - R_{1|2}R_{1|0}e^{2jk_z\Delta}}}^{=\mathfrak{T}_{0|1}}\overbrace{\frac{T_{1|0}}{1 - R_{1|2}R_{1|0}e^{2jk_z\Delta}}}^{=\mathfrak{T}_{1|0}} \tag{C.15}$$

Assuming that the field surface scattering $\mathcal{S}$ results in the corresponding NRCS of $\sigma_s^{pq,(2)}$, the total surface scattering NRCS is calculated as

$$\sigma_s^{pq} = \sigma_s^{pq,(1)} + |e^{4jk_z\Delta}||\mathfrak{T}_{0|1}|^2|\mathfrak{T}_{1|0}|^2\sigma_s^{pq,(2)} \tag{C.16}$$

As can be seen, this is consistent with the formulation presented in Section 7.4.1.1.

# Bibliography


[1] J. Larsen, O. Anisimov, A. Constable, A. Hollowed, N. Maynard, P. Prestrud, T. Prowse, and J. Stone, "Part B: Regional Aspects. Contribution of working group II to the fifth assessment report of the intergovernmental panel on climate change," in *Polar Regions Climate Change 2014: Impacts, Adaptation, and Vulnerability*. Cambridge University Press, 2014, pp. 1567–1612.

[2] Intergovernmental Panel on Climate Change (IPCC), "Climate change 2001: Third assessment report," 2001.

[3] C. Matzler and U. Wegmuller, "Dielectric properties of freshwater ice at microwave frequencies," *Journal of Physics D: Applied Physics*, vol. 20, no. 12, p. 1623, 1987.

[4] A. Stogryn and G. Desargant, "The dielectric properties of brine in sea ice at microwave frequencies," *Antennas and Propagation, IEEE Transactions on*, vol. 33, no. 5, pp. 523–532, 1985.

[5] L. G. Backstrom and H. Eicken, "Capacitance probe measurements of brine volume and bulk salinity in first-year sea ice," *Cold Regions Science and Technology*, vol. 46, no. 3, pp. 167 – 180, 2006.

[6] G. H. Peter Mills, "Sea ice brightness temperature as a function of ice thickness," Peteysoft Foundation, Institute of Environmental Physics, University of Bremen, Tech. Rep., 2011.

[7] P. Mojabi, M. Ostadrahimi, L. Shafai, and J. LoVetri, "Microwave tomography techniques and algorithms: A review," in *Antenna Technology and Applied Electromagnetics (ANTEM), 2012 15th International Symposium on*, June 2012, pp. 1–4.

[8] T. K. Jensen, "Stabilization algorithms for large-scale problems," Ph.D. dissertation, Technical University of Denmark, Kongens Lyngby, Denmark, 2006.

[9] T. N. Papakyriakou, "An examination of relationships among the energy balance, surface properties and climate over snow covered sea ice during the spring season," Ph.D. dissertation, University ofWaterloo, 1999.

[10] P. Wadhams, *Ice in the Ocean*. Gordon and Breach Sciece Publishers, 2000.

[11] D. G. Barber, J. K. Ehn, M. Pucko, S. Rysgaard, J. W. Deming, J. S. Bowman, T. Papakyriakou, R. J. Galley, and D. H. Sogaard, "Frost flowers on young Arctic sea ice: The climatic, chemical, and microbial significance of an emerging ice type," *Journal of Geophysical Research: Atmospheres*, vol. 119, no. 20, pp. 11,593–11,612, 2014.

[12] D. Isleifson, R. Galley, D. Barber, J. Landy, A. Komarov, and L. Shafai, "A study on the C-band polarimetric scattering and physical characteristics of frost flowers on experimental sea ice," *Geoscience and Remote Sensing, IEEE Transactions on*, vol. 52, no. 3, pp. 1787–1798, 2014.

[13] D. Barber and A. Thomas, "The influence of cloud cover on the radiation budget, physical properties, and microwave scattering coefficient of first-year and multiyear sea ice," *Geoscience and Remote Sensing, IEEE Transactions on*, vol. 36, no. 1, pp. 38–50, Jan 1998.

[14] R. G. Onstott, *SAR and Scatterometer Signatures of Sea Ice*. American Geophysical Union, 2013, pp. 73–104.

[15] S. G. Warren and et. al., "Snow depth on arctic sea ice," *J. Climate*, vol. 12, pp. 1814–1826, 1999.

[16] N. Untersteinerg, *The Geophysics of Sea Ice*. NATO ASI Series Plenum Press, 1981.

[17] O. Lecomte, T. Fichefet, M. Vancoppenolle, F. Domine, F. Massonnet, P. Mathiot, S. Morin, and P. Barriat, "On the formulation of snow thermal conductivity in large-scale sea ice models," *Journal of Advances in Modeling Earth Systems*, vol. 5, no. 3, pp. 542–557, 2013.

[18] M. Q. Edens, "An experimental investigation of metamorphism induced microstructure evolution in a model cohesive snow," Ph.D. dissertation, Montana State University, 1997.

[19] S. Colbeck, "An overview of seasonal snow metamorphism," *Rev. Geophys. Space Phys.*, vol. 20, pp. 45–61, 1982.

[20] A. Denoth, "Wet snow pendular regime: the amount of water in ring-shaped configurations," *Cold Regions Science and Technology*, vol. 30, no. 3, pp. 13–18, 1999.

[21] C. A. Balanis, *Advanced Engineering Electromagnetics, 2nd Edition*. Wiley-IEEE Press, 2012.

[22] P. Frubing, "Time and frequency dependence of a debye-type orientational polarizations," University of Potsdam, Tech. Rep., 2015.

[23] C. Matzler and U. Wegmuller, "Dielectric properties of fresh-water ice at microwave frequencies," *J.Phys. D: Appl. Phys.*, vol. 20, pp. 1623–1630, 1987.

[24] T. Meissner and F. Wentz, "The complex dielectric constant of pure and sea water from microwave satellite observations," *Geoscience and Remote Sensing, IEEE Transactions on*, vol. 42, no. 9, pp. 1836–1849, Sept 2004.

[25] A. Sihvola, *Electromagnetic Mixing Formulas and Applications*, ser. Electromagnetic Waves. Institution of Engineering and Technology, 1999.

[26] D. Polder and J. van Santeen, "The effective permeability of mixtures of solids," *Physica*, vol. 12, no. 5, pp. 257 – 271, 1946.

[27] F. T. Ulaby and D. G. Long, *Microwave Radar and Radiometric Remote Sensing*. University of Michigan Press, 2014.

[28] F. Ulaby, R. Moore, and A. Fung, *Microwave Remote Sensing*. Artech house, Norwood, MA, 1986.

[29] A. Stogryn and G. Desargant, "The dielectric properties of brine in sea ice at microwave frequencies," *Antennas and Propagation, IEEE Transactions on*, vol. 33, no. 5, pp. 523–532, May 1985.

[30] G. F. N. Cox and W. Weeks, "Equations for determining the gas and brine volumes in sea-ice samples," *Journal of Glaciology*, vol. 29, no. 102, 1983.

[31] G. Frankenstein and R. Garner, "Equations for determining the brine volume of sea ice," *J. Glaciol.*, vol. 6, no. 48, pp. 943–944, 1967.

[32] M. Hallikainen, F. Ulaby, and M. Abdelrazik, "Dielectric properties of snow in the 3 to 37 GHz range," *Antennas and Propagation, IEEE Transactions on*, vol. 34, no. 11, pp. 1329–1340, 1986.

[33] A. K. Jordan and M. E. Veysoglu., "Electromagnetic remote sensing of sea ice," *Inverse Problems*, vol. 10, pp. 1041–1058, 1994.

[34] M. E. Tiuri, A. Sihvola, E. Nyfors, and M. Hallikaiken, "The complex dielectric constant of snow at microwave frequencies," *Oceanic Engineering, IEEE Journal of*, vol. 9, no. 5, pp. 377–382, Dec 1984.

[35] M. R. Drinkwater and G. Crocker, "Modelling changes scattering in properties of the dielectric and young snow-covered sea ice at GHz frequencies," *Journal of Glaciology*, vol. 34, no. 118, 1988.

[36] G. A. Maykut and N. Untersteiner, "Some results from a time-dependent thermodynamic model of sea ice," *Journal of Geophysical Research*, vol. 76, no. 6, pp. 1550–1575, 1971.

[37] E. Anderson, "Point energy and mass balance model of a snow cover," NOAA Technical Report NWS 19, Tech. Rep., 1976.

[38] N. Ono, "Thermal properties of sea ice: IV; thermal constants of sea ice," *Low Temp. Sci.*, pp. 249–258, 1968.

[39] N. Untersteiner, "On the mass and heat budget of arctic sea-ice," *Arch. Meteorol. Geophys. Bioklimatol.*, pp. 151–282, 1961.

[40] E. E. Ebert and J. A. Curry, "An intermediate one-dimensional thermodynamic sea ice model for investigating ice-atmosphere interactions," *Journal of Geophysical Research: Oceans*, vol. 98, no. C6, pp. 10 085–10 109, 1993.

[41] ——, "An intermediate one-dimensional thermodynamic sea ice model for investigating ice-atmosphere interactions," *Journal of Geophysical Research: Oceans*, vol. 98, no. C6, pp. 10 085–10 109, 1993.

[42] D. G. Barber, "Microwave remote sensing, sea ice and Arctic climate," *Phys. Can.*, vol. 61, pp. 105–111, Sept 2005.

[43] e. a. Caludia Notarnicola, "Retrieval of essential climate variables: Data and methods," GRSS Summer School Notes, 2014.

[44] G. Belchansky, I. Alpatsky, V. Eremeev, I. Mordvintsev, N. Platonov, and D. Douglas, "Estimating multiyear sea-ice concentration using passive microwave data and mlp neural networks," in *Geoscience and Remote Sensing Symposium, 2003. IGARSS '03. Proceedings. 2003 IEEE International*, vol. 4, July 2003, pp. 2332–2334 vol.4.

[45] F. D. Carsey, *Microwave Remote Sensing of Sea Ice*. American Geophysical Union, 1992.

[46] K. Nakamura, H. Wakabayashi, M. Nakayama, K. Naoki, T. Toyota, S. kojima, F. Nishio, and S. Uratsuka, "Study on the sea ice thickness observation in the sea of okhotsk by using dual-frequency and fully polarimetric airborne SAR (PI-SAR) data," in *Geoscience and Remote Sensing Symposium, 2004. IGARSS '04. Proceedings. 2004 IEEE International*, vol. 7, Sept 2004, pp. 4386–4389 vol.7.

[47] T. Matsuoka, S. Uratsuka, M. Satake, A. Nadai, T. Umehara, H. Maeno, H. Wakabayashi, F. Nishio, and Y. Fukamachi, "Deriving sea-ice thickness and ice types in the sea of okhotsk using dual-frequency airborne sar (pi-sar) data," *Annals of Glaciology*, vol. 34, no. 1, pp. 429–434, 2002.

[48] J.-W. Kim, D. jin Kim, and B. J. Hwang, "Estimation of sea ice thickness in the arctic sea using polarimetric parameters of c- and x-band space-borne sar data," in *Geoscience and Remote Sensing Symposium (IGARSS), 2010 IEEE International*, July 2010, pp. 2402–2405.

[49] J. C. Comiso, "Sea ice effective microwave emissivities from satellite passive microwave and infrared observations," *Journal of Geophysical Research: Oceans*, vol. 88, no. C12, pp. 7686–7704, 1983.

[50] J. Karvonen, "Baltic sea ice SAR segmentation and classification using modified pulse-coupled neural networks," *Geoscience and Remote Sensing, IEEE Transactions on*, vol. 42, no. 7, pp. 1566–1574, July 2004.

[51] N. T. Kurtz, S. L. Farrell, M. Studinger, N. Galin, J. P. Harbeck, R. Lindsay, V. D. Onana, B. Panzer, and J. G. Sonntag, "Sea ice thickness, freeboard, and snow depth products from operation icebridge airborne data," *The Cryosphere*, vol. 7, no. 4, pp. 1035–1056, 2013.

[52] B. Holt, P. Kanagaratnam, S. P. Gogineni, V. C. Ramasami, A. Mahoney, and V. Lytle, "Sea ice thickness measurements by ultrawideband penetrating radar: First results," *Cold Regions Science and Technology*, vol. 55, pp. 33–46, 2009.

[53] S. Leinss, G. Parrella, and I. Hajnsek, "Snow height determination by polarimetric phase differences in x-band sar data," *Selected Topics in Applied Earth Observations and Remote Sensing, IEEE Journal of*, vol. 7, no. 9, pp. 3794–3810, Sept 2014.

[54] A. E. Walker and A. Silis, "Snow-cover variations over the Mackenzie River basin, Canada, derived from SSM/I passive-microwave satellite data," *Annals of Glaciology*, vol. 34, no. 1, 2002.

[55] A. J. Devaney, "A filtered backpropagating algorithm for diffraction tomography," *Ultrasonic Imaging*, vol. 4, pp. 336–350, 1982.

[56] K. Golden, D. Borup, M. Cheney, E. Cherkaeva, M. Dawson, K.-H. Ding, A. Fung, D. Isaacson, S. Johnson, A. K. Jordan, J. A. Kon, R. Kwok, S. Nghiem, R. Onstott, J. Sylvester, D. Winebrenner, and I. H. H. Zabel, "Inverse electromagnetic scattering models for sea ice," *Geoscience and Remote Sensing, IEEE Transactions on*, vol. 36, no. 5, pp. 1675–1704, 1998.

[57] M. Dawson, A. Fung, and M. Manry, "Sea ice classification using fast learning neural networks," in *Geoscience and Remote Sensing Symposium, 1992. IGARSS '92. International*, vol. 2, 1992, pp. 1070–1071.

[58] Y. J. Lee, W. Lim, H. T. Ewe, and H. T. Chuah, "A study of dense medium scattering and its applications in sea ice research in Ross Island,Antarctica," in *Geoscience and Remote Sensing Symposium (IGARSS), 2011 IEEE International*, 2011, pp. 5–8.

[59] A. Abubakar, P. van den Berg, and J. Mallorqui, "Imaging of biomedical data using a multiplicative regularized contrast source inversion method," *Microwave Theory and Techniques, IEEE Transactions on*, vol. 50, no. 7, pp. 1761–1771, 2002.

[60] S.-E. Shih and et. al., "Thin saline ice thickness retrieval using time-series c-band polarimetric radar measurements," *Geoscience and Remote Sensing, IEEE Transactions on*, vol. 36, no. 5, pp. 1589–1598, 1998.

[61] C. Davis, "A surface and volume scattering retracking algorithm for ice sheet satellite altimetry," *Geoscience and Remote Sensing, IEEE Transactions on*, vol. 31, no. 4, pp. 811–818, 1993.

[62] Y. J. Lee, W. K. Lim, and H.-T. Ewe, "A study of an inversion model for sea ice thickness retrieval in ross island, antarctica," *Progress In Electromagnetics Research*, vol. 111, pp. 381–406, 2011.

[63] Q. Remund and D. Long, "Large-scale inverse ku-band backscatter modeling of sea ice," *Geoscience and Remote Sensing, IEEE Transactions on*, vol. 41, no. 8, pp. 1821–1833, Aug 2003.

[64] A. Pfaffling and J. E. Reid, "Sea ice as an evaluation target for hem modelling and inversion," *Journal of Applied Geophysics*, vol. 67, no. 3, pp. 242–249, 2009.

[65] C. Wu, X. Zhang, and G. Fang, "A novel technique for radar depth sounding of fast outlet glaciers and ice-sheet margins," *Geoscience and Remote Sensing Letters, IEEE*, vol. 12, no. 3, pp. 587–591, March 2015.

[66] A. Komarov, D. Isleifson, D. Barber, and L. Shafai, "Modeling and measurement of C-band radar backscatter from snow-covered first-year sea ice," *Geoscience and Remote Sensing, IEEE Transactions on*, vol. 53, no. 7, pp. 4063–4078, July 2015.

[67] H. Ewe, M. Veysoglu, C. Hsu, R. Shin, and J. Kong, "Radiative transfer theory for remote sensing of sea ice," in *Geoscience and Remote Sensing Symposium, 1994. IGARSS '94. Surface and Atmospheric Remote Sensing: Technologies, Data Analysis and Interpretation., International*, vol. 1, Aug 1994, pp. 623–625 vol.1.

[68] H. Wakabayashi, T. Matsuoka, K. Nakamura, and F. Nishio, "Polarimetric characteristics of sea ice in the sea of Okhotsk observed by airborne L-band SAR," *Geoscience and Remote Sensing, IEEE Transactions on*, vol. 42, no. 11, pp. 2412–2425, Nov 2004.

[69] E. Nassar, "Numerical and experimental studies of electromagnetic scattering from sea ice," Ph.D. dissertation, Ohio State University, 1997.

[70] S. V. Nghiem and et. al., "Polarimetric remote sensing of geophysical media with layer random medium mode," *Progress In Electrogmagnetics Researchn*, 1991.

[71] F. Chen, *Microwave Scattering and emission models for users.* Artech House, 2010.

[72] D. Isleifson, I. Jeffrey, L. Shafai, J. LoVetri, and D. Barber, "A monte carlo method for simulating scattering from sea ice using FVTD," *Geoscience and Remote Sensing, IEEE Transactions on*, vol. 50, no. 7, pp. 2658–2668, 2012.

[73] V. Isakov, "Uniqueness and stability in multi-dimensional inverse problems," *Inverse Problems*, vol. 9, no. 6, p. 579, 1993.

[74] A. Newton, *Scattering Theory of Waves and Particles*, 2nd ed. Springer-Verlag, 1982.

[75] P. Mojabi and J. LoVetri, "Overview and classification of some regularization techniques for the Gauss-Newton inversion method applied to inverse scattering problems," *Antennas and Propagation, IEEE Transactions on*, vol. 57, no. 9, pp. 2658–2665, 2009.

[76] P. Rocca, G. Oliveri, and A. Massa, "Differential evolution as applied to electromagnetics," *Antennas and Propagation Magazine, IEEE*, vol. 53, no. 1, pp. 38–49, 2011.

[77] A. Abubakar and P. Van den Berg, "Multiplicative regularization technique for location and shape reconstructions of homogeneous objects," in *Antennas and Propagation Society International Symposium, 2002. IEEE*, vol. 1, 2002, pp. 292–295 vol.1.

[78] P. C. Hansen and D. P. O'leary, "The use of the L-curve in the regularization of discrete ill-posed problems," *SIAM J. Sci. Comput.*, vol. 14, no. 6, pp. 1487–1503, Nov 1993.

[79] G. H. Golub, M. Heath, and G. Wahba, "Generalized cross validation as a method for choosing a good ridge parameter," *Technometrics*, vol. 21, pp. 215–224, 1979.

[80] A. Kirsch, *An Introduction to the Mathematical Theory of Inverse Problems*. Springer-Verlag, 1996.

[81] T. M. Habashy and A. Abubakar, "A general framework for constraint minimization for the inversion of electromagnetic measurements," *Progress In Electromagnetics Research*, vol. 46, pp. 265–312, 2004.

[82] A. Abubakar, G. Pan, M. Li, L. Zhang, T. Habashy, and P. van den Berg, "Three-dimensional seismic full-waveform inversion using the finite-difference contrast source inversion method," *Geophysical Prospecting*, vol. 59, no. 5, pp. 874–888, 2011.

[83] A. Devaney and G. Sherman, "Nonuniqueness in inverse source and scattering problems," *Antennas and Propagation, IEEE Transactions on*, vol. 30, no. 5, pp. 1034–1037, Sep 1982.

[84] A. Abubakar, T. M. Habashy, V. L. Druskin, L. Knizhnerman, and D. Alumbaugh, "2.5D forward and inverse modeling for interpreting low-frequency electromagnetic measurements," *Geophysics*, vol. 73, no. 4, pp. F165–F177, July–Aug 2008.

[85] W. K. L. Y. J. Lee and H.-T. Ewe, "A study of an inversion model for sea ice thickness retrieval in ross island, antarctica," *Progress In Electromagnetics Research*, vol. 111, pp. 381–406, 2011.

[86] C. Gilmore, P. Mojabi, A. Zakaria, S. Pistorius, and J. LoVetri, "On super-resolution with an experimental microwave tomography system," *Antennas and Wireless Propagation Letters, IEEE*, vol. 9, pp. 393–396, 2010.

[87] L. Tsang, J. A. Kon, and K.-H. Ding, *Scattering of Electromagnetic Waves, Theories and Applications*. WILEY, 2000.

[88] A. Abubakar, T. M. Habashy, V. L. Druskin, L. Knizhnerman, and D. Alumbaugh, "2.5D forward and inverse modeling for interpreting low-frequency electromagnetic measurements," *Geophysics*, vol. 73, no. 4, pp. F165–F177, 2008.

[89] N. Firoozy, A. Komarov, P. Mojabi, D. Barber, J. Landy, and R. Scharien, "Retrieval of young snow-covered sea-ice temperature and salinity evolution through radar cross-section inversion," *Oceanic Engineering, IEEE Journal of*, vol. PP, no. 99, pp. 1–13, 2015.

[90] N. Firoozy, A. Komarov, J. Landy, D. Barber, P. Mojabi, and R. Scharien, "Inversion-based sensitivity analysis of snow-covered sea ice electromagnetic profiles," *Selected Topics in Applied Earth Observations and Remote Sensing, IEEE Journal of*, vol. 8, no. 7, pp. 3643–3655, July 2015.

[91] N. Firoozy, P. Mojabi, and D. Barber, "Nonlinear inversion of microwave scattering data for snow-covered sea-ice dielectric profile reconstruction," *Geoscience and Remote Sensing Letters, IEEE*, vol. 12, no. 1, pp. 209–213, Jan 2015.

[92] P. Imperatore, A. Iodice, and D. Riccio, "Consistency and validity of perturbative formulations for scattering from rough multilayers," *Antennas and Propagation, IEEE Transactions on*, vol. 60, no. 4, pp. 2019–2027, 2012.

[93] S. A. Tabatabaeenejad, "Forward and inverse models of electromagnetic scattering from layered media with rough interfaces," Ph.D. dissertation, University of Michigan, 2008.

[94] P. Imperatore, A. Iodice, and D. Riccio, "Electromagnetic wave scattering from layered structures with an arbitrary number of rough interfaces," *IEEE Trans. Geosci. Remote Sens*, vol. 47, no. 4, pp. 1056–1072, 2009.

[95] P. Imperatore, "Perturbation theory for electromagnetic wave scattering in random layered structures," Ph.D. dissertation, University of Naples Federico II, Corso Umberto I, 40, 80138 Napoli, Italy, 2010.

[96] A. Darawankul and J. Johnson, "Band-limited exponential correlation function for rough-surface scattering," *Geoscience and Remote Sensing, IEEE Transactions on*, vol. 45, no. 5, pp. 1198–1206, May 2007.

[97] J. Landy, D. Isleifson, A. Komarov, and D. Barber, "Parameterization of centimeter-scale sea ice surface roughness using terrestrial LiDAR," *Geoscience and Remote Sensing, IEEE Transactions on*, vol. PP, no. 99, pp. 1–16, 2014.

[98] E. I. Thorsos and D. R. Jackson, "The validity of the perturbation approximation for rough surface scattering using a gaussian roughness spectrum," *The Journal of the Acoustical Society of America*, vol. 86, pp. 261–277, 1989.

[99] A. Qing, "Electromagnetic inverse scattering of multiple two-dimensional perfectly conducting objects by the differential evolution strategy," *Antennas and Propagation, IEEE Transactions on*, vol. 51, no. 6, pp. 1251–1262, 2003.

[100] N. Baatar, D. Zhang, and C.-S. Koh, "An improved differential evolution algorithm adopting $\lambda$–best mutation strategy for global optimization of electromagnetic devices," *Magnetics, IEEE Transactions on*, vol. 49, no. 5, pp. 2097–2100, 2013.

[101] A. Wirgin, "The inverse crime," labratoire de mecanique et d'acoustique, Tech. Rep., 2006.

[102] N. Firoozy, P. Mojabi, and D. G. Barber, "Balanced inversion of simulated bistatic radar cross-section data for remote sensing of snow-covered sea ice," *Remote Sensing Letters*, vol. 6, no. 5, pp. 399–408, 2015.

[103] N. Firoozy, P. Mojabi, and D. Barber, "Balanced inversion of radar cross section data for snow-covered sea ice dielectric profile reconstruction," in *Radio Science Meeting (Joint with AP-S Symposium), 2014 USNC-URSI*, July 2014, pp. 176–176.

[104] T. Habashy and A. Abubakar, "A general framework for constrained minimization for the inversion of electromagnetic measurements," *Progress in Electromagnetics Research*, vol. 46, pp. 265–312, 2004.

[105] V. Isakov, "uniqueness and stability in multi-dimensional inverse problems," *Inverse Problems*, vol. 9, no. 6, p. 579, 1993.

[106] P. C. Hansen, *Rank-Deficient and Discrete Ill-Posed Problems: Numerical Aspects of Linear Inversion*. SIAM, 1998.

[107] M. Soja, "Electromagnetic models of bistatic radar scattering from rough surfaces with gaussian correlation function," Master's thesis, Chalmers University of Technology, 2009.

[108] N. Firoozy, P. Mojabi, and D. Barber, "Microwave remote sensing of multilayered rough-surface snow-covered sea ice dielectric profile: Sensitivity analysis and inversion," *Geoscience and Remote Sensing Symposium (IGARSS), IEEE International*, pp. 4872–4875, July 2014.

[109] D. Barber, A. Fung, T. Grenfell, S. Nghiem, R. Onstott, V. Lytle, D. Perovich, and A. Gow, "The role of snow on microwave emission and scattering over first-year sea ice," *Geoscience and Remote Sensing, IEEE Transactions on*, vol. 36, no. 5, pp. 1750–1763, Sep 1998.

[110] T. Geldsetzer and et. al., "Dielectric properties of brine-wetted snow on first-year sea ice," *Cold Regions Science and Technology*, vol. 58, no. 1-2, pp. 47–56, 2009.

[111] K. Golden and et. al., "Inverse electromagnetic scattering models for sea ice," *IEEE Trans. Geosci. Remote Sens.*, vol. 36, no. 5, pp. 1675–1704, 1998.

[112] K. Golden, M. Cheney, K.-H. Ding, A. Fung, T. Grenfell, D. Isaacson, J.-A. Kong, S. Nghiem, J. Sylvester, and P. Winebrenner, "Forward electromagnetic scattering models for sea ice," *Geoscience and Remote Sensing, IEEE Transactions on*, vol. 36, no. 5, pp. 1655–1674, 1998.

[113] A. Komarov, L. Shafai, and D. Barber, "Electromagnetic wave scattering from rough boundaries interfacing inhomogeneous media and application to snow-covered sea ice," *Progress in Electromagnetic Research*, vol. 144, pp. 201–219, 2014.

[114] U. of Manitoba. Sea-ice Environmental Research Facility (SERF) 2012. [Online]. Available: http://home.cc.umanitoba.ca/~wangf/serf/

[115] D. G. Barber, S. P. Reddan, and E. F. LeDrew, "Statistical characterization of the geophysical and electrical properties of snow on landfast first-year sea ice," *Journal of Geophysical Research: Oceans*, vol. 100, no. C2, pp. 2673–2686, 1995.

[116] A. Sihvola and J.-A. Kong, "Effective permittivity of dielectric mixtures," *IEEE Trans. Geosci. Remote Sens.*, vol. 26, no. 4, pp. 420–429, 1988.

[117] S. Adams, S. Willmes, D. Schroder, G. Heinemann, M. Bauer, and T. Krumpen, "Improvement and sensitivity analysis of thermal thin-ice thickness retrievals," *Geoscience and Remote Sensing, IEEE Transactions on*, vol. 51, no. 6, pp. 3306–3318, June 2013.

[118] F. Marzano and P. Bauer, "Sensitivity analysis of airborne microwave retrieval of stratiform precipitation to the melting layer parameterization," *Geoscience and Remote Sensing, IEEE Transactions on*, vol. 39, no. 1, pp. 75–91, Jan 2001.

[119] M. Drinkwater, "Limex87 ice surface characteristics: implications for C-band SAR backscatter signatures," *Geoscience and Remote Sensing, IEEE Transactions on*, vol. 27, no. 5, pp. 501–513, Sep 1989.

[120] S. V. Nghiem, R. Kwok, S. H. Yueh, and M. R. Drinkwater, "Polarimetric signatures of sea ice: 2. experimental observations," *Journal of Geophysical Research: Oceans*, vol. 100, no. C7, pp. 13 681–13 698, 1995.

[121] "Sea-ice Environmental Research Facility (SERF)." [Online]. Available: http://home.cc.umanitoba.ca/~wangf/serf/

[122] J. Sylvester and G. Uhlmann, "A global uniqueness theorem for an inverse boundary value problem," *Annals of Mathematics*, vol. 125, no. 1, pp. pp. 153–169, 1987.

[123] G. Poe, *A study of the microwave emission characteristics of the sea ice: Final technical report*, Aerojet ElectroSystems Company, Aerojet-General Corporation, 1972.

[124] J. Landy, D. Isleifson, A. Komarov, and D. Barber, "Parameterization of centimeter-scale sea ice surface roughness using terrestrial LiDAR," *Geoscience and Remote Sensing, IEEE Transactions on*, vol. 53, no. 3, pp. 1271–1286, March 2015.

[125] D. Barber, A. Fung, T. Grenfell, S. Nghiem, R. Onstott, V. Lytle, D. Perovich, and A. Gow, "The role of snow on microwave emission and scattering over first-year sea ice," *Geoscience and Remote Sensing, IEEE Transactions on*, vol. 36, no. 5, pp. 1750–1763, Sep 1998.

[126] D. Barber, "Microwave remote sensing, sea ice and Arctic climate processes," *Physics in Canada*, vol. Sept/Oct, pp. 105–111, 2005.

[127] N. Firoozy, P. Mojabi, J. Landy, and D. Barber, "Landfast first-year snow-covered sea ice reconstruction via electromagnetic inversion," *Selected Topics in Applied Earth Observations and Remote Sensing, IEEE Journal of*, 2016 (accepted for publication).

[128] N. Firoozy, A. Komarov, P. Mojabi, C. Landy, and D. Barber, "First-year snow-covered sea ice polarimetric NRCS inversion in Cambridge Bay, Nunavut," in *Geoscience and Remote Sensing Symposium, 2015. IGARSS 2015. IEEE International*, July 2015-Accepted.

[129] T. Geldsetzer, J. B. Mead, J. J. Yackel, R. K. Scharien, and S. E. L. Howell, "Surface-based polarimetric c-band scatterometer for field measurements of sea ice," *IEEE Transactions on Geoscience and Remote Sensing*, vol. 45, no. 11, pp. 3405–3416, Nov 2007.

[130] J. Landy, D. Isleifson, A. Komarov, and D. Barber, "Parameterization of centimeter-scale sea ice surface roughness using terrestrial lidar," *IEEE Trans. Geosci. Remote Sens.*, vol. 53, no. 3, pp. 1271–1286, March 2015.

[131] F. Ulaby, W. Stiles, and M. Abdelrazik, "Snowcover influence on backscattering from terrain," *IEEE Trans. Geosci. Remote Sens.*, vol. GE-22, no. 2, pp. 126–133, March 1984.

[132] D. Barber and A. Thomas, "The influence of cloud cover on the radiation budget, physical properties, and microwave scattering coefficient of first-year and multiyear sea ice," *IEEE Trans. Geosci. Remote Sens.*, vol. 36, no. 1, pp. 38–50, Jan 1998.

[133] E. P. W. Attema and F. T. Ulaby, "Vegetation modeled as a water cloud," *Radio Science*, vol. 13, no. 2, pp. 357–364, 1978.

[134] A. Fung, *Microwave Scattering and Emission Models and Their Applications*. Arctech House, 1994.

[135] A. Fung, W. Liu, K. Chen, and M. Tsay, "An improved iem model for bistatic scattering from rough surfaces," *Journal of Electromagnetic Waves and Applications*, vol. 16, no. 5, pp. 689–702, 2002.

[136] F. Koudogbo, P. F. Combes, and H.-J. Mametsa, "Numerical and experimental validations of iem for bistatic scattering from natural and manmade rough surfaces," *Progress In Electromagnetics Research*, vol. 46, pp. 203–244, 2004.

[137] W. C. Chew, *Waves and Fields in Inhomogenous Media*. Wiley-IEEE Press, 1999.

[138] P. Imperatore, A. Iodice, and D. Riccio, "Transmission through layered media with rough boundaries: First-order perturbative solution," *IEEE Trans. Antennas Propag.*, vol. 57, no. 5, pp. 1481–1494, May 2009.

[139] R. De Roo and F. Ulaby, "Bistatic specular scattering from rough dielectric surfaces," *IEEE Trans. Antennas Propag.*, vol. 42, no. 2, pp. 220–231, Feb 1994.

[140] N. Pinel, C. Bourlier, and J. Saillard, "Degree of roughness of rough layers: extensions of the rayleigh roughness criterion and some applications," *Progress In Electromagnetics Research*, vol. 19, pp. 41–63, 2010.

[141] C. A. Balanis, *Advanced Engineering Electromagnetics*. Wiley-IEEE Press, 1989.

[142] M. R. Drinkwater and C. G.B., "Modelling changes scattering in properties of the dielectric and young snow-covered sea ice at GHz frequencies," *Journal of Glaciology*, vol. 34, no. 118, 1988.

[143] L. Tsang, J. Kong, and K. Ding, *Scattering of Electromagnetic Waves: Theories and Applications*. John Wiley & Sons Inc., 2000.

[144] D. Barber, A. Fung, T. Grenfell, S. Nghiem, R. Onstott, V. Lytle, D. Perovich, and A. Gow, "The role of snow on microwave emission and scattering over first-year sea ice," *IEEE Trans. Geosci. Remote Sens.*, vol. 36, no. 5, pp. 1750–1763, Sep 1998.

[145] D. Barber, S. Reddan, and E. LeDrew, "Statistical characterization of the geophysical and electrical properties of snow on landfast first-year sea ice," *Journal of Geophysical Research: Oceans*, vol. 100, no. C2, pp. 2673–2686, 1995.

[146] A. Komarov, D. Isleifson, D. Barber, and L. Shafai, "Modeling and measurement of C-band radar backscatter from snow-covered first-year sea ice," *IEEE Trans. Geosci. Remote Sens.*, vol. 53, no. 7, pp. 4063–4078, July 2015.

[147] P. Imperatore, A. Iodice, and D. Riccio, "Physical meaning of perturbative solutions for scattering from and through multilayered structures with rough interfaces," *Antennas and Propagation, IEEE Transactions on*, vol. 58, no. 8, pp. 2710–2724, Aug 2010.

[148] R. Azadegan and K. Sarabandi, "Analytical formulation of the scattering by a slightly rough dielectric boundary, covered with a homogenous dielectric layer," in *Antennas and Propagation Society International Symposium, 2003. IEEE*, vol. 3, June 2003, pp. 420–423 vol.3.

[149] G. Franceschetti, P. Imperatore, A. Iodice, D. Riccio, and G. Ruello, "Scattering from layered structures with one rough interface: A unified formulation of perturbative solutions," *Geoscience and Remote Sensing, IEEE Transactions on*, vol. 46, no. 6, pp. 1634–1643, June 2008.

[150] A. G. Yarovoy, R. V. de Jongh, and L. P. Ligthart, "Scattering properties of a statistically rough interface inside a multilayered medium," *Radio Science*, vol. 35, no. 2, pp. 455–462, 2000.

[151] I. Fuks, "Wave diffraction by a rough boundary of an arbitrary plane-layered medium," *Antennas and Propagation, IEEE Transactions on*, vol. 49, no. 4, pp. 630–639, Apr 2001.

[152] P. Imperatore, A. Iodice, and D. Riccio, "On the regime of validity of volumetric and boundary perturbation -based scattering models for rough multilayer," in *Geoscience and Remote Sensing Symposium (IGARSS), 2012 IEEE International*, July 2012, pp. 3198–3201.

[153] M. Demir, J. Johnson, and T. Zajdel, "A study of the fourth-order small perturbation method for scattering from two-layer rough surfaces," *Geoscience and Remote Sensing, IEEE Transactions on*, vol. 50, no. 9, pp. 3374–3382, 2012.

[154] A. Stogryn, "Equations for calculating the dielectric constant of saline water (correspondence)," *Microwave Theory and Techniques, IEEE Transactions on*, vol. 19, no. 8, pp. 733–736, Aug 1971.

[155] G. P. deLoor, "de loor dielectric properties of heterogeneous mixtures containing water," *Journal of Microwave Power and Electromagnetic Energy*, vol. 3, pp. 67–73, 1968.

[156] W. R. Tinga, W. A. G. Voss, and D. F. Blossey, "Generalized approach to multiphase dielectric mixture theory," *Journal of Applied Physics*, vol. 44, no. 9, pp. 3897–3902, 1973.